Computational Analyses of Complex Flows with Chemical Reactions

by

Kang-Sik Bae

A Dissertation Presented in Partial Fulfillment
of the Requirements for the Degree
Doctor of Philosophy

Approved February 2012 by the
Graduate Supervisory Committee:

Taewoo Lee, Chair
Huei-Ping Huang
Ronald Calhoun
Patrick Phelan
Juan Lopez

ARIZONA STATE UNIVERSITY

May 2012

ABSTRACT

The heat and mass transfer phenomena in micro-scale for the mass transfer phenomena on drug in cylindrical matrix system, the simulation of oxygen/drug diffusion in a three dimensional capillary network, and a reduced chemical kinetic modeling of gas turbine combustion for Jet propellant-10 have been studied numerically. For the numerical analysis of the mass transfer phenomena on drug in cylindrical matrix system, the governing equations are derived from the cylindrical matrix systems, Krogh cylinder model, which modeling system is comprised of a capillary to a surrounding cylinder tissue along with the arterial distance to veins. ADI (Alternative Direction Implicit) scheme and Thomas algorithm are applied to solve the nonlinear partial differential equations (PDEs). This study shows that the important factors which have an effect on the drug penetration depth to the tissue are the mass diffusivity and the consumption of relevant species during the time allowed for diffusion to the brain tissue. Also, a computational fluid dynamics (CFD) model has been developed to simulate the blood flow and oxygen/drug diffusion in a three dimensional capillary network, which are satisfied in the physiological range of a typical capillary. A three dimensional geometry has been constructed to replicate the one studied by Secomb et al. (2000), and the computational framework features a non-Newtonian viscosity model for blood, the oxygen transport model including in oxygen-hemoglobin dissociation and wall flux due to tissue absorption, as well as an ability to study the diffusion of drugs and other materials in the capillary streams. Finally, a chemical kinetic mechanism of JP-10 has been compiled and validated

for a wide range of combustion regimes, covering pressures of 1atm to 40atm with temperature ranges of 1,200 K - 1,700 K, which is being studied as a possible Jet propellant for the Pulse Detonation Engine (PDE) and other high-speed flight applications such as hypersonic missiles. The comprehensive skeletal mechanism consists of 58 species and 315 reactions including in CPD, Benzene formation process by the theory for polycyclic aromatic hydrocarbons (PAH) and soot formation process on the constant volume combustor, premixed flame characteristics.

ACKNOWLEDGMENTS

Firstly, I would like to express my sincere appreciation to all who have been interested in my Ph.D. study. I would also like to thank all committee members who devoted their time to serve as the thesis committee.

I would like to give special thanks to Dr. Dan Robison in Phoenix Analysis and Design Technologies (PADT Inc.) for reviewing my dissertation in detail. Nevertheless his tight schedule, he helped me out to complete this dissertation with all his heart during my doctoral degree process. A thanks to Ian Vicino and Grant Rocha, Biochemistry and Political Science students at ASU who helped during the process. Also, I would like to give special thanks James C. Ianni for providing the KINTECUS computer software to my dissertation.

Now, being the load off my shoulders, I would like to finish a long journey for doctoral degree from Illinois Institute of Technology (2005 – 2007) to Arizona State University (2007-2012).

Immense thanks my wife, Eun-Hye Yun, for her constant and unwavering support and love during my entire track at Arizona State University. Without your devoted drive I would have never continued on my doctoral degree. Thank you to my sisters, Kang-Ja Bae and Kang-He Bae, for showing me the importance of family and forgiveness as well as for providing financial support during my doctoral degree process.

I know clearly I have a heap of debts from my family so far. So, I would like to dedicate myself to my lovely daughter, Su-Young Bae, and my wife from now on.

TABLE OF CONTENTS

Page

CHAPTER Page

CHAPTER Page

APPENDIX Page

LIST OF TABLES

LIST OF FIGURES

Figure Page

Figure Page

Figure Page

Figure Page

NOMENCLATURE

A	area [m^2]
D	diffusion coefficient [cm^2/sec]
E	activation energy [cal/g mol]
h	hill constant
L	capillary length [µm]
$PO_{2,in}$	oxygen partial pressure[mmHg]
Q	the volumetric flow rate [cm^3/sec]
R	gas constant [cal/g mol]
R_1	capillary radius [µm]
R_2	tissue radius [µm]
r_t	tissue radius
r_c	capillary radius
S	consumption rate [cm^3 O_2/cm^3/sec]
T_m	initial temperature of the fuel-air mixture [K]
t	time[µs]
v	average velocity[cm/sec]
W	solubility [cm^3 O2 /cm^3 /mmHg]

Greek symbols

Δt	time step [s]
ρ	density [kg m^{-3}]
ϕ	concentration (or partial pressure)

λ	relaxation time constant[sec]
η	shear viscosity[Pa-s]

Sub/Superscripts

n	present time step
$n+1$	future time step

Chapter 1

INTRODUCTION

This research is divided into an introduction section followed by three major analysis sections, which consist of mass transfer phenomena on the drug in cylindrical matrix system, its simulations of flow and oxygen diffusion in a three-dimensional capillary network, and a reduced chemical kinetics modeling of the combustion for Jet propellent-10.

The principal objective of this study is to build the calculation process for the complex flows with chemical reactions that can be made feasible in related engineering areas.

In Chapter 2 the governing equations are derived from the cylindrical matrix systems, Krogh cylinder model, which modeling system is comprised of a capillary to a surrounding cylinder tissue along with the arterial distance to veins. ADI (Alternative Direction Implicit) scheme and Thomas algorithm are applied to solve the nonlinear partial differential equations (PDEs). This study shows that the important factors which have an effect on the drug penetration depth to the tissue, are the mass diffusivity and the consumption of relevant species during the time allowed for diffusion to the brain tissue.

In chapter 3 a computational fluid dynamics (CFD) model is developed to simulate the flow, delivery of oxygen and other substances in a capillary network. A three-dimensional capillary network has been constructed to replicate the one studied by Secomb et al. (2000), and the computational framework features a non-Newtonian viscosity model of blood, the oxygen transport model including in-

stream oxygen-hemoglobin dissociation and wall flux due to tissue absorption, as well as an ability to study delivery of drugs and other materials in the capillary streams.

The model is first run to compute the volumetric flow rates from the velocity profiles in the segments, and compared with Secomb's work with good agreements. Effects of abnormal pressure and stenosis conditions, as well as those arising from different capillary configurations, on the flow and oxygen delivery are investigated, along with a brief look at the unsteady effects and drug dispersion in the capillary network.

The current approach allows for inclusion of oxygen and other material transport, including drugs, nutrients or contaminants based on the flow simulations. Also, three-dimensional models of complex circulatory systems ranging in scale from macro- to micro-vascular vessels, in principle, can be constructed and analyzed in detail using the current method.

In chapter 4 a reduced chemical kinetic mechanism of the combustion for hydrocarbon jet-fuel, JP-10 ($C_{10}H_{16}$) was studied. It has been studied as a possible Jet propellant for the Pulse Detonation Engine (PDE) and other high-speed flight applications such as aircraft-launched missiles.

It has been specifically targeted because of its high thermal stability and density properties, and availability. The thermal stability of JP-10 is only comparable to the conventional rocket fuel, RP-1. There are two benefits from an aerospace engineering point of view to using JP-10 over RP-1. JP-10 has a higher density, 0.94 g/cm^3 versus 0.81 g/cm^3, and JP-10 is a single molecule rather than a

mixture of paraffins and cycloparaffins. The decomposition of a single molecule is simpler to analyze and control than a mixture of hydrocarbon molecules.

The reaction mechanism used in this study has a strong hierarchical structure. A reduced kinetic mechanism consisted of 59 species and 315 reactions, which are listed in Appendix H. A constant-volume plug flow code was applied to this simulation. The conditions of interest are pressures from 1 - 40atm, inlet temperatures from 900K to 1,700K. Thermodynamic data file using in this study are mainly obtained from Burcat and NASA data.

Chapter 2

MASS TRANSFER PHOENAMENA ON DRUG IN A 2-D CYLINDERICAL MATRIX SYSTEM

2.1 Introduction

2.1.1 Objective and scope of research

The purpose of this study is to build the calculation process for the drug diffusion to the tissue from microcirculation along with the variation of oxygen pressure in cylindrical matrix system.

Time-dependent transport of drug and oxygen in a peripheral nerve by simulating drug and oxygen release, and consumption rate in capillaries and surrounding peripheral nerve tissue using Krogh tissue cylinder symmetry has been studied. This modeling system was made up from a capillary to a surrounding cylinder tissue along with arterial distance to veins.

The consumption rate was treated as a constant in the tissue to make a linear partial differential equation results. The capillary and the tissue equation are solved to give axial and radial oxygen partial pressure profiles for the total system. The drug transport and diffusion to the tissue from capillary was calculated with calculated oxygen conditions in advance.

This study show the facts that the factors have an effect on the drug penetration depth to the tissue were the mass diffusivity, the consumption rate during the time allowed for diffusion. Penetration depth can be controlled by the manipulation of these two factors. The conditions of interest are pressures from 95mmHg to 30mmHg, 0.04cm/sec of the oxygen velocity. All parameters and

materials using in the calculation were obtained from the literature.

Finally, to support the calculation process, the measured data are investigated here and validated through comparisons with O_2 partial pressure at lethal corner of the tissue.

2.1.2 Literature review

The materials presented herein have been described the historical development of the mathematical modeling of drug and oxygen transport to the tissue and the recent developments of multi component transcapillary exchange. It is presented in chronological order.

For the drug diffusion, the most well-known mathematical model of drug release from matrix systems is perhaps the Higuchi equation for planar systems and later it was extended to other geometries [4-5].

Higuchi assumed that the amount of drug initially present in the matrix was substantially larger than drug solubility, and described dissolution as being instantaneous. He divided the matrix into two regions; in one of these, all drugs are dissolved and a concentration gradient exists, and in the other, solid and dissolved drug coexist, making the dissolved drug concentration constant. Using a pseudo-steady state approximation for the drug concentration in the depletion zone, and taking the movement of the border between the zones into account, Higuchi derived his famous square root of time law.

The original Higuchi model has been the subject of numerous generalizations and improvements. Roseman and Higuchi, and later Tojo, included a boundary

diffusion layer in the model. Paul and McSpadden removed the pseudo-steady state approximation, and were able to derive an exact solution to the problem [6-8].

Since this solution is fairly complicated, and involves the solution of a transcendental equation, it has been developed an approximate analytical solution with an explicit expression for the release rate under sink conditions. Bunge proposed a simple adjustment of the original Higuchi equation, which drastically reduced the deviation from the exact solution of D.R.Paul [8, 9].

Abdekhodaie and Cheng derived exact solutions for drug release from both planar and spherical matrices into a finite volume of dissolution medium, which, however, have been criticized. Zhou and Wu made a similar derivation, for planar matrices, and included a boundary layer effect [10-12].

Siepmann and Peppas, among others, have published a series of papers dealing with the mathematical modeling of drug release from delivery systems based on hydroxypropyl methylcellulose. These authors have developed a detailed model combining matrix swelling, diffusion, and polymer dissolution [13].

However, although the effect of drug dissolution has been included, the gradual imbibitions of liquid into the matrix, concentration-dependent diffusion coefficients, and structural changes of the polymer as a result of drug dissolution, the assumption of instantaneous dissolution remains.

The effects of a finite dissolution rate were first investigated by Ayres and Lindstrom, who derived a mathematical model of drug release from suspensions. These authors were able to derive an upper bound of the amount of released drug

analytically, and studied drug release quantitatively by numerical methods. The analytical upper bound derived by Ayres and Lindstrom is fairly complicated, and requires the roots of a transcendental equation to be determined [14].

A more convenient expression for this quantity has been derived by Chandrasekaran and Paul, who treated the matrix as semi-infinite. Kubota et al. used a BASIC program to determine drug release according to the model of Ayres and Lindstrom, and used it to describe the release of betamethasone 17-valerate[15, 16].

Recently, a similar model has been devised by Frenning and Strømme [17], who studied drug release from spherical pellet units into a finite volume of dissolution medium, and also assumed that some of the dissolved drug could become immobilized by adsorption to the pellet constituents. The model is formulated in terms of a pair of coupled nonlinear partial differential equations, which are solved numerically, by using finite differences.

Also, drug release from matrix systems of cylindrical shape is analyzed in detail by using the finite element method by G Frenning [18]. The purpose of this article is to generalize the model of drug release from planar matrix systems and slowly dissolving drugs from spherical matrix systems, which takes the effects of a finite dissolution rate into account.

With the mentioned simplifications, the equations of the model of G. Frenning, in fact, turn out to be equivalent to those given in F.T. Lindstrom. Still, the resulting model is fairly complex and the equations, in general, need to be solved numerically [17, 19].

However, as we demonstrate, it is possible to derive an approximate analytical expression for drug release, which describes the major parts of the release process well. This analytical solution is compared to the numerical one and to drug release models existing in the literature derived under the assumption that dissolution is instantaneous.

For the oxygen diffusion, we reviewed the Krogh cylinder model for the capillary microcirculation and give mathematical descriptions for general conditions. These descriptions will include most previous Krogh models as special cases. Alternative models and other concepts will be considered and discussed following this development.

The first interest in mathematical modeling of the microcirculation developed from experimental investigations to determine the arrangement of blood vessels in tissue. These experiments were being conducted as a result of interest in the mechanism by which oxygen was transported from blood to tissue and how this transfer could be controlled.

August Krogh [20, 21] credited with motivating and laying the basis for the first conceptual models of the microcirculation from about 1918 to 1929. Krogh theorized that the rate of oxygen transport was related to the number and arrangement of capillaries in tissue and to the permeability to oxygen of the capillary walls and surrounding tissues. The first experimental efforts were aimed at obtaining an adequate knowledge of the number, distribution, and surface area of capillaries in muscle tissue. Krogh's investigations showed that, in a cross-section of striated muscle, open capillaries were distributed quite uniformly.

Based on this observation, he concluded that each capillary could be regarded as running parallel to the muscle tissues and supplying a concentric region of tissue surrounding that capillary, and this tissue region was independent of the other parallel capillaries and tissues they supplied. Krogh determined the average radius of a hypothetical tissue cylinder by counting the capillaries in each cross-section and dividing the cross-section's area by the number of capillaries that he found.

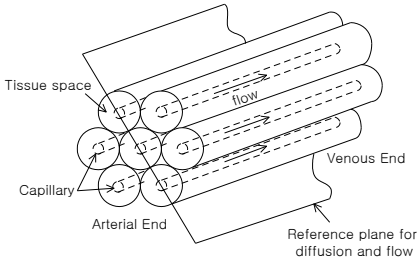

Figure 2.1 A geometric arrangement of the capillaries surrounded by the tissue

Krogh recognized that such an ideal physical geometric arrangement, shown in Figure 2.1, was amenable to a mathematical description. Krogh described the conceptual model in terms of mathematics with a colleague, the Danish mathematician Erlang. The result was the now famous Krogh-Erlang equation given by

$$\phi(r,z) = \phi_0(z) - \frac{K}{2D_r}\left[r_t^2 \log\left(\frac{r}{r_c}\right) - \frac{1}{2}(r^2 - r_c^2)\right]$$

on the tissue annulus $r_c \leq r \leq r_t$, and where $\phi(r,z)$ is the concentration (or partial pressure) of oxygen in volumes of gas per volume of tissue, the tissue radius is r_t, the capillary radius is r_c, the radial oxygen diffusion coefficient is D_r, and the constant rate of oxygen consumption is K.

Although a highly simplified model, the Krogh tissue cylinder model was a

major step in the study of substrate supply to living tissue. He not only initiated the analytical study but set the course for its study from 1919 to the present day.

Krogh also was the first to measure (determine) rates at which oxygen diffuses through tissues, and to originate many other measurements essential to the modeling process. In spite of the passage of time and the development of new, modem methods, many of his techniques and parameter values are still found to be accurate and valid for use in modeling studies of today.

Following Krogh's initial studies, several investigators considered the diffusion of oxygen, lactic acid, and other metabolites through tissues. A. V. Hill in 1928 derived equations which extended the steady state models of Krogh to the unsteady state [22].

However, Hill did not apply his models to geometries or conditions representative of living tissues; thus his results contributed mostly to the formulation of concepts and equations describing the diffusion process rather than applications to actual circulatory systems. Other general treatments of diffusion models were later published by Crank in 1956 [1].

John E. Fletcher studied this complex physic-chemical system by means of a tractable mathematical model clearly necessitates a number of simplifications. This model described (a) unsteady capillary transport by convection, (b) the unsteady substrate exchange kinetics within the capillary, (c) diffusion across a finitely permeable capillary wall and (d) unsteady diffusion and consumption of substrate within the tissue apace [23].

In fact, it was long assumed that changes in cerebral blood flow (CBF) and

in the cerebral metabolic rate of oxygen ($CMRO_2$) are tightly coupled in both resting and active brain state. Recently, the close correlation between resting regional cerebral blood flow and metabolism is well established and implies the presence of a physiological coupling mechanism [24].

Whether cerebral blood flow and cerebral metabolic rate for oxygen is coupled during functional activation of the brain is unclear. Several principal studies in humans and experimental animals suggested that during brief functional activation, regional cerebral blood flow increases more than regional cerebral metabolic rate for oxygen, raising the question whether cerebral blood flow and cerebral metabolic rate for oxygen are mechanistically coupled during transient increases in neuronal activity [25].

An uncoupling of neuronal activity-dependent changes in cerebral blood flow and in blood oxygenation has been postulated as the basic mechanism of contrast generation in functional magnetic resonance imaging. However, the physiological reasons for a greater increase in cerebral blood flow than in cerebral metabolic rate for oxygen during functional activation remains obscure [26].

Also, Buxton and Frank examined the mathematical relationship between cerebral blood flow and cerebral metabolic rate for oxygen using a single-compartment model of O_2 extraction in cerebral tissue. Their calculations predicted that disproportionately large increases in blood flow were required to support relatively small increases in oxidative metabolic rate, which is a result consistent with the apparent uncoupling of cerebral blood flow and cerebral metabolic rate for oxygen [27].

This extreme sensitivity of tissue oxygenation to blood flow was introduced into the model by the assumption of a diffusion barrier at the vascular wall. The presence of oxygen diffusion gradients and the resulting heterogeneity in tissue pO_2 were not included in the model.

When O_2 leaves the capillary, it diffuses along its concentration gradient established by the spatial distribution and rate of oxygen utilization of the mitochondria. The shape of the O_2 diffusion field varies as a function of the O_2 supply and O_2 demand local cerebral metabolic rate for oxygen. The median tissue pO_2 measured in the cerebral cortex of resting, anesthetized animals is 16 mmHg, with a significant number of values below 10 mmHg [28].

Nevertheless, local O_2 utilization does not fail until tissue pO_2 falls below 12 mmHg. Also, the nonlinear dissociation of blood oxyhemoglobin facilitates the unloading of O_2 as intravascular pO_2 falls toward the venous end of the capillary. These phenomena should be included in the estimation of O_2 supply and demand balance during functional activation.

Mintun et al.(2001) [29] performed the image processing by using Positron Emission Tomography (PET) during states of visual activation and hypoxia to examine the relationship of Cerebral Blood Flow (CBF) and oxygen delivery. Image data were derived from quantitative PET blood flow scans that were normalized for variations in global blood flow. Each of nine subjects underwent scanning in two blocks: one block during breathing room air and a second block during hypoxia induced by reducing the inspired O_2 fraction.

In each block, PET studies were done during two control tasks and two visual activation tasks. (*A*) Average blood flow image from the control scans. (*B*) Mean subtraction image (visual activation minus control task) while breathing room air. (*C*) Average subtraction (visual activation minus visual fixation) image during hypoxia scaled to the same maximum as *B*. The black circle illustrates the relative size and position of the spherical region-of-interest used for quantitation of the regional visual cortex CBF.

Note the similarity in magnitude and distribution of the increased blood flow during visual activation. No augmentation of the blood flow response is seen despite the presence of reduced arterial oxygen content [29].

This review is introductory, and is not intended to be comprehensive; also, detailed studies unknown to the author undoubtedly exist in the literature.

2.2 The hypothesis of mathematical theory

Diffusion is the process by which matter is transported from one part of a system to another as a result of random molecular motions. The transfer of heat by conduction is also due to random molecular motions, and there is an obvious analogy between the two processes. This was recognized by Fick (1855) [1], who first put diffusion on a quantitative basis by adopting the mathematical equation of heat conduction. The mathematical theory of diffusion in isotropic substances is therefore based on the hypothesis that that rate of transfer of diffusing substance through unit area of a section is proportional to the concentration gradient measured normal to the section, i.e.

$$F = -D\frac{\partial \phi}{\partial x} \qquad (2.1)$$

where F is the rate of transfer per unit area of section, ϕ the concentration of diffusing substance, x the space coordinate measured normal to the section, and D is called the diffusion coefficient. In some cases, e.g. diffusion in dilute solutions, D can reasonably be taken as constant, while in others, e.g. diffusion in high polymers, it depends very markedly concentration. If F, the amount of material diffusing, and ϕ, the concentration, are both expressed in terms of the same unit of quantity, e.g. gram or gram molecules, then it is clear from Equation (2.1) that D is independent of this unit and has dimensions $(\text{length})^2\ (\text{time})^{-1}$, e.g. cm^2/sec. The negative sign in Equation (2.1) arises because that the diffusion occurs in the direction opposite to that of increasing concentration.

It must be emphasized that the statement expressed mathematically by Equation (2.1) is in general consistent only for an isotropic medium, whose structure and diffusion properties in the neighborhood of any point are the same relative to all directions. Because of this symmetry, the flow of diffusing substance at any point is along the normal to the surface of constant concentration through the point.

2.3 The Conceptual model of the microcirculation

Circulatory systems in higher organisms consist of a series of interconnecting vessels which provide substrates through the pumping action of the heart. The total circulation, made up of the systemic and pulmonary branches, is generally divided into two categories for study.

The major circulation in each branch consists of the large arteries and veins and the small arteries and veins. These vessels generally have diameters greater than 100 µm (10^{-4} meters) and lengths exceeding 750µm**.**

As seen in Figure 2.2 the microcirculation consists of arterioles, pre-capillary arterioles, capillaries, post-capillary venules, and venules. Many investigators have also reported arteriovenous shunts that are called "false capillaries". The function of these vessels is not known [30].

The microcirculatory vessels decrease in size with regular branching (anastomoses) to minimums of approximately 5 µm (5×10^{-6} m) in diameter and 100 to 600 µm in length. The particular minimum diameter and length depends on vessel type and the tissue being considered.

In the macrocirculation, the substrates, sometimes combined with other substances, are transported by flow convection. In the microcirculation, starting at about the end of the pre-capillary arteriole and terminating at the metabolic site in the living cell, the substrates move under the influence of a number of different factors.

While being flow transported within the microcirculation in Figure 2.2, the substrate leaves the plasma, crosses the vessel wall, and diffuses into the tissue. Within the tissue, the substrate diffuses in a three dimensional region across many different histological structures and fluid spaces. In some tissues, such as red muscle, it may also combine reversibly with tissue components for temporary storage or facilitated diffusion. Eventually, the substrate reaches the metabolic site in the cell and is consumed.

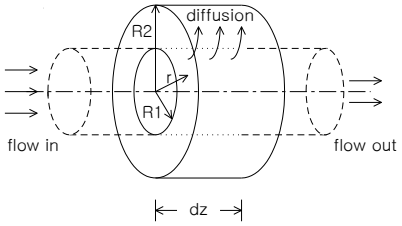

Figure 2.2 A single Krogh tissue cylinder model

Clearly any attempt to describe this complex transport and physiochemical process by means of a physical and mathematical model necessitates a number of idealizations and simplifications. The physical representation of a solid mass tumor is a cylindrical capillary surrounded by a cylindrical mass of tumor cells. Therefore, we were able to assume an axi-symmetric geometry. This simplified geometry was used to model a solid mass tumor in order to reduce the computational processing needed to run the simulation.

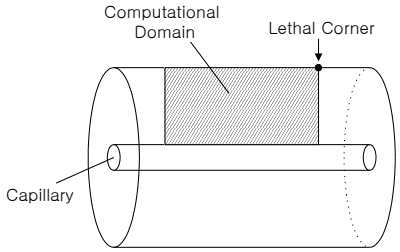

Figure 2.3 Computational domain

Figure 2.3 depicts the 3D representation of the capillary, with the computational domain representing the region of focus in our model. Figure 2.4 show a computed surface with respect to the tissue space of blue-out section in Figure 2.3. The lowest value on the surface occurs at the one point, which is called a lethal corner in this study.

In attempting to formulate functional relationships among the factors just mentioned, one recognizes the purely local character of some of them (e.g., the

value of the diffusion coefficient at a given point and in a given direction) as well as the global nature of others (e.g., the geometrical structure and arrangement of the microcirculatory networks relative to the tissues they supply).

The first factors essentially determine the form of the distributed parameter differential expressions, while the latter determine the domain of definition of these expressions and their associated boundary conditions.

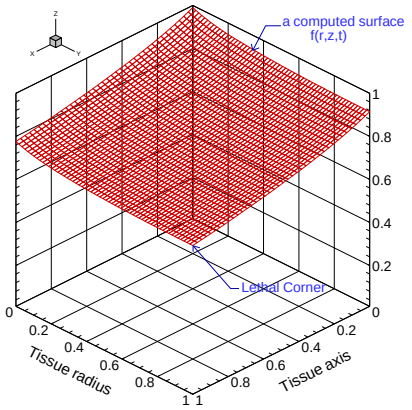

Figure 2.4 A computed surface of drug distribution within a Krogh cylinder tissue space

2.4 Assumption of the flow field

To reduce the complexity of this transport problem to a tractable set of equations, certain assumptions are necessary. Their use leads to an eventual solution for each case studied, but also limits the applicability of the model. The following assumptions have been carefully used to simplify the problem:

1. The system is 2-dimensional axisymetric.

2. The blood velocity is constant and uniform across a capillary cross-section.

3. The diffusion of both the drug and the oxygen to the tissue is from the plasma phase.

4. The drug may be assumed to be completely dissolved in the initial state (i.e., before any release has occurred), and the drug concentration in the matrix is, consequently, the solution to the well-known homogeneous diffusion.

5. There exists a region of tissue which surrounds a given capillary and forms a discrete unit in which the major contributions in the exchange of vital substance taken place.

2.5 Governing Equations

2.5.1 Tissue Equation

Based on the previous assumptions, Fick's first law of diffusion and the conservation of mass, the following set of interactive non-linear partial differential equations for the capillary and tissue regions has been derived. The derivations can be found in Appendix A. Further information on the theory and mathematics of diffusion can be found in Crank [1-3]. Note that the numerical method for the steady state uses an Alternating Direction Implicit(ADI) scheme (see Appendix A) and therefore requires initial or starting conditions be specified for each component. The values for each component over the entire region are set to the arterial inlet concentration.

For drug and oxygen, the general tissue equations can be given by

$$\frac{\partial \phi_i^t}{\partial t} = D_i^t \left(\frac{\partial^2 \phi_i^t}{\partial r^2} + \frac{1}{r} \frac{\partial \phi_i^t}{\partial r} + \frac{\partial^2 \phi_i^t}{\partial z^2} \right) + S_i \qquad (2.2)$$

where, D=diffusivity [cm^2/sec], S=consumption rate [cm^3 O_2/cm^3/sec]

The boundary conditions are as follows:

At r = R_1 $\quad \phi_o|_{R1} = \phi_o^t|_{R1}$

$$\phi_D|_{R1} = \lambda\phi_D^t|_{R1}$$

Also,

$$J_i^r|_{R1} = -D_i^t \frac{\partial \phi_i^t}{\partial r}\Big|_{R1}$$

Where i=drug, and

$$J_i^r|_{R1} = -D_i^t S_i^t \frac{\partial \phi_i^t}{\partial r}\Big|_{R1}$$

Where i= oxygen

At r = R_2

$$\frac{\partial \phi_i^t}{\partial r}\Big|_{R2} = 0 \quad \text{(i=Oxygen)}$$

$$\frac{\partial \phi_i^t}{\partial r}\Big|_{R2} = 0 \quad \text{(i=Drug)}$$

2.5.2 Transport equation for drug in capillary

$$\frac{\partial \phi}{\partial t} + v\frac{\partial \phi}{\partial z} + \frac{2J^r|_{R1}}{R1} = D\frac{\partial^2 \phi}{\partial z^2} \qquad (2.3)$$

where, $J^r = -D\frac{\partial \phi}{\partial r}$

The capillary of length *L* between entrance and exit (see Figure 2.2) are included to allow for the axial diffusion. The boundary conditions are as follows:

For r=R1

$J_i^r|_{R1}$= a constant for each Z (i= drug)

2.5.3 Transport equation for Oxygen in the capillary

$$X_i = X_a - \left(\frac{S}{\gamma_1 v}\right)\frac{\left(R_2^2 - R_1^2\right)}{R_1^2}\Delta l \tag{2.4}$$

$$\phi_i = \left(\frac{\gamma_2 X_i}{l - X_i}\right)^{\gamma_3} \tag{2.5}$$

where the meaning of symbols and their selected values under control conditions are: X: oxygen saturation of blood in the capillary; X_a : oxygen saturation of blood in the a pre-capillary arteriole; ΔL: width of an axial tissue slice, S rate of oxygen consumption, R_2 : radius of a tissue cone, R_1 : radius of a capillary, v: velocity of blood in the capillary, ϕ_i : Partial pressure of O_2 in blood within the capillary; γ_1 to γ_2 : constants, which are obtained from A G. Hudetz [31].

2.6 The numerical method

The use of finite difference approximations to replace the derivatives has been the customary way to solve the tissue and transport equations. The Price, Varga, Warren (PVW) [34] Non-Central analogs was applied to approximate the tissue and drug transport equation. These methods are for non-oscillatory with any spatial grid size, which is useful to decrease non linearity. The PVW analogs have a similarity with Crank-Nicolson [35] analogs except for the first derivative approximations, which is a non-central three point difference. The following analogs are written about the half level in time.

$$\phi_i^{n+\frac{1}{2}} = \frac{1}{2}\left(\phi_i^{n+1} + \phi_i^{n}\right) \tag{2.6}$$

$$\left(\frac{\partial \phi}{\partial t}\right)_i^{n+\frac{1}{2}} = \frac{\left(\phi_i^{n+1} + \phi_i^n\right)}{\Delta t} \tag{2.7}$$

$$\left(\frac{\partial \phi}{\partial z}\right)_i^{n+\frac{1}{2}} = \frac{1}{2}\left(\frac{\left(3\phi_i^{n+1} - 4\phi_{i-1}^{n+1} + \phi_{i-2}^{n+1}\right)}{2\Delta z} + \frac{\left(3\phi_i^{n} - 4\phi_{i-1}^{n} + \phi_{i-2}^{n}\right)}{2\Delta z}\right) \tag{2.8}$$

or

$$\left(\frac{\partial \phi}{\partial z}\right)_i^{n+\frac{1}{2}} = \frac{1}{2}\left(\frac{\left(\phi_i^{n+1} - \phi_{i-1}^{n+1}\right)}{\Delta z} + \frac{\left(\phi_i^{n} - \phi_{i-1}^{n}\right)}{\Delta z}\right) \tag{2.9}$$

$$\left(\frac{\partial^2 \phi}{\partial z^2}\right)_i^{n+\frac{1}{2}} = \frac{1}{2}\left(\frac{\left(\phi_{i+1}^{n+1} - 2\phi_i^{n+1} + \phi_{i-1}^{n+1}\right)}{\Delta z^2} + \frac{\left(\phi_{i+1}^{n} - 2\phi_i^{n} + \phi_{i-1}^{n}\right)}{\Delta z^2}\right) \tag{2.10}$$

Where *i* is the axial position and *n* is the index on time.

The Crank-Nicolson analogs were also used in writing the finite difference approximations to the radial diffusion term. It is written about the half level in time and the i^{th} position in the radial direction for some given axial position.

$$\left(\frac{\partial \phi}{\partial r}\right)_i^{n+\frac{1}{2}} = \frac{1}{2}\left(\frac{\left(\phi_{i+1}^{n+1} - \phi_{i-1}^{n+1}\right)}{2\Delta r} + \frac{\left(\phi_{i+1}^{n} - \phi_{i-1}^{n}\right)}{2\Delta r}\right) \tag{2.11}$$

The finite difference equation of the drug transport equation was solved by using of the general band algorithm, which is described in Appendix B. The description of this general algorithm can be found in Von Rosenberg [36].

The tissue equation was solved by using of the Alternating Direction Implicit (ADI) scheme and general TDMA (Tridiagonal matrix algorithm) [2, 37]. The process of getting a tridiagonal coefficient matrix for computing the tissue equation is to make a traverse of the nodes across the rows and consider the values above and below each node to be constants. These constants go on the right hand sides of the equations as well. After all the nodes have been given new values with the horizontal traverse, we now make a traverse of the nodes by

columns, assuming for this step that the values at nodes to the right and left hand side are constants. There is an obvious bias in these computation processes, but it in the horizontal traverse is balanced by the opposing one of the second step. The process is described in Appendix A.

The numerical solutions allowed to reach a steady state were compared to the steady-state analytical solutions. There is a no-flux at the outer edge of the tissue. In order to reduce non-linearity the finite difference analogs are written about the half level in time, the non-linear terms are calculated using the average value of the dependent variable between the time steps.

$$\phi = \frac{1}{2}(\phi_{i+1}^{n+1} + \phi_i^n) \qquad \text{for n= 1,2,}\cdots \tag{2.12}$$

Here *n* is the index for the nth iteration. The old value is applied in time for the first iteration. The value of ϕ_{i+1}^n is continually upgraded with each successive iteration for the given time step until it is reached at convergence. The convergence criteria are less than 10^{-5}. If a convergence criterion is higher than unity, the results calculated would be similar with that of the analytical solution. It can be defined by user.

The numerical analysis methods used in this study had complicated structures based on the literature [34, 35]. Also, they were being based on well-established subroutines developed earlier including the diffusion, mass flux, general band, general TDMA where the Alternative Direction Implicit(ADI) scheme have been edited for solving the tissue equation, which are listed in Appendix E. The derivations of the analytical solutions are summarized in

Appendix C-D [23, 31, 32 – 34, 38, 39]. The computer capacity using calculation was a 2.4 GHz with 4GB RAM, and Pentium IV Quad processor.

2.7 Application to oxygen diffusion

2.7.1 Material and parameters

Initial conditions used in this modeling, which are based on the physiological range of a typical capillary, are listed in table 2.1

Table 2.1 Dimension and parameter values used in the modeling

Parameters			Description
Capillary Space			
$PO_{2,in}$	30,50,70,95	mmHg	partial pressure
R_1	2.5	µm	capillary radius
L	200	µm	capillary length
V	0.04	cm/sec	average velocity
D_{O2}	1.85×10^{-5}	cm^2/s	diffusivity
S	8.34×10^{-4}	ml / cm^3 sec	consumption rate
h1	0.25		hill constant
Tissue space			
R_2	32	µm	tissue radius
D_{O2}	1.85e-05	cm^2/s	diffusivity
S	8.34×10^{-4}	ml / cm^3 sec	consumption rate
W	2.6×10^{-5}	cm^3 O2 /cm^3 /mmHg	solubility

2.7.2 Oxygen Consumption Rate

The percentage of total incoming oxygen lost from the capillary to the tissues was determined from an overall mass balance on the capillary space comparing the inlet and outlet pO_2 values. The oxygen consumption rate (S) is the rate of

oxygen delivered to the tissues for a given tissue volume,

$$S = \frac{(pO_{2,in} - pO_{2,out})Q}{V_{tissue}}$$

Where Q is the volumetric flow rate, which is a specified model parameter and V_{tissue} is the volume of the whole tissue space, $pO_{2,in}$ and $pO_{2,out}$ are the pressure in inlet and outlet.

2.7.3 Numerical Results and discussion

In Figure 2.5 solutions of the model were first obtained to demonstrate that the model correctly predicted tissue PO_2 distribution in the normal state. Brain tissue oxygen levels at lethal corner using model simulation and neuronal activation are displayed, assuming an arterial PO_2 of 95mmHg. PO_2 histograms calculated using the Krogh cylinder model was compared with the data of Mintun et al. (2001), which have the difference of less than 12% that was an allowable different if we consider 22% of radius difference between 2.5µm(present study) and 3.2µm in capillary [29].

Also, this error is introduced through the radial flux term that ties the capillary and tissue mass balances in the diffusion model with a three point finite difference approximation. Based on the grid size chosen for the radial direction, the error in the flux is always negative, i.e., less oxygen diffuses into the tissue from the capillary.

Cerebral blood flow was held fixed at baseline values to determine whether tissue PO2 would decrease below viable levels. The data show that even without

increasing cerebral blood flow the tissue can maintain adequate oxygen levels for oxidative metabolism under all of these conditions. The level of arterial PO_2 that can be reached before cerebral blood flow would have to increase because of the lack of oxygen in the tissue was determined to be approximately 30 mmHg. The ‘‘lethal corner’’ is seen to be well above critical level (PO_2 = 1 mmHg) in this control state.

The steady state capillary partial pressure profiles for oxygen are shown in Figure 2.6. The graph shows the large gradient of oxygen down the capillary as the blood travels from the arterial to venous end of the capillary, producing steep axial gradients, as well as the oxygen concentration in the tissue moving radially out from these data as initial conditions in the capillary.

In Figure 2.7, the steady state results to normal and arterial hypoxia are shown. There is a steep drop in the pO_2. In arterial hypoxia, the pO_2 of the entering blood is 45mmHg. Note in Figure 2.6 that the partial pressure drop in oxygen from arterial to venous end is 30mmHg as compared to 65 mmHg under normal conditions. As arterial O_2 pressure decreased, the pO2 distribution at the outer boundary of this tissue was remarkably flat. Under these PO_2’s, the release of oxygen from the hemoglobin is operating at the steepest part of the saturation curve, which means a small change in PO_2 releases large amounts of oxygen.

Next we simulated the effect of moderate hypoxemia PO_2 45 mmHg without an increase in capillary flow velocity in Figure 2.8. Most of the pO2 values at normal condition ($pO_{2,in}$ =95mmHg) are in the 15 – 50 mmHg range. There are a few values between 10 to 15mmHg. All PO_2 values remained above 1 mmHg.

The mean tissue PO_2 was 37.6mmHg.

It illustrates that hypoxemia with unchanged capillary flow significantly reduced tissue PO_2 and produced a region of anoxia surrounding the venous end of the capillary PO_2 1 mmHg. When there is an anoxic region developed in the tissue due to insufficient supply of oxygen, the oxygen consumption decreases, which mean less tissue is respiring.

In next three Figure 2.9 – 2.11 the O_2 diffusion models were calculated to examine the effect of increasing oxygen consumption rate. The pO_2 field was calculated for two situations: $CMRO_2$ increased by 15% and by 30% without change in capillary flow. As seen in the first figure, all pO_2 values remained above 1 mmHg, although the average tissue pO_2 was reduced 45.56mmHg at 15% and 43.37 mmHg at 30% $CMRO_2$ increase, respectively. However, in case of hypoxia in the second figure when the average tissue pO_2 was reduced 14.86mmHg at 15% and 14.09 mmHg at 30% $CMRO_2$ increase, the region that PO_2 values remained below 1 mmHg increase to 9.21% at 15% and 17.29% at 30% $CMRO_2$ increase, respectively. With each elevation of $CMRO_2$, tissue pO_2 fell but could be compensated by an appropriate increase in capillary flow. For the capillary to successfully supply oxygen to all surrounding brain tissue, cellular pO2 levels must not drop below 1 mmHg. When cellular pO2 is above 1 mmHg, oxygen consumption rate is the limiting factor, and oxygen consumption is maintained. For any given configuration of the model the pO2 level in the ‘‘lethal corner’’ indicates whether all brain tissue is successfully oxygenated [40].

In Figure 2.12 the relationship between $CMRO_2$ and oxygen partial pressure

drop at lethal corner was calculated because that oxygen supply is characterized by the average tissue pO_2 at the venous end of the Krogh cylinder as a representative value of tissue oxygenation in the weakly supplied micro regions. It is evident from the figure 2.12 that the curve relating oxygen partial pressure at lethal cornet to consumption rate is linear down to until before the arterial PO_2 will be reached at hypoxia level of 60mmHg at normal, 65mmHg at 15% and 70mmHg at 30% $CMRO_2$ increase, respectively. From this figure, we can see even if arterial oxygen partial pressure of 75mmHg at 30% CMRO2 increase, the brain tissue PO2 would be ischemia state(PO_2 < 1mmHg).

In Figure 2.13 it shows that the proportional relationship between arterial oxygen partial pressure and average tissue oxygen pressure. As we expected, as PO_2 decreased, the average tissue oxygen pressure reduced. However, this curve was not linearly down as well as the reduction rate was a little bit slow downed from 60mmHg.

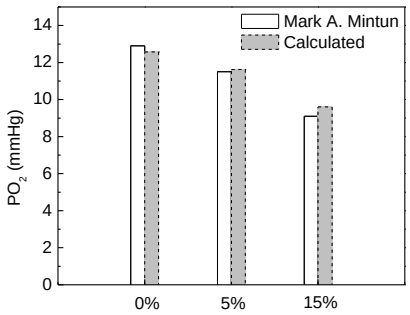

Figure 2.5 Comparison of O_2 partial pressure at lethal corner of the tissue between calculated values and Mark A. Minton [29]

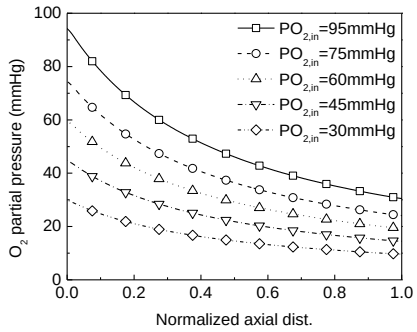

Figure 2.6 O_2 partial pressure distributions in the capillary

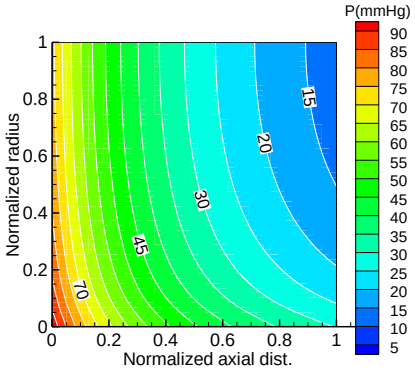

PO_{in} =95mmHg

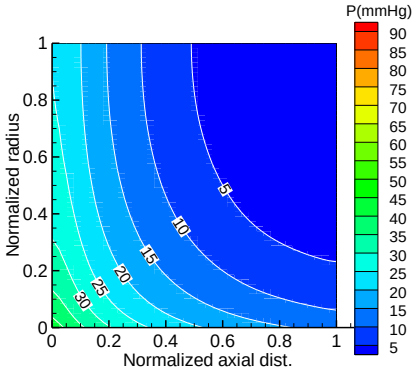

PO_{in} =45 mmHg

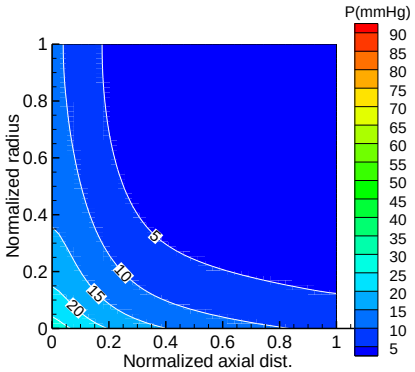

PO_{in} =30 mmHg

Figure 2.7 pO_2 distributions on the tissue with the variation of $PO_{2,in}$

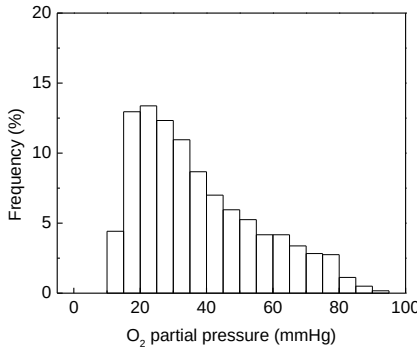

$PO_{2,in}$=95, (3-D), Interval=5mmHg, Mean= 37.61, size=2400

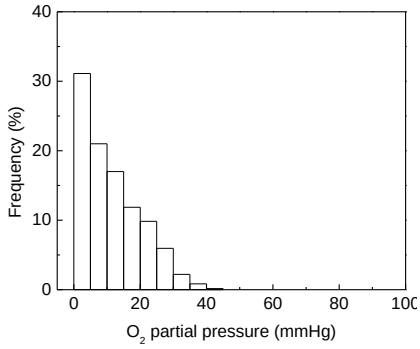

$PO_{2,in}$=45, (3-D), Interval=5mmHg, Mean= 11.31, size=2400

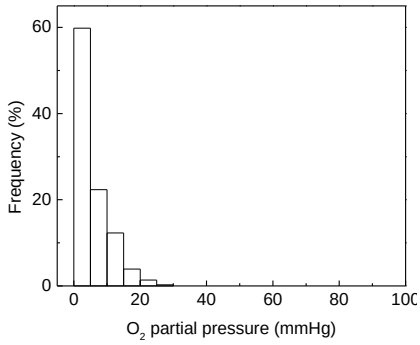

$PO_{2,in}$=30, (3-D), Interval=5mmHg, Mean= 5.15, size=2400

Figure 2.8 pO2 Histogram calculated on the tissue space with the variation of $PO_{2,in}$

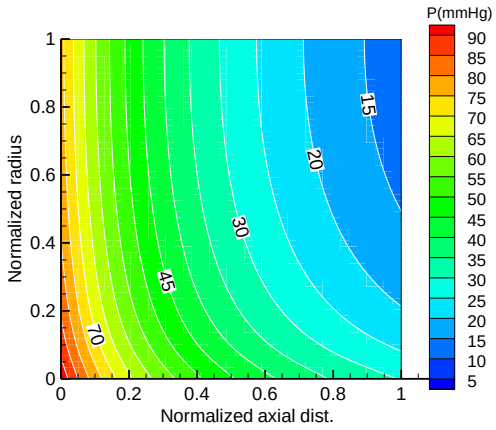

PO_{in} =95 mmHg, S(2-D)

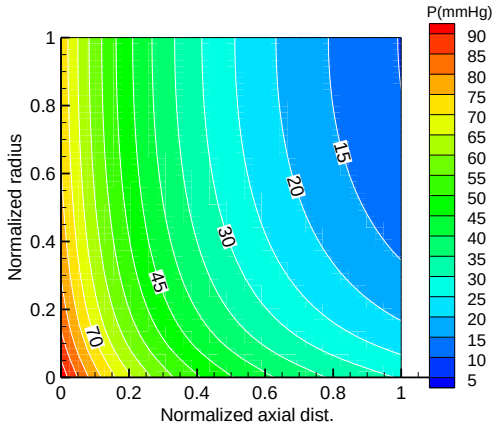

PO_{in} =95 mmHg, S×1.15(2-D)

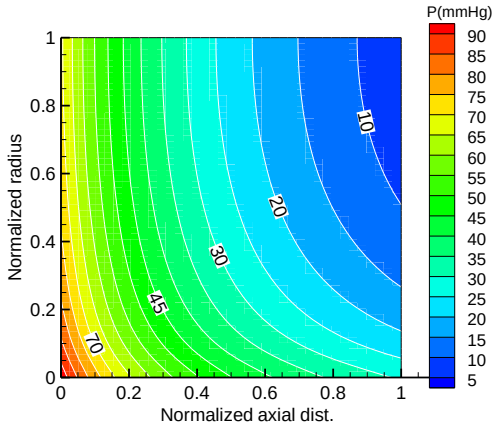

PO_{in} =95 mmHg, S×1.30(2-D)

Figure 2.9 pO_2 distributions on the tissue with the variation of the consumption rate at $pO_{2,\,in}$ of 95mmHg

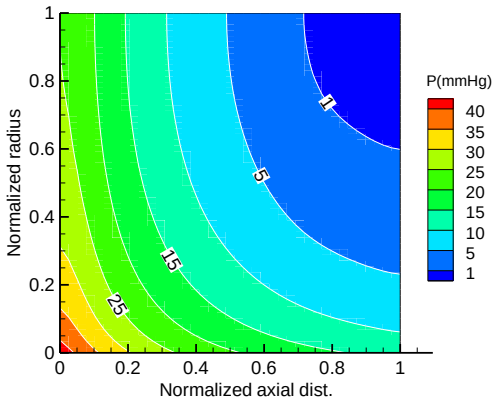

PO_{in} =45 mmHg, S

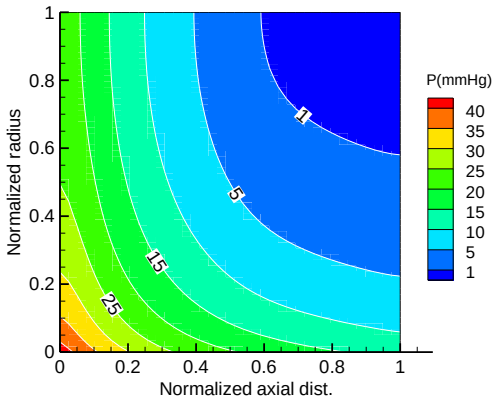

PO_{in} =45 mmHg, S×1.15

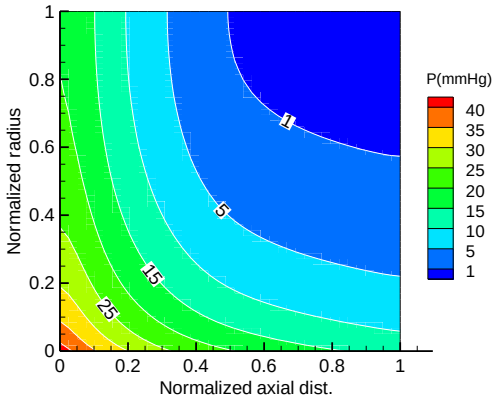

PO_{in} =45 mmHg, S×1.30

Figure 2.10 pO_2 distributions on the tissue with the variation of the consumption rate at $pO_{2,in}$ of 45mmHg

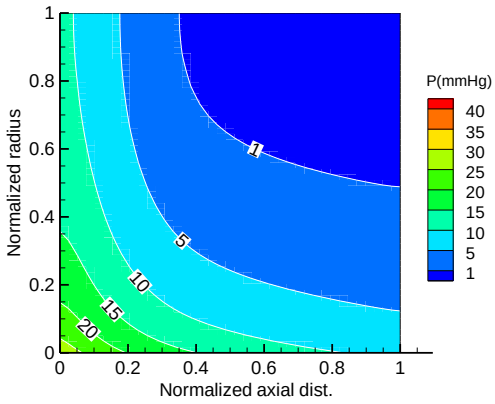

PO_{in} =30 mmHg, S (2-D)

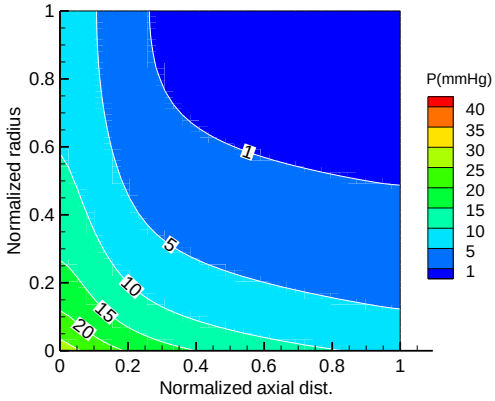

PO_{in} =30 mmHg, S×1.15 (2-D)

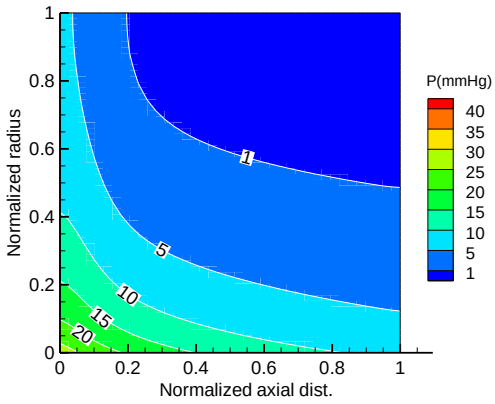

PO_{in} =30 mmHg, S×1.30 (2-D)

Figure 2.11 pO_2 distributions on the tissue with the variation of the consumption rate at $pO_{2,\,in}$ of 30mmHg

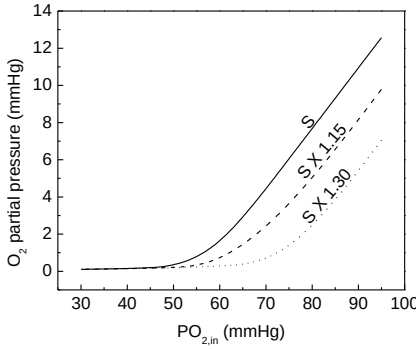

Figure 2.12 O_2 partial pressure at lethal corner with variation of the consumption rate

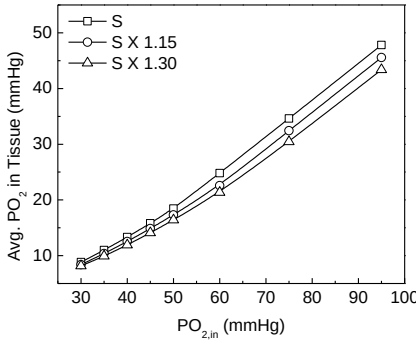

Figure 2.13 Average O_2 partial pressures in the tissue with variation of the consumption rate

2.8 Application to Drug diffusion

2.8.1 Material and parameters

Acetylsalicylic acid (ASA; Sigma-Aldrich ChemieGmbH, Germany; apparent density of 1.35 g/cm3) was used to do the modeling. Initial conditions, which are based on the physiological range of a typical capillary, are given in table 2.2

Table 2.2 Dimension and parameter values used in ASA modeling

Parameters			Description
Capillary Space			
$PO_{2,in}$	30,50,70,95	mmHg	partial pressure
R_1	2.5	μm	capillary radius

L	200	µm	capillary length
V	0.04	cm/sec	Average velocity
D	5.5×10^{-6}	cm^2/s	diffusivity
S	0.05058	ml / cm^3 sec	consumption rate
Tissue space			
R_2	32	µm	tissue radius
D	5.5×10^{-6}	cm^2/s	diffusivity
S	0.05058	ml / cm^3 sec	consumption rate
W	2.89×10^{-3}	cm^3 O2 /cm^3 /mmHg	solubility

2.8.2 ASA Consumption Rate

The percentage of total incoming oxygen lost from the capillary to the tissues was determined from an overall mass balance on the capillary space comparing the inlet and outlet concentration values. The ASA consumption rate (S) is the rate of ASA delivered to the tissues for a given tissue volume,

$$S = \frac{(C_{in} - C_{out})Q}{V_{tissue}}$$

Where Q is the volumetric flow rate, which is a specified model parameter and V_{tissue} is the volume of the whole tissue space, C_{in} and C_{out} are the ASA concentration in inlet and outlet, which are assumed to be 30*m*g and 25.882*m*g.

2.8.3 Numerical results and discussion

Using the above diffusion equations in brain tissue, the fractional release values of ASA concentration were calculated for 40 axial positions and 60 radial positions, starting at the arterial end and at the venous end in the capillary.

If any of the tissue PO_2 values were less than 0.01 mmHg, then the ASA

consumption was set to zero at that location and the tissue radius R_t that defined the boundary of ASA consuming tissue was accordingly fixed. ASA diffusion can be extended at this radius of R_t where there is no oxygen pressure difference between two points in the brain tissue.

After calculating the radial mass flux of ASA based on PO_2 distribution in each tissue slice, ASA concentration in the capillary at each axial position was decreased as much as radial mass flux. After that, the radial ASA concentration distribution using the diffusion equation for the corresponding tissue slice was calculated. This procedure was repeated until it reached convergence conditions.

The steady-state ASA (Acetylsalicylic acid) distributions for the front of the tissue surface are shown in Figure 2.14. The maximum ASA concentration that the human gray matter can control is proportional to the distance of the vertices from the capillary. This trend is due to the decreasing concentration of drug that is coming into the capillary over the process. Also included in the graphs is a large concentration gradient that develops nearly thirty percent of the capillary length at PO_2 of 30mmHg.

Figure 2.15 represents the steady-state two-dimensional ASA tissue distributions. The steep curve was found along the capillary length and outer tissue radius for cases where anoxic regions had been developed. In the case of PO_2 of 30mmHg, ASA concentration distribution in the tissue dropped down to an 85% level as compared to normal condition.

Figure 2.16 illustrates the frequency count of ASA concentration in the human gray matter. The average ASA concentration values are 0.85 at normal,

0.83 at hypoxia and 0.65 at PO_2 of 30mmHg. As we can see in this data, an average ASA concentration in the tissue dropped down in parallel during oxygen partial pressure decrease. The ASA concentration centralized between 0.75 and 1.0 at normal condition.

However, as oxygen partial pressure decreased to 30mmHg, their distributions were comparatively platted by spreading from 1.0 to 0.15 in entire region in the tissue. Its average value goes down to 23% compared to normal condition.

Figure 2.17 – 2.19 shows that the effect of drug consumption rate changes without change in capillary flow. ASA concentration at lethal corner with respect to the consumption rate activation is going down to 4.8% at normal, 5.4% at hypoxia, 19.8% at PO_2 of 30mmHg along with 30% ASA consumption rate increase. ASA concentration levels in the brain tissue are the smallest in the farthest location from incoming blood where the outer edge of the cylinder is at the venous end of the capillary, or the ‘‘lethal corner’’.

Figure 2.20 show an interesting trend in how ASA concentration in the human gray matter changes with an arterial oxygen partial pressure variation. In the range of 95mmHg and 60mmHg of oxygen partial pressure from the plot, an ASA concentration actually reaches a maximum then begins to decrease and level off as an oxygen partial pressure goes down to below 60mmHg.

Furthermore, the fact that human gray matter can tolerate decreasing pO2 to 30mmHg before neuronal viability is threatened fits well with the literature. Experimental measurements of cerebral blood flow during controlled hypoxia in

human subjects show that a large increase in cerebral blood flow as pO2 in reduced to 30 - 35mmHg [41].

Figure 2.21 show the relation between average ASA concentration and an arterial oxygen partial pressure change. Similarly as seen in Figure 2.20, an ASA concentration keeps going constantly in a range between 95mmHg and 60mmHg. Their concentration goes steeply down to 60% level compared with normal condition at anoxic regions of 30mmHg. So far as the experimental results in this regard are concerned, nothing is available in the literature. No doubt such experimental findings could be helpful in modifying the model to compare the results with experimental results. This, in turn, could have been a better source of current information about the aspirin diffusion in the peripheral nerve system.

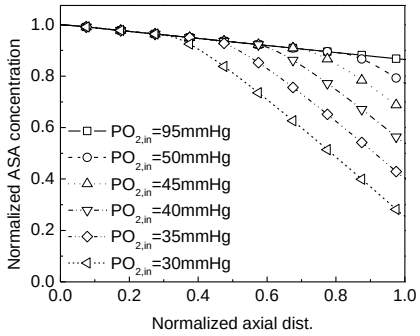

Figure 2.14 Comparison between Normalized ASA (Acetylsalicylic acid) concentration distribution and oxygen partial pressure drop in the capillary. (Normal Condition / ADI solution)

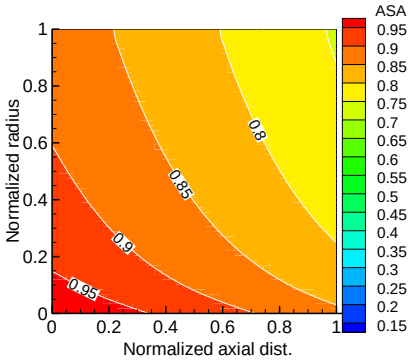

PO_{in}=95 mmHg

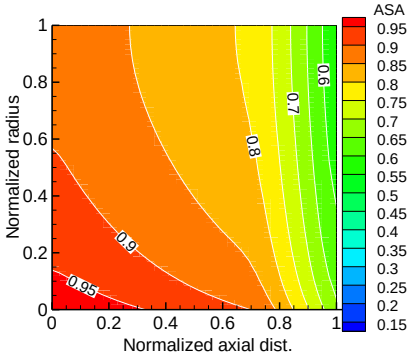

PO_{in}=45 mmHg

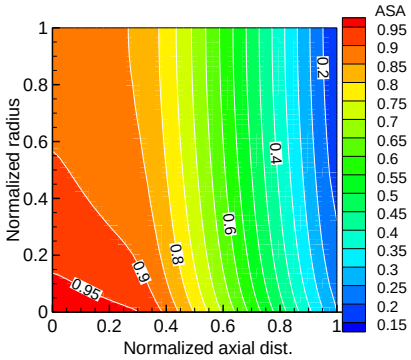

PO_{in}=30 mmHg

Figure 2.15 ASA distributions on the tissue with the variation of $PO_{2,\ in}$

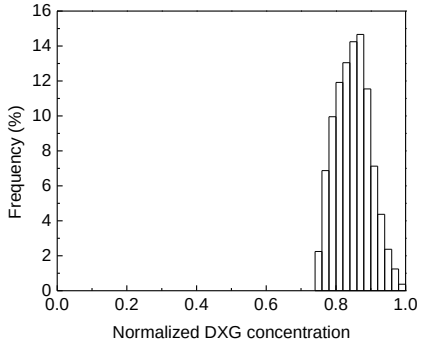

PO_{in}=95, (3-D), Interval=0.02, Mean=0.849, size=2400

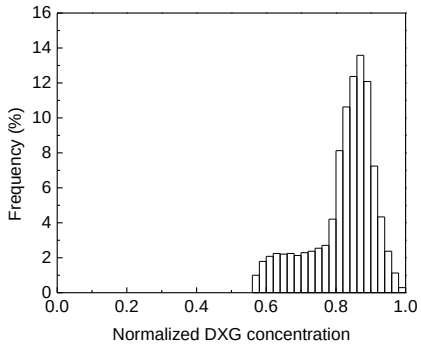

PO_{in}=45, (3-D), Interval=0.02, Mean=0.822, size=2400

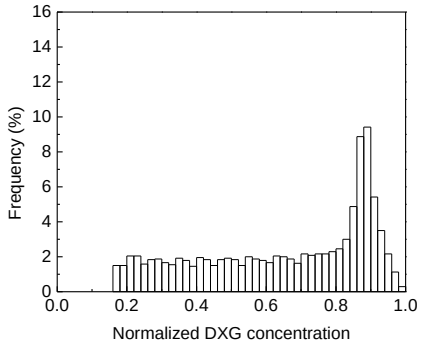

PO_{in}=30, (3-D), Interval=0.02, Mean=0.653, size=2400

Figure 2.16 ASA Histogram calculated on the tissue space with the variation of $PO_{2,in}$

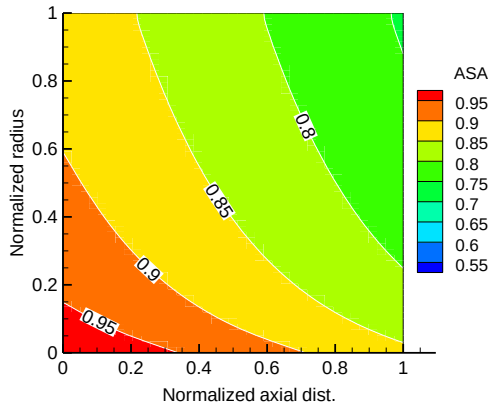

PO_{in}=45 mmHg, S

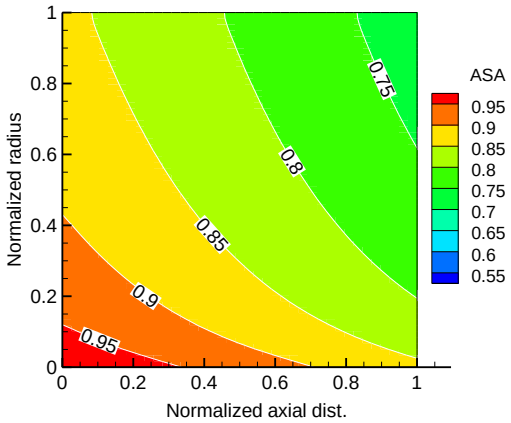

PO_{in}=45 mmHg, S×1.15

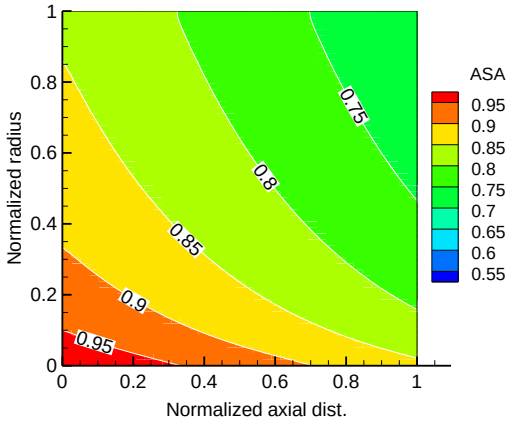

PO_{in}=45 mmHg, S×1.30

Figure 2.17 ASA distributions on the tissue with the variation of the consumption rate at $pO_{2,\,in}$ of 95mmHg

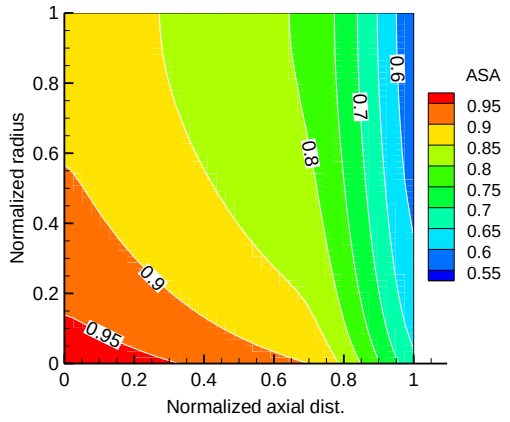

PO_{in}=45 mmHg, S

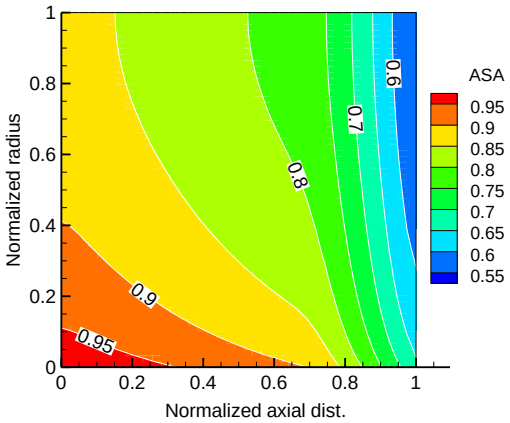

PO_{in}=45 mmHg, S×1.15

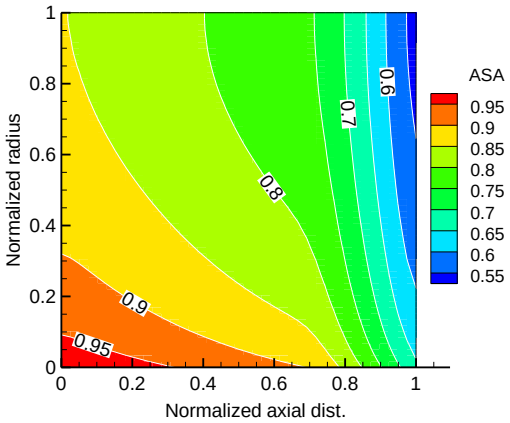

PO_{in}=45 mmHg, S×1.30

Figure 2.18 ASA distributions on the tissue with the variation of the consumption rate at $pO_{2,in}$ of 45mmHg

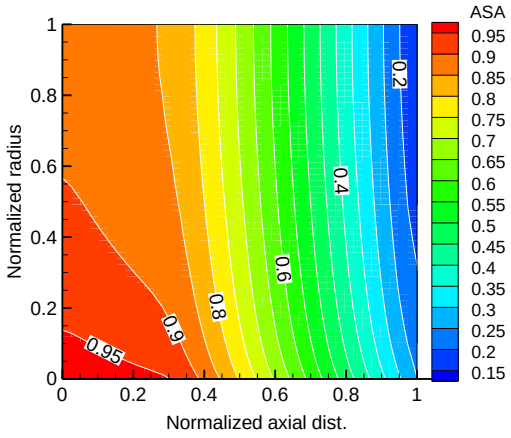

PO_{in}=30 mmHg, S

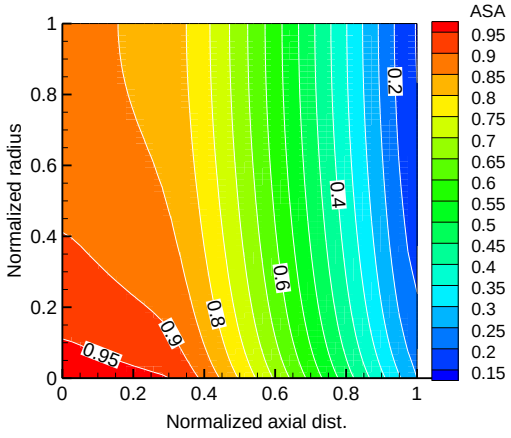

PO_{in}=30 mmHg, S×1.15

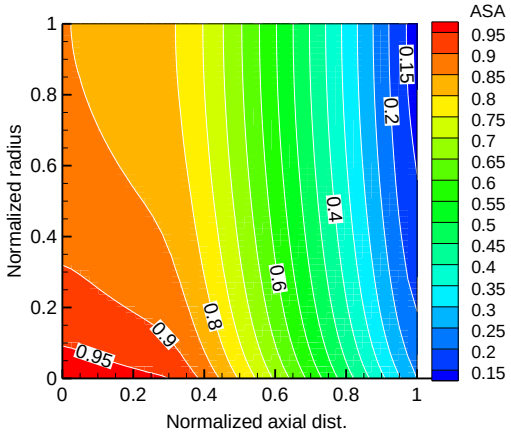

PO_{in}=30 mmHg, S×1.30

Figure 2.19 ASA distributions on the tissue with the variation of the consumption rate at $pO_{2,\,in}$ of 30mmHg

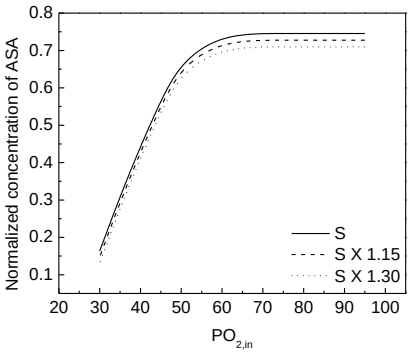

Figure 2.20 Brain tissue ASA level at lethal corner.

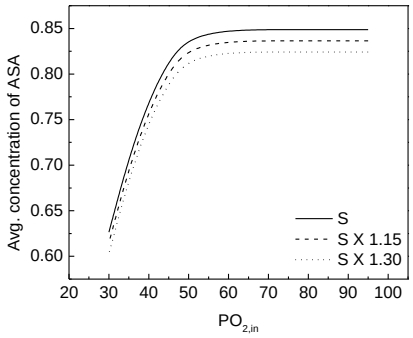

Figure 2.21 Average concentration of ASA on the computed surface

2.9 Conclusions

The central theme of this chapter was to make a calculation process of the general trends in the diffusion of the drug in cylindrical matrix system, which can be applied to determine the exact penetration depth of the drug in the tissue.

Drug diffusion from cylindrical matrix systems has been investigated with special emphasis on the influence of an arterial oxygen partial pressure change and a finite consumption rate on the drug release profile. A mathematical model of the drug diffusion and release processes was formulated in terms of nonlinear partial differential equations (PDEs). These were solved numerically by using well established Fortran subroutines.

An approximately analytical solution, valid during the early stages of the diffusion process, was derived. The numerical solution was compared to the numerical one existing in the literature. From this comparison, it was established that the numerical solution provided a good description of the major part of the diffusion distribution, with respect to some parameters of an arterial oxygen partial pressure and drug consumption rate.

Chapter 3

MASS TRANSFER PHEONOMENA ON OXYGEN/DRUG IN A THREE-DIMENSIONAL CAPILLARY NETWORK

3.1 Introduction

3.1.1 Objective and scope of research

The purpose of this study is to develop the modeling method of the computational fluid dynamics (CFD) to simulate the mass transfer phenomena in micro scale for the drug and oxygen diffusion and other substances in a capillary network. A three-dimensional capillary network has been constructed to replicate the one studied by Secomb et al. (2000) [65], and the computational framework features a non-Newtonian viscosity model of blood, the oxygen transport model including in-stream oxygen-hemoglobin dissociation and wall flux due to tissue absorption, as well as an ability to study drug diffusion and other materials in the capillary streams.

For the validation, the model is first run to compute the volumetric flow rates from the velocity profiles in the segments, and compared with Secomb's work with good agreements. Effects of abnormal pressure and stenosis conditions, as well as those arising from different capillary configurations, on the flow and oxygen delivery are investigated, along with a brief look at the unsteady effects and drug dispersion in the capillary network.

Thus, the aim of this work is to provide and demonstrate an approach based on computational fluid dynamics (CFD), involving the calculations of the volumetric flow rates, oxygen content, and potentially other material transport, by

solving the governing equations of continuity, momentum, species transport and energy through the finite volume method (embedded in a commercial software, FLUENT). Such results for the fluid dynamic and transport effects can then be used as the basis for studying delivery, corrective measures and other applications.

3.1.2 Literature review

The capillary vessels, among other functions, transport oxygen, carbon dioxide and other materials (nutrients, drugs) to and from cells. These smaller blood vessels in the body (the arterioles, venules, and capillaries) make up the so-called microcirculatory system. Larger blood vessels, i.e. arteries and veins with inner diameters greater than approximately 100 μm, are termed "macro vascular".

The two systems have distinguishing characteristics. The macro vascular vessels serve as reservoirs of pressure on the high and low side of the cardiovascular system, as well as a passage for relatively large flow rates of blood between the heart and peripheral organs. The microcirculatory vessels are responsible for regulating flow and also for direct material transport at the cell levels. The transport may involve oxygen, carbon dioxide, nutrients and other biochemical species. About 80% of the total pressure drop in the circulatory system occurs in these microcirculation networks, as the vessel diameters are small and lengths quite large in total (Popel and Johnson, 2005) [42].

The microcirculation system inherently includes complex flow patterns such as bifurcations in forward and backward directions, constrictions and flow turns. It is of both academic and practical biomedical interest to be able to determine the

fluid dynamics of the circulatory systems, as well as the transport characteristics of oxygen, carbon dioxide, and other species, and there have been many works devoted to this topic (Aroesty and Gross, 1997; Hudetz et al., 1993; Hudetz et al., 1996; Hudetz et al., 1997; Malkusch et al., 1995; Motti et al., 1986; , Krogh, 1959) [43-49, 21].

While some of the adverse macro vascular flow conditions and their effects are well known, problems in the micro vascular networks can lead to equally malignant conditions. For example, hypoxia in the brain capillaries can lead to irreversible nerve cell damage in a matter of minutes. The critical transports occur in the micro vascular network, and understanding of this phenomenon is quite important and may suggest methods to improve and optimize circulation at this level under diverse biomedical conditions of interest.

There have been numerous studies of the flow in circulatory systems, with most early works focusing the fluid dynamic aspects, e.g. flow velocity and pressure distributions. Chen and Lu (2004) [50], for example, developed a three dimensional model that uses a finite-element method to determine flow properties in a single, lager vessel (carotid or aorta) bifurcation. This study revealed the effects of the non-Newtonian fluid property and bifurcation geometry on the wall shear stress.

In a paper by Berry et al. (2000) [51], a two dimensional CFD model was used to characterize the blood flow in a coronary artery in the presence of a metallic stent. Dzwinel et al. (2003) [52] modeled red blood cells as discreet particles rather than using a continuum approach. They then studied the blood

dynamics in capillary vessels with diameters of 10 and 25 μm in a simple, straight segment.

Pries et al. (1990) [53] devised a method of determining the flow rate and hematocrit in each segment of a capillary network based on mass conservation at node points. First, a linear analysis was used in the computation of the flow in each segment in the network and the pressure at each node, assuming that the apparent viscosity and other rheological parameters are known. A conservation principle was then applied, where the inflows and outflows must sum to zero at a node point where three segments meet.

Unsteady and three-dimensional flow simulations in realistic geometry are also well within computational fluid dynamic capabilities, as shown for example by Shahcheraghi et al. (2002) [54] who investigated the pulsatile flows in the human aortic arch. Transient coronary microcirculation has also been simulated by Lee et al. (2004) [55]. These are a small subset of the studies that have been done, to serve as illustrations that flow simulation is the first step in studying transport in circulation networks at various scales.

In addition to the above purely fluid dynamical aspects, there has been increasing attention on material transport within the circulatory networks involving oxygen, lipoprotein distributions and drug delivery. An early study by Eggleton et al. (1998) [56] considers the transport of oxygen in a linear capillary channel, by calculating the in-fluid advection of oxygen along with absorption of oxygen at the vessel wall.

The circulation and uptake of oxygen is an important issue at the capillary scales, since they determine the delivery oxygen to tissues in complex capillary networks. An overall model of oxygen uptake has also been set up by Wang and Hicks (2002) [57] to predict the total oxygen uptake in ectothermic vertebrates.

A study by Sinek et al. (2004) [58] again focuses on the tissue side transport, with a two-dimensional model of the nanoparticle drug delivery to tumor regions. We can also find mathematical and computational studies of oxygen or drug transport in vascular network (Goldman, 2003; Stephanou et al., 2005) [59 - 60].

However, thus far these models consider quasi-one-dimensional transport in the network in the sense the flow in each vessel is considered to be one-dimensional. These studies then focus on the vessel wall and tissue transport, to determine the delivery effectiveness. It should also be noted that most studies have used a relatively simple flow balance (see Eq. 14 below) with flow resistance due to the wall friction, and little consideration of the detailed flow patterns through bends, branches, or inlet/exit configurations. It has been shown in a recent study (Pindera et al., 2009) [61] that the flow rates can differ by up to 10 % in angled micro vascular branches when a full three-dimensional model's results are compared with those from a simple one-dimensional model.

For oxygen transport, Popel, Goldman and co-workers (Goldman and Popel, 2000; Federspiel and Popel, 1986; Vadapalli et al., 2002) have used a quasi-one-dimensional capillary transport model to investigate various issues on the oxygen delivery in hexagonally packed muscle fibers. Secomb and co-

workers (Secomb et al., 2000; Pries et al., 2001; Secomb et al., 2004) have done extensive work on oxygen transport from capillary networks to tissues [62-67].

The work can be described in a two-component model, where one component consists of a mathematical prescription of the volumetric flow rate and oxygen partial pressure in the capillary network vessel segments. The oxygen partial pressure at each segment is then used as a source term for distributing oxygen to the tissue in the second component.

When all of the source terms are added from all of the segments in the network using a Green's function method, then the tissue oxygen distribution is determined. Thus, the oxygen transport in the vessel is first modeled, and then used as a "source term" for perfusion into the tissue region.

However, what if the capillary vessels are more complex involving flow turns, divergence, and bifurcations and multiple branches? These will result in static pressure change, and therefore have a potential to change the volumetric flow rate distribution in the capillary segments. If the volumetric flow rate and the corresponding available oxygen content are to be accurately modeled, then these effects need to be taken into account so that the flow rates can accurately be calculated.

If we further expect to simulate a large-scale oxygen transport from the arteries to the network, then such fluid dynamic and transport effects may deviate even further from simple prescriptions based on a one-dimensional model.

3.2 Governing equations

The equations of continuity, conservation of momentum, species transport, energy using this simulation can be written as follows:

Continuity:

$$\frac{\partial \rho}{\partial t} + \nabla \cdot (\rho \vec{v}) = S_m \quad (2.1)$$

Momentum:

$$\frac{\partial}{\partial t}(\rho \vec{v}) + \nabla \cdot (\rho \vec{v} \vec{v}) = -\nabla p + \nabla \cdot (\bar{\bar{\tau}}) + \rho \vec{g} + \vec{F} \quad (2.2)$$

Species:

$$\frac{\partial}{\partial t}(\rho Y_i) + \nabla \cdot (\rho \vec{v} Y_i) = -\nabla \cdot \vec{J}_i + R_i + S_i \quad (2.3)$$

Energy:

$$\frac{\partial}{\partial t}(\rho E) + \nabla \cdot \left(\vec{v}(\rho E + p)\right) = \nabla \cdot \left(k_{eff} \nabla T - \sum_i h_i \vec{J}_i + \left(\bar{\bar{\tau}}_{eff} \cdot \vec{v}\right)\right) + S_h \quad (2.4)$$

In these equations, ρ is the fluid density, *t* is time, $\vec{v}$ is the fluid velocity vector, S_m is a mass source term that can come from either mass added to the continuous phase from the dispersed second phase or as defined by the user, *p* is the static pressure, $\rho \vec{g}$ is the gravitational body force, and $\vec{F}$ is an external body force or user-defined sources. The stress tensor, $\bar{\bar{\tau}}$, is given by:

$$\bar{\bar{\tau}} = \mu \left[(\nabla \vec{v} + \nabla \vec{v}^T) - \frac{2}{3} \nabla \cdot \vec{v} I \right] \quad (2.5)$$

Where μ is the molecular viscosity, *I* is the unit tensor, and the second term on the right hand side has the effect of volume dilation [68].

In equation 2.3, Y_i is the mass fraction of species *i*, R_i is the rate of production of species *i* by chemical reaction, S_i is creation of that species by the dispersed phase

or by any user defined source. In mass diffusion in laminar flows, $\vec{J}_j$ is the diffusion flux of species *j* given by:

$$\vec{J}_i = -\rho D_{i,m} \nabla Y_i \tag{2.6}$$

Where $D_{i,m}$ is the mass diffusion coefficient for species *i* in the mixture, and Y is the mass fraction of species *I* in the mixture.

In mass diffusion turbulent flows, the mass diffusion is in the following form:

$$\vec{J}_i = -\left(\rho D_{i,m} + \frac{\mu_t}{Sc_t}\right) \nabla Y_i \tag{2.7}$$

Where Sc_t is the turbulent Schmidt number ($\frac{\mu_t}{\rho D_t}$ where μ_t is the turbulent viscosity and D_t is the turbulent diffusivity). Note that turbulent diffusion generally overwhelms laminar diffusion, and the specification of detailed laminar diffusion properties in turbulent flows is generally not warranted.

The laminar finite-rate model computes the chemical source terms using Arrhenius expressions, and ignores the effects of turbulent fluctuations. The model is exact for laminar flows, but is generally inaccurate for turbulent flows due to highly non-linear Arrhenius chemical kinetics. The laminar model may, however, be acceptable for the blood flow analysis with relatively slow chemistry and small turbulent fluctuations, such as separation, circulation, and reattachment phenomena. The net source of chemical species *i* due to reaction is computed as the sum of the Arrhenius reaction sources over the N_R reactions that the species participate in:

$$R_i = M_{w,i} \sum_{r=1}^{N_R} \hat{R}_{i,r} \tag{2.8}$$

where $M_{w,i}$ is the molecular weight of species *i* and $\hat{R}_{i,r}$ is the Arrhenius molar

rate of creation/destruction of species *i* in reaction *r*. Reaction may occur in the continuous phase between continuous-phase species only, or at wall surfaces resulting in the surface deposition or evolution of a continuous-phase species. Consider the *r*th reaction written in general form as follows:

$$\sum_{i=1}^{N} v_{i,r}^{'} M_i \underset{k_{b,r}}{\overset{k_{f,r}}{\rightleftarrows}} \sum_{i=1}^{N} v_{i,r}^{''} M_i \qquad (2.9)$$

where

N = number of chemical species in the system

$v_{i,r}^{'}$ = stoichiometric coefficient for reactant *i* in reaction *r*

$v_{i,r}^{''}$ = stoichiometric coefficient for product *i* in reaction *r*

M_i = symbol denoting species *i*

$k_{f,r}$ = forward rate constant for reaction *r*

$k_{b,r}$ = backward rate constant for reaction *r*

Equation 2.9 is valid for both reversible and non-reversible reactions. For non-reversible reactions, the backward rate constant, $k_{b,r}$, is simply omitted. The summations in Equation 2.9 are for all chemical species in the system, but only species that appear as reactants or products will have non-zero stoichiometric coefficients. Hence, species that are not involved will drop out of the equation. For a non-reversible reaction, the molar rate of creation/destruction of species *i* in reaction *r* (in Equation 2.8) is given by

$$\hat{R}_{i,r} = \Gamma\left(v_{i,r}^{''} - v_{i,r}^{'}\right)\left(k_{f,r} \prod_{j=1}^{N} \left[C_{j,r}\right]^{\left(\eta_{j,r}^{'} + \eta_{j,r}^{''}\right)}\right) \qquad (2.10)$$

where

$C_{j,r}$ = molar concentration of species *j* in reaction r (kg mol/m^3)

$\eta'_{j,r}$ = rate exponent for reactant species *j* in reaction *r*

$\eta''_{j,r}$ = rate exponent for product species *j* in reaction *r*

N = the total number of species in the system.

Γ represents the net effect of third bodies on the reaction rate. This term is given by

$$\Gamma = \sum_j^N \gamma_{j,r} C_j \tag{2.11}$$

where $\gamma_{j,r}$ is the third-body efficiency of the *j*th species in the *r*th reaction. By default, FLUENT does not include third-body effects in the reaction rate calculation. It can, however, opt to include the effect of third-body efficiencies if these data are existed.

The forward rate constant for reaction *r*, $k_{f,r}$, is computed by using the Arrhenius expression

$$k_{f,r} = A_r T^{\beta_r} e^{-E_r/RT} \tag{2.12}$$

where

A_r = pre-exponential factor (consistent units)

β_r = temperature exponent (dimensionless)

E_r = activation energy for the reaction (J/kg mol)

R = universal gas constant (J/kg mol-K)

Mass diffusivity can be written by another Arrhenius-type relation to express the diffusion coefficient as follows. [69]

$$D_{AB} = D_0 exp(-E_a/RT) \tag{2.13}$$

where,

D_0 = the tabulated values for the Arrhenius constants [consistent units],

E_a = the activation energy Ea [kJ/kg mol]

R = universal gas constant (kJ/kg mol-K)

D_{AB} = mass diffusivity [m^2/sec]

Letting, $\beta_r \rightarrow 0$ and $E \rightarrow 0$ in Equation 2.12 and 2.13, it becomes

$$A_r \leftrightarrow D_0 \tag{2.14}$$

Therefore, pre-exponential factor A_r in Equation 2.12 is equivalent to the mass diffusion coefficients D_0 of Equation 2.13 in the mass transport phenomena.

In order to enable the Carreau viscosity model, the software required the energy conservation equation (2.4) to be enabled and solved, although, in many cases the temperature was not of much interest to the problem. In Equation 2.4, k_{eff} is the effective conductivity (conductivity (k) plus turbulent conductivity (k_t) defined according to the turbulence model being used), T is the temperature, and the S_h term includes the heat of chemical reaction as well as any user defined heat sources. In the energy equation 2.4, the energy is given by:

$$E = h + \frac{v^2}{2} \tag{2.15}$$

where $\vec{J}_i$ is the diffusion flux of species i (same as Equation 2.6), and given by:

$$\vec{J}_i = -\rho D_{i,m} \nabla Y_i \tag{2.16}$$

where $D_{i,m}$ is the mass diffusion coefficient for species i in the mixture, and Y is the mass fraction of species i. The enthalpy is given by:

$$h = \sum_i Y_i h_i \tag{2.17}$$

where h_i is the enthalpy for species i and is given by:

$$h_i = \int_{T_{ref}}^{T} c_{p,i}\, dT \tag{2.18}$$

where $c_{p,i}$ is the specific heat capacity of species i and T_{ref} is a user defined reference temperature. The first three terms on the right hand side of the energy equation (2.4) represent energy transfer due to conduction, species diffusion, and viscous dissipation, respectively.

In this steady-state, incompressible case with no mass source term, the continuity equation (2.1) became:

$$\nabla \cdot \vec{v} = 0 \tag{2.19}$$

The momentum conservation equation (2.2) in absence of external gravitational or body forces becomes, steady-state, and incompressible can be expressed as:

$$\rho \nabla \cdot (\vec{v}\vec{v}) = -\nabla p + \nabla \cdot (\bar{\bar{\tau}}) \tag{2.20}$$

Although the temperature is not important for this problem, FLUENT required the energy equation to be enabled in order to use the Carreau non-Newtonian viscosity model. Since this case deals with a single species, the species conservation equation is not used.

3.3 Properties of the species

Table 3.1 contains all of the species used in the reaction models discussed in this study. For each species, the pertinent material properties are listed from the literature. In the table 3.1, Carreau model refers to the non-Newtonian viscosity model as discussed in the "Computational Method" section. FLUENT calculates the properties of the mixture based on a user-selected method. Here, the viscosity

is calculated using a mass-weighted mixing law. The density was also calculated by FLUENT using a mixing law; however, all species were set to a constant density of 1020 kg/m^3 so that the flow properties would be consistent with the previous cases (cases without species transport). The actual density of O_2 is approximately 1.3 kg/m^3. This value was used in subsequent calculations, particularly when converting from oxygen partial pressure (PO_2) in mmHg to oxygen mass fraction, and vice versa. A dilute approximation method was used to define the mass diffusion coefficients for each species in the mixture. These coefficients were set to be constants, that is, not dependent upon temperature or other parameter. The diffusion coefficient for oxygen in plasma was found in Federspiel et al. [63, 69].

Table 3.1Properties of the species in the blood mixture

Species	Viscosity (kg/m-s)	Molecular Weight (kg/kg mol)	Mass Diffusion Coefficient (m^2/s)
Plasma	Carreau model	18	$1x10^{-9}$
Oxygen (O_2)	$1.919x10^{-05}$	31.9988	$1.4x10^{-9}$
O_2_Dummy	$1.919x10^{-05}$	31.9988	$1.7x10^{-9}$
HbO_2	Carreau model	68000	$6.9x10^{-10}$
Hb	Carreau model	67968	$6.9x10^{-10}$
DXN	Carreau model	781	1.0×10^{-9}
DXN_dummy	Carreau model	781	1.0×10^{-9}

3.4 Boundary conditions

3.4.1. Boundary conditions for the flow model validation

Secomb et al. have published results online including flow velocity for each segment in their 50 segment network [70], which is listed in Appendix G. Table 3.2 and 3.3 show the segment numbers, inlet diameters, the inlet mass flow rate and pressure outlet used in the present study of inlet and outlet. The material is the

blood, which density is 1020 kg/m^3. At the wall of the capillary, a wall boundary condition was specified with no heat or mass flux.

Table 3.2 The inlet boundary conditions based on the work by Secomb et al.

Inlet number	Seg. No.	Seg. diameter (μm)	Mass flow rate (10^{-11}kg/sec)
1	8	7	2.824
2	9	6	4.943
3	12	6	1.413
4	13	6	2.824
5	27	5	1.413
6	28	5	1.413
7	34	4	0.706

Table 3.3 The outlet boundary conditions based on the work by Secomb et al.

Outlet number	Seg. No.	Seg. Diameter (μm)	Pressure (mmHg)
Outlet 1	1	9	22
Outlet 2	14	5	19
Outlet 3	30	5	25

3.4.2 Boundary conditions for pressure drop case

Because the blood flow within a physiological capillary network is pressure driven along the direction of negative gradient, a computational flow model has been developed to simulate this phenomenon. This case presents more physiologically meaningful boundary conditions over the previous case, where the inlet velocity condition was used. The pressure drop (ΔP) across a capillary network in a rat varies from 5-20 mmHg depending on location, geometry, and other physiological factors [71]. The same geometry that was used in the Secomb validation case (Figure 3.1) is again employed, however, with new inlet and outlet boundary conditions. Also, the same transport equations were solved numerically (2.3, 2.4). The inlet and outlet conditions were chosen to satisfy the ΔP condition, where the pressure inlets were given the value of ΔP and the pressure outlets were

set to 0 mmHg (gauge). Three different values of ΔP were used: 5, 10, and 20 mmHg. For example, in the case where ΔP = 5 mmHg, each of the seven inlets were given a pressure condition of 5 mmHg, while each of the three outlets were given pressure conditions of 0 mmHg.

3.4.3 Boundary conditions for modified inlets and outlets case

In this case, the configuration of the inlets and outlets was altered so that the inlets were spatially grouped. As shown in Figure 3.9, there were seven inlets and three outlets. A ΔP of 10 mmHg was applied to the network, that is, a pressure of 10 mmHg (gauge) was specified at the inlets, and 0 mmHg at the outlets. The purpose of this case was to gain insight into the effects of altering the geometrical configuration of the network.

3.4.4 Boundary conditions for flow blockage case

The effects of a flow blockage were studied using the geometry and inlet/outlet conditions described above (pressure drop case). A "fan" boundary condition was used to model a pressure jump across a circular, cross-sectional area of the capillary tube at two specific locations in the network. The fan condition is a lumped parameter model used to determine the effects of a fan with known characteristics upon some larger flow field [72]. In this case, the "fan" simply provides a pressure increase (as the observer travels in the flow direction) that works against the negative pressure gradient imposed by the inlet and outlet boundary conditions. The pressure increase occurs over a very small distance in

the axial direction. This pressure "jump" is uniform across the circular cross-section of the capillary tube, and does not vary with the flow velocity or any other parameter. The locations of the two blockages were chosen to come before any bifurcations, and to reside within the joints between segments which create a corner or elbow in the geometry. The locations of the pressure jump "fan" conditions assigned are in segment 25 and 32. Figure 3.14 and 3.15 show effect of localized flow constrictions (stenosis) on the static pressure and on the oxygen mass fraction in the capillary network, respectively.

In order to impose this condition, a fan zone was first created using the GAMBIT software. A circular face was created and meshed at the location desired within the network. These two meshed faces each covered the entire cross section of the flow for segment 25 with 5 μm, segment 32 with 4 μm. The fan boundary condition was then specified on each of the two faces, with a pressure jump, ΔP_{jump}, specified which was opposing the zone average flow direction at each of the two faces. The inlet pressures were set to 1350 Pa (10 mmHg) and outlets 0 mmHg, to match the case discussed previously (ΔP = 10 mmHg). At the upper block location (segment 25), the value of ΔP_{jump} were used in successive FLUENT runs: 600 Pa. At the lower block location (segment 32), a ΔP_{jump} of 600 Pa was imposed as well.

3.5. Iterations and Convergence

Good convergence was assumed when the residual values for all of the transport equations fell below a value of 10^{-6}. Generally, it took between 1500

and 2500 iterations to reach this level of convergence. Using a PC with Intel Core 2 Quad CPU Q6600 at 2.40 GHz processor with 4 GB of RAM, the nominal CPU time was a moderate 24 hours for a steady state, two weeks for an unsteady state analysis with the blood, oxygen-hemoglobin and DXN reactions included. Since it takes a pretty much long time to reach at convergence, the computer was often left alone to run overnight. The more the capacity of the computer improves, the less it takes the time to be converged.

3.6 Post processing

In order to report information from the results, several FLUENT tools were used. The diameter of the capillaries (5 μm) is small compared to the dimensions of the entire network. Since the flow velocity at any point along the axial direction in a capillary segment was a distribution in the radial direction, being zero at the capillary wall and greatest along the centerline, it was difficult to display meaningful velocity contours for the entire network. When the velocity contour is displayed for the entire network, only the wall velocity can be viewed, except for any visible inlet/outlet areas. An area-weighted average velocity over cross-sectional areas in representative segments was desired. Since the velocity was uniform along the axial direction for a single segment, or multiple segments with no bifurcations, once the velocity has been averaged over one cross section it is representative of the entire segment or segments.

FLUENT's plane surface creation tool was used to create cross-sectional areas within segments for the purpose of extracting flow data. The plane surface

tool allowed the user to create the surfaces as close to axially perpendicular as possible. However, there was some small error due to the planar surfaces not being exactly perpendicular. The area-weighted average of velocity over this surface was calculated for a typical cross-sectional surface.

FLUENT used the following equations to calculate the following properties:

The area-weighted average of any flow property, $\emptyset$, over the cross-sectional surface [72]:

$$\frac{1}{A}\int \emptyset dA = \frac{1}{A}\sum_{j=1}^{n} \emptyset_i |A_i| \qquad (2.21)$$

where A_i is the area of facet *i*, and *n* is the number of facets that comprise the selected surface. To determine the mass flow rate through the selected cross-sectional surface, the following relation was used:

$$\int \rho \vec{A} \cdot d\vec{A} = \sum \rho_i \vec{v}_i \cdot \vec{A}_i \qquad (2.22)$$

By this method, the flow rate in every segment in the network was compared to Secomb's published flow rate data.

3.7 Geometry and grid

This rat brain geometry of the Three-Dimensional Capillary Network is based on scanning electron microscopy (SEM): Motti, E.D.F., Imhof, H.G., Yasargil, M.G. (1986) The terminal vascular bed in the superficial cortex of the rat. An SEM study of corrosion casts. J. Neurosurg. 65: 834-846. The method for reconstructing the 3D structure from SEM images is described by: Secomb, T.W., Hsu, R., Beamer, N.B. and Coull, B.M. Theoretical simulation of oxygen

transport to brain by networks of microvessels: effects of oxygen supply and demand on tissue hypoxia. Microcirculation 7, 237-247 (2000).

Coordinate values and flow data come from http://www.physiology.arizona .edu /people/secomb/network/brain99, which are given by the following Appendix F and G in detail. Cartesian coordinates of nodes are given in microns. The overall dimensions of the region are 150 x 160 x 140 microns. Figure 3.1 came from describing above Secomb's web. Figure 3.2 show the 3-Dimensional geometry generated in this study with the range of diameter from 4 μm to 9 μm. The Grid is shown in Figure 3.3. The total number of the vertices is 425,734.

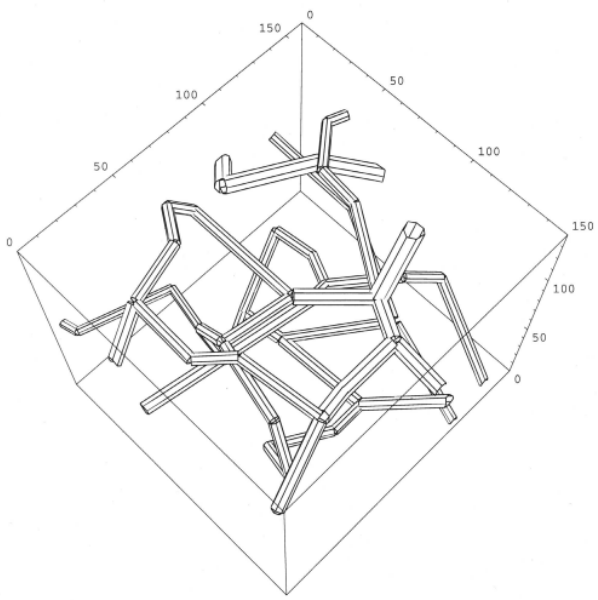

Figure 3.1 Schematic geometry came from Secomb's web

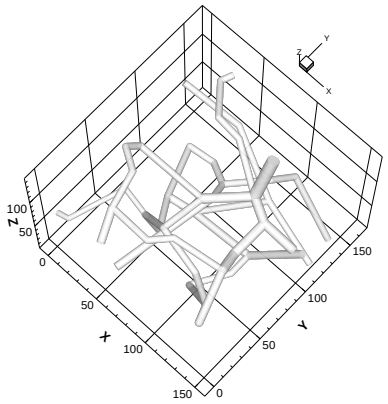

Figure 3.2 Geometry with real diameters

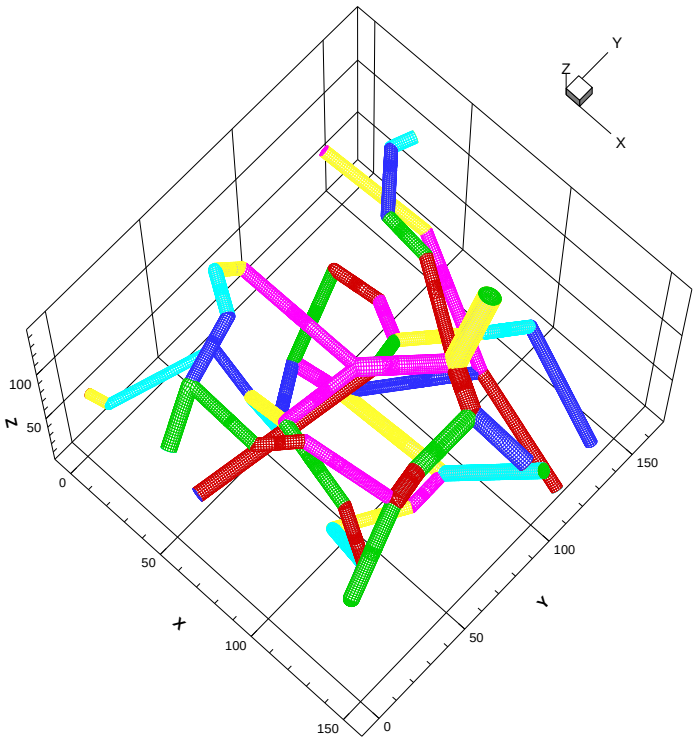

Figure 3.3 Grid with real diameters

3.8 Validation

The verification method consists of three steps. The first step is applying the mass flow rate given by table 3.1 and outflow in 7 inlets and 3 outlets respectively. It is to figure out how much different is the volume flow rate between Secomb's

and calculated data with the properties of blood. Outflow boundary conditions mean that it is converged when inlet and outlet mass flow rate are balanced. As seen on Figure 3.4, the volume flow rate of Segment 23 and the line of segment 45 – 47 are higher than Secomb's data. It means that the diameters of Seg. 23 and the line of Seg. 45 - 47 are smaller than that of real one of 5μm partially, which cause the throttling effect through those cross sections. It makes the pressure drop in forward direction, and pressure jump in backward direction. When the pressure drop of -600Pa are applied in both the segment 23 and 47, the results showed a good agreement with secomb's data in Figure 3.5.

The second step is to change inlet and outlet each other. In other words, there are 3 inlets and 7 outlets in the geometry. It is to provide strong confidence into the boundary conditions whether it is correct or not. The results must be consistent with that of the first step because there is no reason to be different between two cases in the computational fluid dynamics point of view. Summation of mass flow rate of 3 inlets and of 7 outlets is same, only the flow directions are reversed. As expected, the good agreements are shown in Figure 3.6 and 3.7.

However, since the experiments by the Secomb's teams had been completed a long time ago, it is not feasible to check out the exact diameters of segment 23 and the line of 45-47. Therefore, it is reasonable to apply the boundary conditions of the inlet mass flow rate and pressure outlet without the pressure drop inside the capillary network. For the next step, it is to find out pressure outlet conditions from 3 outlets based on this flow validation case of Figure 3.4. They are 22mmHg, 19mmHg, and 22mmHg on outlet 1, outlet 2, and

outlet 3 respectively, which are satisfied at the physiological range of a typical rat capillary [53, 66]. At the wall of the capillary network, a wall boundary condition was specified with no heat or mass flux.

Finally, we compared our volumetric flow rate data with those of Secomb et. al. (2000), in Figure 3.8. As noted above, the capillary network geometry and inlet conditions in the current work were adopted from Secomb et al. (2000), and we use the same segment numbers as that of Secomb's geometry in Figure 3.9. Table 3.1 and 3.2 give the inlet boundary conditions for the mass flow rates, which again are the same between Secomb's (2000) and this work. In Secomb's work (2000), the measured diameters vary from one inlet to the other, which explains the various inlet flow velocities in Table 3.2. At the exit, a fixed pressure boundary condition of 22, 19, and 25 mmHg is applied to outlet 1, outlet 2, and outlet 3 respectively in the current computations. For the analysis of the oxygen diffusion, the oxygen mass fraction is nominally set at 1.3×10^{-4}, with small variations due to static pressure differences corresponding to different flow rates at the inlets. We use the above inlet and exit boundary conditions for the all the subsequent simulations in this work unless otherwise noted [65].

Figure 3.8 shows that the volume flow rates in the capillary streams in the most part are quite similar to the Secomb's data, except in a small number of segments (e.g. 2-4, 10-11, 20-23, 42-49). The agreement between the full computational simulations contained in this work and those in Secomb et al. (2004) is noteworthy in the sense that Secomb et al. (2000) use a relatively simple flow balance method to estimate the flow rates. For example, at a node point

where three segments meet, the inflows and outflow(s) must sum to zero (Secomb et al., 2000, Goldman and Popel, 2000) [67, 65, 62]:

$$Q_1 + Q_2 + Q_3 = J_1(p_1-p_0) + J_2(p_2-p_0) + J_3(p_3-p_0) \quad (2.23)$$

where $Q_{1,2,3}$ are the segment flow rates (negative for outflows), $J_{1,2,3}$ are the segment conductances (given by Poiseuille's law), p_0 is the pressure at the node, and $p_{1,2,3}$ are the pressures in the adjacent nodes. When this equation was applied at every node in the network, a linear system is found that can be solved for the unknown pressures. The segment conductance according to the Poiseuille's law takes into account of the pressure loss due to the wall viscous stresses in a circular duct. As noted earlier, it has been shown in a recent study (Pindera et al., 2009) that the flow rates can differ by up to 10 % in angled microvascular branches when a full three-dimensional model results are compared with those from a simple one-dimensional model. The reason for this difference is attributed to the fact that there can be non-uniform pressure distributions around bends and bifurcations even in microvascular channels [61].

Blood is a viscous fluid mixture consisting of plasma and cells. Table 3.4 summarizes the most important physical properties of blood to calculate Reynolds number($Re_D = \rho VD/\mu$) , V is velocity (m/sec), and Schmidt number. The transport properties for the blood, as represented by the viscosity and the solute diffusivity, are based on their respective plasma values. This occurs because for blood Schmidt number,$Sc = \mu/\rho D$, is much greater than unity. D represents the solute diffusivity (m^2/sec), μ is dynamic viscosity ($Pa \cdot sec$), and ρ is density

(kg/m^3). Reynolds number is simply the ratio of inertial forces to viscous forces and the Schmidt number compares the rates of momentum and diffusion transport.

Laminar boundary layer theory by Bird [73] showed that the concentration boundary layer, distance from that capillary wall over which the solute concentration change from its bulk value to its value at the capillary wall, is much thinner for $Sc \gg 1$ than the momentum boundary layer, the distance from the capillary wall over which the axial velocity change from its bulk value to zero at the capillary wall. The red blood cells also have a similar tendency to accumulate along their axis of flow. This creates a cell-free plasma layer adjacent to the capillary wall. Because of the thinness of the concentration boundary layer, it lies well within the cell-free layer, making it appropriate to base the transport properties on the plasma values [74]. The calculation of the solute concentration within the capillary and the tissue space surrounding the capillary is illustrated in Chapter 2. The Reynolds number and Schmidt number using this simulation are listed in Table 3.5 and 3.6. They show the blood flow is based on the laminar flow as described above. Schmidt number is much greater than unity as well.

Table 3.4 Physical properties of Blood

Variable	Value (dimensional)
Blood Density	$1020\ kg/m^3$
Blood Viscosity	$2.7 \times 10^{-3}\ Pa \cdot s$
$Diffusivity_{\_blood}$	$10^{-11}\ m^2/s$
Oxygen Density	$1.3\ kg/m^3$
Oxygen Viscosity	$1.919 \times 10^{-5}\ Pa \cdot s$
$Diffusivity_{\_oxygen\ in\ capillary}$	$1.4 \times 10^{-9}\ m^2/s$
$Diffusivity_{\_oxygen\ in\ tissue}$	$1.7 \times 10^{-9}\ m^2/s$

Table 3.5 Reynolds and Schmidt number for Blood

No.	Diameter(μm)	Velocity(mm/s)	Re_D	Sc
Inlet 1	7	0.720	1.90×10^{-3}	$2.65 \times 10^{+4}$
Inlet 2	6	1.714	3.89×10^{-3}	$2.65 \times 10^{+4}$
Inlet 3	6	0.490	1.11×10^{-3}	$2.65 \times 10^{+4}$
Inlet 4	6	0.979	2.22×10^{-3}	$2.65 \times 10^{+4}$
Inlet 5	5	0.705	1.33×10^{-3}	$2.65 \times 10^{+4}$
Inlet 6	5	0.705	1.33×10^{-3}	$2.65 \times 10^{+4}$
Inlet 7	4	0.551	8.33×10^{-3}	$2.65 \times 10^{+4}$
Outlet 1	9	1.632	5.55×10^{-3}	$2.65 \times 10^{+4}$
Outlet 2	5	1.410	2.66×10^{-3}	$2.65 \times 10^{+4}$
Outlet 3	5	1.058	2.00×10^{-3}	$2.65 \times 10^{+4}$

Table 3.6 Reynolds and Schmidt number for Oxygen

No.	Diameter(μm)	Velocity(mm/s)	Re_D	Sc
Inlet 1	7	0.720	3.41×10^{-4}	$1.05 \times 10^{+4}$
Inlet 2	6	1.714	6.97×10^{-4}	$1.05 \times 10^{+4}$
Inlet 3	6	0.490	1.99×10^{-4}	$1.05 \times 10^{+4}$
Inlet 4	6	0.979	3.98×10^{-4}	$1.05 \times 10^{+4}$
Inlet 5	5	0.705	2.39×10^{-4}	$1.05 \times 10^{+4}$
Inlet 6	5	0.705	2.39×10^{-4}	$1.05 \times 10^{+4}$
Inlet 7	4	0.551	1.49×10^{-4}	$1.05 \times 10^{+4}$
Outlet 1	9	1.632	9.95×10^{-4}	$1.05 \times 10^{+4}$
Outlet 2	5	1.410	4.78×10^{-4}	$1.05 \times 10^{+4}$
Outlet 3	5	1.058	3.58×10^{-4}	$1.05 \times 10^{+4}$

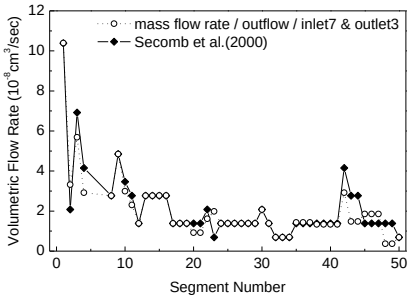

Figure 3.4 Comparison of volumetric flow rates for Secomb's vs. calculated data with inlet mass flow rate and outflow conditions (7 inlets and 3 outlets)

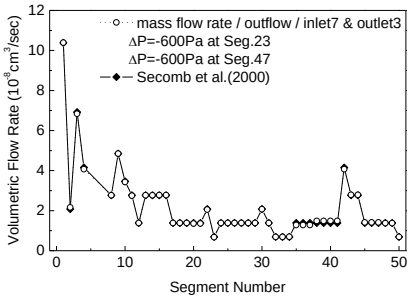

Figure 3.5 Comparison of volumetric flow rates for Secomb's vs. calculated data with inlet mass flow rate and outflow conditions ($\Delta \boldsymbol{P}$ = -600Pa at Seg. 23 and $\Delta \boldsymbol{P}$ = -600Pa at Seg. 47, 7 inlets and 3 outlets)

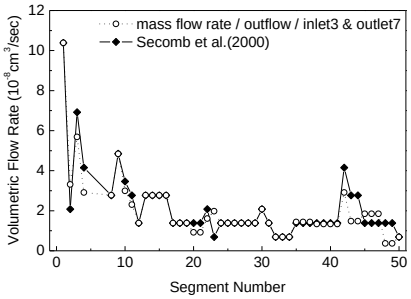

Figure 3.6 Comparison of volumetric flow rates for Secomb's vs. calculated data with inlet mass flow rate and outflow conditions (3 inlets and 7 outlets)

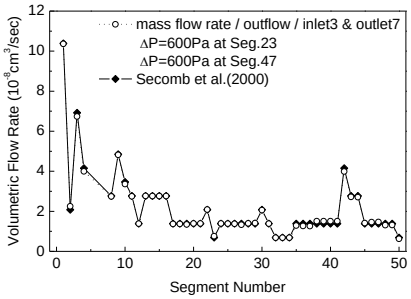

Figure 3.7 Comparison of volumetric flow rates for Secomb's vs. calculated data with inlet mass flow rate and outflow conditions ($\Delta \boldsymbol{P}$ = 600Pa at Seg. 23 and $\Delta \boldsymbol{P}$ = 600Pa at Seg. 47, 3 inlets and 7 outlets)

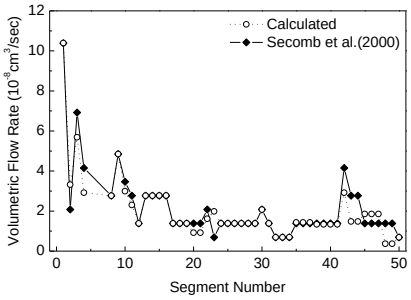

Figure 3.8 Comparison of volumetric flow rates for Secomb's and calculated data (Inlet mass flow rate and P_out1=22mmHg, P_out2=19mmHg, P_out3=25mmHg)

Table 3.7 Comparison of the volume flow rate between Secomb's and calculated data in the inlet and outlet based on Figure 3.8

	Seg. No.	Q(10^{-8} cm^3/sec) Secomb	Q(10^{-8} cm^3/sec) Calculated	% difference
Inlet 1	8	2.769	2.769	0.0
Inlet 2	9	4.846	4.846	0.0
Inlet 3	12	1.385	1.385	0.0
Inlet 4	13	2.769	2.769	0.0
Inlet 5	27	1.385	1.385	0.0
Inlet 6	28	1.385	1.385	0.0
Inlet 7	34	0.692	0.692	0.0
Outlet 1	1	10.385	10.388	-0.03
Outlet 2	14	2.769	2.772	-0.11
Outlet 3	30	2.077	2.071	0.29
				Avg.=0.02%

3.9 Computational methods

The fluid dynamics is in general described by the Navier-Stokes equations (with appropriate treatment of the non-Newtonian viscosity) in which the fluid momentum (the convection term) is balanced by the pressure and viscous forces. In treatments of biological flows, as noted in the introduction, there have been numerous methods to numerically solve the Navier-Stokes equations. The

Navier-Stokes equations can in principle incorporate multi-phase, particle-laden flows. Red blood cells, for example, have been modeled as non-deformable particles in continuum "background" flow by Dzwinel et al. (2003) [52].

Also, both unsteady and steady-state processes can be calculated by discretizing the Navier-Stokes equations in time and space for the given geometry and boundary conditions. Many studies have focused on the fluid dynamic aspect, i.e. flow patterns arising from pressure and velocity profiles.

However, most interesting biological processes involve transport of materials (e.g. oxygen, nutrients, foreign substances, or drugs), and this transport is coupled to the flow motion. That is, the material transport is also governed by a balance equation for convection, diffusion and boundary conditions at the wall for uptake or tissue absorption. This is precisely our approach in computationally simulating the transport of oxygen (and other materials) in a capillary network. The fluid mechanics is solved using a commercial CFD package, FLUENT, while taking into account of the non-linear viscosity, and in addition transport of oxygen in the stream is also computed along with hemoglobin reactions and wall flux terms. This approach is described in further details below.

First, a geometrical model for the capillary network needs to be constructed. To assemble this network with some level of realism and also to compare with existing work, we use the geometry that has been studied in Secomb et al. (2000), as shown in Figure 3.1. The model is a three-dimensional section of a rat brain (more detailed description is referred to Secomb et al., 2000) [65].

In the Secomb's model (2000), the mean vessel diameter is 5.77 μm with a standard deviation of 0.77 μm, therefore the variations in the vessel diameters are about 13%. The effect of varying vessel diameters is currently being investigated in this laboratory. Aside from that aspect, the current geometrical model is a reconstruction of the Secomb's model and consists of seven inlets and two exits as in the original work (Secomb, 2000).

However, in our previous model all of the capillary vessels were made of a uniform diameter of 5 microns and the flow rates are matched with Secomb's model rather than velocity. The connections between the branches of different diameters were difficult to implement without creating sharp edges in the computational meshes, particularly when there are triple junctions as shown in Figure 3.1. Furthermore, when the validation was performed using constant diameter of 5 microns, it showed the noticeable discrepancies primarily in the joint regions as expected where the separation, circulation, reattachment phenomena have been existed.

In Figure 3.9, each of the segments is numbered for later identification purposes, in an identical manner as in Secomb et al. (2000). Using the meshing scheme available in FLUENT, cylindrical meshes were constructed for straight sections while tetrahedral meshes were created for junctions, with a total number of cells being 574,578. Thus, all the flow and transport parameters are computed at 1,541,058 faces embedded in the capillary network.

Blood consists of red blood cells (RBCs), white blood cells, and platelets suspended in plasma. RBCs can be described as being biconcave discs of about 8

μm in diameter (Gijsen, 1999) [75]. Capillary vessels often have smaller diameters then this; hence RBC membranes are viscoelastic, allowing the RBC to deform quite drastically. Plasma itself is considered (and measured to be) a Newtonian fluid, however, blood as a whole displays non-Newtonian effects because of the RBC deformations.

Due to their relatively low concentrations, white blood cells and platelets do not typically make a significant contribution to the blood viscosity (Chen et al., 2000) [76]. The effective blood viscosity that includes the effect of RBC content is a function of several different parameters.

Blood viscosity increases with increased hematocrit (volume percentage of RBCs). This is due to the deformability of the RBCs. Blood viscosity also increases with decreasing temperature, is very high at low shear rates (less than 100 s^{-1}) with a drop to an asymptotic value as shear rate increases, and decreases with a decrease in capillary diameter.

To understand the flow behavior of blood, we use the Carreau-type viscosity model that has been shown to work well for blood flows (Shibeshi and Collins, 2005) [77]:

$$\frac{\eta-\eta_\infty}{\eta_0-\eta_\infty} = [1 + (\dot{\gamma}\lambda)^2]^{(n-1)/2} \qquad (2.24)$$

where η is the non-Newtonian viscosity, n is the power law index which depends on the hematocrit (as well as other blood constituents), λ is the relaxation time constant, and η_0 and η_∞ are the zero and infinite shear viscosities, respectively. The local shear rate $\dot{\gamma}$ is defined as:

$$\dot{\gamma} = \sqrt{\frac{1}{2}\overline{\overline{D}} : \overline{\overline{D}}} \tag{2.25}$$

The rate-of-deformation tensor $\overline{\overline{D}}$ is defined as:

$$\overline{\overline{D}} = \nabla\vec{u} + (\nabla\vec{u})^T \tag{2.26}$$

where, $\vec{u}$ is the local fluid velocity vector, and the superscript "T" means the transpose of the vector.

Shibeshi and Collins (2005) [77] compared several different viscosity models using FLUENT software with parameter values gathered from literature. The resulting velocity profiles (radial and axial), shear stress, and vortex length were investigated and compared. The results of that study indicated that there is significant variation in viscosity (as a function of shear rate) depending on which model is used, and that the appropriateness of the viscosity model depends on the flow conditions.

On the other hand, Hsu et al. (2009) [78] have considered flow in a T-shaped junction and conclude that Carreau-type model better reproduces the real blood flow characteristics out of several others in use (power-law and Casson models).

The Carreau model has been used quite frequently in computational simulations of blood flows, and also can readily be incorporated in the FLUENT computational framework (unlike another often used model, Carreau-Yasuda). The values for the Carreau model parameters that were used in the present work have been obtained from Shibeshi and Collins (2005) [77] and are presented in Table 3.8.

TABLE 3.8 PARAMETERS USED IN THE NON-NEWTONIAN VISOCITY MODEL

Parameters	***Values***
Zero shear viscosity (η_o)	0.056 Pa-s
Infinite shear viscosity (η_∞)	0.0035 Pa-s
Relaxation time constant (λ)	3.313 s
Power law index (n)	0.3568

As blood flows through the capillary network, oxygen is delivered through the capillary wall to the surrounding tissue. As this occurs, the concentration of free O_2 (O_2 dissolved in the stream), decreases (Gibson et al., 1995) [79].

However, there is another mechanism at work which seeks to replenish the O_2 lost to the tissue. Hemoglobin is an oxygen-carrying protein found in the red blood cells of mammals and many other animals. The reaction between oxygen and the hemoglobin is reversible and can be described as:

$$HbO_2 \overset{R_r}{\leftrightarrow} Hb + O_2 \tag{2.27}$$

where R_r is the reaction rate or the dissociation rate. Clark et al. (1985) described a way of modeling the oxygen-hemoglobin binding kinetics by considering three distinct species: free O_2, oxygenated hemoglobin (HbO_2), and non-oxygenated hemoglobin (Hb). As the molar concentration of the free O_2 decreases, so will the molar concentration of HbO_2 as the concentration of Hb increases (due to the hemoglobin's loss of oxygen) [80].

The species conservation equation for two of the species can be expressed as:

$$\frac{\partial [O_2]}{\partial t} = D_{O_2} \nabla^2 [O_2] - T \tag{2.28}$$

and

$$\frac{\partial [HbO_2]}{\partial t} = D_{Hb} \nabla^2 [HbO_2] + T \quad (2.29)$$

where T is the net rate at which the oxygen and hemoglobin bind to form HbO_2. Equilibrium exists, where there is sufficient free O_2 in the blood and no reaction (dissociation or association) takes place. In the limit as $T \to 0$,

$$[HbO_2] = F_{eq}[O_2] \quad (2.30)$$

where F_{eq} is an experimentally determined equilibrium constant. According to Clark et al. (1985), T can be expressed as

$$T = T_a - T_d \quad (2.31)$$

where T_d is the dissociation rate, and T_a is the association rate. The dissociation rate depends upon the concentration of oxygenated hemoglobin and can be written as:

$$T_d = K [HbO_2] \quad (2.32)$$

where K is an experimentally determined dissociation rate constant. If we define the total

molar concentration of hemoglobin to be

$$[Hb_T] = [HbO_2] + [Hb] \quad (2.33)$$

then the association rate is

$$T_a = K([Hb_T] - [HbO_2]) \left(\frac{[O_2]}{[HbO_{50}]}\right)^n \quad (2.34)$$

where $[Hb_{50}]$ and n are parameters found from experimental data (Clark et al., 1985). Implementation of this "reaction" set is relatively straight-forward in the FLUENT computational framework, as is the wall loss rate of oxygen to mimic the oxygen absorption into the surrounding tissue.

To impose oxygen flux at the vessel wall to simulate the delivery of oxygen to the surrounding tissue, a constant O_2 flux condition at the capillary wall surface is desired. However, within FLUENT computational framework, the mass flux boundary condition cannot easily be set up. Therefore, a wall surface reaction was used in place of a mass flux condition. This reaction would consume the O_2 at the capillary wall surface at a determined rate that corresponds to the wall loss rate. In the species conservation equation of oxygen, this would appear as a negative source term which occurs only at the wall surface. To avoid errors involving an apparent mass imbalance in the stoichiometric equation, a dummy species was created and called simply "dummy". The basic stoichiometric equation describing this surface reaction was

$$O_2 \xrightarrow{R_r} dummy \tag{2.35}$$

where R_r represents the rate constant of this reaction. Thus, at the wall the oxygen will be depleted to a dummy species called "dummy" at the rate specified by R_r. The reaction rate R_r is determined from the Arrhenius expression:

$$R_r = A_r T^{\beta_r} e^{-E_r/RT} \tag{2.36}$$

where A_r is called the pre-exponential factor, T is temperature in Kelvin, β_r is a dimensionless temperature exponent, E_r is the activation energy for the reaction in J/kgmol, and R is the universal gas constant in *J/kgmol-K*. For the purposes of this work, a constant value was chosen for the reaction rate, R_r, since the temperature in the entire network is kept at a constant 310 K. Hence, in the FLUENT software, β_r and E_r were set to zero to give us the following relation from equation 2.36:

$$R_r = A_r \tag{2.37}$$

Here, the Pre-Exponential Factor (A_r) equates directly to mass diffusion coefficient (D_0) as described in section 3.2. Mass diffusion coefficients for the oxygen in the blood are given by Table 3.4

The oxygen depletion rate and therefore the surface reaction rate depend on the physiological conditions, and it is possible to examine how the variations in the oxygen transport rate simply by varying the above parameter, R_r. However, the surface oxygen depletion rate was set constant as the baseline case. Depending on physiological conditions, the oxygen uptake rate can certainly be different, and if there were such conditions with available estimates on the oxygen uptake rate data the current simulations would allow for input of such altered distribution of oxygen in the capillary network.

The aforementioned geometry, governing equations and reaction kinetic equations are solved using the upwind scheme in FLUENT code with double precision. Various pressure, inlet/exit conditions were run along with introduction of blockages in the capillary network, as will be discussed in the next section. The resistance to blood flow decreases with decreasing vessel diameter in small vessels (<0.33 mm diameter), which is known as the Fahraeus-Lindqvist effect (Goldsmith et al., 1989). This effect could be due to a number of factors, such as, the Fahraeus effect itself since the lowering of the viscosity of a red cell suspension would result from a lowering of the hematocrit in the vessel (Shibeshi and Collins, 2005). In the present study, the capillary network consists of segments of equal diameter, so the Fahraeus-Lindqvist effect is neglected [77, 81].

Because the blood flow within a physiological capillary network is driven by the pressure gradient, the flow model can be set up where we specify the pressure at the inlets and exits. The pressure drop (ΔP) across a capillary network in a rat varies from 5-20 mmHg depending on location, geometry, and other physiological factors [42], and the pressure drop was set at the inlet with the exit pressure being set to 0 mmHg (gauge pressure). Three different values of ΔP were also tested: 5, 10, and 20 mmHg. For example, in the case where ΔP = 5 mmHg, each of the seven inlets were given a pressure condition of 5 mmHg, while each of the three outlets were set at pressure of 0 mmHg.

3.10 Results and discussion

Although the magnitude of the pressure non-uniformity may be small, fluid-dynamically they can alter the flow streamlines and therefore how the flow is distributed in a bifurcation or a triple junction (see Figure 3.3). These discrepancies will further be amplified in downstream junctions, further enlarging the difference between full three-dimensional model and one-dimensional model results. Indeed, in Figure 3.2 the largest differences, although rare, occur in segments far downstream of the inlets after having gone several flow bends and bifurcations. For example, the segments 19-20 involve a triple junction, a bend and are far downstream of inlets 1 and 3, as do the segment 21-22, 39-40, and 39-40. The segment 30 is straight, but it is downstream of a triple bend and far removed from inlets 6 and 7 as well. These are locations where the differences in the data are more pronounced in Figure 3.8.

Thus, it appears that flow bends, constrictions and bifurcations can cause non-uniform pressure distributions and flow patterns that can alter downstream flow rates in complex three-dimensional capillary networks. One of the advantages of the current fully three-dimensional computational framework is that most of these complex effects can be captured and accounted for. As shown in Figure 3.9, there are indeed many flow turns and branches in the current model, and some of the discrepancies in Figure 3.8 are attributed to this effect as noted above.

An example of the flow patterns that can be visualized using the current computational model based on the numerical solutions of the fundamental governing equations is illustrated in Figure 3.10, where we plot the detailed velocity vectors at a junction between segments 1, 2, 3 and 24. The junction walls are "hidden" in Figure 3.10 to show the internal velocity vectors. Segment 1 is an exit, so that the streams from the three other segments join to flow out through segment 1. Right at the junction, the fluid streams merge and the velocity field can involve some complex flow patterns.

Also, it can be observed that the velocity magnitudes are much smaller close to the walls, due to the viscous effects. All of the flow velocities and therefore the volumetric flow rates in the segments, which are integrated from the velocity data, are computed in this manner, instead of relying on one-dimensional models. Again, the flow rates and also the flow patterns will affect the transport of oxygen and other materials in the capillary network.

A full computational model is able to take into account of all of the pressure non-uniformities and their effects on the local volumetric flow rates and flow patterns across a large range of scales and geometries. In addition, the current approach allows us to use a more realistic non-Newtonian viscosity model such as the one shown in Eq. 2.24, whereas in one-dimensional network models as in Secomb et al. (2000) [65] a constant viscosity is used in a Poiseuille's law regardless of the shear rates. These aspects may be of importance since the transport characteristics depend on the volumetric flow rates, which in turn depend on the exact viscosity and the fully three-dimensional geometry.

Using the fundamental governing equations to solve the fluid mechanics of the capillary flow, the full flow effects are accounted for and quite accurate flow distributions in complex, three-dimensional geometry at arbitrary scales can be computed. The primary function of the capillary network is to transport and distribute oxygen and other essential substances.

Since the capillary diameter is quite small, this transport often is determined by the flow rate in the longitudinal direction. The net amount available for oxygen transport across the capillary wall, for example, is determined by the wall flux and the flow rate.

For this reason, it is important to obtain correct flow rate in complex capillary network geometry, and based on this information we can assess the effects of changes in the conditions within the capillary network and examine essential bio-transport processes such as oxygen distribution and drug delivery.

For the above inlet and exit conditions, we have run the flow and oxygen transport calculations for both unsteady and steady-state. The unsteady calculations were an attempt to observe the time evolution of the flow and oxygen distributions, with the inlet and exit boundary conditions suddenly applied at $t = 0$ in a stepwise manner.

Therefore, it does not yet fully simulate the pulsating pressure field representative of physiological processes. Using this framework, however, more realistic pressure fluctuations as a function of time can in principle be applied, as in pulsating flows.

Figure 3.11 illustrates the development of the oxygen partial pressure at various time steps after the application of the boundary conditions. It can be observed that steady-state is achieved in less than 1.0 sec. Due to the short distances involved in a capillary network, both the flow and oxygen transport is established in a short amount of time in comparison to, say, the time scale of pulsatile pressure fluctuations.

For this reason, it appears that steady-state computations suffice to characterize the main features of flow and transport in capillary networks of this scale. In the remainder of this work, we confine our interests to steady-state results.

The steady-state data from Figure 3.8 can be visualized as a contour plot of oxygen mass fraction in the capillary network as shown in Figure 3.12, which shows the spatial distribution more directly. As shown in Table 3.2 and 3.3, the volumetric flow rate conditions are different from one inlet to the other, and

Figure 3.12 shows that the higher volumetric flow rates are associated with higher oxygen mass fractions by a roughly proportional amount.

This is due to the higher available supply of oxygen at larger flow rates, at constant wall loss conditions that exist throughout the capillary network. This also affects the oxygen distribution in the rest of the capillary network. At low-activity or low-oxygen-demand conditions, the oxygen is well supplied (Ellsworth et al., 2009) [82].

It is only during hyper-active states or stenosis conditions that the oxygen delivery becomes critical and regions of hypoxia can develop. Hypoxia can lead to irreversible brain cell damage in minutes. The ability to compute and visualize the exact distributions of oxygen in the capillaries is, therefore, an important tool to investigate the above and other specific conditions that may arise.

Abnormal pressure conditions are frequently observed in circulatory systems, and are referred to as hyper- or hypo-tension. They are known to be the causes of a variety of malignant physiological conditions. In this work, we consider the consequences of altered pressure conditions on flow and transport phenomena, although based on the pressure changes local mechanical wall stresses or possibly deformations, for example, can also be calculated.

Figure 3.13 shows the changes in the oxygen mass fraction partial pressure in the capillary network at three difference pressure differences from the inlet to exit: 5, 10 and 20 mm Hg. Again, the exit pressure is fixed and the inlet pressures are adjusted to result in above pressure differences from the inlets to the exits. Higher pressure difference between the inlet and exit, obviously, causes an

increase in the flow speed, and the consequence is that the residence time for the oxygen-containing stream in the capillary network is reduced. Substantial differences in the oxygen mass fraction can be seen at different pressure conditions, with highest oxygen levels at 20 mm Hg pressure drop. For examples, about equal levels of oxygen are found close to the inlet, with the levels diverging further into the network at different pressure conditions.

Again, the higher flow speed and lower residence time conspire to reduce the transport through the vessel walls leaving more oxygen in the stream at higher pressure conditions. From further calculations, it is found that for each 25% increase in the pressure drop from the normal condition there is a 15% increase in the oxygen that is leaving the network on the average. That essentially amounts to 15 % decrease in oxygen being delivered through the vessel walls. Higher residence time associated with low volumetric flow rates at low pressure conditions would indicate more successful delivery of oxygen through the vessel walls.

On the other extreme, however, hypotension or excessively low pressure difference may cause insufficient fluid momentum to reach all of the capillary network branches leading to localized spots of low oxygen delivery. In general, higher pressure at the inlet results in increased static pressure through the capillary vessels, leading to increased vessel stress in a proportionate manner.

Stenosis refers to an abnormal narrowing of arterial blood vessels, caused by a number of factors including inflammation and accumulation of lipoprotein.

Stenoses in capillary networks can be particularly problematic, as they may not be subject to as obvious early symptoms or diagnosis as in coronary vessels.

Although flow constrictions associated with stenosis can be circumvented in the current capillary network due to redundant branches, stenosis can in general cause serious medical conditions ranging from reduced oxygen delivery to heart attacks even from those in capillary vessels.

Moreover, hypertension is believed to cause narrowing of the capillary vessels, which will yet increase the local pressure initiating a vicious cycle of increasing flow restrictions. In this work, we simulate the stenosis points as local pressure increases at the segments 25 and 32, i.e. downstream of the inlets 5 and 7 (see Figure 3.1). Local pressure increase is fluid dynamic manifestation of a flow constriction such as stenosis. For example, an orifice placed in a pipe acts to increase the downstream pressure device in fluid flows, according to $\Delta p = \frac{1}{2}\rho V_1^2\left[\left(\frac{A_1}{A_2}\right)^2 - 1\right]$ where the subscripts "1" and "2" refer to the upstream and downstream conditions respectively. Then, the severity of the stenosis can be equated with the magnitude of the pressure increase at that point. In principle, any arbitrary area ratio, A_1/A_2, can be simulated by setting the pressure increase appropriately.

Figure 3.14 shows the static pressure distribution involving these two stenosis points (here, set up as complete blockage of the flow) in the capillary network. The most pronounced reductions in the static pressures are observed at segments 21 through 24 and segment 32. These segments are, as expected, points

directly downstream of the stenosis points. Overall, however, the pressure reduction in the other parts of the network is relatively minor, and the reason for this is the redundancy in the flow channels in this particular network, with multiple inlets and exits along with interconnections. The large number of inlets, in comparison to the number of stenosis points, allows for nearly normal circulation in the network. This obviously will not be the case in isolated networks with small number of inlets.

The oxygen mass fraction shows a similar effect in Figure 3.15 where the lowered oxygen levels are found upstream of the stenosis points as the flow is not able to proceed in these segments and the oxygen content is stagnantly depleted through the vessel walls.

The baseline geometry for the capillary network again follows that provided by Secomb et al. (2000) [65]. While retaining the basic geometry, however, we can alter number and designations of the inlets and exits, to see the effects on the pressure and oxygen distributions.

As can be seen in the previous plots thus far, both the static pressure and the oxygen levels are highly non-uniform in the current network configuration. To be sure, the highest peaks of both the pressure and oxygen levels are found at the seven inlets. Outside of these peaks and low levels at the exits, there is still a fairly high level of non-uniformity.

The optimum capillary network configuration would be one where the oxygen undergoes a linear, monotonic decrease with minimum pressure loss. This will be an indication that the oxygen is being delivered through the vessel

walls in a nearly uniform manner and that the flow resistance is the minimum. Biological systems exhibit naturally evolved configurations, and it is of interest to see how optimum configurations may be reached in capillary networks. A full permutation of the inlet and exit configurations would require much computational time, and we defer such complete investigation to a subsequent work using a systematic optimization algorithm.

Here, we test three alterations to the inlet and exit configurations to check their effects on the pressure and oxygen level distributions. The variable parameters are the number and location of the inlets and exits, altered from the seven inlets/three exit configuration shown in Figure 3.12.

First, we consider a configuration with an equal number of inlets and exits, five each. Next, we rearrange the inlets and exits so that there are three inlets and seven exits. The volumetric flow rates and the oxygen mass fraction for the two modified configurations are shown in Figs. 3.16 and 3.17, respectively, along with those from the original configuration.

It can be observed in Figure 3.16 that a substantial change in flow rates occurs, with the Conf. 2 showing the most uniform. It should be noted that in order to make a meaningful comparison the total volumetric flow rate is fixed in all of the configurations. Thus, the larger number of exits in the original configuration is associated with generally lower flow rates in the inlets and large flow rates at the three exits (e.g. segment 1 in Figure 3.16). The converse is true for 3 inlets/7 exits configuration. Overall, an equal number of inlets and exits are expected to yield the most uniform flow rates, as verified in Figure 3.16.

It is of interest to see how the uniformity of the flow rates translates to the oxygen distribution, as in Figure 3.17. It can be seen that the extreme levels, both high and low, are found for the uneven number of inlets and exits, and again the 5 inlet/5 exit configuration exhibits the most moderate variations. This is indicative of the gradual depletion in the stream, or more uniform diffusion through the vessel walls.

Transport of other materials, such as drugs, nutrients or other foreign substance, can also be tracked using the current computational framework, so long as their in-stream and wall diffusion properties are known. The wall diffusion in most instances is a strong function of the local physiological conditions.

We take a liquid drug, digoxin ($C_{41}H_{64}O_{14}$), as an example case, by "injecting" it at the inlet(s) and show its distribution in the capillary network under two different injection conditions. Digoxin is a widely used drug for treatment of heart conditions, including arterial fibrillation and flutter. First, digoxin is injected uniformly at all of the seven inlets so simulate a case where the injection occurs far upstream of the capillary in Figure 3.19. This is compared with a capillary injection where the same total amount is injected at only one of the inlets (inlet 7 in Figure 3.20), in Figure 3.18. It can be observed that the localized capillary injection results in digoxin diffusing only to segments connected to the inlet 7, which is to be expected.

The multiple injection scheme results in a drug distribution in the capillary which is quite similar to that of oxygen shown in previous plots. The reason is

that the stream flow patterns are identical and the capillary distribution is primarily due to the flow patterns minus the wall diffusional losses. Almost any drug and its delivery can be simulated in the capillary and other networks using this framework, as long as its diffusive and biochemical reactive properties, if applicable, are known. Dissolution and other phase changes can also be handled using standard thermodynamic models, as needed.

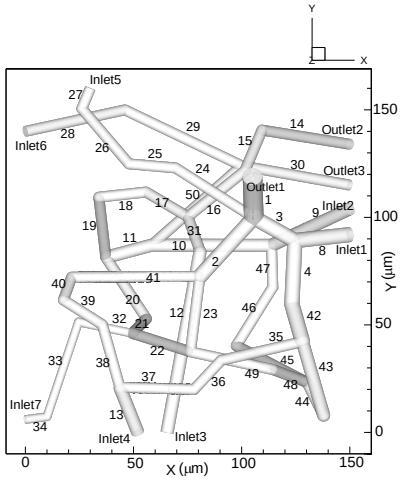

Figure 3.9 Segment number in the geometry of the capillary network

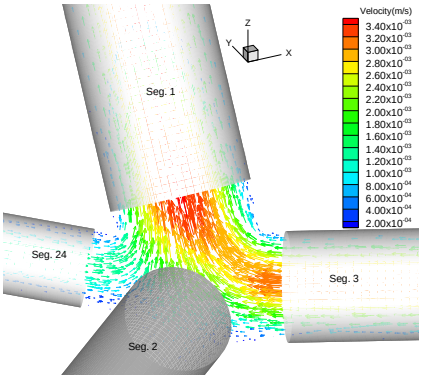

Figure 3.10 Detailed vector plot of the velocity field at a junction from the current computational model.

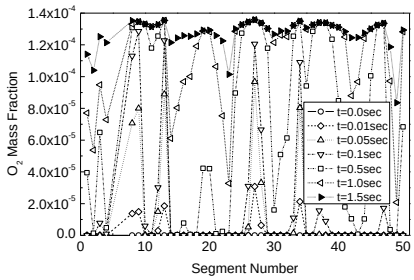

Figure 3.11 Development of the oxygen distribution in the capillary network over time

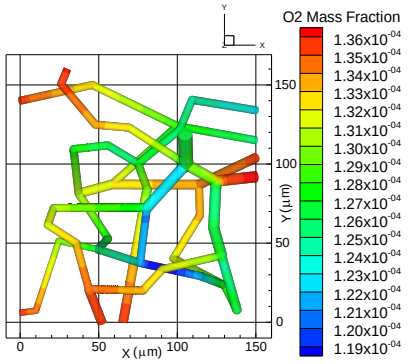

Figure 3.12 Steady-state distribution of oxygen in the capillary network.

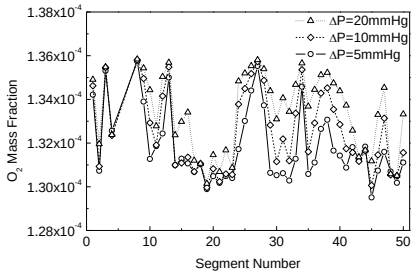

Figure 3.13 Effects of pressure changes on the oxygen mass fraction in the capillary network

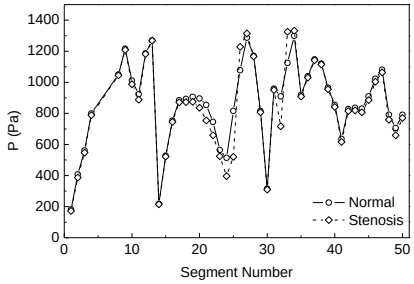

Figure 3.14 Effect of localized flow constrictions (stenosis) on the static pressure in the capillary network.

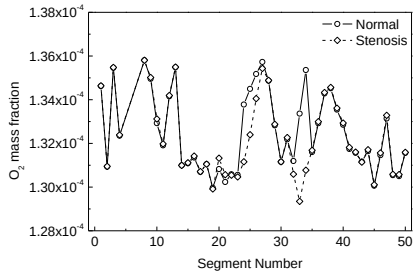

Figure 3.15 Effect of localized flow constrictions (stenosis) on the oxygen mass fraction in the capillary network.

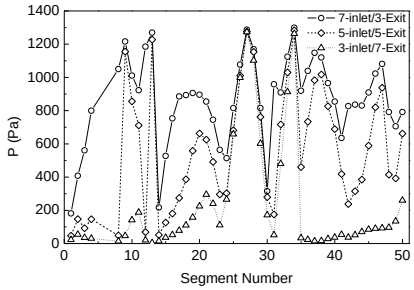

Figure 3.16 Pressure distributions for different inlet and exit configurations.

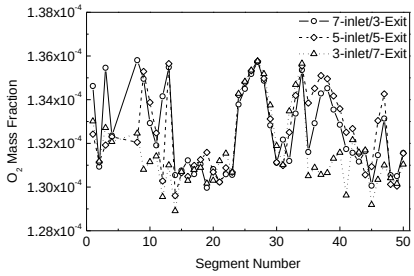

Figure 3.17 Distributions of the oxygen mass fraction for different inlet and exit configurations.

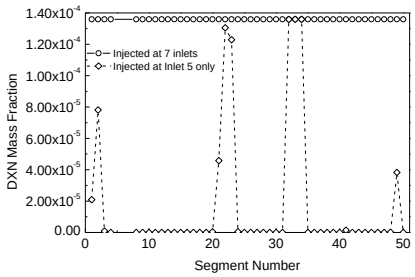

Figure 3.18 The steady-state digoxin distribution in the capillary network.

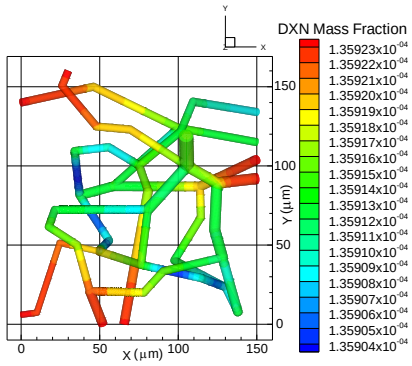

Figure 3.19 The steady-state digoxin distribution in the capillary network.

(All 7 inlets injected)

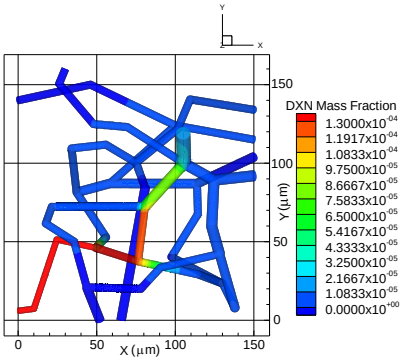

Figure 3.20 The steady-state digoxin distribution in the capillary network

(Only inlet No. 7 injected)

3.11 Conclusions

A realistic three-dimensional model of a capillary network is used to simulate the flow processes and transport of oxygen. The governing equations are from the fundamental conservation principles, and the solutions are obtained numerically via a use of commercial software called FLUENT. Additional hemoglobin-oxygen kinetics along with oxygen in-stream diffusion and delivery through the vessel walls are incorporated in the above computational framework. The results for the volumetric flow rate have been compared with the data of Secomb et al. (2000), and good agreement is found. In addition, current approach allows for inclusion of oxygen and other material transport, including drugs, nutrients or contaminants.

Moreover, three-dimensional models of complex circulatory systems ranging in scale from macro- to micro-vascular vessels in principle can be constructed and analyzed in detail using the current method. Potential applications are delivery methods for drug or nutrients tailored for individual circulatory network geometry, design of surgical alterations for optimized microcirculations, and so on. A number of flow and oxygen transport conditions was examined using the current method for this particular example of microvascular network, including pressure variations, unsteady effects, stenosis conditions and changes in the inlet and exit configurations.

Chapter 4

A REDUCED CHEMICAL KINETICS OF GAS TURBINE COMBUSTION FOR JET PROPELLENT-10

4.1 Introduction

4.1.1 Objective and scope of research

The purpose of this study is to build a reduced chemical kinetic mechanism of the combustion for hydrocarbon jet-fuel, JP-10 ($C_{10}H_{16}$), which is being studied as a possible Jet propellant for the Pulse Detonation Engine (PDE) and other high-speed flight applications such as aircraft-launched missiles.

It has been specifically targeted because of its high thermal stability and density properties, and availability. The thermal stability of JP-10 is only comparable to the conventional rocket fuel, RP-1. There are two benefits from an aerospace engineering point of view to using JP-10 over RP-1. JP-10 has a higher density, 0.94 g/cm^3 versus 0.81 g/cm^3, and JP-10 is a single molecule rather than a mixture of paraffins and cycloparaffins. The decomposition of a single molecule is simpler to analyze and control than a mixture of hydrocarbon molecules.

The conditions of interest are inlet temperatures from 900-1,700K, pressures from 1- 40atm so that the combustion of JP-10/O_2/Ar mixture can be calculated. A premixed constant-volume plug flow combustor code is applied to this modeling.

This study shows that the cracking reactions are favoured at high temperatures because the energy is available for promoting the endothermic reactions. The rupture of the C-C bond of the initial molecule and the subsequent

formation of olefins and smaller radical compounds are the steps that control the reaction kinetics. High temperatures, e.g. above 1500 K, produce the C_6 and C_5 species in important concentrations.

Finally, to support the development of this JP-10 reaction mechanism, the oxidation and pyrolysis data is investigated here and validated through comparisons with measured shock tube data for initial pressures of 1, 3, and 6atm, for a range of temperature from 1378K to 1671K.

4.1.2 Literature review

A major advantage for using hydrocarbon fuels is for their heat absorbing reaction properties. Supersonic and hypersonic vehicles will face severe thermal environments, particularly in the engine. For example, at Mach 8 a combustor surface that is not cooled will surpass 3,000 K, which far exceeds known structural material capability.

The thermal decomposition reactions of hydrocarbon fuels feature a substantial activation energy barrier and hence, offer a potential heat sink. Moreover, the resulting heat-of-combustion of decomposition products remains essentially unchanged or slightly increased. These endothermic reactions are supported by the energy extracted from heated air, for instance, aerodynamically heated inlet air or compressor bleeds [83].

Gaseous fuels, such as hydrogen, do not offer the same heat capacity as hydrocarbon fuels, because they do not undergo thermal decomposition. Low density, gaseous fuels also require a large onboard storage capacity. By using

high-density liquid fuels, the size of the vehicle can be compacted, thereby increasing engine efficiency. A key development in making the PDE viable would be demonstrating the rapid formation of the detonation wave in a spark-ignited combustor, fueled with a conventional storable hydrocarbon [84].

JP-10 or exo-tricyclodecane ($C_{10}H_{16}$) is a rather unusual jet fuel as it is composed of only one large molecule, whereas most other jet fuels contain a mixture of hydrocarbons. Although the single molecule makes modeling the initial cracking mechanisms easier, it is too large number of independent variables compromises the results of path and sensitivity analyses for a complete detailed description of the reaction mechanisms [85].

Under pyrolysis conditions it is assumed that the initial scission is between a C-C bond rather than an H-abstraction or C-H bond scission [85 - 88].

Richard J. Green et al. [89] studied high-temperature JP-10 pyrolysis using a micro flow tube reactor and Gas Chromatography/Mass Spectrometer (GC/MS) for analysis. A heated quartz tube was used to eliminate possibilities of surface reactions. With a 2 ms residence time, JP-10 begins to decompose above 900 K, and is mostly decomposed by 1,300 K. Initially, the major product was cyclopentadiene (C_5H_6, CPD). However, CPD is unstable at high temperatures and is quickly transformed into other products.

At higher temperatures, the major products were benzene, propyne, and C_4H_x (x = 4, 6, 8), with smaller amounts of C_7H_x (x = 6, 8, 10) and a variety of C_8 and C_{10} species. Some minor products with higher retention times than JP-10 could not be identified with certainty on the MS spectra; however, it was concluded that

these large molecules are more than likely highly unsaturated and possibly aromatic. From the pattern of products observed, it is clear that at high temperatures dehydrogenation and cyclization reactions are present, in addition to the main processes leading to ring opening.

Shamit Nakra et al. [90] studied that decomposition of JP-10 in a small flow tube reactor over the temperature range up to 1,700 K on the millisecond time scale. For comparison, the decomposition behavior of cyclopentadiene (C_5H_6) and benzene (C_6H_6) was studied under identical conditions. Products of pyrolysis were identified by chemical ionization (CI) and electron impact ionization (EI) mass spectrometry. On the experimental time scale, JP-10 begins to decompose above 900 K and is completely decomposed by 1,300 K. In the initial decomposition, the principal products are cyclopentadiene (C_5H_6), benzene, propyne (C_3H_6), and C_4H_x. At high temperatures, the cyclopentadiene decomposes, and the principal species observed are benzene, acetylene (C_2H_2), and ethylene (C_2H_4).

From the combination of EI and CI spectra, it was confirmed that the C_6 product observed is benzene, with few if any other C_6H_x products. Similarly, the C_5 product is cyclopentadiene, with no cyclopentene (C_5H_8) or other C_5H_x products. The observed product distribution is inconsistent with both equilibrium speciation and predictions of existing JP-10 kinetic models.

Davidson et al. [86] investigated the post-shock gas mixtures of pure JP-10 in a single pulse shock tube at conditions between 1.2 atm to 1.5 atm and 1,100 K to 1,700 K.

High-speed UV absorption spectrum of JP-10 decomposition products showed evidence of cyclopentene as an initial decomposition product with near unity yield. This result is supportive of the hypothesis that the first step of the decomposition path for JP-10 is the breaking of a C-C bond and the formation of cyclopentene (C_5H_8). Due to the short test time (~50 ms) the spectra did not show other products, such as benzene (C_6H_6), because these are expected to form through secondary chemical reactions.

4.1.3 Pulse Detonation Engine

By replacing a constant burning fuel, as in a ramjet or rocket, it is possible to use impulses created by sequential detonations as thrust. These impulses are very rapid explosions that can propagate over 2,000 m/s (Ma = 6.0). In principle, detonations are an extremely efficient means of combusting a fuel-oxidizer mixture and releasing its chemical energy content. The high flame speed of detonation combustion provides stronger evidence that it occurs as a constant volume process, unlike as found with the pulsejet, where its unsteady state deflagration combustion actually is a constant pressure process [87, 91].

Bussing T. et al. [87] theoretically determined that depending on the compression ratio, an engine that uses detonation in place of constant burning could be 30 % to 50 % more fuel-efficient assuming the same propulsive efficiency could be maintained.

In addition to fuel efficiency, it has been proposed that a Pulse Detonation Engine (PDE) could also provide advantages of lower weight and cost when

compared to existing gas turbine engines. Unlike complicated turbine engine designs, in its simplest configuration, a PDE is just a long detonation tube closed at one end with few moving parts. The PDE operates on the principles of cyclical filling and detonation. The tube is filled with an air-fuel mixture that is ignited at the closed end of the tube and detonates within the constraints of the tube dimensions. This initiates a detonation wave that propagates at supersonic speed until it exits the tube. The tube is purged of the combustion products and a new mixture of air and fuel is injected, repeating the cycle. This simple unsteady state combustion process eliminates the need for pumps, turbines or even compressors [92].

The theory behind a PDE is simple, though the applied technology is complicated. Although there are potential applications spanning the entire flight envelope including subsonic, supersonic, and hypersonic flight, there are still many unresolved issues concerning the PDE. Fuel-air mixing, detonable mixture injection, reliable thrust measurements, characterization of cycle loss, and efficient detonation initiation are only some examples of areas that need to be researched before a practical and affordable PDE can be realized [91].

4.2 Thermal cracking of JP-10

Kinetic analysis is useful to understand the main frame of a complex mechanism and to determine the most important reaction routes, in particular when the mechanism has to be reduced. Such kinetic analyses have been described in this study on JP-10 oxidation. Hydrocarbon cracking process

involves the rupture of C-C molecular bonds creating lighter hydrocarbons from heavier hydrocarbons, which has been called as beta scission. It is an important reaction in the combustion of thermal cracking of hydrocarbons and the formation of free radicals. Free radicals are formed upon splitting the carbon-carbon bond. Free radicals are extremely reactive and short-lived. When a free radical undergoes a beta scission, the free radical breaks two carbons away from the charged carbon producing an olefin (e.g. ethylene, C_2H_4) and a primary free radical, which has two fewer carbon atoms.

Cracking reactions are being endothermic and thermodynamically controlled by high temperatures. Thermal cracking or pyrolysis, catalytic cracking, and hydrocracking are the three methods of hydrocarbon cracking. Pyrolysis is carried out in the absence of oxygen and occurs at the highest temperatures above 1,000 K. Catalytic cracking occurs at temperatures between 200 ℃ and 600 ℃ and pressures around 1 atm. As the name suggests, hydrocracking occurs in the presence of hydrogen at temperatures between 250 ℃ and 400 ℃ and under high pressures, typically between 80atm and 200atm [93].

In the present study, we focused on thermal cracking and oxidation of JP-10, which is based on the published literature to place reliance on this study. Thermal cracking usually involves a beta scission at a bond located to the carbon atom having the unpaired electron and there is little transfer of the radical from one hydrocarbon chain to another. The unpaired electron cannot move from one carbon atom to another on the chain, inhibiting isomerization reactions. For this reason, thermal cracking generally produces high yields of ethylene, low yields of

methane, and low yields of evenly distributed α-olefins, which gives a high ratio of olefinic to paraffinic products. There is also an absence of isomerized products because of the immobility of the unpaired electron [93].

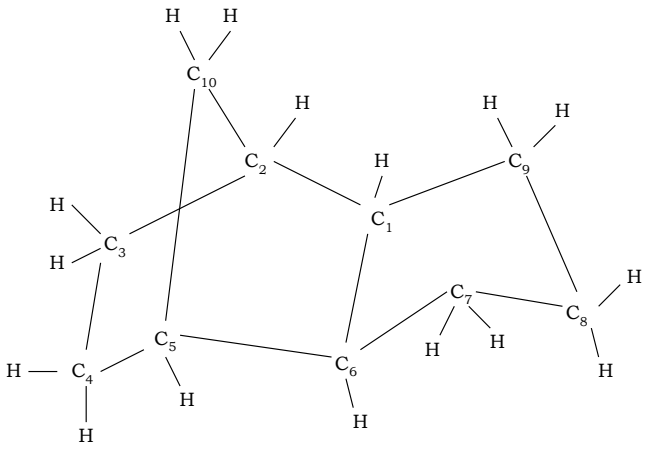

Figure 4.1 Structure of JP-10.

Figure 4.1 shows the location of the seven distinctive C-C bonds (1-2, 1-5, 2-3, 1-9, 9-10, 7-8, 8-9) in JP-10 which might break assuming that the first step is a C-C bond-scission rather than an C-H bond-scission or H-abstraction reaction. F. A. Williams, D. F. Davidson, A. Laskin [85, 94 - 96], have suggested the 1-5 C-C bond break would be the most likely first opening, followed by two beta scissions to open the resultant large rings, finally giving as products,

$$\text{JP-10} \rightarrow C_2H_2 + 2C_2H_4 + 1,3\text{-}C_4H_6$$

Olivier Herbinet et al. [97, 99] has also suggested that the first step may involve this type of isomerization to yield 5, 8 and 9 membered unsaturated cyclanes and that the products of this decomposition would be similar to that seen with cyclopentane. This first 1-5 C-C bond break, however, may be susceptible to reconnection.

Li et al. [85] have suggested that cyclopentene, C_5H_8, could be formed by breaking a C-H bond of a CH_2 group. This rupture would then be followed by four C-C bond scissions that break two of the five membered rings leaving cyclopentene and two different sets of products. Similar product distributions would be attained by H-abstraction reactions.

$$JP\text{-}10 \rightarrow C_5H_8 + C_2H_4 + C_3H_3 + H$$

$$JP\text{-}10 \rightarrow C_5H_8 + C_2H_2 + C_3H_5 + H$$

$$JP\text{-}10 + H \rightarrow C_5H_8 + C_2H_4 + C_3H_3 + H_2$$

$$JP\text{-}10 + H \rightarrow C_5H_8 + C_2H_2 + C_3H_5 + H_2$$

In their model, the formation of cyclopentene is secondary to the formation of 1, 3-butadiene by reaction 1a. If the 1-9 C-C bond breaks occurs first, this may be followed immediately by the beta-scission of the 2-3, 6-10 or 7-8 C-C bonds. The subsequent scission of the 5-6 C-C bonds would then form cyclopentene and an un-branched C_5 chain [98].

$$JP\text{-}10 \rightarrow C_5H_8 + \text{other } C_5 \text{ products}$$

Decomposition of Cyclopentene

JP-10 is formed by the hydrogenation of dicyclopentadiene (DCP), and a brief comparison of the kinetics and absorption spectra associated with a related cyclic C_5 compound (cyclopentene, C_5H_8) should offer some insight into the interpretation of the absorption spectra of the more complicated decomposition products of JP-10. Cyclopentene decomposes through the following series of reactions. [99, 100]

$$C_5H_8 \rightarrow C_5H_6 + H_2$$

$$C_5H_6 \rightarrow C_5H_5 + H$$

$$C_5H_6 + R \rightarrow C_5H_5 + RH$$

$$C_5H_5 \rightarrow C_2H_2 + C_3H_3$$

The following oxidation process after cyclopentene decomposition is based on typical pathways combined with a common secondary chemistry mechanism, which is including in the 1, 3-butadiene oxidation mechanism. Variations are the temperature, pressure, initial concentration and stoichiometry, which will all have an effect on the relative importance of the direct decomposition or H abstraction/oxidation pathways. At later times, but before the rapid formation of radical's characteristic of the exponential phase of ignition, the expected dominant species are likely to be stable and include: ethylene, acetylene, possibly benzene, carbon monoxide and formaldehyde.

Benzene formation:

Reaction-path analysis has shown that the main source of benzene (C_6H_6) is the propargyl-propargyl ($C_3H_3 + C_3H_3$) self-combination reaction, with the remainder from H addition to phenyl (C_6H_5).[102 - 104] All reaction mechanisms used in this study is given in Appendix H. Oxidation and breakdown can occur at nearly any stage of JP-10 combustion. Figure 4.2 shows the main pathways leading to the formation of the first aromatic ring in the diffusion flames of JP-10, cyclopentadiene and acetylene. For the JP-10 diffusion flame, the C_3H_4 isomers are formed from the direct decomposition of the Cyclopentene as was observed in the premixed flame previously presented. On the other hand, for the acetylene diffusion flame, the C_3H_4 isomers are formed from the reaction of methyl radicals

with acetylene present in large quantity. In both cases, the propargyl and allyl radicals react with one another to form benzene. In contrary to the alkane flames, the normal butadienyl radical (*n*-C_4H_5) is found very important to the formation of the first aromatic ring. This species is formed from the reaction of acetylene with vinyl radicals. Later, benzene molecules are formed from the addition of acetylene onto the butadienyl radical. While not important for the alkane flames, this pathway contributes up to 40% of the total rate of benzene formation for the acetylene diffusion flame. These four laminar flames show that the mode of combustion (premixed or diffusion) might have little influence on the pathways leading to the formation of soot precursors such as benzene.

However, the chemical structure of the fuel affects significantly the mechanisms of benzene formation by enabling or disabling entire reaction pathways. A detailed representation of the chemistry of soot precursors is thus required to properly predict the formation of benzene in various flames with different fuels. [102]

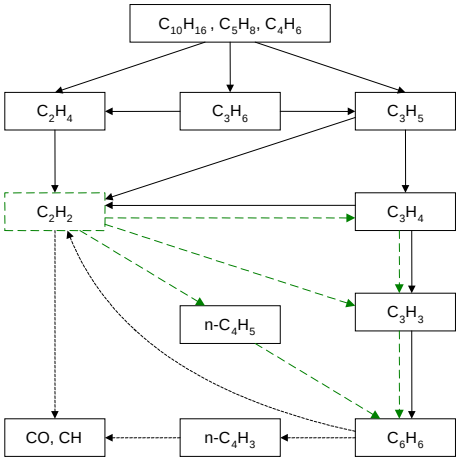

Figure 4.2 Main pathways leading to the formation of benzene for the alkane flames (solid lines) and the acetylene flame (dashed line).

C_4 Chemistry:

The reaction subset was constructed based on a critical review of the literature [101-105] so that the benzene formation process can be coupled with JP-10 kinetic modeling. The emphasis was placed on the C_4H_6 species as described in [104]. The C_4H_2, NC_4H_3, IC_4H_3 and C_4H_4 reaction mechanisms were established as a logical part of the C_4H_6 mechanism. A detailed description of the pyrolysis kinetics of 1, 3-butadiene and its isomers is beyond the primary scope of the present study. However, to ensure that artifacts in the pyrolytic part of the model do not influence the oxidative kinetics of 1, 3-butadiene, the literature is closely examined on the thermal reactions of C_4H_6 and incorporates the relevant kinetic features into the model. The mechanisms of the thermal decomposition of 1, 3-butadiene have been discussed extensively in the literature [106-112]. The initial step was thought to be: (a) C - C bond rupture to form two vinyl radicals [108, 110, and 111]

$$1,3\text{-}C_4H_6 \rightarrow C_2H_3 + C_2H_3$$

and/or (b) the formation of ethylene and acetylene. [107, 109, 110] The second pathway, originally proposed [107,109] to occur as a concerted unimolecular process, was lately considered [110] to proceed in two steps via the formation of vinylidene.

The formation of the C_4H_5 radicals—namely, $HC\cdot=CH—CH=CH_2$ (*n*-C_4H_5), $H_2C=C\cdot—CH=CH_2$ (*i*-C_4H_5) are described by the reactions of H ejection and abstraction from C_4H_6:

$$1,3\text{-}\ C_4H_6 \rightarrow n\text{-}C4\ H5 + H\cdot$$

$$1,3\text{-}\ C_4H_6 \rightarrow i\text{-}C_4H_5\cdot + H\cdot$$

$$1,3\text{-}\ C_4H_6 + R\cdot \rightarrow n\text{-}C_4H_5\cdot + HR$$

$$1,3\text{-}\ C_4H_6 + R\cdot \rightarrow i\text{-}C_4H_5\cdot + HR$$

where $R\cdot = H\cdot$; $\cdot CH_3$, $\cdot C_2H_3$, and $\cdot C_3H_3$. $i\text{-}C_4H_5\cdot$ are resonantly stabilized and are thus more stable than $n\text{-}C_4H_5\cdot$. In the present model, the mutual isomerization of $\cdot C_4H_5$ is described by 1,2-H shift:

$$n\text{-}C_4H_5\cdot \leftrightarrow i\text{-}C_4H_5\cdot \leftrightarrow CH_2{=}C{=}C\cdot{-}CH_3$$

Reactions of 1,3-butadiene with $\cdot OH$. Liu et al. [113] reported the overall rate constant in the temperature range of 305–1173 K. Based on their analysis, the major reaction channel is $\cdot OH$ addition at temperatures <1000 K, while the H abstraction by $\cdot OH$ is the major channel at higher temperatures. Here only the H-abstraction reactions are included in the model,

$$1,3\text{-}C_4H_6 + \cdot OH \rightarrow n\text{-}C_4H_5\cdot + H_2O$$

$$1,3\text{-}C_4H_6 + \cdot OH \rightarrow n\text{-}C_4H_5\cdot + H_2O$$

Additional fragmentation reactions of 1,3-butadiene and 1,2-butadiene were also considered. They are

$$1,3\text{-}C_4H_6 \rightarrow C_4H_4 + H_2$$

$$1,3\text{-}C_4H_6 \rightarrow \cdot C_2H_3 + \cdot C_2H_3$$

$$1,2\text{-}C_4H_6 \rightarrow \cdot C_3H_3 + \cdot CH_3$$

$$1,3\text{-}C_4H_6 + H\cdot \rightarrow \cdot C_2H_4 + \cdot C_2H_3$$

After the radical pool is established, there are three separate pathways contributing to the overall reactions. These three pathways are described in Figure 4.3 and are seen as a result of the different starting reactions of 1,3-butadiene, that

is, with H, O, and OH. The relative contribution of each pathway does not vary drastically as a function of equivalence ratio. The rates of these pathways range from being nearly equal in fuel-lean cases to being different by just a few factors under the fuel-rich condition.

Pathway I is the fastest under all flow-reactor conditions. Similar to the pyrolysis case, this pathway starts with the chemically activated reaction of 1,3-butadiene with the H atom to yield vinyl and ethylene. Ethylene is consumed either by its reaction with the O· atom to yield the methyl and formyl radicals, or through H abstraction by H· and ·OH radicals to produce the vinyl radical. Thus, Pathway I can be viewed as that of ethylene oxidation with the addition of the initial, chemically activated H-atom attack on 1, 3-butadiene.

Pathway II starts from the reactions of 1, 3-butadiene with the O atom, with the subsequent reactions involving mostly the $\cdot C_3H_5$ radicals. The allyl radical tends to combine with H· and $\cdot CH_3$, forming propene and 1-butene, respectively. Propene and 1-butene are subsequently consumed by the chemically activated reaction of H· (or $\cdot CH_3$) addition $\rightarrow$ $\cdot CH_3$ (or H·) elimination to yield ethylene. The allyl pathway has a net effect of reducing the radical pool concentrations, because each reaction step following allyl formation involves either radical–radical combination or the exchange of the H atom for a lesser reactive methyl radical. In all flow-reactor experiments, the propene concentrations in the oxidation of butadiene are larger than those in pyrolysis. This trend is clearly caused by an increase in the contribution of Pathway II with a decrease in the equivalence ratio.

In general, Pathway III proceeds at a slower rate than the first two pathways. This route starts with H abstraction of 1, 3-butadiene by ·OH and under fuel-rich conditions, also by the H atom. Diacetylene is produced from the decomposition of ·C_4H_5 via C_4H_4 and C_4H_3 and is oxidized through its reactions with O· and ·OH.

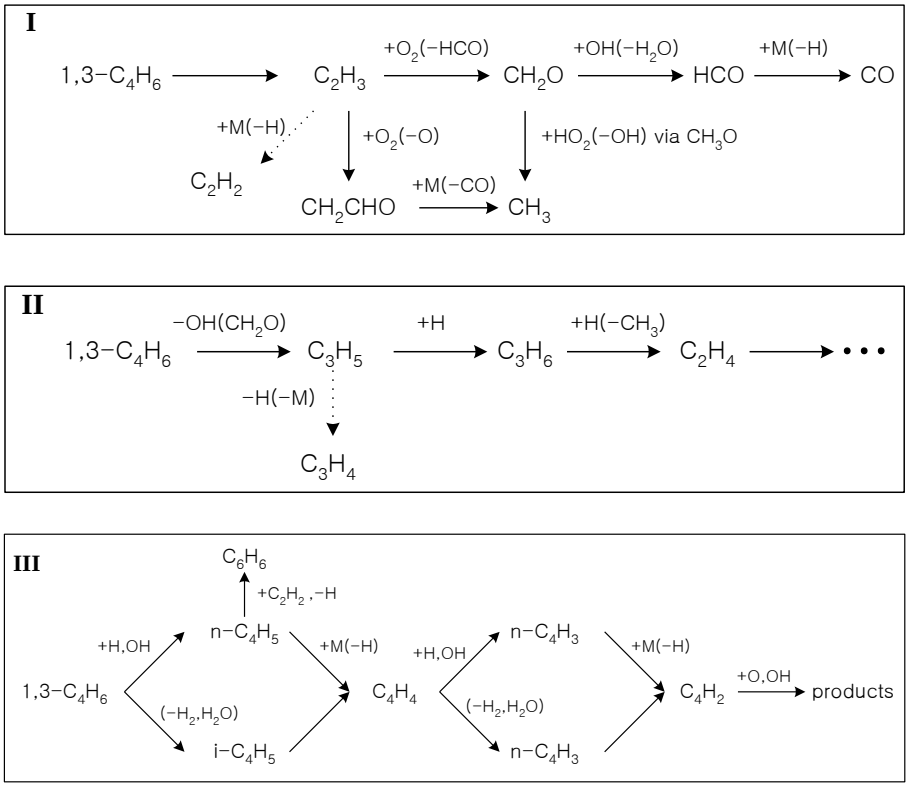

Figure 4.3 Oxidative reaction pathways of 1, 3-butadiene.

C_1 - C_3 Chemistry:

The C_1-C_3 subset of the reaction mechanism is based on Sandiego mechanism [115] and GRI-Mech 3.0 [114]. This model was expanded to describe acetylene and ethylene oxidation in burner stabilized fuel-rich flames and in counter flow diffusion flames, and subsequently in the prediction of acetylene and ethylene flame speeds and ignition delay times. The details of model development and verification against experimental data of C_3 hydrocarbons are found in [114]. In

summary, combined with the C_1-C_2 subset, the C_3 model was shown to predict a wide range of combustion data. The data included product distribution in the pyrolysis and oxidation of propyne and propene in a flow reactor under fuel-lean, stoichiometric, and fuel-rich conditions; the shock-tube ignition delay times of propyne, allene, and propene; and the laminar flame speeds of propyne, propene, and propane.

Ethylene is an important intermediate product in the oxidation of higher-order hydrocarbons such as JP-10, *n*-decane and other aviation fuels. Figure 4.4 describes a typical reaction-path diagram starting ethylene (C_2H_4) to CO_2 at a temperature of 1500 K and pressure of 1atm. Such diagrams, resulting from combining the sensitivity and cluster analysis, are useful in identifying important species and skeletal mechanisms.

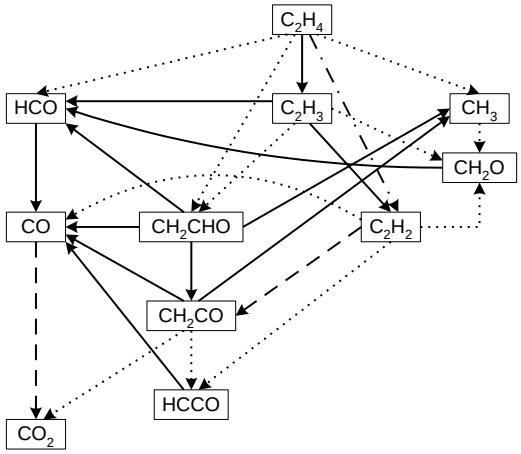

Figure 4.4 Reaction pathway diagram showing the most active carbon species starting from C_2H_4 to CO_2.

In Figure 4.4, the hydroxide radical (OH), oxygen radical (O) and other two side species (H, HO_2) are chosen as side species, and any reaction with the

hydroxide radical is a dashed line, any reaction with the oxygen radical is a dotted line, any reaction with H and HO_2 respectively is a solid line and a dot dash line. The main oxidation path in Fig. 4.4 is the vinyl (C_2H_3) path that mainly produces acetylene (C_2H_2) and vinoxy (CH_2CHO) radical, which are oxidized by OH and O attack respectively, and the vinoxy (CH_2CHO), which decomposes rapidly to produce ketene (CH_2CO). The O attack on C_2H_4 is also important because both of its paths are chain branching, the path through methyl (CH_3) ultimately become less than that through vinoxy radicals, and through HCO ultimately becomes CO_2 [116].

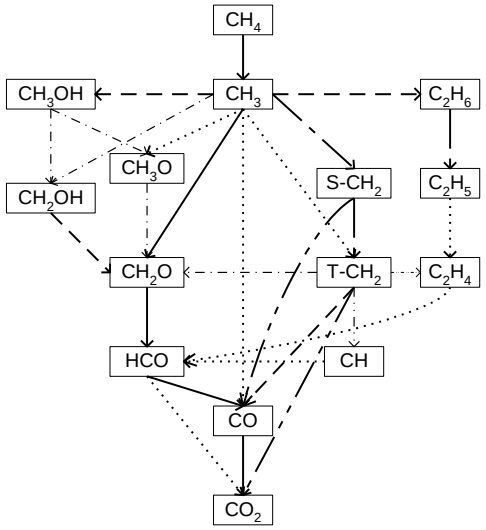

Figure 4.5 Reaction pathway diagram showing the most active carbon species starting from CH_4 to CO_2 [117]

In Figure 4.5, solid, dashed, dotted, and dot dashed lines are used to indicate the magnitude of a reaction pathway. Solid line is a main one. Based on this figure, it is observed that the contribution of the species at the right-side branch (starting from the CH_3 recombination reaction) are not significant compared to the

other major reaction pathways. Therefore, only the following species (and the reactions involving those species) were retained in the reduced chemical kinetics mechanism: N_2, H, O_2, OH, O, H_2, H_2O, HO_2, H_2O_2, CO, CO_2, HCO, CH_2O, CH_4, CH_3, T-CH_2, S-CH_2, CH_3O, CH_2OH, and CH_3OH [117].

It is clear that the conditions of the present study (pressure higher than 1atm and temperature between 1200 and 1700 K) are those of the intermediate temperature range where HO_2 radicals play a significant role [118]. Kinetic analysis shows that these radicals are mainly formed by reaction of alkyl radicals with O_2:

$$R + O_2 = \text{alkene} + HO_2 \qquad (1)$$

However, since we checked out the decenes only at trace levels in jet fuels such as JP-10 oxidation, the major pathways for large alkyl radicals are thermal decomposition and isomerization; consequently, reaction (1) was only written for radicals with six carbon atoms or less. Kinetic analysis shows an important contribution of ethyl, propyl, butyl, and pentyl radical reactions with O_2 at high pressure with the formation of alkenes through reaction (1). However, at high reaction extent, HCO radicals become the main source of HO_2 radicals through reaction (2):

$$HCO + O_2 = CO + HO_2 \qquad (2)$$

When pressure increases, the importance of reaction (2) decreases because of the competitive process (3):

$$HCO + M = H + CO + M \qquad (3)$$

and a growing fraction of HO_2 radicals is formed from H atoms through reaction

(4):

$$H + O_2 + M = HO_2 + M \quad (4)$$

Reactions of HO_2 radicals form H_2O_2, which is mainly produced at low reaction extent, by reaction with JP-10:

$$C_{10}H_{16} + HO_2 \rightarrow H_2O_2 + C_3H_3 + C_2H_4 + C_5H_8$$

$$C_{10}H_{16} + HO_2 \rightarrow H_2O_2 + C_3H_5 + C_2H_2 + C_5H_8 \quad (5)$$

As soon as HO_2 radical's concentration begins to grow, their self-reaction becomes the main source of H_2O_2:

$$HO_2 + HO_2 = H_2O_2 \quad (6)$$

with a small contribution of H-donor intermediates:

$$XH + HO_2 = X + H_2O_2 \quad (7)$$

In the temperature range of the present study, H_2O_2 decomposes to form two OH radicals:

$$H_2O_2 + M = OH + OH + M \quad (8)$$

Under the present conditions, the OH radical was found to be the most important chain carrier for the consumption of JP-10 and of intermediates, including CH_2O and CO. Even at the highest temperature (1300 K) of the present study, reaction (4) dominates over the high temperature chain-branching process:

$$H + O_2 = OH + O \quad (9)$$

Finally, the chain-branching process under the present conditions is controlled by the reaction sequence (7) + (8), which forms two OH radicals from a single HO_2 radical through H_2O_2 decomposition. This statement is based on the literature [118] and confirmed by sensitivity analysis and hierarchical cluster

analysis, which shows that, in the major portion of the temperature range of this study, the computation is very sensitive to the rate constant of reaction (8). However, above 1300 K, although reaction (4) is largely dominant over reaction (9) in the range 10-40atm, with large amounts of HO_2 and H_2O_2 being formed as shown above, the most sensitive reaction is reaction (9) [118].

4.3 Governing equations

The general governing equations are the one-dimensional balance equations for continuity, the chemical species and energy. In unstretched premixed flames, here we consider a planar steady state flame configuration normal to the *x*-direction with the unburnt mixture at $x \rightarrow +\infty$, and the burnt gas at $x \rightarrow -\infty$. The equations governing conservation of overall mass, species mass and energy are [117]:

Continuity

$$\frac{\partial \rho}{\partial t} + \frac{d(\rho u)}{dx} = 0$$

Species

$$\frac{d(\rho Y_i)}{dt} + \rho u \frac{dY_i}{dx} = -\frac{dj_i}{dx} + \dot{m}_i$$

Energy

$$\rho c_p \left(\frac{dT}{dt} + u\frac{dT}{dx}\right) = \frac{d}{dx}\left(\lambda \frac{dT}{dx}\right) - \sum_{i=1}^{n} h_i \dot{m}_i - \sum_{i=1}^{n} c_p j_i \frac{dT}{dx}$$

In the above equations u is the velocity components in x directions. Furthermore, ρ is the density, Y_i the mass fraction of species i, j_i the diffusion flux,

mi the chemical production rate of species *i* per unit mass, *T* the temperature, c_p the heat capacity at constant pressure, λ the thermal conductivity and h_i the specific enthalpy of species *i*. The diffusion flux j_i may be related to the diffusion velocity V_i by

$$j_i = \rho_i V_i = \rho Y_i V_i$$

where $\rho_i = \rho Y_i$ is the partial density. The chemical production rate $\dot{m}_i$ contains contributions from all reactions, ie.,

$$\dot{m}_i = M_i \sum_{k=1}^{r} v_{ik} w_k$$

where M_i is the molecular weight of species *i* and the reaction rates are given by

$$w_k = k_{fk}(T) \prod_{j=1}^{n} \left(\frac{\rho Y_j}{M_j}\right)^{v'_{kj}} - k_{bk}(T) \prod_{j=1}^{n} \left(\frac{\rho Y_j}{M_j}\right)^{v''_{kj}}$$

The stoichiometric coefficients of the forward and backward step for species *j* in reaction *k* are denoted by v'_{kj} andv''_{kj}. The rate coefficients $k_{fk}(T)$ and $k_{bk}(T)$ are expressed in the form

$$k_k = A_k T^{n_k} exp\left(-\frac{E_k}{RT}\right)$$

where A_k is the frequency factor, n_k is the pre-exponential temperature exponent, and E_k is the activation energy of reaction *k.*

4.4 The Kinetic Mechanism for JP-10

The kinetic mechanism used here as a common basis for all flame calculations is listed in Appendix H and I. These data are compilations from the

recent literature. The units of A_k are

$$\left[\frac{1}{\sec K^{n_k}}\right], \qquad \left[\frac{cm^3}{\text{mole sec } K^{n_k}}\right], \qquad or \qquad \left[\frac{cm^6}{mole^2 sec K^{n_k}}\right]$$

for a uni-molecular, bi-molecular or tri-molecular reaction, respectively. The activation energy is given in [cal/mole], and the universal gas constant is R = 1.986 *cal*/g mole K. Lindemann reactions and Troe methods to represent pressure fall-off reactions were used in this study.

Lindemann Reactions :

The classical Lindemann low pressure reaction can be represented as follows:

Reactants + M [LIN:A_0;m_0;E_{a0}] ==> Products

or

Reactants + M [LIN:A_0;m_0;E_{a0};(Enhanced bodies if present)] ==> Products

The A_0, m_0, E_{a0} are values used in the Arrhenius rate expression at the low pressure limit:

$$k_0 = A_0 T^{m_0} exp\left(-{}^{E_0}/_{RT}\right)$$

The A, m, and Ea values present before the reaction (not shown) are used in the Arrhenius rate expression at the high pressure limit. An overall rate constant, k_f, is then computed:

$$k_f = k_\infty \left(\frac{\frac{k_0[M]}{k_\infty}}{1+\frac{k_0[M]}{k_\infty}}\right) F$$

The F parameter shown above is always one for Lindemann reactions. Note that k_f and F are equal for forward and backward reactions; $[M] = \sum_{i=1}^{n} \frac{\rho Y_i}{M_i} = p/RT$ is

the molar density of the mixture.

Troe Reactions:

The TROE fall-off reaction can be represented as follows:

Reactants + M [TROE:A_0;m_0;Ea_0;P_1;P_2;P_3; (P_4)] ==> Products

or

Reactants + M[TROE:A_0;m_0;Ea_0;P_1;P_2;P_3;(P_4;)(Enhanced third bodies if present)] ==> Products

The A_0, m_0, E_{a0} are values used in the Arrhenius rate expression at the low-pressure limit. The A, m, and E_a values present before the reaction (not shown) are used in the Arrhenius rate expression at the high-pressure limit. The Troe parameters P_1, P_2 and P_3 (P_4 is optional) allow it to compute the Troe Factor, F:

$$k_f = k_\infty \left(\frac{\frac{k_0[M]}{k_\infty}}{1 + \frac{k_0[M]}{k_\infty}} \right) F$$

$$\log F = \left[1 + \left[\frac{\log\left(\frac{k_0[M]}{k_\infty}\right) + c}{n - 0.14\left(\log\frac{k_0[M]}{k_\infty} + c\right)} \right]^2 \right]^{-1} \log F_c$$

$$c = -0.4 - 0.67 \log F_c$$

$$n = 0.75 - 1.27 \log F_c$$

$$F_c = (1 - P_1) - \exp\left({}^{-T}/_{-P_2}\right) + P_1 exp\left({}^{-T}/_{P_3}\right) + exp\left({}^{-P_4}/_{T}\right)$$

where P_1, P_2, P_3, P_4 are constants. Pressure dependent reactions are described by the Troe-formulation [133]. Once *F* is computed, it is inserted into equation 4. In

some references P1=a, P2=T***, P3=T* and P4=T**. The troe centering parameters are given by:

Fc11 = 0.5

Fc17 = 0.265 exp(-T/94 K) + 0.735 exp(-T/1756 K) + exp(-5182 K/T)

Fc33 = 0.2176 exp(-T/271 K) + 0.7824 exp(-T/2755 K) + exp(-6570 K/T)

Fc54 = 0.217 exp (-T/74 K) + 0.783 exp(-T/2941 K) + exp(-6964 K/T)

Fc55 = 0.38 exp(-T/73 K) + 0.62 exp(-T/1180 K).

Fc83 = 0.16 exp(-T/125 K) + 0.84 exp(-T/2219 K) + exp(-6882 K/T)

Fc89 = 0.832 exp(-T/1203 K)

Fc101 = 0.7

Fc138 = 0.586 exp(-T/279 K) + 0.414 exp(-T/5459 K)

Fc150 = 1.0

Fc162 = 0.5

Fc163 = 0.5

Fc199 = 0.5

Fc202 = 0.2

Fc206 = 0.5

Fc215 = 0.98 exp(-T/1097 K) + 0.02 exp(-T/1097 K) + exp(-6860 K/T)

Fc218 = 0.825 exp(-T/1341 K) + 0.175 exp(-T/60000 K) + exp(-10140 K/T)

Fc221 = 0.24 exp(-T/1946 K) + 0.76 exp(-T/38 K)

Fc233 = exp(-T/645.4 K) + exp(-6844 K/T)

Fc235 = 2.17 exp(-T/251 K) + exp(-1185 K/T)

Fc236 = exp(-T/1310 K) + exp(-48100 K/T)

where *T* is in degrees Kelvin. Equations for transport properties are given, for instance, in [116]. Their choice, however, is left to the digression of the groups contributing the individual chapters. It should be noted that only transport properties for nonsteady state species are needed in calculations based on reduced mechanisms. Therefore the sometimes unknown properties of the steady-state species are of minor importance only, even in the calculations based on detailed mechanisms. Thermochemical properties are based on Burcat data[120] and NASA polynomials[121], for instance, but their choice too is left to the digression of the individual groups.

4.5 Kinetic modeling

For simulating the oxidation of JP-10 in premixed flames, we used the Premix computer code, the KINTECUS computer software version 4.0 [122], which was developed by James C. Ianni (Kintecus © Copyright 1995-2011 James C Ianni). This application involves a constant-volume batch reactor or a tubular flow reactor with constant volumetric flow rate. With this approach one writes the governing differential equation for the concentration, *C*, for each of the chemical species, *i*, in the mechanism.

$$\frac{dC_i}{dt} = \sum_j v_{ij} r_j$$

The entire set of ordinary differential equations is then solved simultaneously, where *t* is the batch holding time of flow reactor residence time, v_{ij} the stoichiometric coefficient for component *i* in the j^{th} reaction, and r_j is the rate

expression for the j^{th} reaction. This approach requires a numerical value for the rate constant for each elementary step in the mechanism, which is usually expressed as the Arrhenius parameter.

$$k_i = A_i T^m exp\left(\frac{-E_a}{RT}\right)$$

The parameter data for each elementary reaction in the mechanism-based kinetic model are located in the Appendix H and I. Regardless of the source of the kinetic data, it is important to ensure that the data are thermodynamically consistent, i.e., thermodynamics requires that the ratio of the forward (k_{for}) and reverse (k_{rev}) rate constants for an elementary reaction equals the equilibrium constant (K_i) for the reaction.

$$\frac{k_{for}}{k_{rev}} = K_i$$

In other words, it computes species concentrations from the balance between the net rate of production of each species by chemical reactions and the difference between the input and output flow rates of species. These rates are computed from the kinetic reaction mechanism and the rate constants of the elementary reactions calculated at the experimental temperature, using the modified Arrhenius equation, and thermodynamic data as well.

The reaction mechanism used in this study has a strong hierarchical structure. It is based on the San Diego mechanism developed earlier [115] where the reaction mechanisms of Benzene (C_6H_6, BEN) and 1, 3-CycloPentaDiene (C_5H_6, CPD) including in C_6H_5, C_5H_8, C_5H_5, C_4H_2, N-C_4H_3, I-C_4H_3, C_4H_4, N-C_4H_5 and I-C_4H_5 have been updated, which are listed in Appendix H. The reaction

mechanism used here consisted of 59 species and 311 reactions. A constant-volume plug flow code was applied to this simulation. The conditions of interest are pressures from 1 - 40atm, inlet temperatures from 900K to 1,700K. Since most of C_1-C_3 reaction mechanisms have been presented in detail in previous paper [119], only the important reactions related to the formation and dissociation of BEN and CPD were described in Section 5.2. Thermodynamic data file using in this study are mainly obtained from Burcat, NASA, and GRI-Mech 3.0 [120,121,114]. The input data used for the reactant feed in the simulation are shown in Table 4.1.

Table 4.1 Initial conditions for kinetic simulation

T5 (K)	P5 (atm)	n/V (kmol/cm^3)	JP10 (%)	JP10 (mol/cm^3)	O2 (%)	O2 (mol/cm^3)	Ar (%)	Ar (mol/cm^3)
1469	1.25	1.0371E-05	0.2	2.0742E-08	2.82	2.9246E-07	96.98	1.0058E-05
1492	1.16	9.4758E-06	0.2	1.8952E-08	2.79	2.6438E-07	97.01	9.1925E-06
1527	1.15	9.1788E-06	0.2	1.8358E-08	2.81	2.5792E-07	96.99	8.9025E-06
1584	1.19	9.1563E-06	0.2	1.8313E-08	2.81	2.5729E-07	96.99	8.8807E-06
1629	1.2	8.9782E-06	0.2	1.7956E-08	2.87	2.5767E-07	96.93	8.7025E-06
1671	1.05	7.6584E-06	0.2	1.5317E-08	2.99	2.2899E-07	96.81	7.4141E-06
1447	3.18	2.6785E-05	0.198	5.3034E-08	2.76	7.3926E-07	97.04	2.5992E-05
1451	3.08	2.5871E-05	0.2	5.1742E-08	2.81	7.2697E-07	96.99	2.5092E-05
1457	3.18	2.6601E-05	0.2	5.3202E-08	2.76	7.3418E-07	97.04	2.5813E-05
1460	3.02	2.5211E-05	0.2	5.0421E-08	2.83	7.1346E-07	96.97	2.4447E-05
1469	3.02	2.5056E-05	0.2	5.0112E-08	2.83	7.0909E-07	96.97	2.4297E-05
1473	3.16	2.6146E-05	0.2	5.2293E-08	2.76	7.2164E-07	97.04	2.5372E-05
1493	3.11	2.5388E-05	0.2	5.0776E-08	2.81	7.1340E-07	96.99	2.4624E-05
1502	3.11	2.5236E-05	0.198	4.9967E-08	2.76	6.9651E-07	97.04	2.4489E-05
1507	3.03	2.4505E-05	0.2	4.9010E-08	2.82	6.9105E-07	96.98	2.3765E-05
1512	3.32	2.6762E-05	0.2	5.3523E-08	2.82	7.5468E-07	96.98	2.5954E-05
1527	3.23	2.5781E-05	0.2	5.1561E-08	2.76	7.1154E-07	97.04	2.5017E-05
1535	3.23	2.5646E-05	0.2	5.1292E-08	2.81	7.2066E-07	96.99	2.4874E-05
1378	6.17	5.4571E-05	0.2	1.0914E-07	2.89	1.5771E-06	96.91	5.2885E-05
1406	6.03	5.2271E-05	0.2	1.0454E-07	2.81	1.4688E-06	96.99	5.0698E-05

1407	6.26	5.4226E-05	0.2	1.0845E-07	2.79	1.5129E-06	97.01	5.2605E-05
1414	6.34	5.4647E-05	0.2	1.0929E-07	2.78	1.5192E-06	97.02	5.3019E-05
1428	6.13	5.2319E-05	0.2	1.0464E-07	2.63	1.3760E-06	97.17	5.0838E-05
1453	5.99	5.0245E-05	0.2	1.0049E-07	2.86	1.4370E-06	96.94	4.8707E-05
1456	6.05	5.0643E-05	0.2	1.0129E-07	2.86	1.4484E-06	96.94	4.9094E-05
1490	6.4	5.2351E-05	0.2	1.0470E-07	2.76	1.4449E-06	97.04	5.0801E-05
1500	1	8.1253E-06	0.2	1.6251E-08	2.81	2.2832E-07	96.99	7.8807E-06
1500	5	4.0626E-05	0.2	8.1253E-08	2.81	1.1416E-06	96.99	3.9403E-05
1500	40	3.2501E-04	0.2	6.5002E-07	2.81	9.1328E-06	96.99	3.1523E-04

4.6 Fundamentals of spontaneous ignition

Spontaneous ignition, or autoignition, is a process whereby a combustible mixture undergoes a chemical reaction that leads to the rapid evolution of heat in the absence of any concentrated source of ignition, such as a flame or spark. In the lean-premix combustor, and other types of low-emissions combustors where fuel and air are premixed before combustion, spontaneous ignition must be avoided at all costs because it could damage combustor components and produce unacceptably high levels of pollutant emissions.

Spontaneous ignition delay time may be defined as the time interval between the creation of a combustible mixture, say by injecting fuel into a flowing airstream at high temperature, and the onset of flame. Ignition delay times are often correlated using the wolfer equation [123].

$$t_i = 0.43P^{-1.19}\exp\left(\frac{4650}{T_m}\right) \tag{4.1}$$

where t_i is the ignition delay time in *msec*, P is the pressure in bars, and T_m is the initial mixture temperature in degrees K. To accommodate the effects of the

equivalence ratio on ignition delay time, Equation 4.1 may be modified and expressed in a more general form as

$$t_i = A[Fuel]^n[O_2]^{-m} exp\left(\frac{E}{RT_m}\right) \quad (4.2)$$

or

$$t_i = AP^{-n}\phi^{-m} exp\left(\frac{E}{RT_m}\right) \quad (4.3)$$

where *A*, *n*, and *m* are constants that are determined experimentally, *P* is the pressure (usually expressed in atmosphere or bars), *E* is the activation energy in cal/g mol, *R* is the gas constant(1.986 cal/g mol), T_m is the initial temperature of the fuel-air mixture in degrees K.

Table 4.2 Experimental values of constants in Equation 4.2 for aerospace fuels.

Fuel	*E* (kcal/g mol)	A	*n*	*m*	Comments
JP-10	54.0	3.47×10^{-15}	0.67	1.27	Davidson et al.(Eqn 4.2)
JP-10	46.834	7.63×10^{-16}	0.40	1.20	Colket & Spadaccini(Eqn 4.2)
Jet A	29.6	-	1.0	0.37	Lefebvre, A. H. et al.(Eqn 4.3)

In view of their practical importance, measurements of spontaneous ignition delay time have been conducted for many fuels over wide ranges of ambient conditions and in a variety of test vehicles, including rapid-compression machines, shock tubes, and continuous flow devices. The test methods employed and the results obtained are described in reviews by Mullins [124], Spadaccini and Te Velde [125], Goodger and Eissa [126], and Lundberg [127].

Freeman, Cowell, and Lefebvre [128, 129] used a continuous flow apparatus to measure autoignition delay time. Twenty-five equispaced fuel-injection points ensured rapid mixing of gaseous fuel or fuel vapor with heated air at entry to the test section. The concept is shown schematically in Figure 4.6, where the ignition delay time is defined as length (L) divided by the gas velocity U. This method has the advantage that when spontaneous ignition occurs, it does so under conditions that closely simulate those prevailing in the premixing passages of advanced combustors. Some of the results obtained for JP-10/O_2/Ar mixtures are shown in Figure 4.7 through 4.9

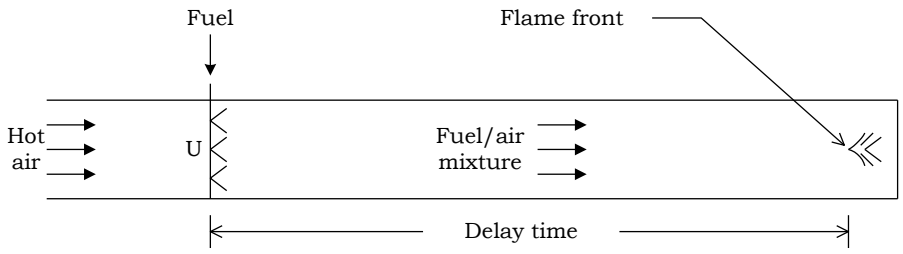

Figure 4.6 Basis of ignition delay time measurement technique.

The form of Equation 4.2 and 4.3 suggests that a plot of $log\ t_i$ vs. $1/T_m$ should yield a straight line with a positive slope, and this is checked out by the results presented in Figure 4.8. The values of E given by the slope of the lines in these figures are 29.6 kcal/g mol for kerosine (Jet A).

The Influence of pressure on t_i is of great practical interest in view of the continuing trend toward engines of higher pressure ratio. Its importance is apparent from inspection of the experiment data plotted in Figure 4.5 and 4.6,

which show a pronounced effect of pressure on t_i. Analysis of these and other data [130] led to values for n in equation 4.2 of 1.0 for Jet A (see Table 4.2)

There appears to be little agreement between different workers in regard to the influence of equivalence ratio on ignition delay time. Mullins [124] observed no effect, whereas Ducourneau [131] and Spadaccini and Te Velde [125] both found strong effects. Lefebvre at al [130] examined the influence of ϕ on t_i for several fuels and found in all cases that delay times were reduced by an increase in equivalence ratio. For aviation kerosine(Jet A), the measured value for m was 0.37.

The explanation for the marketed lack of consistency between different workers in regard to the influence of ϕ on t_i probably lies in the mode of fuel injection. With liquid fuels, there is always the potential for stoichiometric combustion in regions close to the evaporating spray. Thus, measured ignition delay time may be close to those for stoichiometric mixtures, even though the average equivalence ratio of the mixture differs appreciably from the stoichiometric value.

Just now close will depend on the top-size distribution in the spray, because this governs the initial rate of fuel evaporation and also the length of time that stoichiometric “streaks” of fuel-air mixture can survive. The number of fuel injection points is also important. In this context, it is of interest to note that Tacina [132] obtained much more consistent autoignition data with a single orifice injector than with a 41- hole injector, which ostensibly should have provided a more uniform fuel-air mixture.

Presumably, this was because with a single injector the rate of fuel-air mixing was so slow that the bulk of the prereactions leading up to the onset of ignition took place in near-stoichiometric mixtures, regardless of the average equivalence ratio. With gaseous fuels, the inconsistencies associated with slow fuel evaporation are no longer present, but the measured ignition delay time are still very dependent on the time required for the fuel and air to form a combustible mixture. As with liquid fuels, the longer the mixing time, the closer the measured ignition delay times will approach stoichiometric values.

Another probable reason for the conflicting evidence of the effect of the equivalence ratio on ignition delay time is that in continuous flow experiments, that fuel is almost invariably at a much lower temperature than the hot airstream into which it is injected. This has the advantage of closely stimulating the actual engine situation but, from a fundamental viewpoint, it has drawback that any change in ϕ must also change the temperature in the initial fuel-air mixing zones could be very pronounced and could largely offset the effect of this change in temperature on t_i, will always be such as to oppose the change in t_i caused by the change in ϕ. The net result is that measurements of t_i, carried out in continuous flow device will always under predict the effect of a change in ϕ on t_i by an amount that depends on the difference in temperature between the hot airstream and the injected fuel gas or vapor.

In summary, autoignition data are very apparatus-dependent and, in particular, very fuel injector-dependent. Considerable caution should be exercised in comparing and selecting autoignition data and in no circumstances should

experimentally derived equation for t_i, be extrapolated to pressures and temperatures outside the range of their experimental verification. Such extrapolations could lead to erroneous results because differences in reaction routes may occur over different levels of temperature and pressure. When liquid fuels are injected into air at high pressures and temperatures, very fine atomization is needed to promote rapid vaporization, thereby reducing the risk of spontaneous ignition in the fuel preparation region.

4.7 Results and Comparison

4.7.1 JP-10 comprehensive skeletal mechanism for 58species

It is performed with one-dimensional simulations of laminar flames using a reduced chemical kinetics mechanism for JP-10/O_2/Ar mixture combustion, consisting of 58 species and 315 reactions, which are listed in Table 4.3 and appendix H respectively.

Table 4.3 Summary of reduced mechanisms for 58species

No. of species	Temperature range	Pressure range	species
58	900-1,700K	1-40atm	H, HE, O_2, OH, O, AR, HO_2, H_2, H_2O, H_2O_2, CO, CO_2, HCO, CH_3, CH_4, CH_2O, TCH_2, SCH_2, C_2H_4, CH_3O, C_2H_5, C_2H_6, CH, C_2H_2, C_2H_3, CH_2CHO, C_2H_4O, HCCO, CH_2CO, C_2H, CH_2OH, CH_3OH, CH_3CHO, CH_3CO, C_2H_5OH, CH_2CH_2OH, CH_3CHOH, CH_3CH_2O, C_3H_4, C_3H_3, C_3H_5, C_3H_6, C_3H_8, IC_3H_7, NC_3H_7, C_4H_2, NC_4H_3, IC_4H_3, C_4H_4, NC_4H_5, IC_4H_5, C_4H_6, CYC_5H_5, CYC_5H_6, C_6H_5, C_6H_6, C_5H_8, $C_{10}H_{16}$

The objective of this work is to examine the impact of the operating conditions and the Benzene formation process by using the theory for polycyclic aromatic hydrocarbons (PAH) and soot formation reaction process on the constant volume combustor, premixed flame characteristics.

For the validation of these reaction mechanisms, calculated OH mole fraction profile was compared to the experimental shock tube data of Davidson et al. [94] in Figure 4.7. The line represent measurement and the dot are calculated data using a reduced kinetic model of JP-10 in this study. The OH mole fraction profile rises rapidly at ignition and then decays slowly but does not return to zero during the measured test time. The pattern of calculated OH mole fraction profile was the same as that of experimental data. The calculated peak OH mole fraction is 1,449.43ppm, which is 19.28% higher than that of measured data, and the ignition time is 390.8μsec, which is 8.5% faster than that of experiment. There are ±15% experimental errors in Davidson et al.'s [94] measurement data due to variations in the temperature and pressure rise during the ignition process. Therefore, taking it into account, this calculated result is acceptable [94].

Figure 4.8 show the ignition delay time of various pressures of 1atm, 3atm and 6atm as function of temperatures. It is compared to the shock tube data by GC analyses of Davidson et al. [94]. Since OH mole fraction have trend to overestimate in case of 1atm, above 1,500K especially, the peak CH mole fraction were checked instead of that of OH mole fraction in the case of 1atm, 3atm and 6atm for all temperature ranges as it is. Actually, the data of shock tube ignition delay time are based on the peak CH mole fraction checked out in the experiment.

Most of the ignition time from this calculation was being located between the lines of the data from Davidson et al.'s experiment [94]. In particular, the modeling results give reasonable agreement with the data obtained from Davidson et al. [94] for a range of pressure from 1, 3, and 6atm. Applied initial conditions and % difference between calculated and experimental data are given in Table 4.1, and 4.6.

Figure 4.9 shows the autoignition time of a reduced JP-10 kinetic mechanism over a range of temperatures from 900K to 1,700K, and pressures from 1atm to 40atm. Initial conditions applied are temperature 1,500K, which are summarized in table 4.1. Ignition time at 5atm and 40atm is average 75.86% and 95.75% faster than that of 1atm respectively.

Flame temperature is perhaps the most important property in combustion because it has a controlling effect on the rate of chemical reaction. The term "flame temperature" may imply a measured value or a calculated one. If the latter, it is usually the adiabatic flame temperature. This is the temperature that the flame would attain if the net energy liberated by the chemical reaction that converts the fresh mixture into combustion products were fully utilized in heating those products. In practice, heat is lost from the flame by radiation and convection, so the adiabatic flame temperature is rarely achieved.

Nevertheless, it plays an important role in the determination of combustion efficiency and in heat-transfer calculations. In high-temperature flames, say above 1,800K, dissociation of combustion products occurs to a significant extent and absorbs much heat. At low temperatures, combustion of a stoichiometric or lean

fuel-air mixture would be expected to give only CO_2 and H_2O; however, at higher temperature, these products are unstable and partly revert to simpler molecular and atomic species and radicals, principally CO, H_2, O, H, and OH. The energy absorbed in dissociation is considerable, and its effect is to substantially reduce the maximum flame temperature.

Factors influencing the adiabatic flame temperature are fuel/air ratio, initial temperature and pressure, and vitiation of the inlet air by products of combustion.

The variation of adiabatic flame temperature rise with change in initial temperature and pressure is illustrated in Figure 4.10. The departure from linearity as the flame temperature rise is due partly to the increase in specific heat of the combustion products with an increase in temperature and, at the high temperatures above 1,800K, to the effects of dissociation. An increase in initial air temperature will always increase the flame temperature. However, the extent of their increase diminishes with an increase in flame temperature. For a constant inlet temperature, an increase in pressure yields a higher flame temperature, which are at 5atm and 40atm is an average 1.53% and 2.66% higher than that of 1atm and 1,700K respectively in Figure 4.10.

For a constant inlet mixture temperature, ignition time delay decreased for a range of pressure from 1 atm to 40 atm in Figure 4.10. This expected agreement is good under nearly all conditions. Furthermore, it is not expected to be a significant drawback in using a constant-volume combustor model with updated kinetic reaction mechanism of JP-10.

Temperature plays a key role in the reacting system kinetics as shown in

Figure 4.11 - 4.14. The left side shows mole fraction profiles for the inlet temperature of 1,100K and the right side for 1,500K. Diagrams for compound concentrations as a function of time are presented. The minimal concentration of the reaction product in the kinetic diagram is 1×10^{-10} mol/cm^3. Overall, the main compounds produced during the JP-10 pyrolysis are Benzene(C_6H_6), cyclopentene(C_5H_8), cyclopentadiene(C_5H_6,CPD), 1,3-butadiene(C_4H_6), propylene(C_3H_6), allene(C_3H_4), ethane(C_2H_6), ethylene(C_2H_4), acethylene(C_2H_2) and methane(CH_4). The influence of the reaction parameters, such as temperature and initial reactant concentrations, on the final product concentration, is discussed as follows. Initial conditions are given in table 4.4.

Table 4.4 Initial conditions of JP-10 pyrolysis for temperature influence

T (K)	P (atm)	n/V (kmol/cm^3)	JP10 (%)	JP10 (mol/cm^3)	O_2 (%)	O_2 (mol/cm^3)	Ar (%)	Ar (mol/cm^3)
1,100	5	4.0626E-05	0.2	8.1253E-08	2.81	1.1416E-06	96.99	3.9403E-05
1,500	5	4.0626E-05	0.2	8.1253E-08	2.81	1.1416E-06	96.99	3.9403E-05

Figure 4.11 shows the mole profiles for the JP-10/ O_2/Ar mixture, the products CO_2 and H_2O, and the intermediate species H_2 and CO. Modeling data show that the peak mole fractions of CO are nearly the same in both 1,100K and 1,500K flames, where ignition occurs. The more the temperature increase, the faster ignition delay time is, 0.005633sec at 1,100K, 0.000166sec at 1,500K.

Following on from the JP-10 cracking mechanism, as proposed in this work (see Appendix H); the hydrogen is included in the initiation reaction. JP-10 begins to decompose above 900 K and is completely decomposed by 1300 K [90]. Here,

the hydrogen molecules become radicals under high temperature conditions and then crack JP-10 molecules by the β-scission reaction, leading to formation of the α-olefins, such as ethylene (C_2H_4), propylene (C_3H_6), etc.(Nikravech, 1990). This reaction sequence is evidenced as follows; when the temperature of the feed mixture is increased from 1,100K to 1,500K, hydrogenation reactions of the olefins and acetylene (C_2H_2) compounds are favoured and hence, saturated molecules are produced. This is shown in Figure 4.12 - 4.14, where the acetylene concentration slightly increases and the CH_4 concentration is favoured, in comparison to the situation shown in both 1,100K and 1,500K flames, where the ethane (C_2H_6), 1,3-butadiene(C_4H_6) and allene (C_3H_4), CPD (C_5H_6) molecule also increases.

Since almost all of the intermediate products such as ethylene, allene, butadiene, CPD, and BEN have occurred before the ignition of JP-10, it is essential to figure out the ignition delay time in order to check out their mole fractions. Also, it is said that the ignition delay time is governed by the reaction process of the intermediate products including in CPD, BEN. Especially, when the ground to air missile is vertically launched by using of the cold launching system from the military vehicle, the ignition delay time is a more important thing than anything else. It is because if the ignition delay time cannot be exactly calculated in the cold launching system, the missile will fall down back into the launch site directly. So, for the next step, the mole fractions are calculated with the variation of the inlet temperature and pressure covering from 1atm to 40atm, and with the micro scale time.

Figure 4.15 - 4.20 show mole fraction profiles for JP-10 as a function of time at inlet temperature is 1500K, inlet pressure is 40atm. Figure 4.21 – 4.26 show that mole fraction profiles of JP-10 for 58species as a function of inlet temperature at inlet pressure from 1, 3, 6, 9atm at 100 µsec to 20, 40atm at 20 µsec. Mole fraction profiles for JP-10 with 49species with an inlet temperature of 1,500 K over pressures from 1atm to 40atm, and a range of residence times for 50 µsec, 100µsec in Figure 4.27 and 4.28 respectively.

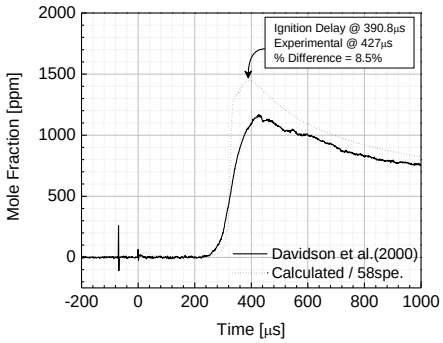

Figure 4.7 Comparison of ignition delay time with OH mole fraction between experimental and calculated data. Initial conditions are 0.2% Jp-10, 2.83% O2, balance Ar, Equivalence ratio= 0.99, T=1,460K and P=3.02atm.

Table 4.5 Ignition time data based on OH mole fraction

T (K)	P (atm)	JP-10 (%)	O_2 (%)	ϕ	t(µs) Davidson et al.	t(µs) Calculated	% Difference
1447	3.18	0.2	2.76	1	462	440.0	4.8%
1460	3.02	0.2	2.83	0.99	427	390.8	8.5%
1502	3.11	0.2	2.76	1	276	272.5	1.3%
						Max.	8.5%
						Min.	1.3%
						Avg.	4.8%
						Median	4.8%

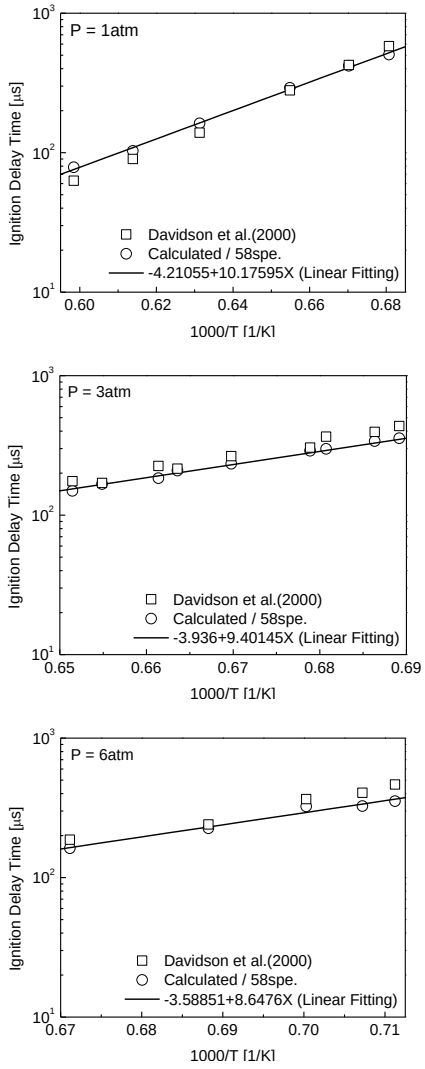

Figure 4.8 Comparison of ignition delay time based on CH mole fraction with the variation of pressure and temperature between experiment and modeling data. Initial conditions are lasted in table 4.3.

Table 4.6 Ignition time data based on CH mole fraction

T (K)	P (atm)	JP-10 (%)	O_2 (%)	ϕ	t(μs) Davidson et al.	t(μs) Calculated	% Difference
1469	1.25	0.2	2.82	0.99	580	504.8	13.0%
1492	1.16	0.2	2.79	1.00	425	419.7	1.3%
1527	1.15	0.2	2.81	1.00	280	291.5	-4.1%
1584	1.19	0.2	2.81	1.00	139	162.5	-16.9%
1588	1.23	0.2	2.74	1.02	140	161.5	-15.3%
1629	1.2	0.2	2.87	0.97	90	102.8	-14.3%
1671	1.05	0.2	2.99	0.94	63	78.6	-24.7%
1406	3.3	0.2	2.82	0.99	755	522.8	30.7%
1451	3.08	0.2	2.81	1.00	435	355.8	18.2%
1457	3.18	0.2	2.76	1.01	395	339.8	14.0%
1469	3.02	0.2	2.83	0.99	365	298.5	18.2%
1473	3.16	0.2	2.76	1.01	305	289.5	5.1%
1493	3.11	0.2	2.81	1.00	265	233.4	11.9%
1507	3.03	0.2	2.82	0.99	212	204.9	3.3%
1507	3.11	0.2	2.76	1.01	215	208.6	3.0%
1512	3.32	0.2	2.82	0.99	225	184.1	18.2%
1527	3.23	0.2	2.76	1.01	170	167.2	1.7%
1535	3.23	0.2	2.81	1.00	175	149.4	14.6%
1580	3.17	0.2	1.76	1.01	90	100.7	-11.9%
1378	6.17	0.2	2.89	0.97	675	421.2	37.6%
1406	6.03	0.2	2.81	1.00	465	352.7	24.2%
1407	6.26	0.2	2.79	1.00	455	345.2	24.1%
1414	6.34	0.2	2.78	1.01	405	325.7	19.6%
1428	6.13	0.2	2.63	1.06	365	324.1	11.2%
1453	5.99	0.2	2.86	0.98	240	225.7	6.0%
1456	6.05	0.2	2.86	0.98	271	218.2	19.5%
1490	6.4	0.2	2.76	1.01	187	162.3	13.2%
						Max.	37.6%
						Min.	-24.7%
						Avg.	8.2%
						Median	11.9%

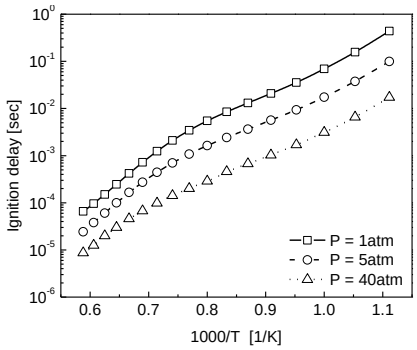

Figure 4.9 Autoignition of a reduced JP-10 mechanism over a range of initial temperatures and pressures that are listed at table 4.1 in case of T=1,500K (0.2% JP-10, 2.81%, O2, Balance Ar, Equivalence ratio = 1.0)

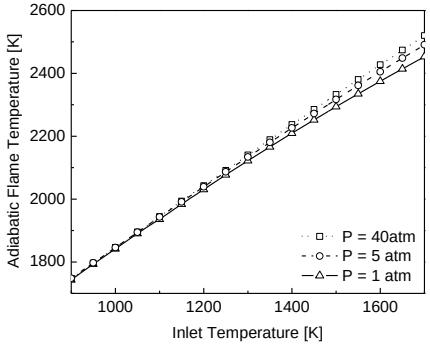

Figure 4.10 Adiabatic flame temperatures as function of inlet temperature and pressure. (0.2% JP-10, 2.81%, O2, Balance Ar, Equivalence ratio = 1.0)

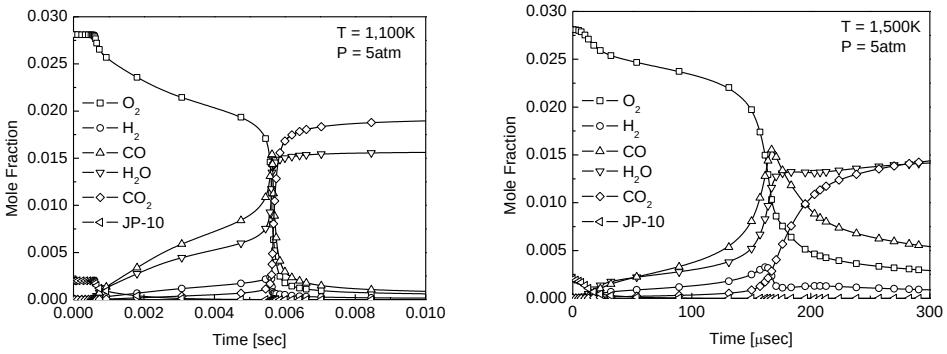

Figure 4.11 Mole fraction profiles for O_2, H_2, H_2O, CO, CO_2 and JP-10 (0.2% JP-10, 2.81%, O2, Balance Ar, Equivalence ratio = 1.0)

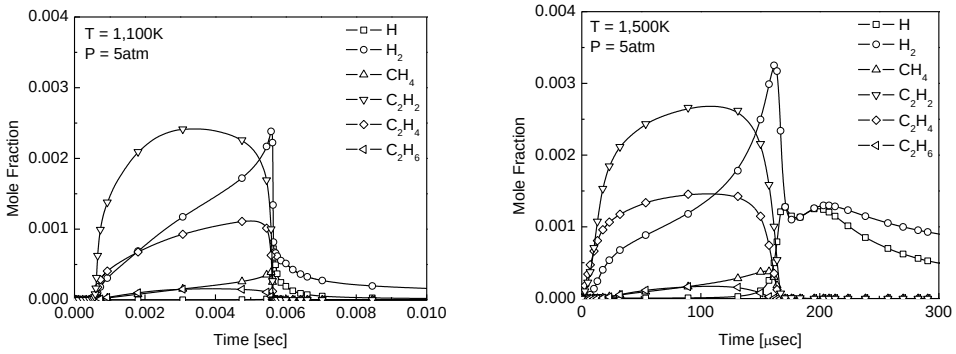

Figure 4.12 Mole fraction profiles for CH_4, C_2-hydricarbons, and hydrogen radical (0.2% JP-10, 2.81%, O2, Balance Ar, Equivalence ratio = 1.0)

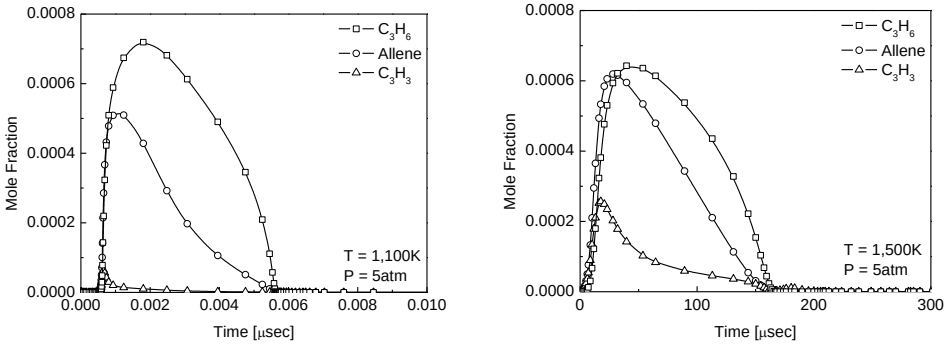

Figure 4.13 Mole fraction profiles for C_3-C_4 hydrocarbons
(0.2% JP-10, 2.81%, O2, Balance Ar, Equivalence ratio = 1.0)

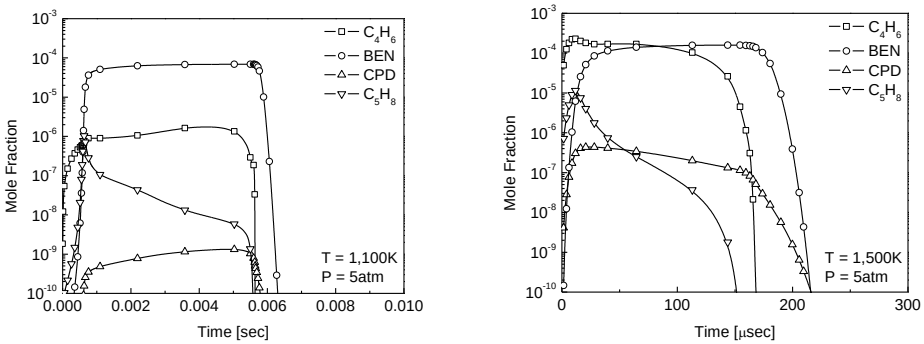

Figure 4.14 Mole fraction profiles for C_5-C_6 hydrocarbons
(0.2% JP-10, 2.81%, O2, Balance Ar, Equivalence ratio = 1.0)

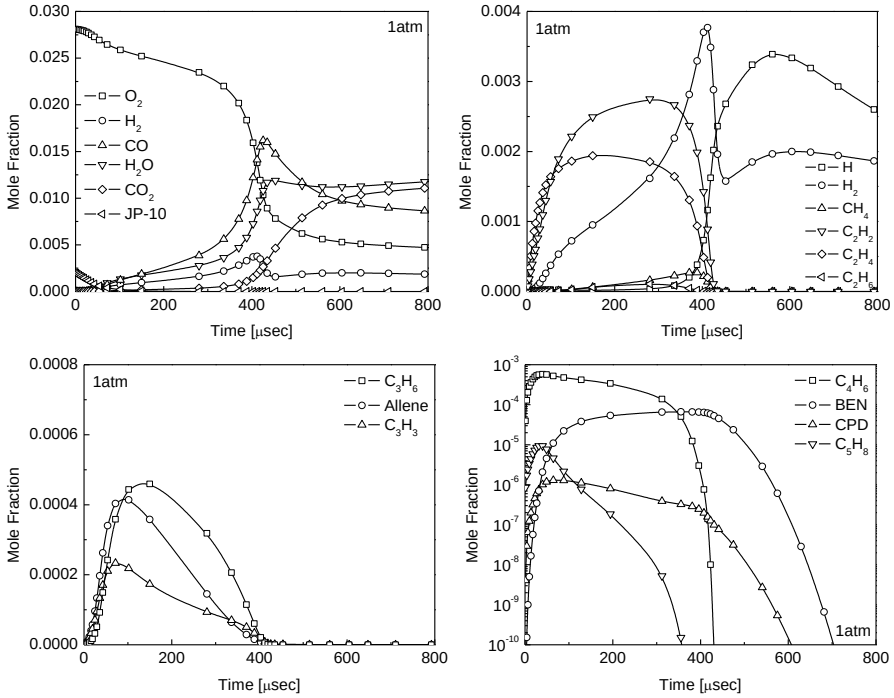

Figure 4.15 Mole fraction profiles for JP-10 as a function of time at inlet temperature = 1500K, inlet pressure = 1atm (0.2% JP-10, 2.81%, O2, Balance Ar, Equivalence ratio = 1.0)

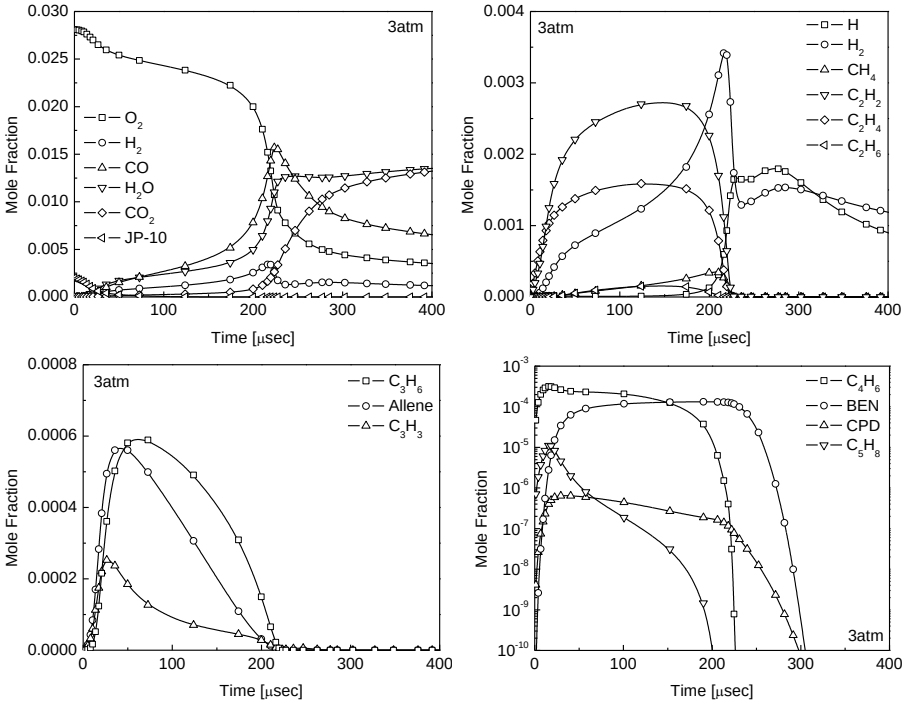

Figure 4.16 Mole fraction profiles for JP-10 as a function of time at inlet temperature = 1500K, inlet pressure = 3atm (0.2% JP-10, 2.81%, O2, Balance Ar, Equivalence ratio = 1.0)

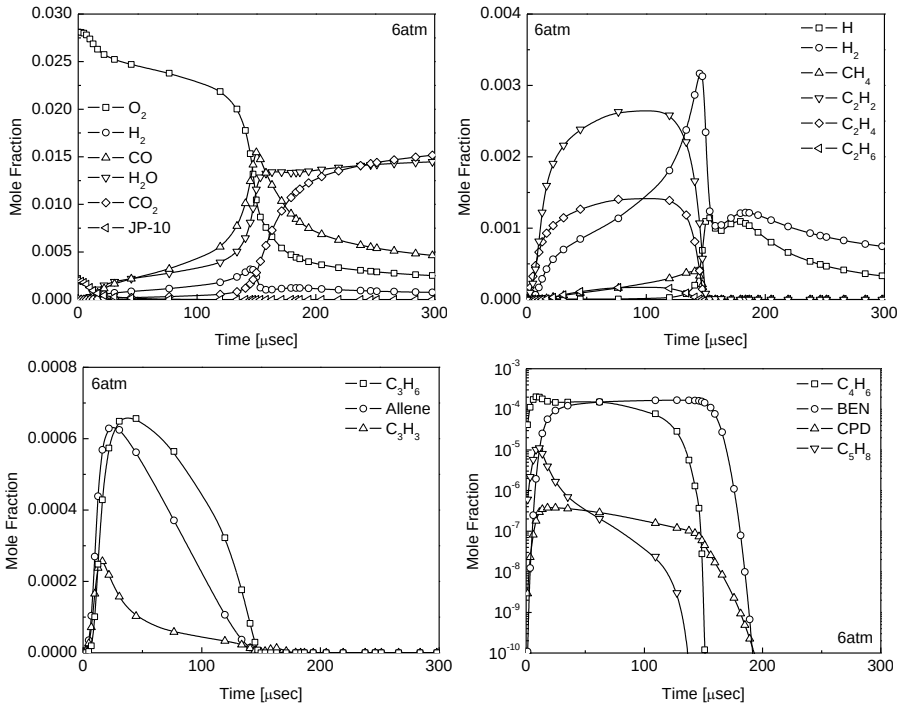

Figure 4.17 Mole fraction profiles for JP-10 as a function of time at inlet temperature = 1500K, inlet pressure = 6atm (0.2% JP-10, 2.81%, O2, Balance Ar, Equivalence ratio = 1.0)

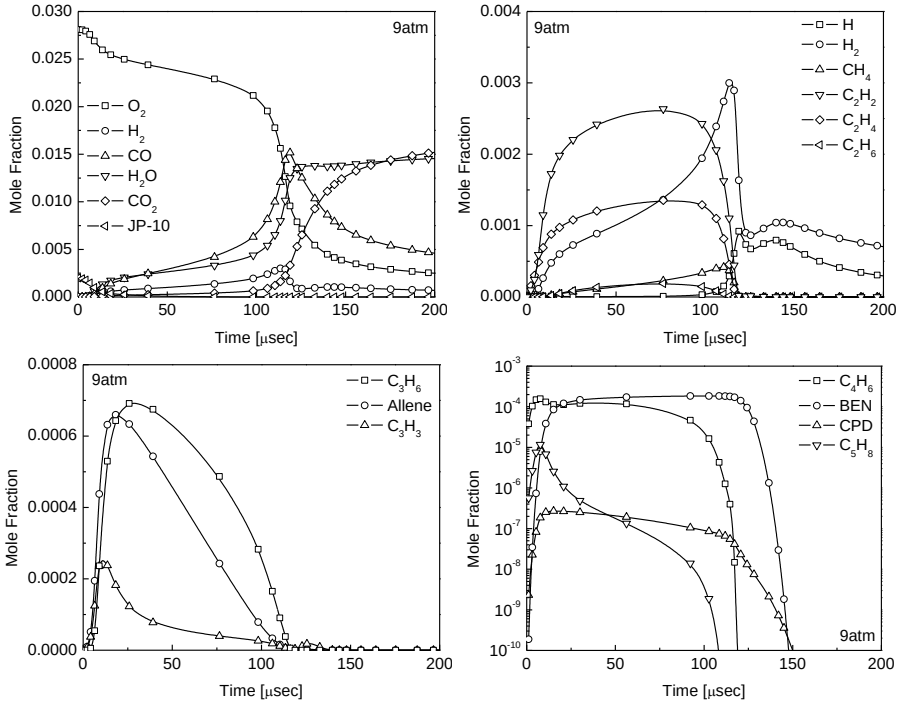

Figure 4.18 Mole fraction profiles for JP-10 as a function of time at inlet temperature = 1500K, inlet pressure = 9atm (0.2% JP-10, 2.81%, O2, Balance Ar, Equivalence ratio = 1.0)

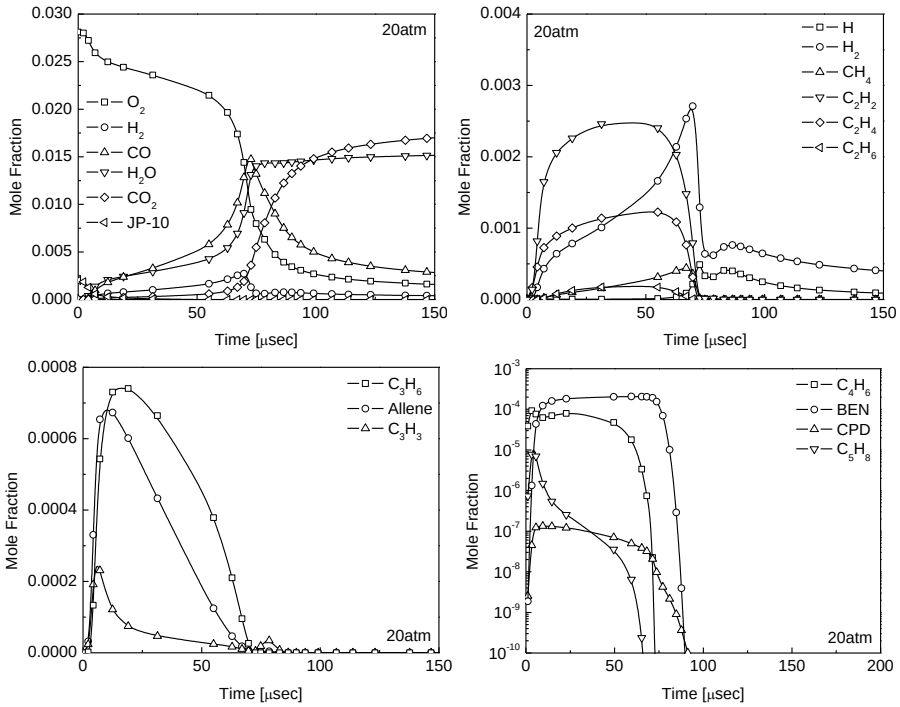

Figure 4.19 Mole fraction profiles for JP-10 as a function of time at inlet temperature = 1500K, inlet pressure = 20atm (0.2% JP-10, 2.81%, O2, Balance Ar, Equivalence ratio = 1.0)

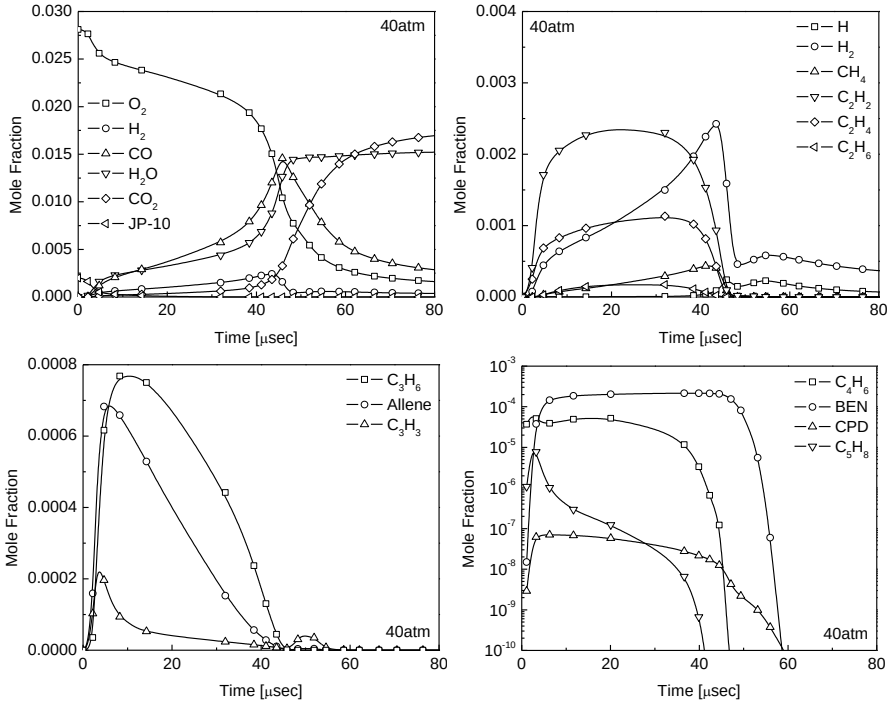

Figure 4.20 Mole fraction profiles for JP-10 as a function of time at inlet temperature = 1500K, inlet pressure = 40atm (0.2% JP-10, 2.81%, O2, Balance Ar, Equivalence ratio = 1.0)

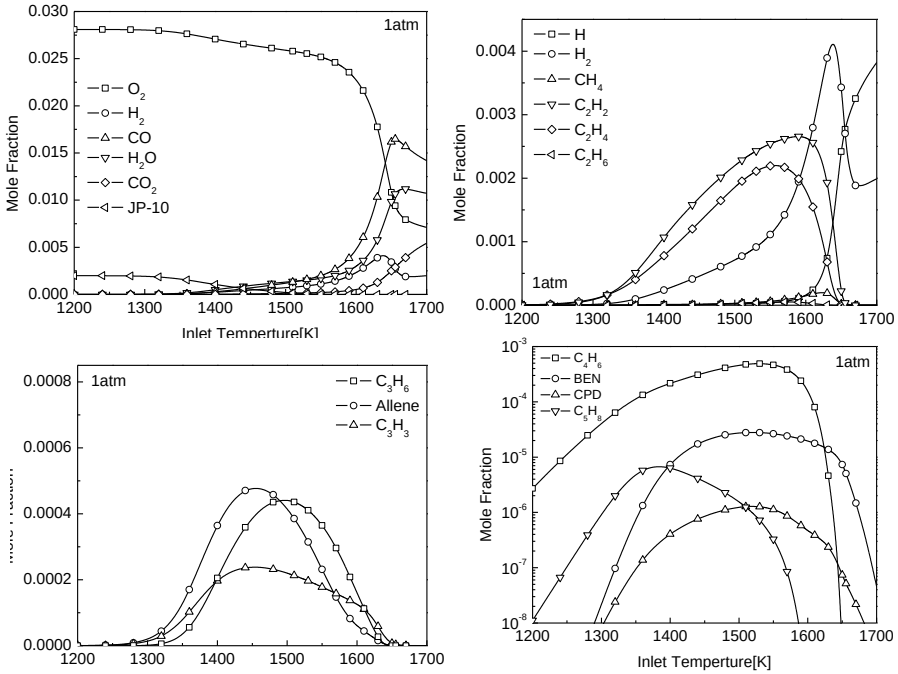

Figure 4.21 Mole fraction profiles for JP-10 as a function of inlet temperature at inlet pressure = 1atm, time=100μsec (0.2% JP-10, 2.81%, O2, Balance Ar, Equivalence ratio = 1.0)

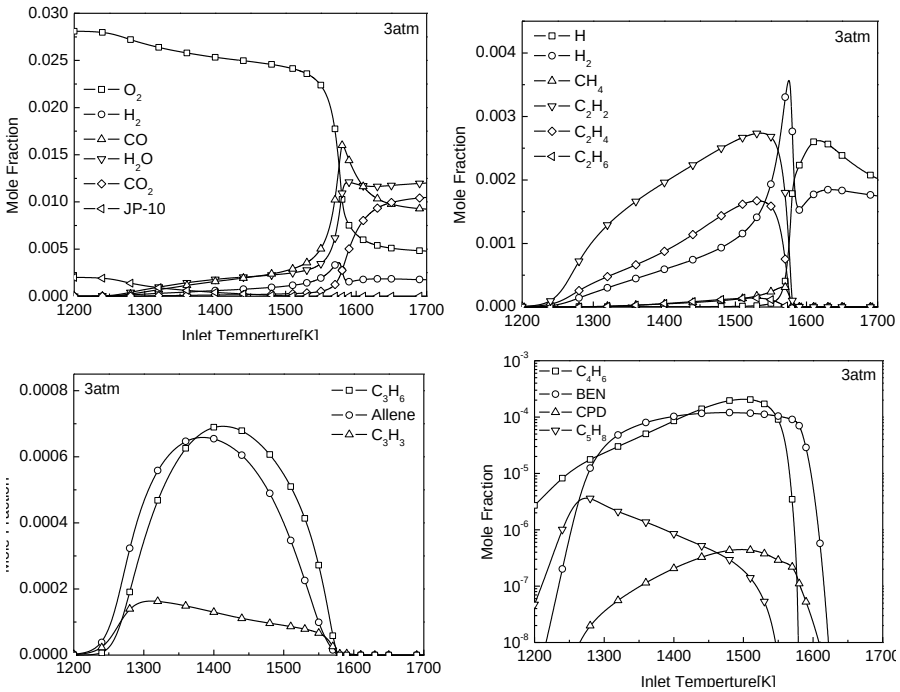

Figure 4.22 Mole fraction profiles for JP-10 as a function of inlet temperature at inlet pressure = 3atm, time=100μsec (0.2% JP-10, 2.81%, O2, Balance Ar, Equivalence ratio = 1.0)

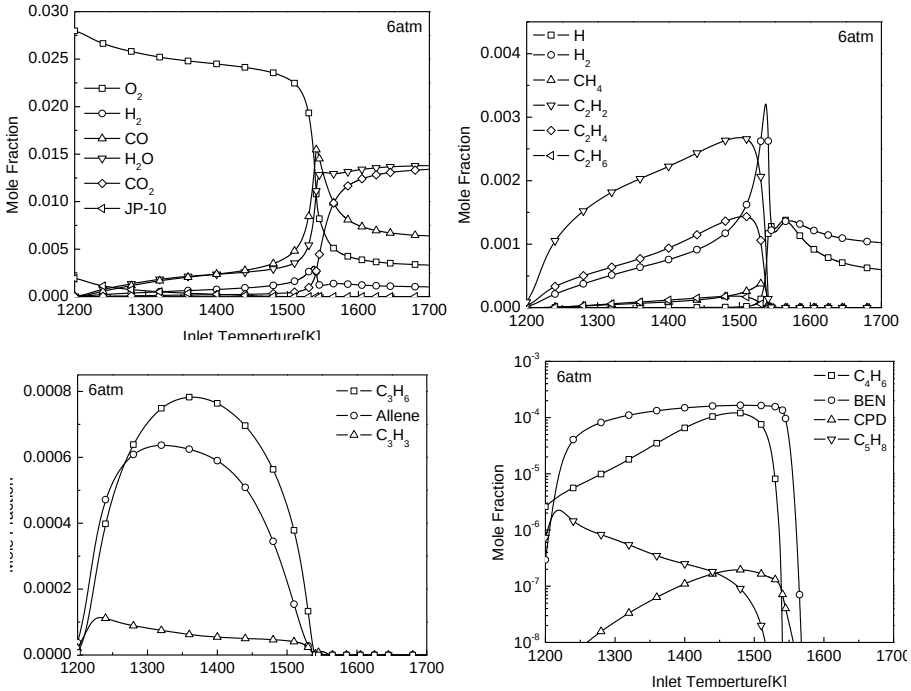

Figure 4.23 Mole fraction profiles for JP-10 as a function of inlet temperature at inlet pressure = 6atm, time=100μsec (0.2% JP-10, 2.81%, O2, Balance Ar, Equivalence ratio = 1.0)

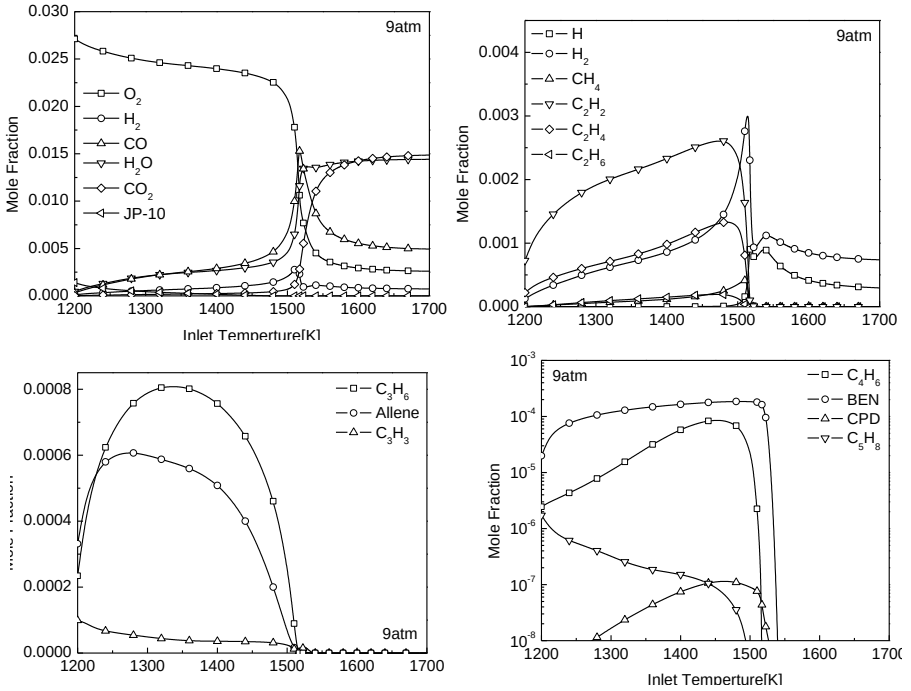

Figure 4.24 Mole fraction profiles for JP-10 as a function of inlet temperature at inlet pressure = 9atm, time=100μsec (0.2% JP-10, 2.81%, O2, Balance Ar, Equivalence ratio = 1.0)

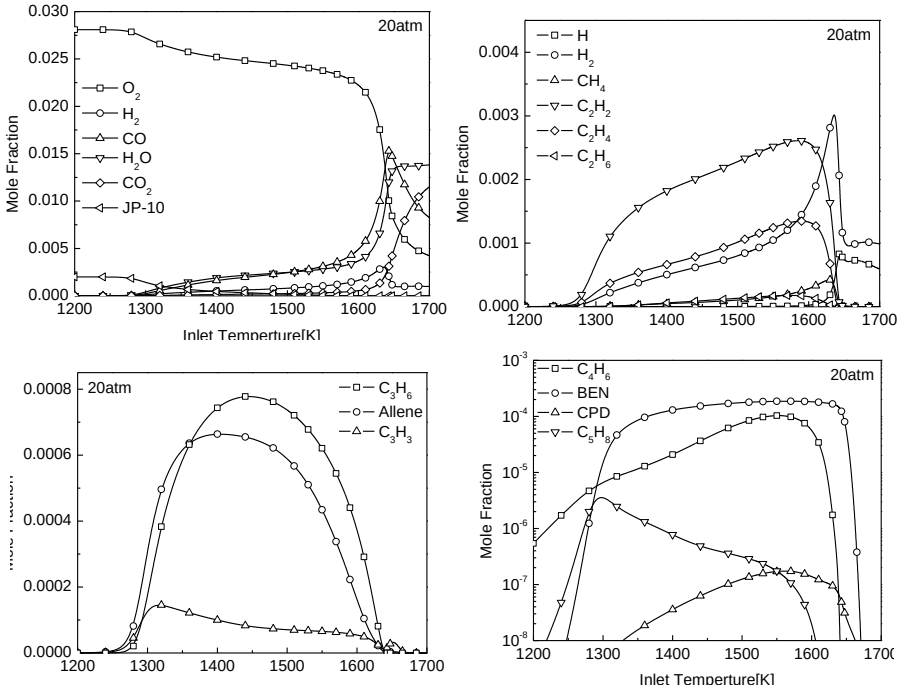

Figure 4.25 Mole fraction profiles for JP-10 as a function of inlet temperature at inlet pressure = 20atm, time=20μsec (0.2% JP-10, 2.81%, O2, Balance Ar, Equivalence ratio = 1.0)

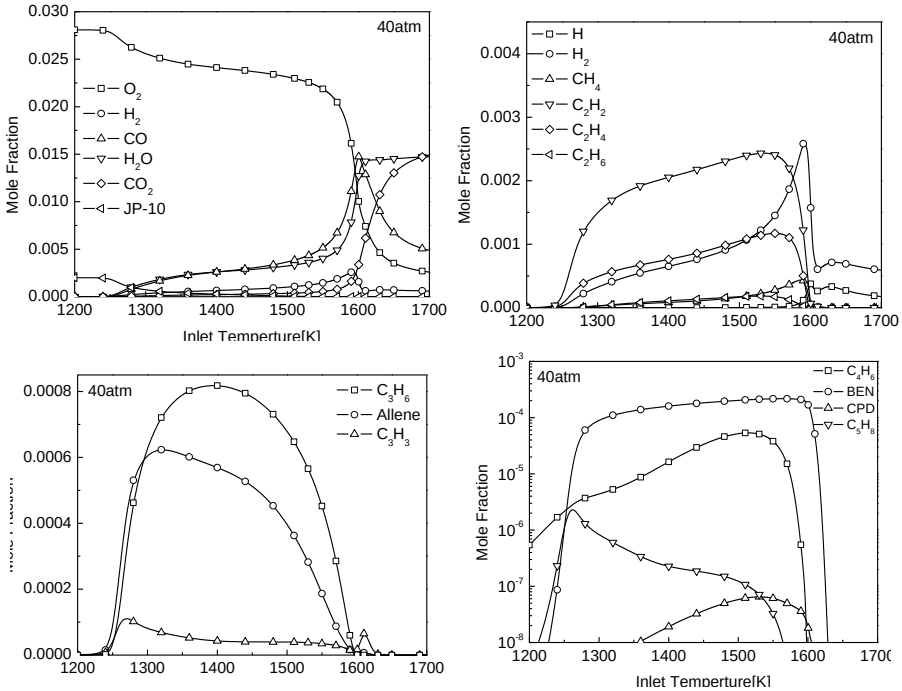

Figure 4.26 Mole fraction profiles for JP-10 as a function of inlet temperature at inlet pressure = 40atm, time=20μsec (0.2% JP-10, 2.81%, O2, Balance Ar, Equivalence ratio = 1.0)

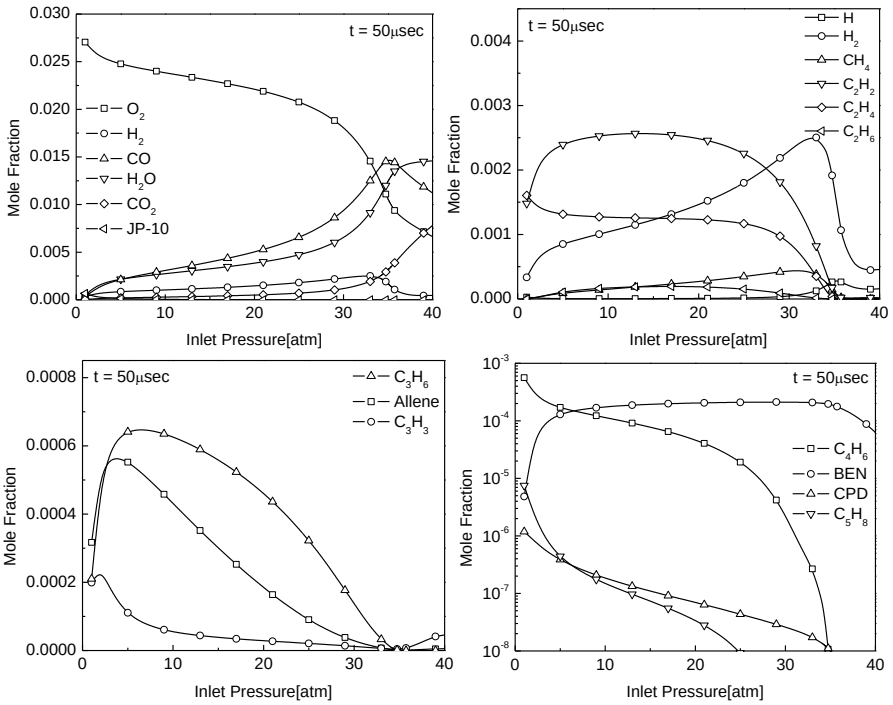

Figure 4.27 Mole fraction profiles for JP-10 as a function of inlet pressure at inlet temperature = 1500K, time=50μsec (0.2% JP-10, 2.81%, O2, Balance Ar, Equivalence ratio = 1.0)

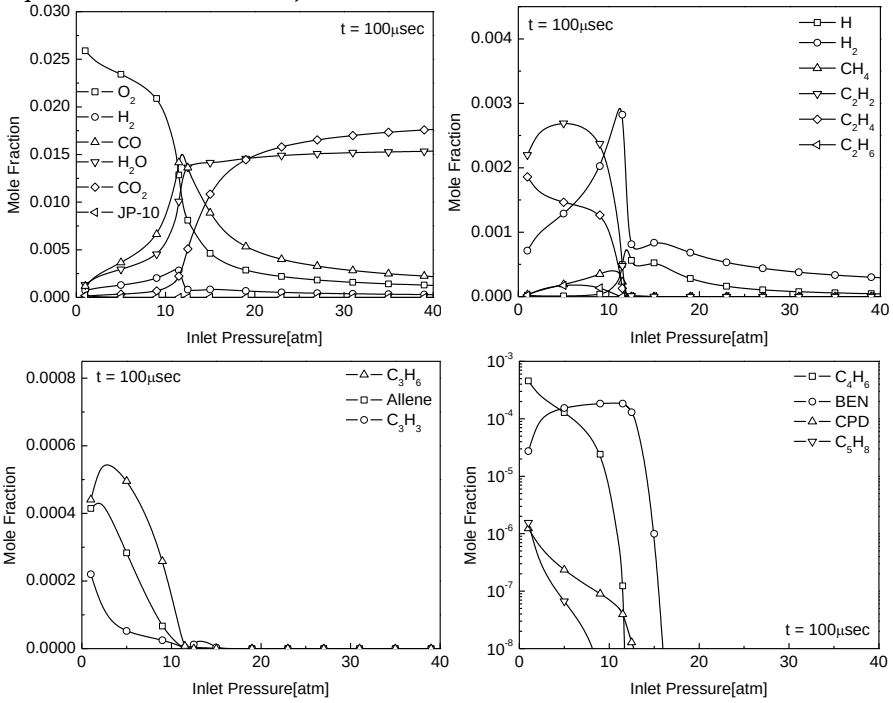

Figure 4.28 Mole fraction profiles for JP-10 as a function of inlet pressure at inlet temperature = 1500K, time=100μsec (0.2% JP-10, 2.81%, O2, Balance Ar, Equivalence ratio = 1.0)

4.7.2 JP-10 comprehensive skeletal mechanism for 49species

The purpose of this study is to develop reduced chemical kinetic mechanisms that could be used in large eddy simulations of gas turbine combustors. Using Atropos Version 1.00, a computer program that automates the mechanism reduction process by normalized sensitivity coefficients, reduced chemical kinetic mechanisms of forty-nine species and 219 reaction steps for JP-10 combustion have been generated from 49 species, 265 reaction steps of Sandiego mechanism. It was determined to be the maximum allowable number that could be implemented into a CFD code while maintaining reasonable computer time and memory requirements. The species and reduced kinetic mechanisms in the comprehensive high-temperature and pressure skeletal mechanisms are listed in Table 4.7 and Appendices I, respectively.

Table 4.7 Summary of reduced mechanisms for 49species

No. of species	Temperature range	Pressure range	species
49	900-1,700K	1-40atm	H, HE, O_2, OH, O, AR, HO_2, H_2, H_2O, H_2O_2, CHO, CO, CO_2, HCO, CH_3, CH_4, CH_2O, TCH_2, SCH_2, C_2H_4, CH_3O, C_2H_5, C_2H_6, CH, C_2H_2, C_2H_3, CH_2CHO, C_2H_4O, HCCO, CH_2CO, C_2H, CH_2OH, CH_3OH, CH_3CHO, CH_3CO, C_2H_5OH, CH_2CH_2OH, CH_3CHOH, CH_3CH_2O, C_3H_4, C_3H_3, C_3H_5, C_3H_6, C_3H_8, IC_3H_7, NC_3H_7, C_4H_6, C_5H_8, $C_{10}H_{16}$

The simplification of hydrocarbon mechanisms consists of three steps. The first step is the construction of a skeletal network by eliminating unimportant

reaction steps under a specified flame condition. The second step is to eliminate the fastest reactions that consume or produce the steady-state species. The last step involves linear algebra with the set of mass balance leading to the final form of the reduced mechanism and the corresponding net production rates that are linear combinations of elementary reaction rates. The starting full mechanisms are from Sadiego mechnism [120].

Sensitivity analysis, reaction path analysis are employed for this purpose. More specifically, kintecus can generate Normalized Sensitivity Coefficients (NSC) at any time or times during a simulation run. Normalized sensitivity coefficients are the partial derivatives of each species with respect to each reaction constant normalized by multiplying by Rate Constant/Concentration of Species, which is defined by

$$NSC = \left(\frac{\frac{\partial [Species]}{[Species]}}{\frac{\partial k}{k}} \right)_k = \left(\frac{\partial \ln [Species]}{\partial \ln k} \right)_k$$

It is a matrix with signed numbers, which indicate the reactions that have the biggest influence on certain species. By examining the matrix and sorting the largest NSC's by reactions for each species one can see that the large positive NSC's are the major sources and the large negative NSC's are the major sinks [134]. A reaction that has a very small NSC for a species indicates that the reaction has almost no influence on the species no matter what the rate constant or the reaction's concentration of reactant species. The thought might occur that if a sum of the squares of the NSC's for each reaction is taken, then the reactions

might show evidence that they could be dropped since reactions with very small NSC's should have no effect on any of the species. This might be true for most kinetic mechanisms, but in some cases this is not the case. NSC only tests for direct routes of influence of species X; it does not directly show strongly interacting reactions. A very simple method to see which reactions can actually be "thrown out the window" is a method of principal component analysis used by Turanyi, Vajda and Valko[135] applied to the normalized sensitivity analysis matrix, S. The steps described by this paper can easily be done in finding NSC matrices, S_1, S_2 ,S_3...S_n , at various times in the simulation. By using a spreadsheet program, all the S's at each calculated time can be concatenated into one big matrix, BS. Again, it is necessary to transpose each S before concatenating all of them into BS. Now multiply BS by its transpose, BST * BS = D. Determine the eigenvalues, e, and eigenvectors, v, of D. Now, calculate the lower threshold for the eigenvalues by multiplying the number of NSC matrices calculated by the number of species (which are not constants in simulation) by 1×10^{-4}, call this L. Note all the eigenvalues that are equal or under L, call these LL. Now the last step, for all the elements of each eigenvector of each respective LL that are greater than 0.2 mark those. Those elements of the eigenvectors correspond to reactions that have no overall effect on the kinetics scheme and can be safely "thrown out the window".

Now, all of the above process described here was performed by using Atropos, the Kintecus software addition name. The following equation describes the Overall Sensitivity Coefficients B_r :

$$B_r = \sum_{i=1}^{(total\ \#\ NSC\ files)} \sum_{j}^{(total\ \#\ species)} \left(\frac{\partial [\ln [Species]_{i,j}}{\partial \ln k_r} \right)^2$$

It can be seen that B_r are actually the diagonal entries of S^TS and are an excellent way to represent the total "flux" or movement of mass that any reaction *r* can accomplish. The larger the reaction's B_r the more overall system movement of mass is going through it.

These values can be seen in Atropos' output beginning with the line, "The diagonal entries of TRANSPOSE(S)*S (B_r) are shown below". The B_r array data does not represent the importance of a reaction *r*. That can only be determined through the analysis of the principle components of the top eigenvalues. These important values can be checked out after the following line in Atropos' output: "All eigenvalues with Principle Components displayed and". The reactions containing the largest principle components for the largest eigenvalues are the most influential reactions throughout the chemical kinetic run. The reactions containing the largest principle components for the smallest eigenvalues are the least influential reactions throughout the chemical kinetic run. For a full explanation on all those very important quantities refer to the main paper [135].

For the next step, complex hierarchical cluster analysis [136,137] on temporal concentration profiles obtained from the sensitivity analysis has been performed. One way of displaying this information is a reaction pathway diagram. It is to analyze all species and to determine which species or groups of species (or subgroups, etc.) are positively, zero or negatively correlated to each other and with other groups/species in either a pictorially or numeric output or both.

In order to test the validity of our reduced mechanism, the calculated data is compared to the experimental OH mole fraction profile and shock tube data of Davidson et al. (2001) [94]. The validation was performed using the constant volume combustor model for both the reduced mechanism for 49 species and high-temperature skeletal mechanisms for 58 species covering pressures of 1, 5, and 40atm and equivalence ratios of 1.0, with the temperature ranges of 1,200 - 1,700 K and the pressure range of 1, 3, and 6atm shown in Figure 4.29 and 4.30 respectively. The reduced mechanism well reproduces the curves to show the good agreement with the experimental data. The reduced skeletal mechanism performs quite well for all cases, with an average difference of 10.1% based on OH mole fraction at 3atm and 9.7% based on CH mole fraction at 1, 3, and 6 atm, $\varphi = 1.0$, which data are listed in table 4.8 and 4.9, respectively.

In Figure 4.31, the reduced mechanism for 49 species well predicts the ignition delay time compared to the skeletal mechanism of 58species for the full range of the validation conditions. The adiabatic flame temperature also shows a good performance, with some discrepancy primarily in the high-temperature, high-pressure regions as expected in Figure 4.32. The oxidation and breakdown can occur at nearly any stage of combustion. For instance, consumption of initially formed PAH (polycyclic aromatic hydrocarbons) and their precursors can suppress their contribution to growth processes while acetylene formed in benzene destruction might play a significant role in the formation and growth of PAH and soot. The amounts of PAH and soot in the final combustion products depend on conditions such as temperature, pressure, fuel to oxygen ratio. Also,

combustion involves complex competition between species formation and destruction which, without oxidation, can lead to increasing large PAH and even soot particles. Therefore, this flame temperature discrepancy results in the lack of PAH formation process from the reduced mechanism for 49species.

Figure 4.33 show that comparison of mole fraction as a function time of between 58species and 49species for JP-10 at temperature of 1460K, inlet pressure of 3.02atm. The results from the 58 species JP-10 combustion model are in black and the reduced JP-10 combustion model for 49species is in color. Fuel conditions are 0.2% JP-10, 2.83%, O2, Balance Ar, Equivalence ratio is 1.0. As seen on this Figure 4.33, there is some discrepancy primarily in the H mole fraction between 49species and 58species. It has been shown that the reaction pathway of 49species is different from that of 58species. PAH formation process has an effect on H mole fraction. The present work identified chemical reaction pathways responsible for fuel consumption, e.g., bimolecular reactions leading to more reactive radicals, unimolecular decay, or both.

Figures 4.34 – 4.37 show that mole fraction profiles for JP-10 with 49species as a function of inlet temperature at inlet pressure from 1atm to 40atm. Mole fraction profiles for JP-10 with 49species with an inlet temperature of 1,500 K over pressures covering from 1atm to 40atm, and a range of residence times for 50 µsec, 100µsec are shown in Figure 4.38 and 4.39 respectively.

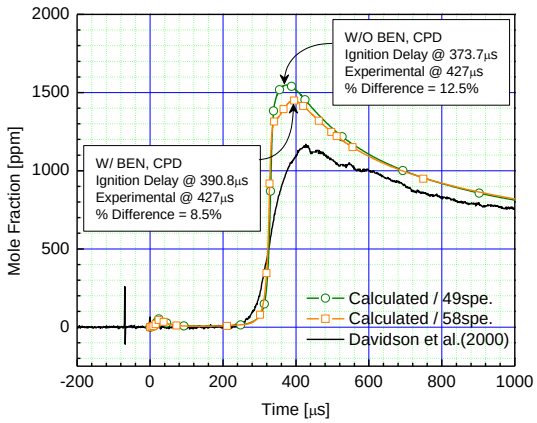

Figure 4.29 Comparison of ignition delay time with OH mole fraction between 58species and 49 species for JP-10. Initial conditions are 0.2% Jp-10, 2.83% O2, balance Ar, Equivalence ratio= 0.99, T=1,460K and P=3.02atm.

Table 4.8 Ignition time data based on OH mole fraction (49 species)

T (K)	P (atm)	JP-10 (%)	O_2 (%)	ϕ	t(μs) Davidson et al.	t(μs) Calculated	% Difference
1447	3.18	0.2	2.76	1	462	416.1	9.9%
1460	3.02	0.2	2.83	0.99	427	373.7	12.5%
1502	3.11	0.2	2.76	1	276	254.3	7.9%
						Max.	12.5%
						Min.	7.9%
						Avg.	10.1%
						Median	9.9%

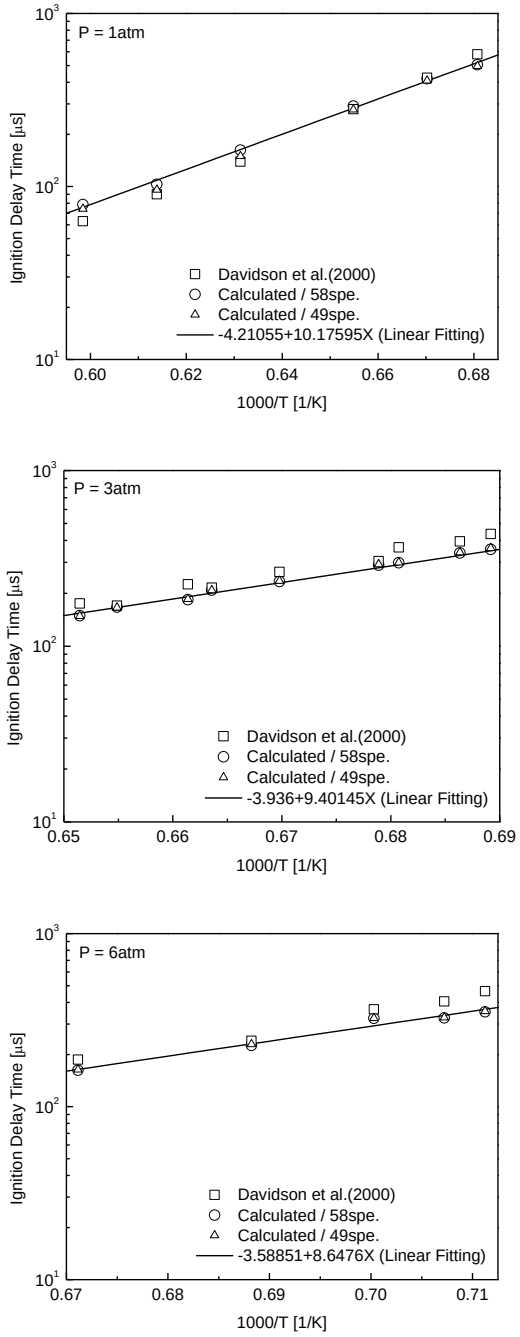

Figure 4.30 Comparison of ignition delay time based on CH mole fraction with the variation of pressure and temperature between 58species and 49species for JP-10. Initial conditions are lasted in table 4.3.

Table 4.9 Ignition time data based on CH mole fraction (49species)

T (K)	P (atm)	JP-10 (%)	O_2 (%)	ϕ	t(μs) Davidson et al.	t(μs) Calculated	% Difference
1469	1.25	0.2	2.82	0.99	580	495.9	14.5%
1492	1.16	0.2	2.79	1.00	425	408.5	3.9%
1527	1.15	0.2	2.81	1.00	280	278.4	0.6%
1584	1.19	0.2	2.81	1.00	139	149.8	-7.8%
1588	1.23	0.2	2.74	1.02	140	145.2	-3.7%
1629	1.2	0.2	2.87	0.97	90	95.7	-6.3%
1671	1.05	0.2	2.99	0.94	63	74.2	-17.8%
1406	3.3	0.2	2.82	0.99	755	527.5	30.1%
1451	3.08	0.2	2.81	1.00	435	361.3	16.9%
1457	3.18	0.2	2.76	1.01	395	342.0	13.4%
1469	3.02	0.2	2.83	0.99	365	299.3	18.0%
1473	3.16	0.2	2.76	1.01	305	292.3	4.2%
1493	3.11	0.2	2.81	1.00	265	235.2	11.3%
1507	3.03	0.2	2.82	0.99	212	205.1	3.3%
1507	3.11	0.2	2.76	1.01	215	208.2	3.2%
1512	3.32	0.2	2.82	0.99	225	185.6	17.5%
1527	3.23	0.2	2.76	1.01	170	165.5	2.7%
1535	3.23	0.2	2.81	1.00	175	148.4	15.2%
1580	3.17	0.2	1.76	1.01	90	95.8	-6.4%
1378	6.17	0.2	2.89	0.97	675	423.9	37.2%
1406	6.03	0.2	2.81	1.00	465	355.9	23.5%
1407	6.26	0.2	2.79	1.00	455	348.7	23.4%
1414	6.34	0.2	2.78	1.01	405	327.0	19.3%
1428	6.13	0.2	2.63	1.06	365	324.6	11.1%
1453	5.99	0.2	2.86	0.98	240	229.2	4.5%
1456	6.05	0.2	2.86	0.98	271	221.1	18.4%
1490	6.4	0.2	2.76	1.01	187	163.7	12.5%
						Max.	37.2%
						Min.	-17.8%
						Avg.	9.7%
						Median	11.3%

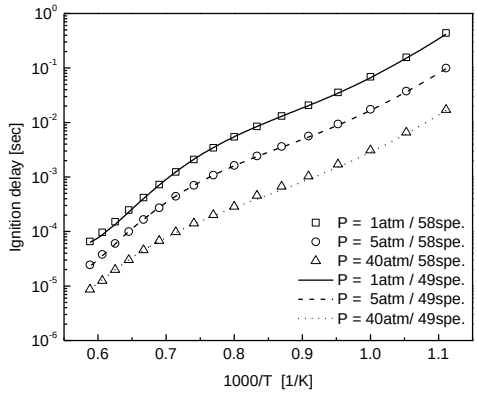

Figure 4.31 Comparison autoignition delay time between 58species and 49 species model of a reduced JP-10 mechanism over a range of initial temperatures and pressures that are listed at table 4.1 in case of T=1,500K. (0.2% JP-10, 2.81%, O2, Balance Ar, Equivalence ratio = 1.0)

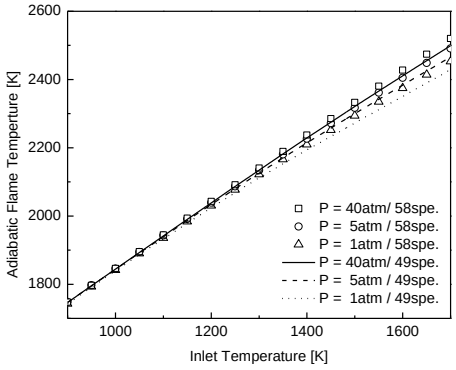

Figure 4.32 Comparison of adiabatic flame temperatures between 58species and 49 species model as function of inlet temperature and pressure. (0.2% JP-10, 2.81%, O2, Balance Ar, Equivalence ratio = 1.0)

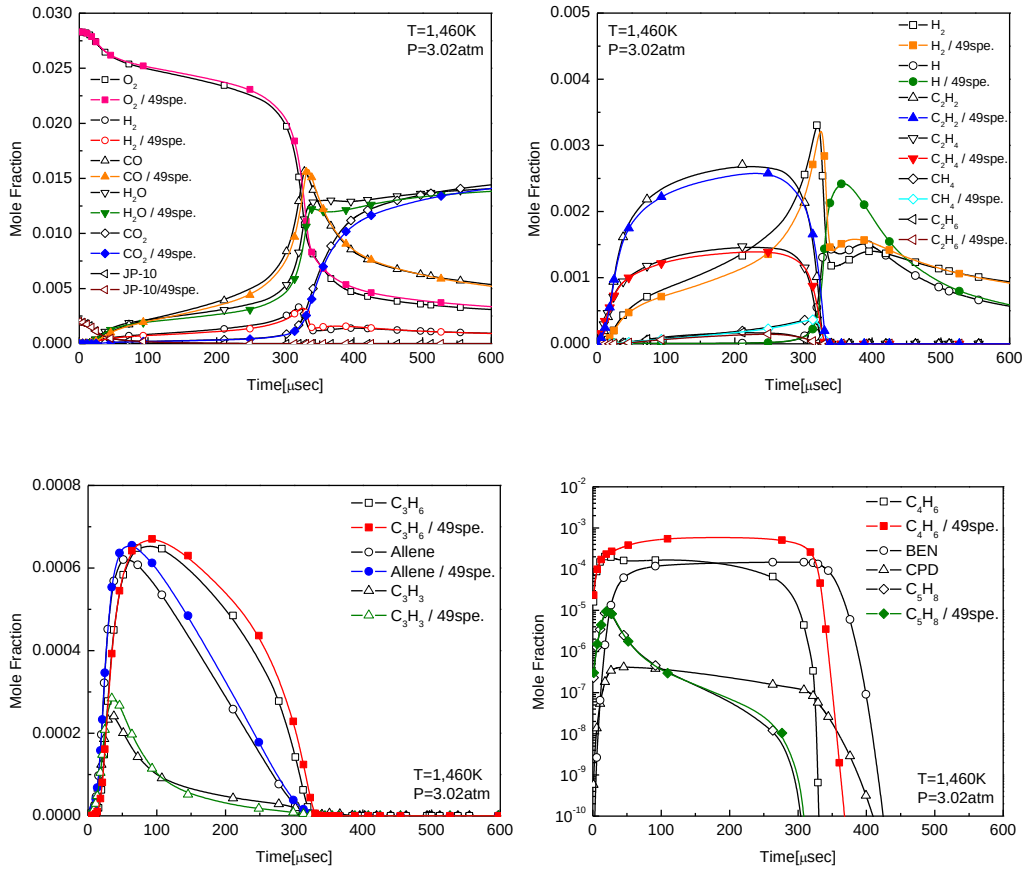

Figure 4.33 Comparison of mole fraction as a function time of between 58species and 49species for JP-10 at temperature = 1460K, inlet pressure = 3.02atm. The results from the 58 species JP-10 combustion model are in black and the reduced (49species) JP-10 combustion model is in color. (0.2% JP-10, 2.83%, O2, Balance Ar, Equivalence ratio = 1.0)

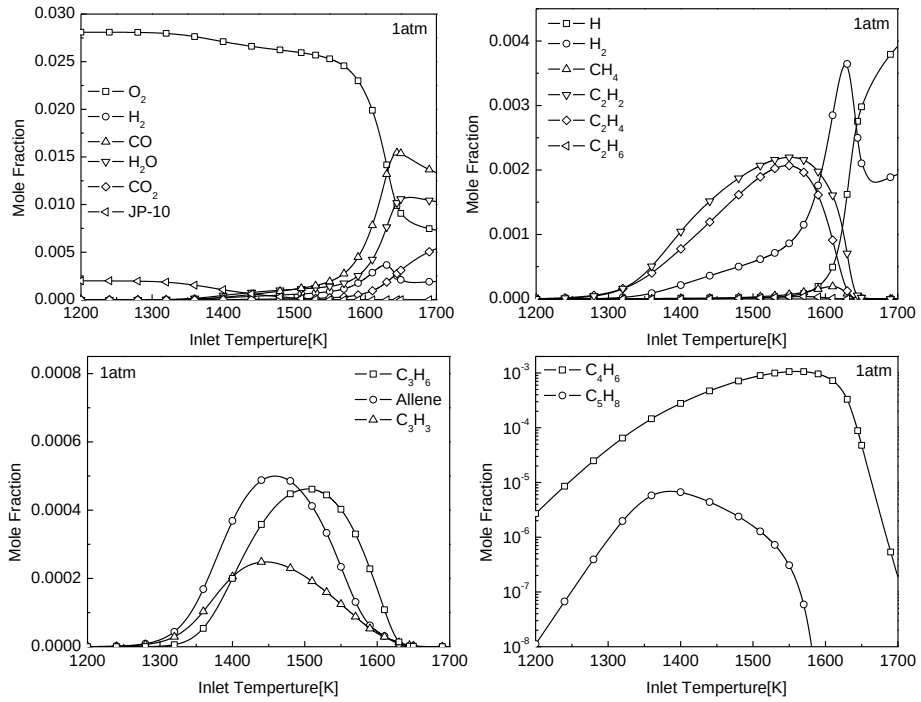

Figure 4.34 Mole fraction profiles for JP-10 with 49species as a function of inlet temperature at inlet pressure = 1atm, time=100μsec (0.2% JP-10, 2.81%, O2, Balance Ar, Equivalence ratio = 1.0)

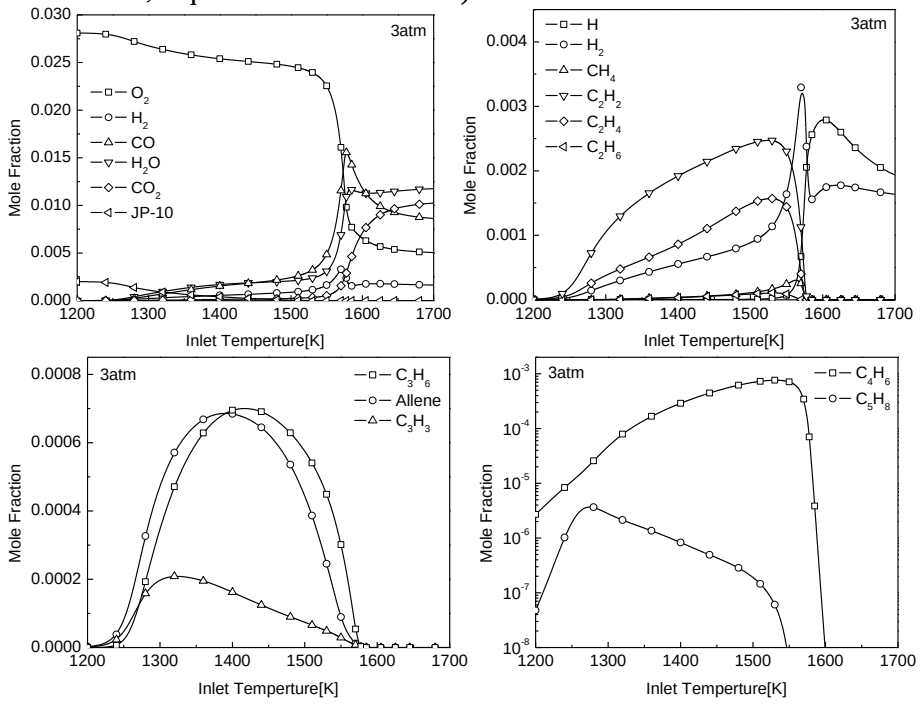

Figure 4.35 Mole fraction profiles for JP-10 with 49species as a function of inlet temperature at inlet pressure = 3atm, time=100μsec (0.2% JP-10, 2.81%, O2, Balance Ar, Equivalence ratio = 1.0)

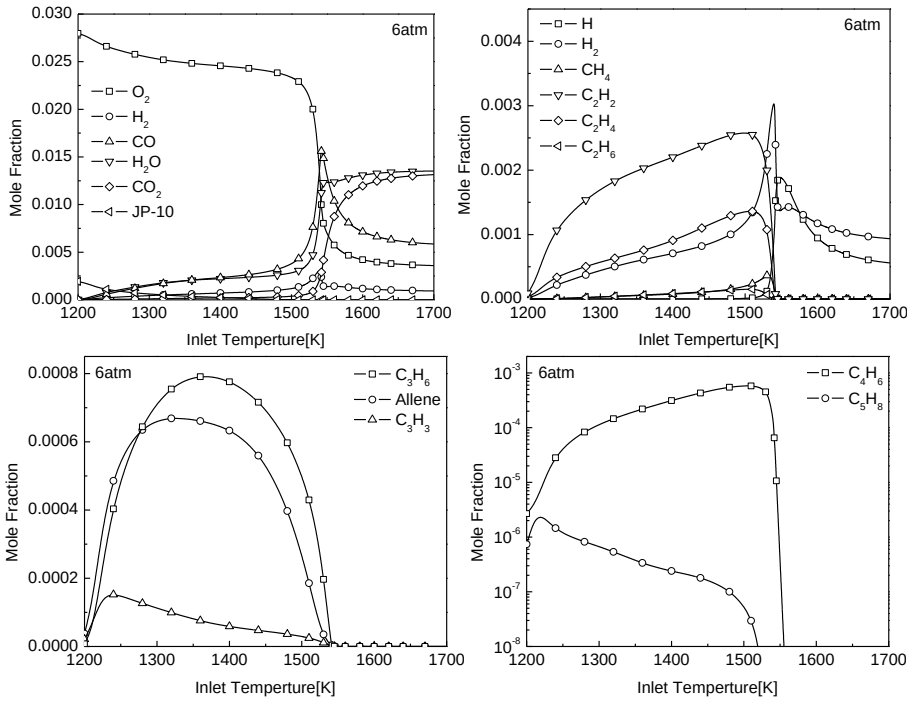

Figure 4.36 Mole fraction profiles for JP-10 with 49species as a function of inlet temperature at inlet pressure = 6atm, time=100μsec (0.2% JP-10, 2.81%, O2, Balance Ar, Equivalence ratio = 1.0)

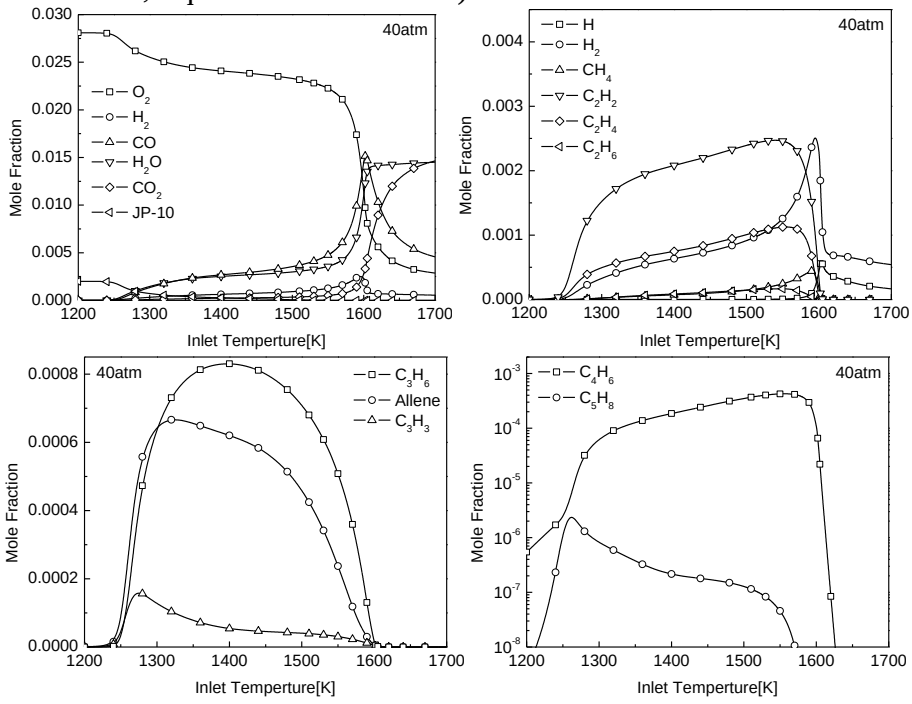

Figure 4.37 Mole fraction profiles for JP-10 with 49species as a function of inlet temperature at inlet pressure = 40atm, time=20μsec (0.2% JP-10, 2.81%, O2, Balance Ar, Equivalence ratio = 1.0)

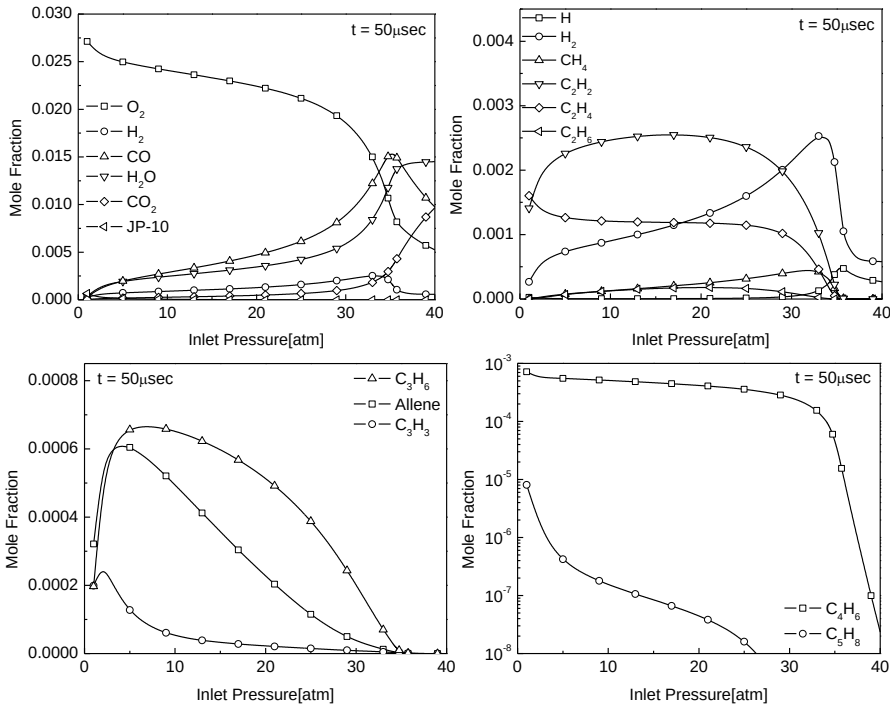

Figure 4.38 Mole fraction profiles for JP-10 with 49species as a function of inlet pressure at inlet temperature = 1500K, time = 50μsec (0.2% JP-10, 2.81%, O2, Balance Ar, Equivalence ratio = 1.0)

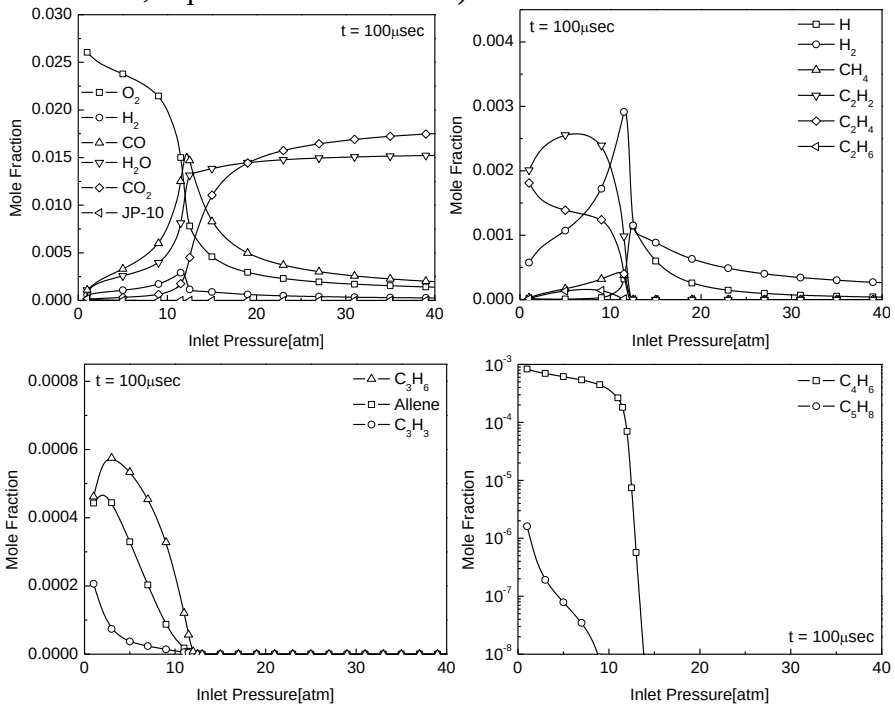

Figure 4.39 Mole fraction profiles for JP-10 with 49species as a function of inlet pressure at inlet temperature = 1500K, time=100μsec (0.2% JP-10, 2.81%, O2, Balance Ar, Equivalence ratio = 1.0)

4.8 Conclusions

A complete kinetic study for the process of JP-10 thermal cracking, including the temperature profile along with the variation of the pressure and the time, would be a very difficult exercise. Nevertheless, the objective of the kinetic study performed in this present work was aimed at providing only a general range of information regarding the influences of operating parameters, such as the type of reacting pressure and the optimal temperatures on the reaction rates of those precursor species involved in the mechanism for JP-10 decomposition and the lighter hydrocarbons formation.

This study was carried out at the high temperatures required to crack JP-10 thermally, which far exceeds onboard engine capabilities. This will be more likely to increase the probability of a lower olefin and higher aromatic product yield with thermal cracking. From the time dependence of the JP-10 decomposition, the formation of small molecules is observed as the inlet temperature goes from 1,100 K up to 1,500K. Higher temperatures, e.g. above 1500 K, produce the C_6 and C_5 species in important concentrations. This result showed that the cracking reactions are favoured at high temperatures because the energy is available for promoting the endothermic reactions. The rupture of the C-C bond of the initial molecule and the subsequent formation of olefins and smaller radical compounds are the steps that control the reaction kinetics.

A reduced kinetic mechanism described here agrees reasonably well with the measurements of ignition delay for inlet temperature from 900K – 1700K, pressure from 1 – 40 atm. Also, the fact that the temperature dependence of the

benzene and CPD molecules exists during the process of JP-10 decomposition is observed in this study. In the initial decomposition, the principal products were cyclopentadiene, benzene, allene, and C_4H_x.

Finally, since a reduced kinetic mechanism of JP-10 including in BEN and CPD molecule was successfully built for the first step, it can be possibly controlled by new data analyzed by means of the gas chromatography-mass spectrometry (GC–MS). The high-temperature mechanism also shows fairly good performance, with noticeable discrepancies primarily in the low-temperature, high-pressure regions as expected. The results of this numerical work may be used to establish the optimal operating parameters for the new grades of JP-10 combustion, with regard to their potential applications and in the actual production process design and scale-up.

Chapter 5

SUMMARY AND RECOMMENDATIONS

5.1 Summary

For mass transfer phenomena on drug in a 2-D cylindrical matrix system:

Drug diffusion to the tissue from the microcirculation by using of cylindrical matrix systems has been investigated with special emphasis on the influence of an arterial oxygen partial pressure change and a finite consumption rate on the drug release profile. A mathematical model of the drug diffusion and release processes was formulated in terms of nonlinear partial differential equations (PDEs). These were solved numerically by using well established Fortran subroutines, which can be applied to determine the penetration depth of the drug by the tissue.

An approximately analytical solution, valid during the early stages of the diffusion process, was derived. The numerical solution was compared to the numerical one existing in the literature. From this comparison, it was established that the numerical solution provided a good description of the major part of the diffusion distribution, with respect to some parameters of an arterial oxygen partial pressure and drug consumption rate.

For mass transfer phenomena on oxygen/drug in 3-D Capillary Network :

A computational fluid dynamics (CFD) model has been developed to simulate the flow, delivery of oxygen and other substances in a capillary network. A three-dimensional capillary network has been constructed to replicate the one studied by Secomb et al. (2000), and the computational framework features a non-Newtonian viscosity model of blood, the oxygen transport model including in-

stream oxygen-hemoglobin dissociation and wall flux due to tissue absorption, as well as an ability to study delivery of drugs and other materials in the capillary streams. The model is first run to compute the volumetric flow rates from the velocity profiles in the segments, and compared with Secomb's work with good agreements. Effects of abnormal pressure and stenosis conditions, as well as those arising from different capillary configurations, on the flow and oxygen delivery are investigated, along with a brief look at the unsteady effects and drug dispersion in the capillary network. The current approach allows for inclusion of oxygen and other material transport, including drugs, nutrients or contaminants based on the flow simulations. Also, three-dimensional models of complex circulatory systems ranging in scale from macro- to micro-vascular vessels, in principle, can be constructed and analyzed in detail using the current method.

For a reduced Chemical Kinetics of the Combustion for Jet propellent-10:

A reduced kinetic mechanism described here is designed to focus on conditions relevant to flames, high temperature ignition. It was derived by beginning with simple chemical systems then proceeding gradually to more complex systems. In this research approach, the numbers of species and reactions are kept to the minimum needed to describe the systems and phenomena addressed, thereby minimizing as much as possible the uncertainties in the rate parameters employed. Therefore, as the database for the present mechanism evolves, it can be applicable to an increasing number of combustion processes such as other high-speed flight applications. Another reduced mechanism for 49species generated by the sensitivity and cluster analysis has also been studied

that compare well to available ignition delay measurements for JP-10.

It seems that my dissertation is a set of different research topics, though. In fact, they are being based on the in-depth theory of the heat and mass transfer phenomena in micro scale. Specifically speaking, the governing equations of the combustion including the continuity, momentum, species, and energy equations are the same as that of the drug diffusion. In other words, if the species is the drug in the species equation, it would be the drug diffusion. Also, if the hydrocarbon fuel such as JP-10 is applied to the species, it would be called as JP-10 combustion. Only the different thing between two cases is that the combustion basically is on the basis of the one dimensional flow analysis. Therefore, I can definitely tell my major that it is "Based on CFD (computational fluid dynamics) in its application to the computational combustion of Jet fuels".

5.2 Recommendations

Using commercial computational fluid dynamics (CFD) software to investigate the micro scale heat and mass transfer phenomena such as the drug diffusion to the brain tissue and the combustion area for the Pulse Detonation Engine (PDE) and for other high-speed flight applications such as aircraft-launched, ship-launched, or ground-launched hypersonic missiles could be potentially powerful. However, there is still more work to be done in the area of classic CFD as follows:

<u>For mass transfer phenomena on oxygen/drug in 3-D Capillary Network</u> :

1. It is to apply the tissue to the space surrounding the 3-Dimensional capillary network.

2. It is to put the periodic pressure conditions based on physiology range in inlets.

For a reduced Chemical Kinetics of the Combustion for Jet propellent-10:

1. It is to create CFD source code that the JP-10 reaction mechanism can be coupled to the continuity, momentum, species transport, energy equation, and grid generation including in the combustor and nozzle of the Pulse Detonation Engine (PDE) and of the hypersonic missiles. This will be on going work.
2. It is to add the calculation process of the specific thrust to the above code.
3. It is to develop the chemical kinetics of the low temperature oxidation mechanism below 900K including in the transient range for JP-10 so that the comprehensive skeletal mechanism can well predict the ignition delay compared to the shock tube data for the full range of validation conditions, with a little bit of discrepancy in the negative temperature coefficient (NTC) region.
4. The thermodynamic data using this simulation can be replaced by the recent data.

REFERENCES

1. J. Crank, The Mathematics of Diffusion, Paperback Edition, Oxford Univ. Press, Oxford, 1975.

2. Joe D. Hoffman, Numerical Methods for Engineers and Scientists, McGraw-Hill, 1992

3. J. Noye, Numerical Solutions of Partial Differential Equations, Univ. of Melbourne, 1981.

4. T. Higuchi, Rate of release of medicaments from ointment bases containing drugs in suspension, J. Pharm. Sci. 50 (1961) 874– 875.

5. T. Higuchi, Mechanisms of sustained action medication: theoretical analysis of the rate of release of solid drugs dispersed in solid matrices, J. Pharm. Sci. 52 (1963) 1145–1149.

6. T.J. Roseman, W. Higuchi, Release of medroxyprogesterone acetate from a silicone polymer, J. Pharm. Sci. 59 (1970) 353–357.

7. K. Tojo, Intrinsic release rate from matrix-type drug delivery systems, J. Pharm. Sci. 74 (1985) 685– 687.

8. D.R. Paul, S.K. McSpadden, Diffusional release of a solute from a polymeric matrix, J. Membr. Sci. 1 (1976) 33–48.

9. A.L. Bunge, Release rates from topical formulations containing drugs in suspension, J. Control. Release 52 (1998) 141–148.

10. M.J. Abdekhodaie, Y.-L. Cheng, Diffusional release of a dispersed solute from planar and spherical matrices into finite external volume, J. Control. Release 43 (1997) 175–182.

11. Y. Zhou, X.Y. Wu, Theoretical analyses of dispersed-drug release from planar matrices with a boundary layer in a finite medium, J. Control. Release 84 (2002) 1 – 13.

12. F. Zheng, Diffusional release of a dispersed solute from planar and spherical matrices into finite external volume–summary of critique by Feng Zheng, J. Control. Release 55 (1998) 99.

13. J. Siepmann, A. Streubel, N.A. Peppas, Understanding and predicting drug delivery from hydrophilic matrix tablets using the ‘‘sequential layer’’ model, Pharm. Res. 3 (2002) 306– 314.

14. J.W. Ayres, F.T. Lindstrom, Diffusion model for drug release from suspensions: I. Theoretical considerations, J. Pharm. Sci. 66 (1977) 654–662.

15. S.K. Chandrasekaran, D.R. Paul, Dissolution-controlled transport from dispersed matrixes, J. Pharm. Sci. 71 (1982) 1399–1402.

16. K. Kubota, E.H. Twizell, H.I. Maibach, Drug-release from a suspension with a finite dissolution rate—theory and its application to a betamethasone 17-valerate patch, J. Pharm. Sci. 83 (1994) 1593–1599.

17. G. Frenning, M. Strømme, Drug release modeled by dissolution, diffusion, and immobilization, Int. J. Pharm. 250 (2003) 137– 145.

18. G. Frenning, Ulrika Brohede, Maria Strømme, Finite element analysis of the release of slowly dissolving drugs from cylindrical matrix systems, Journal of controlled Release 107 (2005) 320 – 329

19. F.T. Lindstrom, J.W. Ayres, Diffusion model for drug release from suspensions: II. Release to a perfect sink, J. Pharm. Sci. 66 (1977) 662–668.

20. A. Krogh, The number and distribution of capillaries in muscles with calculations of the oxygen pressure head necessary for supplying the tissue. J. *Physiol*. 52, 409-415 (1919).

21. A. Krogh, *The Anatomy and Physiology of Capillaries*,New York, NY, Hafner,1959.

22. A. Hill, The diffusion of oxygen and lactic acid through tissues, *Proc. Roy. Sot. Ser. B* 104, 39-96 (1928).

23. John E. Fletcher, A model describing the unsteady transport of substrate to tissue from the microcirculation, SIAM J, Appl Math, Vol 29, No. 3, November 1975

24. W. Kuschinsky, O.B. Paulson, Capillary circulation in the brain, Cerebrovasc. Brain Metabol. Rev. 4 (1992)261–286.

25. R.J. Seitz, P.E. Roland, Vibratory stimulation increases and decreases the regional cerebral blood flow and oxidative metabolism: a positron emission tomography (PET) study, Acta Neurol. Scand. 86 (1992) 60-67.

26. S. Ogawa, R.S. Menon, D.W. Tank, S.-G. Kim, H. Merkle, J.M. Ellerman, K. Ugurbil, Functional brain mapping by blood oxygenation level-dependent contrast

magnetic resonance imaging: a comparison of signal characteristics with a biophysical model, Biophys. J. 64 (1993) 803-812.

27. R.B. Buxton, L.R. Frank, A model for the coupling between cerebral blood flow and oxygen metabolism during neural stimulation, J. Cereb. Blood Flow Metab. 13 (1997) 64-72.

28. D.W. Lubbers, H. Baumgartl, W. Zimelka, Heterogeneity and stability of local *p*O2 distribution within the brain tissue, Adv. Exp. Med. Biol. 345 (1994) 567–574.

29. Mark A. Mintun, Brian N. Lundstrom, Abraham Z. Snyder, Andrei G. Vlassenko, Gordon L. Shulman, and Marcus E. Raichle, Blood flow and oxygen delivery to human brain during functional activity: Theoretical modeling and experimental data, PNAS, June 5, vol. 98, No. 12, 6859-6864, 2001.

30. B. Zweifach, Functional Behavior of the Microcirculation, Charles C. Thomas, Springfield, I11, 1961.

31. A.G. Hudetz, J.H. Halsey Jr., C.R. Horton, K.A. Conger, D.D. Reneau, Mathematical simulation of cerebral blood flow in focal ischemia, Stroke 13 (1982) 693–700.

32. D.D. Reneau, D.F. Bruley, M.H. Knisely, A computer simulation for prediction of oxygen limitations in cerebral gray matter, J. Assoc. Adv. Med. Instrum. 4 (1970) 211–223.

33. William H.Press, Brain P.Flannery, Saul A. Teukolsky, William T. Vetterling, Numerical recipes in fortran : the art of scientific computing", Second edition, Cambridge University Press, 1992.

34. Price, H.S., R.S. Varga, and J . E . Warren, "Application of Oscillation Matrices to Diffusion-Connection Equations", J. Math and Physics, 45, 301-311 (1966).

35. Crank, J.; Nicolson, P. (1947). "A practical method for numerical evaluation of solutions of partial differential equations of the heat conduction type". *Proc. Camb. Phil. Soc.* 43 (1): 50–67.

36. Von Rosenberg, D.U., Methods for the Numerical Solution of Partial Differential Equations, American Elsevier, New York (1975).

37. Conte, S.D. and C. deBoor, Elementary Numerical Analysis, McGraw-Hill, New York, 1972.

38. Bird, R.B., W.E. Stewart, and E.N. Lightfoot. Transport Phenomena. John Wiley & Sons, New York, 1960.

39. Ashim K. Datta, Biological and Bioenvironmental Heat and Mass Transfer, ISBN: 0-8247-0775-3

40. Guyton, A. C. & Hall, J. E. (1996) *Textbook of Medical Physiology* (Saunders, Philadelphia), 9th Ed., pp. 513–523.

41. Shimojyo, S., Scheinberg, P., Kogure, K. & Reinmuth, O. M. (1968), *Neurology* 18,127–133.

42. Popel, A. S. and Johnson, P. C., "Microcirculation and Hemorheology," *Annu. Rev. Fluid Mech.*, vol. 37, pp. 43-69, 2005.

43. Aroesty, J. and Gross, J.F., "Convection and Diffusion in the Microcirculation," *Microvascular Research*, vol. 2, pp. 247-267, 1997.

44. Hudetz, A. G., Greene, A. S., Fehér, G., Knuese, D. E. and Cowley, Jr., A. W., "Imaging System for Three-Dimensional Mapping of Cerebrocortical Capillary Networks *in Vivo*," *Microvascular Research*, vol. 46, pp. 293-309, 1993.

45. Hudetz, A. G., Fehér, G. and Kampine, J. P., "Heterogeneous Autoregulation of Cerebrocortical Capillary Flow: Evidence for Functional Thoroughfare Channels" *Microvascular Research*, vol. 51, pp. 131-136, 1996.

46. Hudetz, A. G., "Blood Flow in the Cerebral Capillary Network: A Review Emphasizing Observations with Intravital Microscopy," *Microcirculation*, vol. 4, no. 2, pp. 233-252, 1997.

47. Malkusch, W., Konerding, M. A., Klapthor, B. and Bruch, J., "A Simple and Accurate Method for 3-D Measurements in Microcorrosion Casts Illustrated with Tumor Vascularization," *Analytical Cellular Pathology*, vol. 9, no. 1, pp. 69-81, 1995.

48. Motti, E. D. F., Imhof, H. G. and Yasargil, M. G., "The Terminal Vascular Bed in the Superficial Cortex of the Rat: An SEM Study of Corrosion Casts," *Journal of Neurosurgery*, vol. 65, no. 6, pp. 834-846, 1986.

49. Prothero, J. and Burton, A. C., "The Physics of Blood Flow in Capillaries: I. The Nature of the Motion," *Biophysical Journal*, vol. 1, pp. 565-579, 1961.

50. Chen, J. and Lu, X.-Y., "Numerical Investigation of the Non-Newtonian Blood Flow in a Bifurcation Model with a Non-planar Branch," *Journal of Biomechanics*, vol. 37, pp. 1899-1911, 2004.

51. Berry, J. L., Santamarina, A., Moore Jr., J. E., Roychowdhury, S. and Routh, W. D., "Experimental and Computational Flow Evaluation of Coronary Stents," *Annals of Biomedical Engineering*, vol. 28, pp. 386-398, 2000.

52. Dzwinel, W., Boryczko, K. and Yuen, D. A., "A Discrete-particle Model of Blood Dynamics in Capillary Vessels," *Journal of Colloid and Interface Science*, vol. 258, pp. 163-173, 2003.

53. Pries, A. R., Secomb, T. W., Gaehtgens, P. and Gross, J. F., "Blood Flow in Microvascular Networks: Experiments and Simulation," *Circulation Research*, vol. 67, pp. 826-834, 1990.

54. Shahcheraghi, N., Dwyer, H.A., Cheer, A.Y., Barakat, A.I. and Rutaganira, T., "Unsteady and Three-Dimensional Simulation of Blood Flow in the Human Aortic Arch", *Journal of Biomechanical Engineering*, 124 (4), pp. 378-387, 2002.

55. Lee, J.C.J., Pullan, A.J. and Smith, N.P., "A Computational Model of Microcirculatory Network Structure and Transient Coronary Microcirculation", Proceedings of the 26th Annual IEEE EMBS Conference, September, 2004.

56. Eggleton, C.D., Roy, T.K. and Popel, A.S., "Predictions of Capillary Oxygen Transport in the Presence of Fluorocarbon Additives", Am. J. Physiol (Heart Circ. Physiol.), 275, 44, H2250-2257, 1998.

57. Wang T. and Hicks, J.W., "An Integrative Model to Predict Maximum O_2 Uptake in Animals with Central Vascular Shunts", *Zoology*, 105, 45-53, 2002.

58. Sinek, J., Frieboes, H., Zheng, X. and Cristini, V., "Two-Dimensional Chemotherapy Simulations Demonstrate Fundamental Transport and Tumor Response Limitations Involving Nanoparticles", *Biomedical Microdevices*, 6:4, 297-309, 2004.

59. Goldman, D., "Computational modeling of drug delivery by microvascular networks", Proceedings of the 29th Annual IEEE Bioengineering Conference, 321- 322, March, 2003.

60. Stephanou, A., McDougall, S.R., Anderson, A.R.A., Chaplain, M.A.J. and Sherratt, J.A., "Mathematical modeling of flow on 2D and 3D vascular networks: Applications to anti-angiogenic and chemotherapeutic drug strategies", *Mathematical and Computer Modeling*, 41, pp. 1137–1156, 2005.

61. Pindera, M.Z., Ding, H., Athavale, M.A. and Chen, Z., "Accuracy of 1D Microvascular Flow Models in the Limit of Low Reynolds Numbers", *Microvascular Research*, 77, 273-280, 2009.

62. Goldman D. and Popel, A., "A Computational Study of the Effect of Capillary Network Anastomoses and Tortuosity on Oxygen Transport", *J. Theor. Biol*., 206, 181-194, 2000.

63. Federspiel, W. J. and Popel, A. S., "A Theoretical Analysis of the Effect of the Particulate Nature of Blood on Oxygen Release in Capillaries", *Microvascular Research*, vol. 32, pp. 164-189, 1986.

64. Vadapalli, A., Goldman, D., and Popel, A. S., "Calculations of Oxygen Transport by Red Blood Cells and Hemoglobin Solutions in Capillaries," *Art Cells Blood Subs Immob Biotech*, vol. 30, no. 3, pp. 157-188, 2002.

65. Secomb, T. W., Hsu, R., Beamer, N. B. and Coull, B. M., "Theoretical Simulation of Oxygen Transport to Brain by Networks of Microvessels: Effects of Oxygen Supply and Demand on Tissue Hypoxia," *Microcirculation*, vol. 7, pp. 237-247, 2000.

66. Pries, A. R., Reglin, B. and Secomb, T. W., "Structural Adaptation of Vascular Networks: Role of the Pressure Response," *Hypertension*, vol. 38, pp. 1476-1479, 2001.

67. Secomb, T. W., Hsu, R., Park, E. Y. H. and Dewhirst, M. W., "Green's Function Methods for Analysis of Oxygen Delivery to Tissue by Microvascular Networks," *Annals of Biomedical Engineering*, vol. 32, no. 11, pp. 1519-1529, 2004.

68. G. K. Batchelor. An Introduction to Fluid Dynamics. Cambridge Univ. Press, Cambridge, England, 1967.

69. Diran Basmadjian, Mass Transfer, ISBN 0-8493-2239-1, 2004

70. T. W. Secomb. (2007, Jan.). Microvascular networks: 3D Structural Information. University of Arizona, Home Page of Timothy W. Secomb, Ph.D. [Online]. Available: http://www.physiology.arizona.edu/people/secomb/network.html

71. A. S. Popel, and P. C. Johnson, "Microcirculation and Hemorheology," *Annu. Rev. Fluid Mech.*, vol. 37, pp. 43-69, 2005.

72. FLUENT User's Guide. Lebanon, NH: FLUENT, Inc. 2004.

73. Bird, Stewart, and Lightfoot, Laminar boundary layer theory, 1960

74. Ronald L. Fournier, Basic Transport Phenomena in Biomedical Engineering, ISBN 1-56032-708-1, 1999.

75. Gijsen, F. J. H, van de Vosse, F. N. and Janssen, J.D., "The Influence of the Non-Newtonian Properties of Blood on the Flow in Large Arteries: Steady Flow in a Carotid Bifurcation Model," *Journal of Biomechanics*, vol. 32, pp. 601-608, 1999.

76. Chen, Q., Schlichtherle, M. and Wahlgren, M., "Molecular Aspects of Severe Malaria," *Clinical Microbiology Reviews*, vol. 13, no. 3, pp. 439-450, 2000.

77. Shibeshi, S. S. and Collins, W. E., "The Rheology of Blood Flow in a Branched Arterial System," *Appl Rheol.*, vol. 15, no. 6, pp. 398-405, 2005.

78. Hsu, C.-H., Vu, H.-H. and Kang, Y.-H. (2009), "The rheology of blood flow in a branched arterial system with three-dimensional model: a numerical study", *Journal of Mechanics*, Vol. 25, No. 4, pp. 21-25, 2009.

79. Gibson, Q. H., Kreuzer, F., Meda, E. and Roughton, F. J. W., "The Kinetics of Human Hemoglobin in Solution and in the Red Cell at 37 °C," *J. Physiol. (Lond.)*, vol. 129, pp. 65-85, 1995.

80. Clark Jr., A., Federspiel, W .J., Clark, P. A. A. and Cokelet, G. R., "Oxygen Delivery from Red Cells," *Biophysical Journal*, vol. 47, pp. 171-181, 1985.

81. Goldsmith, H.L., Cokelet, G.R., and Gaehtgens, P. (1989), "Robin Fahraeus: Evolution of His Concepts in Cardiovascular Physiology," *Am. J. Physiol. Heart Circ. Physiol.*, vol. 257, no. 3, pp. H1005-H1015 ,1989.

82. Ellsworth, M. L., Ellis, C.G., Goldman, D., Stephenson, A. H., Dietrich, H.H. and Sprague, R. S., "Erythrocytes: Oxygen Sensors and Modulators of Vascular Tone", *Physiology* 24: 107-116, 2009.

83. Curran, E. and Murphy, S., "Scramjet Propulsion: Progress in Astronautics and Aeronautics", volume 189, pp. 757–820. A. Inst. of Aeronautics and Astronautics Inc., Virginia, 2000.

84. Hitch, B. "The Effect of Autoignition-Promoting Additives on Deflagration-to-Detonation", AIAA 3719, 2002.

85. Li, S., Varatharajan, B., and Williams, F. "Chemistry of JP-10 Ignition". AIAA,volume 39, no. 12, pp. 2351–2356, 2001.

86. Davidson, D., Horning, D., Oehlschlaeger, M., and Hanson, R. "The Decomposition Products of JP-10". AIAA 3707, 2001.

87. Bussing, T. and Pappas, G. “An Introduction to Pulse Detonation Engines”. AIAA 0263, 1994.

88. Williams, F., Hanson, R., and Segal, C. “Fundamental Investigations of Pulse-Detonation Phenomena”. In “JANNAF”, pp. 151–161. CPIA Publications, 1999.

89. Green, R., Nakra, S., and Anderson, S. “Breakdown Behaviour of Fuels for Pulse Detonation Engines”. Chem. Dep., U. of Utah N00014-01-0-541, 2001. Work Performed under ONR contract.

90. Shamit Nakra, Richard J. Green, Scott L. Anderson, “Thermal decomposition of JP-10 studied by micro-flow tube pyrolysis-mass spectrometry”, *Combustion and Flame*, 144 (2006) 662–674

91. Dean, A., “Recent Developments in Approaches to Pulse Detonation Propulsion”, AIAA 2003-4510, 2003.

92. Povinelli, L. and Yungster, S., “Real Gas Effects on the Performance of Hydrocarbon-Fueled Pulse Detonation Engines”, pp. 387–394, AIAA 2003-0712.

93. Gates, B., Katzer, J., and Schuit, G. Chemistry of Catalytic Processes. McGraw-Hill Book Company, New York, USA, 2nd edition, 1979.

94. D. F. Davidson, D. C. Horning, J. T. Herbon, and R. K. Hanson, “Shock Tube Measurements of JP-10 Ignition”, Proceeding of the Combustion Institute, Vol. 28, 2000/pp.1687-1692.

95. A. Laskin, H. Wang, and C. K. Law, “Detailed kinetic modeling of 1,3-butadiene oxidation at high temperatures”, Int. J. Chem. Kinet., in press.

96. F. A. Williams, R. K. Hanson and C. Segal, “Fundamental Investigations of Pulse Detonation Phenomena”, Proceedings of JANNAF CF/APS/PSJS Joint Meeting, Coco Beach, October 1999.

97. Olivier Herbinet, Baptiste Sirjean, Roda Bounaceur, Rene´ Fournet, Fre´de´rique Battin-Leclerc, Ge´rard Scacchi, and Paul-Marie Marquaire, “Primary Mechanism of the Thermal Decomposition of Tricyclodecane”, *J. Phys. Chem. A* 2006, *110*,11298-11314

98. W. Tsang, “Thermal Decomposition of Cyclopentane and Related Compounds”, Int. J. Chem. Kinet. 10, 599-617 (1978).

99. S. W. Benson and H. E. O.Neal, .Kinetic Data on Gas Phase Unimolecular Reactions,. NSRDA-NBS 21, February 1970.

100. A. Burcat and M. Dvinyaninov, .Detailed Kinetics of Cyclopentadiene Decomposition Studied in a Shock Tube,. Int. J. Chem. Kinet. 29, 505-515 (1997).

101. G. Bikas and N. Peters, Kinetic Modelling of *n*-Decane Combustion and Autoignition, *COMBUSTION AND FLAME* 126:1456–1475 (2001)

102. G. Blanquart, P. Pepiot-Desjardins, H. Pitsch, Chemical mechanism for high temperature combustion of engine relevant fuels with emphasis on soot precursors, Combustion and Flame 156 (2009) 588–607

103. Henning Richter and Jack B., Howard, Formation and consumption of single-ring aromatic hydrocarbons and their precursors in premixed acetylene, ethylene and benzene flames, Phys. Chem. Chem. Phys., 2002, 4, 2038–2055

104. Alexander Laskin, Hai Wang, Chung K. Law, Detailed Kinetic Modeling of 1,3-Butadiene Oxidation at High Temperatures, Int J Chem Kinet 32: 589–614, 2000

105. Seiser, H., Pitsch, H., Seshadri, K., Pitz, W.J., and Curran, H. J., "Extinction and Autoignition of n-Heptane in Counterflow Configuration",Proceedings of the Combustion Institute, Volume 28, p. 2029-2037, 2000

106. Hidaka, Y.; Higashihara, T.; Ninomiya, N.; Masaoka, H.; Nakamura, T.; Kawano, H., Shock tube and modeling study of 1,3-butadiene pyrolysis, Int J Chem Kinet 1996, 28, 137.

107. Skinner, G. B.; Sokoloski, E. M., Shock-tube experiments on the pyrolysis of ethylene, J Phys Chem 1960, 64, 1028.

108. Kiefer, J. H.; Wei, H. C.; Kern, R. D.; Wu, C. H., The high temperature pyrolysis of 1,3-butadiene: heat of formation and rate of dissociation of vinyl radical, Int J Chem Kinet 1985, 17, 225.

109. Rao, V. S.; Takeda, K.; Skinner, G. B., Shock tube studies of gas phase reactions preceding the soot formation process, Int J Chem Kinet 1988, 20, 153.

110. Kiefer, J. H.; Mitchell, K. I.; Wei, H. C., Thermal isomerization and decomposition of 2-butyne in shock waves, Int J Chem Kinet 1988, 20, 787.

111. Benson, S. W.; Haugen, G. R., Metal Catalysis in Aliphatic Isocyanate-Alcohol Reactions, J Phys Chem 1967, 71, 1735.

112. Colket, M. B.Eastern States Section Fall Meeting; The Combustion Institute: Providence, RI, 1983.

113. Liu, A.; Mulac, W. A.; Jonah, C. D., Rate constants for the gas-phase reactions of hydroxyl radicals with 1,3-butadiene and allene at 1 atm in argon and over the temperature range 305-1173 K, J Phys Chem 1988, 92, 131.

114. Gregory P. Smith, David M. Golden, Michael Frenklach, Nigel W. Moriarty, Boris Eiteneer, Mikhail Goldenberg, C. Thomas Bowman, Ronald K. Hanson, Soonho Song, William C. Gardiner, Jr., Vitali V. Lissianski, and Zhiwei Qin http://www.me.berkeley.edu/gri_mech/

115. UCSD, The san diego mechanism, version 20051201, jp-10 chemistry version 20021001, 2010, URL http://maeweb.ucsd.edu/combustion.

116. Oran, E., Boris, J.: Detailed Modeling of Combustion Systems, Prog. Energy Combustion Sci., 7, pp.1-72.

117. Altay, H. Murat, Kedia, Kushal S., Speth, Raymond L. and Ghoniem, Ahmed F.(2010) 'Two-dimensional simulations of steady perforated-plate stabilized premixed flames', Combustion Theory and Modelling, 14: 1, 125-154

118. Philippe Dagaut, Marcelline Reuillon, Jean-Claude Boettner and Michel Cathonnet, "Kerosene combustion at pressure up to 40atm : Experimental study and detailed chemical kinetic modeling", Twenty-Fifth Symposium (International) on Combustion/The Combustion Institute, 1994, pp. 919-926

119. Westbrook, C.K. and Dryer, F.L., "Chemical Kinetic Modeling of Hydrocarbon combustion," *Prog. Energy Combust. Sci*., vol. 10, no. 1, 1984, pp. 1-57.

120. Alexander Burcat and Branko Ruscic, "Third Millennium Ideal Gas and Condensed Phase Thermochemical Database for Combustion with updates from Active Thermochemical Tables", ANL-05/20 and TAE 960, Technion-IIT, Aerospace Engineering, and Argonne National Laboratory, Chemistry, Division, September 2005.

121. NASA polynomials are available in http://cea.grc.nasa.gov

122. Ianni, James C., "A Comparison of the Bader-Deuflhard and the Cash-Karp Runge-Kutta Integrators for the GRI-MECH 3.0 Model Based on the Chemical Kinetics Code Kintecus", pg.1368-1372, Computational Fluid and Solid Mechanics 2003, K.J. Bathe editor, Elsevier Science Ltd., Oxford, UK., 2003

123. Wolfer, H. H., "Der Zundverzug im Dieselmotor", V.D.I. Forschungsh, Vol. 392, pp.15-24, 1938

124. Mullins, B. P., “Spontaneous Ignition of Liquid Fuels”, AGARDograph 4, 1955.

125. Spadaccini, L. J., and Te Velde, J. A., “Autoignition Characteristics of Aircraft-Type Fuels”, NASA CR 159886, 1980.

126. Goodger, E. M., and Eissa, A. F. M., “Spontaneous Ignition Research; Review of Experimental Data”, *Journal of the Institute of Energy,* Vol. 84, pp.84-89, 1987.

127. Lundberg, K., Ulstein Turbine Technical Report UTU94003, 1994.

128. Freeman, G., and Lefebvre, A. H., “Spontaneous Ignition Characteristics of Gaseous Hydrocarbon-Air Mixtures”, *Combustion and Flame,* Vol. 58, No. 2, pp. 153-62, 1984.

129. Cowell, L. H., and Lefebvre, A. H., “Influence of Pressure on Autoignition Characteristics of Gaseous Hydrocarbon-Air Mixtures”, SAE Paper 860068, 1986.

130. Lefebvre,A. H., Freeman, W., and Cowell, L., “Spontaneous Ignition Delay Characteristics of Hydrocarbon Fuel/Air Mixtures”, NASA CR-175064, 1986.

131. Ducourneau, F, “Inflammation Spontanee de Melanges Riches Air-Kerosine”, *Entropie,* Vol. 10, No. 59, pp.11-18, 1974

132. Tacina, R. R., “Autoignition in a Premixing-Prevaporizing Fuel Duct Using Three Different Fuel Injection System at Inlet Air Temperature to 1250K”, NASA TM-83938, 1983

133. R. G. Gilbert, K. Luther, and J. Troe., “Theory of thermal unimolecular reactions in the fall-off range. ii. weak collision rate constants”, Ber. Bunsenges. Phys. Chem., 87:169 -177, 1983.

134. Gautier, O.; Carr JR., R. W.; Seigneur, C., Variational sensitivity analysis of a photochemical smog mechanism Int. J. Chem. Kin., 17, pp1347-1364. , 1985

135. Vajda, S.; Valko, P.; Turanyi, T, Principal component analysis of kinetic models, International Journal of Chemical Kinetics, Int. J. Chem. Kin., 17, pp55-81. , 1985

136. Anderberg, Michael R., *Cluster Analysis for Application*s, Academic Press, New York, 1973

137. Hartigan, John A., *Clustering Algorithm*s, John Wiley & Sons, New York, 1975

APPENDIX A

TISSUE EQUATION

The fundamental differential equation of diffusion in an isotropic medium was derived from Fick's law [1]. Since velocities are unchanging with time and unchanging along the capillary, the momentum conservation principle reduces to a simple force balance. Accordingly, a force balance is made on an elemental fluid element, Δz long, located between radii r and $r + \Delta r$, as shown in Figure 2.2.

Also, the net amount of material transferred into the element by radial and axial diffusion and the net increase or decrease due to chemical reaction acting on the element are in balance, and their sum equals zero:

$$2\pi r\Delta r\Delta z\frac{\partial \phi_i^t}{\partial t} = 2\pi r\Delta r(J_i^z|z - J_i^z|z + \Delta z) + 2\pi\Delta z(rJ_i^r|r - rJ_i^r|r + \Delta r) + 2\pi r\Delta r\Delta z S_i \quad \text{(A1.1)}$$

where $J_i^z = -D_i^t\frac{\partial \phi_i^t}{\partial z}$ and $J_i^r = -D_i^t\frac{\partial \phi_i^t}{\partial r}$

Dividing by $2\pi r\Delta r\Delta z$ and arranging,

$$\frac{\partial \phi_i^t}{\partial t} = \frac{(J_i^z|z - J_i^z|z + \Delta z)}{\Delta z} + \frac{1}{r}\frac{(rJ_i^r|r - rJ_i^r|r + \Delta r)}{\Delta r} + S_i$$

Letting $\Delta r, \Delta z \rightarrow 0$ then gives

$$\frac{\partial \phi_i^t}{\partial t} = -\frac{\partial J_i^z}{\partial z} - \frac{1}{r}\frac{\partial}{\partial r}(rJ_i^r) + S_i \quad \text{(A2.2)}$$

Substituting $J_i^z = -D_i^t\frac{\partial \phi_i^t}{\partial z}$ and $J_i^r = -D_i^t\frac{\partial \phi_i^t}{\partial r}$ into above equation (A2.2) and rearranging to get

$$\frac{\partial \phi_i^t}{\partial t} = D_i^t\left(\frac{\partial^2 \phi_i^t}{\partial r^2} + \frac{1}{r}\frac{\partial \phi_i^t}{\partial r} + \frac{\partial^2 \phi_i^t}{\partial z^2}\right) + S_i \quad \text{(A2.3)}$$

which is the general tissue equation for diffusion in cylinderical coordinates, and it is the local character of substrate diffusion in a two dimensional anisotropic medium and being consumed at a rate of S_i which may depend on the local concentration.

From numerical stability consideratrions, unconditionally stable implicit finite difference methods are the obvious choice. Implicit finite difference methods yield systems of coupled finite difference equations, which must be

solved simultaneously. For the space dimension, tridiagonal systems of equations result, which can be solved very efficiently by the Thomas algorithm. However, for more than one space dimension, as in the present case, banded systems of equations result, which require a large amount of effort to solve. Alternating-direction implicit (ADI) methods can be used to solve such problems more efficiently for the unsteady diffusion equation (A2.3)

The alternating-direction implicit (ADI) approcah consists of soving the PDE of (A2.3) in two steps. In the first time step, the spatial derivatives in one direction, say *y*, are evaluated at the known time level *n* and the other spatial derivatives, say *x,* are evaluated at the unknown tiem level n+1. On the next time step, the process is reversed.

Now, we consider the two-dimensional diffusion equation, Eqn (A.2.3). For the first step, the semi-discrete finite approximation yields

$$\frac{\phi_{i,j}^{n+\frac{1}{2}}-\phi_{i,j}^{n}}{\Delta t}=D_i\left[\frac{\phi_{i+1,j}^{n+\frac{1}{2}}-2\phi_{i,j}^{n+\frac{1}{2}}+\phi_{i-1,j}^{n+\frac{1}{2}}}{(\Delta r)^2}+\frac{1}{r}\frac{\phi_{i+1,j}^{n+\frac{1}{2}}-\phi_{i-1,j}^{n+\frac{1}{2}}}{2\Delta r}+\frac{\phi_{i,j+1}^{n}-2\phi_{i,j}^{n}+\phi_{i,j-1}^{n}}{(\Delta z)^2}\right]+S_i \quad \text{(A2.4)}$$

$$\frac{\phi_{i,j}^{n+1}-\phi_{i,j}^{n+\frac{1}{2}}}{\Delta t}=D_i\left[\frac{\phi_{i+1,j}^{n+\frac{1}{2}}-2\phi_{i,j}^{n+\frac{1}{2}}+\phi_{i-1,j}^{n+\frac{1}{2}}}{(\Delta r)^2}+\frac{1}{r}\frac{\phi_{i+1,j}^{n+\frac{1}{2}}-\phi_{i-1,j}^{n+\frac{1}{2}}}{2\Delta r}+\frac{\phi_{i,j+1}^{n+1}-2\phi_{i,j}^{n+1}+\phi_{i,j-1}^{n+1}}{(\Delta z)^2}\right]+S_i \quad \text{(A.2.5)}$$

Replacing the exact spatial derivatives in the partial differential equation (A2.3) by the three-point second-order central difference approximations at grid point (i, j) repectively, yield a tridiagonal system of PDEs, (A2.6 and A2.7), which can be solved by the general thomas algorithm. Equation (A2.4 and A2.5)

is a second-order centered-difference representation of equation (A.2.3), , which can be solved as following process.

For j=2,....., n

$$\left(\frac{D_i\Delta t}{2r\Delta r}-\frac{D_i\Delta t}{(\Delta r)^2}\right)\phi_{i-1,j}^{n+\frac{1}{2}}+\left(1+\frac{2D_i\Delta t}{(\Delta \mathrm{r})^2}\right)\phi_{i,j}^{n+\frac{1}{2}}-\left(\frac{D_i\Delta t}{(\Delta r)^2}+\frac{D_i\Delta t}{2r\Delta r}\right)\phi_{i+1,j}^{n+\frac{1}{2}}$$
$$=\frac{D_i\Delta t}{(\Delta z)^2}\phi_{i,j-1}^{n}+\left(1-\frac{2D_i\Delta t}{(\Delta \mathrm{z})^2}\right)\phi_{i,j}^{n}+\left(\frac{D_i\Delta t}{(\Delta z)^2}\right)\phi_{i,j+1}^{n}+S_i\Delta t \qquad \text{(A 2.6)}$$

With the BCs

$$\left(\frac{\partial\phi}{\partial r}\right)_{i+1,j}=0 \quad \text{at wall}$$

For i=2,.....n

$$-\frac{D_i\Delta t}{(\Delta \mathrm{z})^2}\phi_{i,j-1}^{n+1}+\left(1+\frac{2D_i\Delta t}{(\Delta \mathrm{z})^2}\right)\phi_{i,j}^{n+1}-\left(\frac{D_i\Delta t}{(\Delta \mathrm{z})^2}\right)\phi_{i,j+1}^{n+1}$$
$$=\left(\frac{D_i\Delta t}{(\Delta \mathrm{r})^2}-\frac{D_i\Delta t}{2r\Delta r}\right)\phi_{i-1,j}^{n+\frac{1}{2}}+\left(1-\frac{2D_i\Delta t}{(\Delta \mathrm{r})^2}\right)\phi_{i,j}^{n+\frac{1}{2}}+\left(\frac{D_i\Delta t}{(\Delta \mathrm{r})^2}+\frac{D_i\Delta t}{2r\Delta r}\right)\phi_{i+1,j}^{n+\frac{1}{2}}+S_i\Delta t \text{ (A.2.7)}$$

With the BCs

$$\left(\frac{\partial\phi}{\partial z}\right)_{i,j+1}=0 \quad \text{at wall}$$

When applied at every point in a finite difference grid, Eqn (A.2.6) yields a tridiagonal system of equations along each row of grid points (i.e., along lines of constant *j*), and Eqn(A2.7) yields a tridiagonal system of equations along each column of grid points (i.e., along lines of constant *i*). These tridiagonal systems of equations can be solved by the general thomas algorithm.

APPENDIX B

DRUG TRANSPORT EQUATION IN CAPILLARY

The capillary equation for drug includes axial diffusion as well as axial convection and radial flux at the capillary wall. The mass balance takes the form:

$$v\pi R_1^2(\phi|z-\phi|z+\Delta z)+\pi R_1^2(J^z|z-J^z|z+\Delta z)-2\pi R_1\Delta z J^r|R_1=\pi R_1^2\Delta z\frac{\partial\phi}{\partial t} \quad \text{(B2.1)}$$

Again the limit is taken on each term after division by $\pi R_1^2\Delta z$. Rearranging terms and noting $J^z=-D\frac{\partial\phi}{\partial z}$ the resulting equation is

$$\frac{\partial\phi}{\partial t}+v\frac{\partial\phi}{\partial z}+\frac{2J^r|_{R1}}{R1} = D\frac{\partial^2\phi}{\partial z^2} \quad \text{(B2.2)}$$

The Price, Varga, Warren (PVW) [34] finite difference analogs were used in approximating the equation (B2.2). The base point for the finite difference approximations of the individual exact partial derivatives is grid point (i, n + 1/2). These analogs have been used in applying for the first and second order terms which arise in the convection-diffusion problem to their own state variable formulation. The resulting finite difference approximation is

$$\frac{\phi_i^{n+1}-\phi_i^n}{\Delta t}+\frac{\nu}{2}\left\{\frac{3\phi_i^{n+1}-4\phi_{i-1}^{n+1}+\phi_{i-2}^{n+1}}{2\Delta z}+\frac{3\phi_i^n+4\phi_{i-1}^n+\phi_{i-2}^n}{2\Delta z}\right\}+f$$
$$=\frac{D}{2}\left\{\frac{\phi_{i+1}^{n+1}-2\phi_i^{n+1}+\phi_{i-1}^{n+1}}{2\Delta z}+\frac{\phi_{i+1}^n-2\phi_i^n+\phi_{i-1}^n}{2\Delta z}\right\} \quad \text{(B.2.3)}$$

where $f = S_1\left(\frac{R_1^2-R^{*2}}{R_1^2}\right)+S_2\left(\frac{R^{*2}-R_2^2}{R_1^2}\right)$

After rearranging the equation (B2.3), the equation for the band matrix system may be written as

$$\left(\frac{\nu\Delta t}{4\Delta z}\right)\phi_{i-2}^{n+1}-\left\{\left(\frac{\nu\Delta t}{\Delta z}\right)+\left(\frac{D\Delta t}{2(\Delta z)^2}\right)\right\}\phi_{i-1}^{n+1}+\left\{1+\left(\frac{3\nu\Delta t}{4\Delta z}\right)+\left(\frac{D\Delta t}{(\Delta z)^2}\right)\right\}\phi_i^{n+1}-\left(\frac{D\Delta t}{2(2\Delta z)^2}\right)\phi_{i+1}^{n+1}$$

$$=\left(-\frac{\nu\Delta t}{4\Delta z}\right)\phi_{i-2}^n+\left\{\left(\frac{\nu\Delta t}{\Delta z}\right)+\left(\frac{D\Delta t}{2(\Delta z)^2}\right)\right\}\phi_{i-1}^n+\left\{1-\left(\frac{3\nu\Delta t}{4\Delta z}\right)-\left(\frac{D\Delta t}{(\Delta z)^2}\right)\right\}\phi_i^n-$$
$$\left(\frac{D\Delta t}{2(2\Delta z)^2}\right)\phi_{i+1}^n-f\Delta t \quad \text{(B.2.4)}$$

Equation (B2.4) can be solved by using general band algorithm.

APPENDIX C

ANALYTICAL TISSUE EQUATION FOR DRUG

Assuming the consumption rates of each component is constant under aerobic conditions and a different constant under anaerobic conditions, the following equations can be used in determining the drug distributions in the cylindrical matrix system. The general governing equation for mass diffusion in cylindrical coordinate system is

$$D\left(\frac{1}{r}\frac{\partial}{\partial r}\left(r\frac{\partial\phi}{\partial r}\right)+\frac{1}{r^2}\left(\frac{\partial^2\phi}{\partial\theta^2}\right)+\frac{\partial^2\phi}{\partial z^2}\right)-S(r)=\frac{\partial\phi}{\partial t} \quad \text{(C3.1)}$$

steady state equation in radial direction becomes

$$D\frac{1}{r}\frac{d}{dr}\left(r\frac{d\phi}{dr}\right)-S(r)=0 \quad \text{(C3.2)}$$

where the consumption rate is a function of the radial position. Integrating between R_l and R_2 yields

$$\int_{\left(r\frac{dc}{dr}\right)|R_1}^{\left(r\frac{dc}{dr}\right)|R_2} d\left(r\frac{d\phi}{dr}\right)=\int_{R_1}^{R_2}\frac{S}{D}rdr \quad \text{(C3.3)}$$

yields

$$R_2\frac{d\phi}{dr}\Big|R_2-R_1\frac{d\phi}{dr}|R_1=\int_{R_1}^{R_2}\frac{S}{D}rdr \quad \text{(C3.4)}$$

Let $S(r) = s_1$ for $R_1 \le r \le R_*$

$= s_2$ for $R_* \le r \le R_2$

Where s_1 and s_2 are constants.

Since at $r = R_2$, $\frac{d\phi}{dr}|R_2 = 0$, equation (A3.12) can be written

$$-R_1\frac{d\phi}{dr}|R_1=\int_{R_1}^{R_*}\frac{s_1}{D}rdr+\int_{R_*}^{R_2}\frac{s_2}{D}rdr \quad \text{(C3.5)}$$

or

$$\frac{d\phi}{dr}\Big|R_1=\frac{s_1}{2D}\frac{\left(R_1^2-R_*^2\right)}{R_1}+\frac{s_2}{2D}\frac{\left(R_*^2-R_2^2\right)}{R_1} \quad \text{(C3.6)}$$

To calculate the drug distribution, the data of the oxygen front (R_*) is required. The mass flux term can be evaluated as

$$J_i^r|R_1 \text{ (capillary)} = -D_i^t\frac{d\phi}{dr}|R_1 \quad \text{(C3.7)}$$

or

$$J_i^r|R_1 \text{ (capillary)} = \frac{s_1}{2R_1}(R_*^2-R_1^2)+\frac{s_2}{2R_1}(R_2^2-R_*^2) \quad \text{(C3.8)}$$

To solve for the drug distributions, the following equations have been derived.

For $R_1 \leq r < R_*$

$$r\frac{d\phi}{dr} - R_1\frac{d\phi}{dr}|R_1 = \int_{R_1}^{r}\frac{s_1}{D}rdr \quad \text{(C3.9)}$$

and then integration and rearrangement yields

$$\phi = \phi\left|R_1 + \frac{s_1}{4D}(r^2 - R_1^2) + \left[R_1\frac{d\phi}{dr}|R_1 - \frac{s_1 R_1^2}{2D}\right]\ln\left(\frac{r}{R_1}\right) \quad \text{(C3.10)}$$

And for $R_* \leq r \leq R_2$

$$r\frac{d\phi}{dr} - R_1\frac{d\phi}{dr}|R_1 = \int_{R_1}^{R_*}\frac{s_1}{D}rdr + \int_{R_*}^{r}\frac{s_2}{D}rdr \quad \text{(C3.11)}$$

And integrating, it becomes

$$\phi = \phi|R_1 + \left[\frac{s_1}{2D}(R_*^2 - R_1^2) + R_1\frac{d\phi}{dr}|R_1\right]\ln\left(\frac{r}{R_1}\right) + \frac{s_2}{4D}(r^2 - R_1^2) \quad \text{(C3.12)}$$

APPENDIX D

ANALYTICAL TISSUE EQUATION FOR OXYGEN

The general governing equation for mass diffusion of oxygen in cylindrical coordinate system is

$$D\left(\frac{1}{r}\frac{\partial}{\partial r}\left(r\frac{\partial \phi}{\partial r}\right)+\frac{1}{r^2}\left(\frac{\partial^2 \phi}{\partial \theta^2}\right)+\frac{\partial^2 \phi}{\partial z^2}\right)+\frac{S_i}{W_i^t}=\frac{\partial \phi}{\partial t} \quad \text{(D4.1)}$$

Steady state equation in radial direction becomes

$$D_i^t\frac{1}{r}\frac{d}{dr}\left(r\frac{d\phi_i^t}{dr}\right)+\frac{S_i}{W_i^t}=0 \quad \text{(D4.2)}$$

where *D*: diffusivity, *S*: consumption rate, *W*: solubility.

The boundary conditions are

BC: $\frac{d\phi_i^t}{dr}=0$ at r=R_2

$\phi_i^t=\phi_i^c$ at r=R_1

Integrating Eq (D4.2) with respect to the radial direction coordinate (r) and applying BC becomes

$$\frac{d\phi_i^t}{dr}=\frac{S_i}{2D_i^tW_i^t}\left(\frac{R_2^2}{r}-r\right) \quad \text{(D4.3)}$$

Integrating again, applying BC at r=R1 to get

$$\phi_i^t=\phi_i^c+\frac{S_iR_2^2}{2D_i^tW_i^t}\ln\left(\frac{r}{R_1}\right)+\frac{S_iR_1^2}{4D_i^tW_i^t}\left(1-\frac{R_2^2}{r}\right) \quad \text{(D4.4)}$$

APPENDIX E

FORTRAN CODE

```
      PROGRAM RADFLX
      DIMENSION PHIOLD(60,2),FLX(4,40),PHI(40,60,2),PHINEW(40,60,2)
      DIMENSION R(40,60),YR(40,60),RR(40,60),XZ(40,60),XYZ(40,60)
      DIMENSION YYR(40,60),XXYZ(40,60),RS(40,2)
      DIMENSION PHIDXG(60,2),DXG(40,60,2),DCDR(40,2),DXGDIF(40,60,2)
      DIMENSION DSS1(2),DSS2(2),XSF(3),XNCDXG(60,2),BR(40)
      REAL XHEMAT,SOLPL,SF,PHIDIF,PHISOL,PHISS,DFC,CMAX
       OPEN(3,FILE='pdatin.dat')
      OPEN(4,FILE='cdatin.dat')
      OPEN(5,FILE='inputdat.dat')
      OPEN(6,FILE='flx.dat')
      OPEN(7,FILE='rs.dat')
      OPEN(8,FILE='xcdxg.dat')
      OPEN(9,FILE='x_poc_r.dat')
      OPEN(10,FILE='x_dxg_r.dat')
      READ(5,*) XL,R1,R2,NTOTAL,NP1,NINCR,NCOMP,ICASE,NCASES
      READ(5,*) PHIDIF,PHISOL,PHISS,XHEMAT,SOLPL,SF
      READ(5,*) DFC,(DSS1(J),J=1,2),(DSS2(J),J=1,2),CMAX,(XSF(J),J=1,3)
       DO 10 K=1,NCASES
      READ(3,*) (PHIOLD(J,K),J=1,NTOTAL)
      READ(4,*) (PHIDXG(J,K),J=1,NTOTAL)
       DO 20 I=1,NP1
      IT=I+NINCR
      XLAM=1.0
      PHIX=PHIOLD(IT,K)*XLAM
      DR=(R2-R1)/(NTOTAL-1)
      XXL=XL/(NP1-1)
      DO 30 J=1,NTOTAL
      XJ=J-1
      XI=I-1
       R(I,J)=DR*XJ+R1
      YR(I,J)=R(I,J)*SF
      YYR(I,J)=(R(I,J)-R1)/(R2-R1)
      XZ(I,J)=XXL*XI
      XYZ(I,J)=XZ(I,J)*SF
      XXYZ(I,J)=XZ(I,J)/XL
      PHI(I,J,K)=(PHISS/(2.*PHIDIF*PHISOL))*(R2**2*ALOG(R(I,J)/R1)+(R1*
     **2/2.)*(1.-R(I,J)**2/R1**2))
       PHINEW(I,J,K)=PHIX-PHI(I,J,K)
      IF(PHINEW(I,J,K).LE.0.001.OR.(R(I,J).EQ.R2)) GOTO 88
   30 CONTINUE
   88 RS(I,K)=R(I,J)
   20 CONTINUE
       WRITE(7,16) (RS(I,K),I=1,NP1)
   10 CONTINUE
      DO 70 K=1,NCASES
       DO 70 J=1,NTOTAL
      DO 70 I=1,NP1
      XJ=J-1
       R(I,J)=DR*XJ+R1
      NC=I+NINCR
      DR=(R2-R1)/(NTOTAL-1)
       RR(I,J)=DR*XJ+R1
      DCDR(I,K)=(DSS2(1)/(2*DFC))*((R1**2-RS(I,1)**2)/R1)+(DSS2(2)/
     *(2*DFC))*((RS(I,1)**2-R2**2)/R1)
```

```
      IF (R(I,J).GE.R1.AND.R(I,J).LT.RS(I,1).OR.(R(I,J).EQ.R2)) THEN
      DXGDIF(I,J,K)=(DSS2(1)/4*DFC)*(RR(I,J)**2-R1**2)+(R1*DCDR(I,K)
     *-(DSS2(1)*R1**2)/(2*DFC))*ALOG(RR(I,J)/R1)
      ELSEIF (R(I,J).GE.RS(I,1).AND.R(I,J).LT.R2) THEN
      DXGDIF(I,J,K)=((DSS2(1)/2*DFC)*(RS(I,1)**2-R1**2)+(R1*DCDR(I,K))
      *)*ALOG(RR(I,J)/R1)+(DSS2(2)/(4*DFC))*(RR(I,J)**2-R1**2)
      ENDIF
      DXG(I,J,K)=PHIDXG(NC,K)+DXGDIF(I,J,K)*XSF(3)
 70 CONTINUE
      DO 80 K=1,NCASES
       DO 80 J=1,NTOTAL
      DO 80 I=1,NP1
      IF (DXG(I,J,K).LT. 0.0) THEN
      DXG(I,J,K)=0.0
      ENDIF
 80 CONTINUE
      DFAC1=XSF(1)*DSS1(1)
      DFAC2=XSF(2)*DSS1(1)
      DO 60 JJ=ICASE,NCOMP
      DO 61 J=1,NP1
      BR(J)=(RS(J,1)*RS(J,1))/(R1*R1)
      IF(JJ.EQ.1) THEN
      FLX(JJ,J)=PHISS*(1.-BR(J))/(SOLPL*(1.-XHEMAT))
      ELSEIF(JJ.EQ.2) THEN
      FLX(JJ,J)=DFAC1*(1.-BR(J))+DFAC2*(BR(J)-R2*R2/(R1*R1))
      ENDIF
       DIF=ABS(FLX(JJ,J))
      IF(DIF.LE..1E-5) FLX(JJ,J)=0.0
 61 CONTINUE
 16 FORMAT(5E15.7)
 60 CONTINUE
      DO 180 JJ=ICASE,NCOMP
       WRITE(6,185) (FLX(JJ,J),J=1,NP1)
185 FORMAT(5E15.7)
180 CONTINUE
      DO 190 K=1,NCASES
      DO 191 I=1,NTOTAL
      XNCDXG(I,K) = PHIDXG(I,K)
191 CONTINUE
       WRITE(8,195) (XNCDXG(J,K),J=1,NTOTAL)
195 FORMAT(10F8.4)
190 CONTINUE
       DO 200 K=1,NCASES
       DO 200 I=1,NP1
        WRITE(9,205) (PHINEW(I,J,K),J=1,NTOTAL)
205 FORMAT(60(1X,F8.4))
200 CONTINUE
       DO 210 K=1,NCASES
       DO 210 I=1,NP1
        WRITE(10,215) (DXG(I,J,K),J=1,NTOTAL)
215 FORMAT(60(1X,F8.4))
210 CONTINUE
       STOP
       END
```

```
      PROGRAM FDMDXG
      DIMENSION AR(60,2),BR(60,2),CR(60,2),RHSR(60)
      DIMENSION AZ(60,2),BZ(60,2),CZ(60,2),RHSZ(60)
      DIMENSION XAR(2),DRAT1(2),DRAT2(2)
      DIMENSION PHIOLD(2,60,40),XTEST(2,60,40),PHINEW(2,60,40)
      DIMENSION CPD(2,60),TEST(6,60),XCTEST(2,60),XPLAS(60),FLX(2,40)
      DIMENSION ABAND(60,2),BBAND(60),CBAND(60,2),DBAND(60),SBAND(60)
      DIMENSION WORK(60,2),AL(60,2),BE2(60),GAM2(60)
      DIMENSION YOP(2,60,40),YDP(2,60,40),XX(40),YY(60),XY(60),XYZ(2,60,40)
      REAL DR,DZ
      COMMON/BLOCK1/DCDZ,VDC,R1,R2
      COMMON/BLOCK2/DIAG,VD,VD2,VD4,NTOTM1,DT,DZ,DR,VEL,NINCR
     *,NN,POIN
      COMMON/BLOCK3/DDXG1,NITER,N,IFR1,IFR2,XL,TMAX,TIMEIN,FAC,INDEX
      COMMON/BLOCK4/KIT,SF
      COMMON/BLOCK5/COEF1(2),COEF2(2),DIFTIS(2)
      COMMON/BLOCK6/XDMAX,DLAM
      OPEN(2,FILE='flx.dat')
      OPEN(3,FILE='pdatin.dat')
      OPEN(4,FILE='x_poc_r.dat')
      OPEN(5,FILE='inputdat.dat')
      OPEN(6,FILE='output1.dat')
      OPEN(7,FILE='output2.dat')
      OPEN(8,FILE='output3.dat')
      READ(5,*) (DIFTIS(I),I=1,2),DDXG1
      READ(5,*) NITER,NINCR,M,N,IFR1,IFR2,TFAC
      READ(5,*) VEL,POIN,CDXG,R1,R2,TIMEIN
      READ(5,*) XDMAX,DLAM,XL
      READ(5,*) (COEF1(I),I=1,2),(COEF2(I),I=1,2),EPGS1,EPGS2
      READ(5,*) TMAX,FAC,INDEX,SF
      XM=M
      DR=(R2-R1)/XM
      NP1=N+1
      XN=NP1
      DZ=XL/XN
      DT=TFAC*DZ/VEL
      NP2=N+2
      NM1=N-1
      NN=NINCR+NP1
      NINM1=NINCR-1
      NNM1=NN-1
      NNM2=NN-2
      NTOTAL=NN+NINCR
      NTOTM1=NTOTAL-1
      MCOL=7
      NROW=NTOTAL-1
      DO 100 JJ=1,2
      READ(2,*) (FLX(JJ,J),J=1,NP1)
  100 CONTINUE
      DO 110 JZ =1,2
      READ(3,*) (CPD(JZ,J),J=1,NTOTAL)
  110 CONTINUE
      DO 120 JJ=1,2
      DO 120 J=1,NP1
      READ(4,*) (PHIOLD(JJ,I,J),I=1,M)
```

```
120 CONTINUE
      CPD(2,1)=CDXG
      XCTEST(2,1)=CDXG
      TEST(2,1)=CDXG
      DO 932 J=1,NTOTAL
      XPLAS(J)=CPD(1,J)
     XCTEST(2,J)=CDXG
     TEST(2,J)=CPD(2,J)
932 CONTINUE
      DO 930 JJ=1,2
      DO 930 J=1,NP1
      DO 930 I=1,M
      XTEST(JJ,I,J)=PHIOLD(JJ,I,J)
930 CONTINUE
      DCDZ=DDXG1*(2.*DZ**2)
      VD=VEL/DZ
      VD2=VD/2.
      VD4=VD/4.
      VDC=VD+DCDZ
      DO 51 J=1,MCOL
      DO 51 I=1,NROW
      ABAND(I,J)=0.0
      CBAND(I,J)=0.0
 51 CONTINUE
     ISTD=0
     IPR1=0
     IPR2=0
      NIF=1
     DIAG=1./DT+3.*VEL/(4.*DZ)
999 CONTINUE
      IF(TIMEIN.GE.TMAX) GOTO 698
      IF(INDEX.EQ.1) DT=DT*FAC
      TIMEIN=TIMEIN+DT
      IPR1=IPR1+1
      IPR2=IPR2+1
      DO 39 KIT=1,NITER
      WRITE(6,42) TIMEIN,KIT,ISTD
 42 FORMAT(' ',2X,'TIME =',F8.4,' ITER =',I5,/,8X,'ISTD =',I5)
     IF(IPR1.NE.IFR1) GOTO 439
      DO 200 JJ=1,2
      WRITE(6,201)(XCTEST(JJ,J),J=1,NTOTAL)
201 FORMAT(1X,10F8.4)
200 CONTINUE
      DO 202 JJ=1,2
      DO 202 J=1,NP1
      WRITE(6,201)(XTEST(JJ,I,J),I=1,5)
202 CONTINUE
439 CONTINUE
898 CONTINUE
      CALL DFXG(NTOTAL,CPD,ABAND,BBAND,CBAND,DBAND,FLX)
      CALL BAND(NROW,MCOL,ABAND,BBAND,CBAND,DBAND,SBAND,WORK,
     *AL,BE2,GAM2)
      JX=1
      DO 969 J=2,NTOTAL
      XCTEST(2,J)=SBAND(JX)
```

```
      JX=JX+1
  969 CONTINUE
      CALL DXGADI(JJ,M,NP1,AR,BR,CR,RHSR,AZ,BZ,CZ,RHSZ,XAR,DRAT1
      *,DRAT2,ISTD,XPLAS,XCTEST,CPD,PHIOLD,PHINEW)
      DO 996 JJ=1,2
      DO 180 J=1,NTOTAL
      IF(ABS(XCTEST(2,J)-TEST(2,J))/XCTEST(2,J).GT.EPGS1) GOTO 181
  180 CONTINUE
       DO 996 J=1,NP1
       DO 996 I=1,M
       IF(ABS(PHINEW(JJ,I,J)-XTEST(JJ,I,J))/PHINEW(JJ,I,J).GT.EPGS2)
     *GOTO 181
  996 CONTINUE
       GOTO 182
  181 CONTINUE
      DO 962 JJ=1,2
      DO 183 J=1,NTOTAL
       TEST(2,J)=XCTEST(2,J)
  183 CONTINUE
       DO 962 J=1,NP1
      DO 962 I=1,M
      XTEST(JJ,I,J)=PHINEW(JJ,I,J)
  962 CONTINUE
   39 CONTINUE
  182 CONTINUE
      ISTD=1
      DO 96 J=1,NTOTAL
      IF(ABS(XCTEST(2,J)-CPD(2,J))/XCTEST(2,J).GT.EPGS1) GOTO 492
   96 CONTINUE
      DO 97 JJ=1,2
      DO 97 J=1,NP1
      DO 97 I=1,M
      IF(ABS(PHINEW(JJ,I,J)-PHIOLD(JJ,I,J))/PHINEW(JJ,I,J).GT.EPGS2)
     *GOTO 492
   97 CONTINUE
      WRITE(6,342) TIMEIN
  342 FORMAT(1H1,5(/),15X,'STEADY STATE REACHED',2X,F8.4)
      GOTO 698
  492 CONTINUE
      DO 684 J=1,NTOTAL
      CPD(2,J)=XCTEST(2,J)
  684 CONTINUE
      DO 810 JJ=1,2
      DO 810 J=1,NP1
      DO 810 I=1,M
      PHIOLD(JJ,I,J)=PHINEW(JJ,I,J)
  810 CONTINUE
      IF(IPR2.EQ.IFR2) GOTO 698
   66 CONTINUE
      IF(IPR1.EQ.IFR1) IPR1=0
      GOTO 999
  698 CONTINUE
      XYY=0.0
      DO 1150 J=1,NTOTAL
      XYY=XYY+DZ
```

```
      IF (J.EQ.1) THEN
      XY(1)=-0.25
      ELSE
      XY(J)=XYY/XL-0.25
      ENDIF
1150 CONTINUE
      XXYZ=0.0
      DDZ=XL/N
      XXD=1/(NP1-1)
      DO 1170 J=1,NP1
      IF(J.EQ.1) THEN
      XX(1)=0.0
      ELSE
      XXYZ=XXYZ+1
      XX(J)=XXYZ/N-XXD
      ENDIF
 1170 CONTINUE
      YYD=1/(M-1)
      DO 1180 I=1,M
      IF(I.EQ.1) THEN
      YY(1)=0.0
      ELSE
      YXYZ=YXYZ+1
      YY(I)=YXYZ/(M-1)-YYD
      ENDIF
1180 CONTINUE
      DO 1190 I=1,M
      DO 1190 J=1,NP1
      XYZ(1,I,J)=XX(J)
      XYZ(2,I,J)=YY(I)
1190 CONTINUE
      DO 1200 JZ=1,2
      DO 1201 J=1,NTOTAL
      IF (JZ.EQ.1) THEN
      CPD(1,J)=CPD(JZ,J)
      ELSEIF (JZ.EQ.2) THEN
      CPD(2,J)=CPD(JZ,J)
      ENDIF
 1201 CONTINUE
 1200 CONTINUE
      DO 1210 J=1, NTOTAL
      WRITE(7,1205) XY(J),CPD(1,J),CPD(2,J)
 1205 FORMAT (F8.4,2X,2(2X,F8.4))
 1210 CONTINUE
      DO 1110 JZ=1,2
      WRITE(8,1115) (CPD(JZ,J),J=1,NTOTAL)
1115 FORMAT(10F8.4)
1110 CONTINUE
      DO 1220 JZ=1,2
       DO 1220 J=1,NP1
       DO 1220 I=1,M
      JZK=JZ
      JX=J
      IY=I
      IF (JZ.EQ.1) THEN
```

```
      YOP(1,I,J)=PHIOLD(JZK,IY,JX)
      ELSEIF (JZ.EQ.2) THEN
      YDP(2,I,J)=PHIOLD(JZK,IY,JX)/CDXG
      ENDIF
 1220 CONTINUE
      OPEN(9,FILE='xyop.dat',STATUS='UNKNOWN')
      WRITE(9,1041) NP1,M
       DO 1300 I=1,M
      DO 1300 J=1,NP1
      WRITE(9,1040) XYZ(1,I,J),XYZ(2,I,J),YOP(1,I,J)
 1300 CONTINUE
      OPEN(10,FILE='xyDXG.dat',STATUS='UNKNOWN')
      WRITE(10,1042) NP1,M
       DO 1310 I=1,M
      DO 1310 J=1,NP1
      WRITE(10,1040) XYZ(1,I,J),XYZ(2,I,J),YDP(2,I,J)
 1310 CONTINUE
 1040 FORMAT(2(2X,F8.4),2X,F8.4)
 1041 FORMAT('TITLE="OXYGEN PRESSURE"',/,'VARIABLES=X,Y,P',/,
     * 'ZONE I=',I3,2X,'J=',I2,2X,'F=POINT',/)
 1042 FORMAT('TITLE="DXG CONCENTRATION"',/,'VARIABLES=X,Y,DXG',/,
     * 'ZONE I=',I3,2X,'J=',I2,2X,'F=POINT',/)
      IF(IPR2.EQ.IFR2) IPR2=0
       IF(IPR2.EQ.0) GOTO 66
      STOP
       END
      SUBROUTINE DXGADI(JJ,M,NP1,AR,BR,CR,RHSR,AZ,BZ,CZ,RHSZ,XAR,DRAT1
      *,DRAT2,ISTD,XPLAS,XCTEST,CPD,PHIOLD,PHINEW)
      DIMENSION XNEW(60)
      DIMENSION AR(60,2),BR(60,2),CR(60,2),RHSR(60)
       DIMENSION AZ(60,2),BZ(60,2),CZ(60,2),RHSZ(60)
       DIMENSION XAR(2),DRAT1(2),DRAT2(2),XZV(2)
       DIMENSION PHIAVG(3,60,40),TMET(2,60,40),PHIOLD(2,60,40),PHINEW(2
      *,60,40)
       DIMENSION CPD(2,60),XCTEST(2,60),XPLAS(60)
      COMMON/BLOCK1/DCDZ,VDC,R1,R2
       COMMON/BLOCK2/DIAG,VD,VD2,VD4,NTOTM1,DT,DZ,DR,VEL,NINCR
      *,NN,POIN
      COMMON/BLOCK3/DDXG1,NITER,N,IFR1,IFR2,XL,TMAX,TIMEIN,FAC
      *,INDEX
      COMMON/BLOCK4/KIT,SF
      COMMON/BLOCK5/COEF1(2),COEF2(2),DIFTIS(2)
      COMMON/BLOCK6/XDMAX,DLAM
      RAT1=DT/(DR*DR)
      RAT2=DT/(DZ*DZ)
      DO 340 JJ=1,2
      DRAT1(JJ)=DIFTIS(JJ)*RAT1
      DRAT2(JJ)=DIFTIS(JJ)*RAT2
      XZV(JJ)=-DRAT2(JJ)
 340 CONTINUE
       MM1=M-1
      DO 540 JJ=1,2
       YSUM=1.0
      DO 5 I=2,MM1
      YSUM=YSUM+1
```

```
      AR(I,JJ)=-DRAT1(JJ)*(1.-DR/(2.*(R1+YSUM*DR)))
    5 CONTINUE
      AR(M,JJ)=-2.*DRAT1(JJ)
      XAR(JJ)=-DRAT1(JJ)*(1.-DR/(2.*(R1+DR)))
      DO 4 I=1,M
      BR(I,JJ)=1.+2.*DRAT1(JJ)
    4 CONTINUE
      XSUM=0.0
      DO 6 I=1,MM1
      XSUM=XSUM+1
      CR(I,JJ)=-DRAT1(JJ)*(1.+DR/(2.*(R1+XSUM*DR)))
    6 CONTINUE
      DO 8 J=1,NP1
      AZ(J,JJ)=XZV(JJ)
      CZ(J,JJ)=XZV(JJ)
    8 CONTINUE
      DO 7 J=2,N
      BZ(J,JJ)=1.+2.*DRAT2(JJ)
    7 CONTINUE
      BZ(1,JJ)=1.0+DRAT2(JJ)
      BZ(NP1,JJ)=1.0+DRAT2(JJ)
  540 CONTINUE
      DO 807 J=1,NP1
      DO 807 I=1,M
      PHIOLD(JJ,I,J)=PHINEW(JJ,I,J)
  807 CONTINUE
      DO 2 JJ=1,2
      IF(ISTD.EQ.1.AND.(JJ.EQ.1)) GOTO 2
      IF(JJ.EQ.2.AND.(PHIOLD(1,M,NP1).GE.20.0)) GOTO 2
      DO 401 J=1,NP1
      NC=J+NINCR
      DO 10 I=1,M
      PHIAVG(JJ,I,J)=0.5*(PHINEW(JJ,I,J)+PHIOLD(JJ,I,J))
      IF(JJ.EQ.1) TMET(1,I,J)=-COEF1(1)*PHIAVG(1,I,J)/(COEF1(2)+PHIAVG(1
     *,I,J))
      IF(JJ.EQ.2) TMET(2,I,J)=-XDMAX*(1.0-PHIAVG(2,I,J)/(COEF2(1)
     *+PHIAVG(2,I,J)))
   22 CONTINUE
      IF(J.NE.1) GOTO 11
      RHSR(I)=DRAT2(JJ)*PHIOLD(JJ,I,2)+(1.-DRAT2(JJ))*PHIOLD(JJ,I,1)
     *+TMET(JJ,I,J)*DT
      GOTO 12
   11 IF(J.NE.NP1) GOTO 13
      RHSR(I)=DRAT2(JJ)*PHIOLD(JJ,I,N)+(1.-DRAT2(JJ))*PHIOLD(JJ,I,NP1)
     *+TMET(JJ,I,J)*DT
      GOTO 12
   13 JP1=J+1
      JM1=J-1
      RHSR(I)=DRAT2(JJ)*(PHIOLD(JJ,I,JM1)+PHIOLD(JJ,I,JP1))
     *+(1.-2.*DRAT2(JJ))*PHIOLD(JJ,I,J)+TMET(JJ,I,J)*DT
   12 IF(I.NE.1) GOTO 10
      IF(JJ.EQ.1) RHSR(I)=RHSR(I)+XPLAS(NC)*(-XAR(1))
      IF(JJ.EQ.2) RHSR(I)=RHSR(I)+DLAM*XCTEST(2,NC)*(-XAR(2))
   10 CONTINUE
      CALL THOMAS(JJ,M,M,AR,BR,CR,RHSR,XNEW)
```

```
      DO 401 I=1,M
      IF(XNEW(I).LE.0.0) XNEW(I)=0.0
      PHINEW(JJ,I,J)=XNEW(I)
  401 CONTINUE
    2 CONTINUE
      DO 806 JJ=1,2
       DO 806 J=1,NP1
      DO 806 I=1,M
      PHIOLD(JJ,I,J)=PHINEW(JJ,I,J)
  806 CONTINUE
      DO 30 JJ=1,2
      IF(ISTD.EQ.1.AND.(JJ.EQ.1)) GOTO 30
      IF(JJ.EQ.2.AND.PHIOLD(1,M,NP1).GE.20.0) GOTO 30
      DO 403 I=1,M
      DO 15 J=1,NP1
      NC=J+NINCR
      PHIAVG(JJ,I,J)=0.5*(PHINEW(JJ,I,J)+PHIOLD(JJ,I,J))
      IF(JJ.EQ.1) TMET(1,I,J)=-COEF1(1)*PHIAVG(1,I,J)/(COEF1(2)+PHIAVG(1
      *,I,J))
       IF(JJ.EQ.2) TMET(2,I,J)=-XDMAX*(1.0-PHIAVG(2,I,J)/(COEF2(1)
      *+PHIAVG(2,I,J)))
   23 CONTINUE
      IF(I.NE.1) GOTO 16
      IF(JJ.EQ.1) RHSZ(J)=-CR(1,JJ)*PHIOLD(JJ,2,J)-(-1.+2.*DRAT1(JJ
     *))*PHIOLD(JJ,1,J)+CPD(1,NC)*(-XAR(JJ))+TMET(1,I,J)*DT
       IF(JJ.EQ.2) RHSZ(J)=-CR(1,JJ)*PHIOLD(JJ,2,J)-(-1.+2.*DRAT1(JJ
     *))*PHIOLD(JJ,1,J)+DLAM*CPD(2,NC)*(-XAR(JJ))+TMET(2,I,J)*DT
      GOTO 15
   16 IF(I.NE.M) GOTO 17
      MM1=M-1
       RHSZ(J)=DRAT1(JJ)*2.*PHIOLD(JJ,MM1,J)-(-1.+2.*DRAT1(JJ))*PHIOLD(JJ
      *,M,J)+TMET(JJ,I,J)*DT
       GOTO 15
   17 IP1=I+1
      IM1=I-1
      RHSZ(J)=PHIOLD(JJ,IM1,J)*(-1.*AR(I,JJ))+(1.-2.0*DRAT1(JJ))*PHIOLD(
     *JJ,I,J)+TMET(JJ,I,J)*DT+PHIOLD(JJ,IP1,J)*(-1.*CR(I,JJ))
   15 CONTINUE
      CALL THOMAS(JJ,M,NP1,AZ,BZ,CZ,RHSZ,XNEW)
      DO 403 J=1,NP1
      IF(XNEW(J).LE.0.0) XNEW(J)=0.0
      PHINEW(JJ,I,J)=XNEW(J)
  403 CONTINUE
   30 CONTINUE
      RETURN
      END
      SUBROUTINE DFXG(NTOTAL,CPD,ABAND,BBAND,CBAND,DBAND,FLX)
      DIMENSION CPD(2,60),FLX(2,40)
       DIMENSION ABAND(60,2),BBAND(60),CBAND(60,2),DBAND(60)
       COMMON/BLOCK1/DCDZ,VDC,R1,R2
      COMMON/BLOCK2/DIAG,VD,VD2,VD4,NTOTM1,DT,DZ,DR,VEL,NINCR
     *,NN,POIN
      COMMON/BLOCK4/KIT,SF
      J=2
      DO 51 I=2,NTOTM1
```

```
      J=J+1
      NC=J-NINCR
      BBAND(I)  = (DIAG+2.*DCDZ)*DT
      ABAND(I,1)=-VDC*DT
      ABAND(I,2)= VD4*DT
      CBAND(I,1)=-DCDZ*DT
      IF(J.GT.NINCR.AND.J.LE.NN) THEN
      DBAND(I)=(CPD(2,J-1)*VDC+CPD(2,J)*(2./DT-DIAG-2.*DCDZ)
     *+CPD(2,J-2)*(-VD4)+(FLX(2,NC)*SF)+CPD(2,J+1)*DCDZ)*DT
      ELSE
      DBAND(I)=(CPD(2,J-1)*VDC+CPD(2,J)*(2./DT-DIAG-2.*DCDZ)+CPD(2,
     *J+1)*DCDZ+CPD(2,J-2)*(-VD4))*DT
      ENDIF
      IF(J.EQ.4) DBAND(2)=DBAND(2)-CPD(2,1)*VD4*DT
   51 CONTINUE
      BBAND(NTOTAL)=BBAND(NTOTM1)-DCDZ*DT
      DBAND(NTOTAL)=(CPD(2,NTOTM1)*VDC+CPD(2,NTOTAL)*(2./DT-DIAG
     *-2.*DCDZ)+CPD(2,NTOTAL)*DCDZ+CPD(2,NTOTM1)*(-VD4))*DT
      BBAND(1)=(1./DT+VD2+2.*DCDZ)*DT
      CBAND(1,1)=-DCDZ*DT
      DBAND(1)=(CPD(2,1)*(VD2+DCDZ)+CPD(2,2)*(1./DT-VD2-2.*DCDZ)+CPD(2,
     *3)*DCDZ-CPD(2,1)*(-VD2-DCDZ))*DT
      RETURN
      END
      SUBROUTINE BAND(NROW,MCOL,ABAND,BBAND,CBAND,DBAND,SBAND
     *,WORK,AL,BE2,GAM2)
      DIMENSION ABAND(60,2),BBAND(60),CBAND(60,2),DBAND(60)
      DIMENSION SBAND(60),WORK(60,2),AL(60,2),BE2(60),GAM2(60)
      NROW=59
      MCOL=2
      DO 1 J=1,NROW
      DO 1 K=1,MCOL
      IF (K.GE.J) ABAND(J,K)=0.0
      IF ((K-NROW-1+J).GE.0.0) CBAND(J,K)=0.0
    1 CONTINUE
      DO 8 J=1,NROW
      DO 3 IK=1,MCOL
      K=MCOL+1-IK
      KP1=K+1
      SUM=0.0
      IF (KP1.GT.MCOL) GOTO 3
      DO 2 IP=KP1,MCOL
      JLP=J-IP
      MPK=IP-K
      IF(IP.LT.J) SUM=SUM+AL(J,IP)*WORK(JLP,MPK)
    2 CONTINUE
    3 AL(J,K)=ABAND(J,K)-SUM
      SUM=0.0
      DO 4 IP=1,MCOL
      JLP=J-IP
      IF(J.GT.IP) SUM=SUM+AL(J,IP)*WORK(JLP,IP)
    4 CONTINUE
      BE2(J) = BBAND(J)-SUM
      IF(BBAND(J).EQ.SUM) GOTO 10
      DO 6 K=1,MCOL
```

```
      IK=K+1
      SUM=0.0
      IF(MCOL.LT.IK) GOTO 6
      DO 5 IP=IK,MCOL
      IMK=IP-K
      JLPMK=J-IMK
      IF(J.GT.IMK) SUM=SUM+AL(J,IMK)*WORK(JLPMK,IP)
    5 CONTINUE
    6 WORK(J,K)=(CBAND(J,K)-SUM)/BE2(J)
      SUM=0.0
      DO 7 IP=1,MCOL
       JLP=J-IP
      IF(J.GT.IP) SUM=SUM+AL(J,IP)*GAM2(JLP)
    7 CONTINUE
    8 GAM2(J)=(DBAND(J)-SUM)/BE2(J)
      DO 30 IJ=1,NROW
      J=NROW+1-IJ
       SUM=0.0
      DO 9 IP=1,MCOL
       JPP=J+IP
      IF(NROW.GE.JPP) SUM=SUM+WORK(J,IP)*SBAND(JPP)
    9 SBAND(J)=GAM2(J)-SUM
   30 CONTINUE
      DO 960 J=1,NROW
      IF(SBAND(J).LE.0.0) SBAND(J)=0.0
  960 CONTINUE
      RETURN
   10 CONTINUE
      WRITE (6,11) J
   11 FORMAT (50X,28H BBAND=0 MATRIX IS SINGULAR//59X,3HJ =,I2)
      END
      SUBROUTINE THOMAS(JJ,M,MX,A,B,C,DYY,XTHETA)
      DIMENSION A(60,2),B(60,2),C(60,2),DYY(60),XTHETA(60)
      DIMENSION F(M),XDELTA(M)
      F(1)=C(1,JJ)/B(1,JJ)
      XDELTA(1)=DYY(1)/B(1,JJ)
      DO K=2,MX
      X1=B(K,JJ)-A(K,JJ)*F(K-1)
      X1=1./X1
      F(K)=C(K,JJ)*X1
      XDELTA(K)=X1*(DYY(K)-A(K,JJ)*XDELTA(K-1))
      END DO
      XTHETA(MX)=XDELTA(MX)
      DO K=MX-1,1,-1
      XTHETA(K)=XDELTA(K)-F(K)*XTHETA(K+1)
      END DO
      RETURN
      END
```

APPENDIX F

COORDINATE VALUES FOR 3-D CAPILLARY NETWORK

Seg No.	node from			node to			Length
	x	y	z	x	y	z	
1	105.0	119.0	140.0	105.6	99.9	107.0	38.13
2	105.6	99.9	107.0	80.7	72.6	110.6	37.12
3	105.6	99.9	107.0	124.6	89.2	108.4	21.85
4	124.6	89.2	108.4	123.2	59.7	102.6	30.10
5(not connected)	0.0	108.0	87.0	14.2	95.3	95.7	20.94
6(not connected)	14.2	95.3	95.7	30.7	141.1	83.0	50.31
7(not connected)	30.7	141.1	83.0	55.0	160.0	79.0	31.04
8	150.0	92.0	95.0	124.6	89.2	108.4	28.85
9	150.0	104.0	60.0	113.8	87.0	20.6	56.14
10	113.8	87.0	20.6	58.4	87.1	10.6	56.30
11	58.4	87.1	10.6	37.2	81.4	17.7	23.07
12	65.5	0.0	86.5	80.8	84.3	91.3	85.81
13	52.0	0.0	113.0	43.7	21.0	126.6	26.36
14	150.0	134.0	29.0	109.4	140.6	74.0	60.97
15	109.4	140.6	74.0	101.5	121.7	89.5	25.69
16	101.5	121.7	89.5	75.1	100.3	75.2	36.87
17	75.1	100.3	75.2	55.8	111.8	62.5	25.81
18	55.8	111.8	62.5	34.0	109.4	61.7	21.95
19	34.0	109.4	61.7	37.2	81.4	17.7	52.25
20	37.2	81.4	17.7	56.0	52.9	35.7	38.60
21	56.0	52.9	35.7	49.4	46.1	72.0	37.52
22	49.4	46.1	72.0	76.3	37.5	112.7	49.54
23	76.3	37.5	112.7	80.7	72.6	110.6	35.44
24	105.6	99.9	107.0	69.4	123.0	112.6	43.31
25	69.4	123.0	112.6	47.9	124.9	113.1	21.59
26	47.9	124.9	113.1	26.1	150.6	100.9	35.84
27	26.1	150.6	100.9	30.0	160.0	101.4	10.19
28	0.0	140.0	74.0	46.0	150.0	49.0	53.30
29	46.0	150.0	49.0	100.0	124.0	38.0	60.93
30	100.0	124.0	38.0	150.0	115.0	13.0	56.62
31	80.8	84.3	91.3	75.1	100.3	75.2	23.40
32	49.4	46.1	72.0	24.6	51.4	69.7	25.46
33	24.6	51.4	69.7	10.0	7.3	67.7	46.50
34	10.0	7.3	67.7	0.0	6.0	64.0	10.74
35	128.1	42.2	114.6	90.5	33.5	127.2	40.60
36	90.5	33.5	127.2	78.0	20.0	127.0	18.40
37	78.0	20.0	127.0	43.7	21.0	126.6	34.32
38	43.7	21.0	126.6	35.6	50.1	127.3	30.21
39	35.6	50.1	127.3	17.6	61.6	122.0	22.01
40	17.6	61.6	122.0	21.4	72.2	110.4	16.17
41	21.4	72.2	110.4	80.7	72.6	110.6	59.30
42	123.2	59.7	102.6	128.1	42.2	114.6	21.78

43	128.1	42.2	114.6	138.0	7.6	94.3	41.32
44	138.0	7.6	94.3	130.2	23.3	84.3	20.18
45	130.2	23.3	84.3	97.5	40.3	20.9	73.33
46	97.5	40.3	20.9	114.4	67.6	22.8	32.16
47	114.4	67.6	22.8	113.8	87.0	20.6	19.53
48	130.2	23.3	84.3	114.5	29.2	110.7	31.28
49	114.5	29.2	110.7	76.3	37.5	112.7	39.14
50	58.4	87.1	10.6	100.0	124.0	38.0	61.99

APPENDIX G

FLOW DATA FROM SECOMB'S WORK FOR 3-D CAPILLARY NETWORK

Segment number	Diameter micron	Flow 10^{-8} m^3/s	Velocity mm/s
1	9	10.385	1.632
2	7	2.077	0.54
3	7	6.923	1.799
4	7	4.154	1.079
5	8	2.769	0.551
6	8	2.769	0.551
7	8	2.769	0.551
8	7	2.769	0.72
9	6	4.846	1.714
10	6	3.462	1.224
11	6	2.769	0.979
12	6	1.385	0.49
13	6	2.769	0.979
14	5	2.769	1.41
15	5	2.769	1.41
16	5	2.769	1.41
17	5	1.385	0.705
18	5	1.385	0.705
19	5	1.385	0.705
20	5	1.385	0.705
21	5	1.385	0.705
22	5	2.077	1.058
23	5	0.692	0.353
24	5	1.385	0.705
25	5	1.385	0.705
26	5	1.385	0.705
27	5	1.385	0.705
28	5	1.385	0.705
29	5	1.385	0.705
30	5	2.077	1.058
31	5	1.385	0.705
32	4	0.692	0.551
33	4	0.692	0.551
34	4	0.692	0.551
35	5	1.385	0.705
36	5	1.385	0.705
37	5	1.385	0.705
38	5	1.385	0.705
39	5	1.385	0.705
40	5	1.385	0.705

41	5	1.385	0.705
42	7	4.154	1.079
43	6	2.769	0.979
44	5	2.769	1.41
45	5	1.385	0.705
46	5	1.385	0.705
47	5	1.385	0.705
48	5	1.385	0.705
49	5	1.385	0.705
50	5	0.692	0.353

APPENDIX H

REACTION MECHANISMS OF JP-10 FOR 58 SPECIES

No.	Reactions		*A*	*n*	*E*	Ref.
1	$H + O_2 \leftrightarrow OH + O$		3.52E+16	-0.7	71.4	Rightley et al.,1997
2	$H + O_2 + AR \leftrightarrow HO_2 + AR$		7.00E+17	-0.8	0.0	GRI-Mech 3.0
3	$H_2 + O \leftrightarrow OH + H$		5.06E+04	2.67	26.3	Rightley et al.,1997
4	$H_2 + OH \leftrightarrow H_2O + H$		1.17E+09	1.3	15.2	Rightley et al.,1997
5	$H_2O + O \leftrightarrow 2OH$		7.60E+00	3.84	53.5	Rightley et al.,1997
6[a]	$H + H + M1 \leftrightarrow H_2 + M1$		1.30E+18	-1	0.0	Saxena et al.,2006
7[a]	$H + OH + M2 \leftrightarrow H_2O + M2$		4.00E+22	-2	0.0	Saxena et al.,2006
8[a]	$O + O + M3 \leftrightarrow O_2 + M3$		6.17E+15	-0.5	0.0	Saxena et al.,2006
9[a]	$H + O + M4 \leftrightarrow OH + M4$		4.71E+18	-1	0.0	Saxena et al.,2006
10[a]	$O + OH + M4 \leftrightarrow HO_2 + M4$		8.00E+15	0	0.0	Saxena et al.,2006
11[b]	$H + O_2 + M5 \leftrightarrow HO_2 + M5$	k_0	5.75E+19	-1.4	0.0	Troe,2000
		k_∞	4.65E+12	0.44	0.0	
12	$HO_2 + H \leftrightarrow 2OH$		7.08E+13	0	1.2	Mueller et al,1999
13	$HO_2 + H \leftrightarrow H_2 + O_2$		1.66E+13	0	3.4	Mueller et al,1999
14	$HO_2 + H \leftrightarrow H_2O + O$		3.10E+13	0	7.2	Rightley et al.,1997
15	$HO_2 + O \leftrightarrow OH + O_2$		2.00E+13	0	0.0	Warnatz,1984
16	$HO_2 + OH \leftrightarrow H_2O + O_2$		2.89E+13	0	-2.1	Rightley et al.,1997
17[b]	$2OH + M6 \leftrightarrow H_2O_2 + M6$	k_0	2.30E+18	-0.9	-7.12	Rightley et al.,1997
		k_∞	7.40E+13	-0.37	0.0	
18	$2HO_2 \leftrightarrow H_2O_2 + O_2$		3.02E+12	0	5.8	Rightley et al.,1997
19	$H_2O_2 + H \leftrightarrow HO_2 + H_2$		4.79E+13	0	33.3	Yetter et al.,1991
20	$H_2O_2 + H \leftrightarrow H_2O + OH$		1.00E+13	0	15.0	Yetter et al.,1991
21	$H_2O_2 + OH \leftrightarrow H_2O + HO_2$		7.08E+12	0	6.0	Rightley et al.,1997
22	$H_2O_2 + O \leftrightarrow HO_2 + OH$		9.63E+06	2	16.7	Rightley et al.,1997
23	$CO + OH \leftrightarrow CO_2 + H$		4.40E+06	1.5	-3.1	Rightley et al.,1997
24	$CO + HO_2 \leftrightarrow CO_2 + OH$		6.00E+13	0	96.0	Rightley et al.,1997
25	$CO + O_2 \leftrightarrow CO_2 + O$		1.00E+12	0	199.6	Saxena et al.,2006
26[a]	$HCO + M7 \leftrightarrow CO + H + M7$		1.86E+17	-1	71.1	Lindstedt et al.,1997
27	$HCO + H \leftrightarrow CO + H_2$		5.00E+13	0	0.0	Saxena et al.,2005
28	$HCO + O \leftrightarrow CO + OH$		3.00E+13	0	0.0	Rightley et al.,1997
29	$HCO + O \leftrightarrow CO_2 + H$		3.00E+13	0	0.0	Rightley et al.,1997
30	$HCO + OH \leftrightarrow CO + H_2O$		3.00E+13	0	0.0	Teang et al.,1986
31	$HCO + O_2 \leftrightarrow CO + HO_2$		7.58E+12	0	1.7	Timonen et al.,1988
32	$HCO + CH_3 \leftrightarrow CO + CH_4$		5.00E+13	0	0.0	Saxena et al.,2005
33[b]	$H + HCO + M8 \leftrightarrow CH_2O + M8$	k_0	1.35E+24	-2.57	1.78	GRI-Mech 3.0
		k_∞	1.09E+12	0.48	-1.09	
34	$CH_2O + H \leftrightarrow HCO + H_2$		5.74E+07	1.9	11.5	Li, 2004

35	$CH_2O + O \leftrightarrow HCO + OH$		3.50E+13	0	14.7	Rightley et al.,1997
36	$CH_2O + OH \leftrightarrow HCO + H_2O$		3.90E+10	0.89	1.7	Rightley et al.,1997
37	$CH_2O + O_2 \leftrightarrow HCO + HO_2$		6.00E+13	0	170.2	Baulch et al.,1992
38	$CH_2O + HO_2 \leftrightarrow HCO + H_2O_2$		4.11E+04	2.5	42.7	Eiteneer et al.,1998
39	$CH_4 + H \leftrightarrow H_2 + CH_3$		1.30E+04	3	33.6	Hewson et al.,1999
40	$CH_4 + OH \leftrightarrow H_2O + CH_3$		1.60E+07	1.83	11.6	Hewson et al.,1999
41	$CH_4 + O \leftrightarrow CH_3 + OH$		1.90E+09	1.44	36.3	Frenklash et al.,1992
42	$CH_4 + O_2 \leftrightarrow CH_3 + HO_2$		3.98E+13	0	238.1	Lindstedt et al.,1997
43	$CH_4 + HO_2 \leftrightarrow CH_3 + H_2O_2$		9.03E+12	0	103.1	Lindstedt et al.,1997
44	$CH_3 + H \leftrightarrow TCH_2 + H_2$		1.80E+14	0	63.2	Frenklach et al.,1992
45	$CH_3 + H \leftrightarrow SCH_2 + H_2$		1.55E+14	0	56.4	Frenklach et al.,1992
46	$CH_3 + OH \leftrightarrow SCH_2 + H_2O$		4.00E+13	0	10.5	Grotheer et al., 1992
47	$CH_3 + O \leftrightarrow CH_2O + H$		8.43E+13	0	0.0	Frenklach et al.,1992
48	$CH_3 + TCH_2 \leftrightarrow C_2H_4 + H$		4.22E+13	0	0.0	Baulch et al.,1992
49	$CH_3 + HO_2 \leftrightarrow CH_3O + OH$		5.00E+12	0	0.0	Baulch et al.,1992
50	$CH_3 + O_2 \leftrightarrow CH_2O + OH$		3.30E+11	0	37.4	Zeller et al., 1988
51	$CH_3 + O_2 \leftrightarrow CH_3O + O$		1.10E+13	0	116.4	Zeller et al., 1988
52	$CH_3 + CH_3 \leftrightarrow C_2H_4 + H_2$		1.00E+14	0	133.9	Hidaka et al., 1990
53	$CH_3 + CH_3 \leftrightarrow C_2H_5 + H$		3.16E+13	0	61.5	Lim et al., 1994
54[b]	$H + CH_3 + M9 \leftrightarrow CH_4 + M9$	k_0	2.47E+33	-4.76	10.2	GRI-Mech 3.0
		k_∞	1.27E+16	-0.63	1.6	
55[b]	$2CH_3 + M8 \leftrightarrow C_2H_6 + M8$	k_0	1.27E+41	-7	11.6	Hewson et al.,1999
		k_∞	1.81E+13	0	0.0	
56	$SCH_2 + OH \leftrightarrow CH_2O + H$		3.00E+13	0	0.0	Frenklach et al.,1992
57	$SCH_2+AR \leftrightarrow TCH_2+AR$		9.00E+12	0	2.5	GRI-Mech 3.0
58	$SCH_2 + O_2 \leftrightarrow CO + OH + H$		3.13E+13	0	0.0	Frenklach et al.,1992
59	$SCH_2 + CO_2 \leftrightarrow CO + CH_2O$		3.00E+12	0	0.0	Leung et al., 1995
60[a]	$SCH_2 + M10 \leftrightarrow TCH_2 + M10$		6.00E+12	0	0.0	Frenklach et al.,1992
61	$TCH_2 + H \leftrightarrow CH + H_2$		6.02E+12	0	-7.5	Baulch et al.,1992
62	$TCH_2 + OH \leftrightarrow CH_2O + H$		2.50E+13	0	0.0	Frenklach et al.,1992
63	$TCH_2 + OH \leftrightarrow CH + H_2O$		1.13E+07	2	12.6	Frenklach et al.,1992
64	$TCH_2 + O \leftrightarrow CO+2H$		8.00E+13	0	0.0	Frank et al., 1986
65	$TCH_2 + O \leftrightarrow CO + H_2$		4.00E+13	0	0.0	Frank et al., 1986
66	$TCH_2 + O_2 \leftrightarrow CO_2 + H_2$		2.63E+12	0	6.2	Leung et al., 1995
67	$TCH_2 + O_2 \leftrightarrow CO + OH + H$		6.58E+12	0	6.2	Leung et al., 1995
68	$TCH_2 + TCH_2 \leftrightarrow C_2H_2+2H$		1.00E+14	0	0.0	Frenklach et al.,1992
69	$CH + O \leftrightarrow CO + H$		4.00E+13	0	0.0	Peters et al., 1993
70	$CH + O_2 \leftrightarrow HCO + O$		1.77E+11	0.76	-2.0	Markus et al., 1996

71	$CH + H_2O \leftrightarrow CH_2O + H$		1.17E+15	-0.75	0.0	Leung et al., 1995
72	$CH + CO_2 \leftrightarrow HCO + CO$		48	3.22	-13.5	Markus et al., 1996
73	$CH_3O + H \leftrightarrow CH_2O + H_2$		2.00E+13	0	0.0	Li et al., 1998
74	$CH_3O + H \leftrightarrow SCH_2 + H_2O$		1.60E+13	0	0.0	Li et al., 1998
75	$CH_3O + OH \leftrightarrow CH_2O + H_2O$		5.00E+12	0	0.0	Li et al., 1998
76	$CH_3O + O \leftrightarrow OH + CH_2O$		1.00E+13	0	0.0	Li et al., 1998
77	$CH_3O + O_2 \leftrightarrow CH_2O + HO_2$		4.28E-13	7.6	-14.8	Li et al., 1998
78[a]	$CH_3O + M9 \leftrightarrow CH_2O + H + M9$		7.78E+13	0	56.5	Saxena et al.,2005
79	$C_2H_6 + H \leftrightarrow C_2H_5 + H_2$		540	3.5	21.8	Frenklach et al.,1992
80	$C_2H_6 + O \leftrightarrow C_2H_5 + OH$		1.40E+00	4.3	11.6	Frenklach et al.,1992
81	$C_2H_6 + OH \leftrightarrow C_2H_5 + H_2O$		2.20E+07	1.9	4.7	Frenklach et al.,1992
82	$C_2H_6 + CH_3 \leftrightarrow C_2H_5 + CH_4$		5.50E-01	4	34.7	Frenklach et al.,1992
83[b]	$C_2H_6 + M8 \leftrightarrow C_2H_5 + H + M8$	k_0	4.90E+42	-6.43	448	Hewson et al.,1999
		k_∞	8.85E+20	-1.23	427.8	
84	$C_2H_6 + HO_2 \leftrightarrow C_2H_5 + H_2O_2$		1.32E+13	0	85.7	Baulch et al.,1992
85	$C_2H_5 + H \leftrightarrow C_2H_4 + H_2$		3.00E+13	0	0.0	Frenklach et al.,1992
86	$C_2H_5 + O \leftrightarrow C_2H_4 + OH$		3.06E+13	0	0.0	Frenklach et al.,1992
87	$C_2H_5 + O \leftrightarrow CH_3 + CH_2O$		4.24E+13	0	0.0	Frenklach et al.,1992
88	$C_2H_5 + O_2 \leftrightarrow C_2H_4 + HO_2$		2.00E+12	0	20.9	Frenklach et al.,1992
89[b]	$C_2H_5 + M9 \leftrightarrow C_2H_4 + H + M9$	k_0	3.99E+33	-4.99	167	Feng et al., 1993
		k_∞	1.11E+10	1.037	153.9	
90	$C_2H_4 + H \leftrightarrow C_2H_3 + H_2$		4.49E+07	2.12	55.9	Bhargava et al., 1998
91	$C_2H_4 + OH \leftrightarrow C_2H_3 + H_2O$		5.53E+05	2.31	12.4	Bhargava et al., 1998
92	$C_2H_4 + O \leftrightarrow CH_3 + HCO$		2.25E+06	2.08	0.0	Baulch et al.,1992
93	$C_2H_4 + O \leftrightarrow CH_2CHO + H$		1.21E+06	2.08	0.0	Baulch et al.,1992
94	$C_2H_4 + C_2H_4 \leftrightarrow C_2H_3 + C_2H_5$		5.01E+14	0	270.8	Hidaka et al., 1999
95	$C_2H_4 + O_2 \leftrightarrow C_2H_3 + HO_2$		4.22E+13	0	241.1	Baulch et al., 1994
96	$C_2H_4 + HO_2 \leftrightarrow C_2H_4O + OH$		2.23E+12	0	71.9	Baulch et al.,1992
97	$C_2H_4O + HO_2 \leftrightarrow CH_3 + CO + H_2O_2$		4.00E+12	0	71.2	Baulch et al.,1992
98[a]	$C_2H_4 + M9 \leftrightarrow C_2H_3 + H + M9$		2.60E+17	0	404.1	Baulch et al., 1994
99[a]	$C_2H_4 + M9 \leftrightarrow C_2H_2 + H_2 + M9$		3.50E+16	0	299.3	Baulch et al., 1994
100	$C_2H_3 + H \leftrightarrow C_2H_2 + H_2$		4.00E+13	0	0.0	Saxena et al.,2005
101[b]	$C_2H_3 + M9 \leftrightarrow C_2H_2 + H + M9$	k_0	1.51E+14	0.1	137	Williams et al.,2001
		k_∞	6.38E+09	1	157.5	
102	$C_2H_3 + O_2 \leftrightarrow CH_2O + HCO$		1.70E+29	-5.312	27.2	Marinov et al., 1998
103	$C_2H_3 + O_2 \leftrightarrow CH_2CHO + O$		7.00E+14	-0.611	22.0	Williams et al.,2001
104	$C_2H_3 + O_2 \leftrightarrow C_2H_2 + HO_2$		5.19E+15	-1.26	13.9	Williams et al.,2001
105	$C_2H_2 + O \leftrightarrow HCCO + H$		4.00E+14	0	44.6	Frank et al., 1986

106	$C_2H_2 + O \leftrightarrow TCH_2 + CO$		1.60E+14	0	41.4	Frank et al., 1986
107	$C_2H_2 + O_2 \leftrightarrow CH_2O + CO$		4.60E+15	-0.54	188.0	Waly et al., 2001
108	$C_2H_2 + OH \leftrightarrow CH_2CO + H$		1.90E+07	1.7	4.2	Lindstedt et al.,1997
109	$C_2H_2 + OH \leftrightarrow C_2H + H_2O$		3.37E+07	2	58.6	Lindstedt et al.,1997
110	$CH_2CO + H \leftrightarrow CH_3 + CO$		1.50E+09	1.43	11.3	Petrova et al., 2006
111	$CH_2CO + O \leftrightarrow TCH_2 + CO_2$		2.00E+13	0	9.6	Lindstedt et al.,1997
112	$CH_2CO + O \leftrightarrow HCCO + OH$		1.00E+13	0	8.4	Lindstedt et al.,1997
113	$CH_2CO + CH_3 \leftrightarrow C_2H_5 + CO$		9.00E+10	0	0.0	Lindstedt et al.,1997
114	$HCCO + H \leftrightarrow SCH_2 + CO$		1.50E+14	0	0.0	Frank et al., 1986
115	$HCCO + OH \leftrightarrow HCO + CO + H$		2.00E+12	0	0.0	Westbrook et al.,1984
116	$HCCO + O \leftrightarrow 2CO + H$		9.64E+13	0	0.0	Frank et al., 1986
117	$HCCO + O_2 \leftrightarrow 2CO + OH$		2.88E+07	1.7	4.2	Williams et al.,2001
118	$HCCO + O_2 \leftrightarrow CO_2 + CO + H$		1.40E+07	1.7	4.2	Williams et al.,2001
119	$C_2H + OH \leftrightarrow HCCO + H$		2.00E+13	0	0.0	Frenklach et al.,1992
120	$C_2H + O \leftrightarrow CO + CH$		1.02E+13	0	0.0	Frenklach et al.,1992
121	$C_2H + O_2 \leftrightarrow HCCO + O$		6.02E+11	0	0.0	Frenklach et al.,1992
122	$C_2H + O_2 \leftrightarrow CH + CO_2$		4.50E+15	0	105.0	Frenklach et al.,1992
123	$C_2H + O_2 \leftrightarrow HCO + CO$		2.41E+12	0	0.0	Frenklach et al.,1992
124	$CH_2OH + H \leftrightarrow CH_2O + H_2$		3.00E+13	0	0.0	Li et al., 1998
125	$CH_2OH + H \leftrightarrow CH_3 + OH$		2.50E+17	-0.93	21.5	Saxena et al.,2005
126	$CH_2OH + OH \leftrightarrow CH_2O + H_2O$		2.40E+13	0	0.0	Li et al., 1998
127	$CH_2OH + O_2 \leftrightarrow CH_2O + HO_2$		5.00E+12	0	0.0	Li et al., 1998
128[a]	$CH_2OH + M9 \leftrightarrow CH_2O + H + M9$		5.00E+13	0	105.1	Li et al., 1998
129[a]	$CH_3O + M9 \leftrightarrow CH_2OH + M9$		1.00E+14	0	80.0	Li et al., 1998
130	$CH_2CO + OH \leftrightarrow CH_2OH + CO$		1.02E+13	0	0.0	Li et al., 1998
131	$CH_3OH + OH \leftrightarrow CH_2OH + H_2O$		1.44E+06	2	-3.5	Li et al., 1998
132	$CH_3OH + OH \leftrightarrow CH_3O + H_2O$		4.40E+06	2	6.3	Saxena et al.,2005
133	$CH_3OH + H \leftrightarrow CH_2OH + H_2$		1353.8	3.2	14.6	Jodkowski et al.,1999
134	$CH_3OH + H \leftrightarrow CH_3O + H_2$		68.3	3.4	30.3	Jodkowski et al.,1999
135	$CH_3OH + O \leftrightarrow CH_2OH + OH$		1.00E+13	0	19.6	Li et al., 1998
136	$CH_3OH + HO_2 \leftrightarrow CH_2OH + H_2O_2$		6.20E+12	0	81.1	Li et al., 1998
137	$CH_3OH + O_2 \leftrightarrow CH_2OH + HO_2$		2.00E+13	0	188.0	Li et al., 1998
138[b]	$CH_3OH + M9 \leftrightarrow CH_3 + OH + M9$	k_0	2.95E+44	-7.35	399	Held et al., 1998
		k_∞	1.90E+16	0	383.9	
139	$CH_2CHO \leftrightarrow CH_2CO + H$		1.05E+37	-7.189	185.6	Marinov et al., 1995
140	$CH_2CHO + H \leftrightarrow CH_3 + HCO$		5.00E+13	0	0.0	Li, 2004
141	$CH_2CHO + H \leftrightarrow CH_2CO + H_2$		2.00E+13	0	0.0	Li, 2004
142	$CH_2CHO + O \leftrightarrow CH_2O + HCO$		1.00E+14	0	0.0	Li, 2004

143	$CH_2CHO + OH \leftrightarrow CH_2CO + H_2O$		3.00E+13	0	0.0	Li, 2004
144	$CH_2CHO + O_2 \leftrightarrow CH_2O + CO + OH$		3.00E+10	0	0.0	Li, 2004
145	$CH_2CHO + CH_3 \leftrightarrow C_2H_5 + CO + H$		4.90E+14	-0.5	0.0	Li, 2004
146	$CH_2CHO + HO_2 \leftrightarrow CH_2O + HCO + OH$		7.00E+12	0	0.0	Li, 2004
147	$CH_2CHO + HO_2 \leftrightarrow CH_3CHO + O_2$		3.00E+12	0	0.0	Li, 2004
148	$CH_2CHO \leftrightarrow CH_3 + CO$		1.17E+43	-9.8	183.3	Li, 2004
149	$CH_3CHO \leftrightarrow CH_3 + HCO$		7.00E+15	0	341.9	Li, 2004
150[b]	$CH_3CO + M9 \leftrightarrow CH_3 + CO + M9$	k_0	1.20E+15	0	52.3	Li, 2004
		k_∞	3.00E+12	0	69.9	
151	$CH_3CHO + OH \leftrightarrow CH_3CO + H_2O$		3.37E+12	0	-2.6	Li, 2004
152	$CH_3CHO + OH \leftrightarrow CH_2CHO + H_2O$		3.37E+11	0	-2.6	Li, 2004
153	$CH_3CHO + O \leftrightarrow CH_3CO + OH$		1.77E+18	-1.9	12.5	Li, 2004
154	$CH_3CHO + O \leftrightarrow CH_2CHO + OH$		3.72E+13	-0.2	14.9	Li, 2004
155	$CH_3CHO + H \leftrightarrow CH_3CO + H_2$		4.66E+13	-0.3	12.5	Li, 2004
156	$CH_3CHO + H \leftrightarrow CH_2CHO + H_2$		1.85E+12	0.4	22.4	Li, 2004
157	$CH_3CHO + CH_3 \leftrightarrow CH_3CO + CH_4$		3.90E-07	5.8	9.2	Li, 2004
158	$CH_3CHO + CH_3 \leftrightarrow CH_2CHO + CH_4$		2.45E+01	3.1	24.0	Li, 2004
159	$CH_3CHO + HO_2 \leftrightarrow CH_3CO + H_2O_2$		3.60E+19	-2.2	58.6	Li, 2004
160	$CH_3CHO + HO_2 \leftrightarrow CH_2CHO + H_2O_2$		2.32E+11	0.4	62.4	Li, 2004
161	$CH_3CHO + O_2 \leftrightarrow CH_3CO + HO_2$		1.00E+14	0	176.6	Li, 2004
162[b]	$C_2H_5OH + M9 \leftrightarrow CH_3 + CH_2OH + M9$	k_0	3.00E+16	0	243	Saxena et al.,2005
		k_∞	5.00E+15	0	343.1	
163[b]	$C_2H_5OH + M9 \leftrightarrow C_2H_4 + H_2O + M9$	k_0	1.00E+17	0	226.0	Saxena et al.,2005
		k_∞	8.00E+13	0	272.0	
164	$C_2H_5OH + OH \leftrightarrow CH_2CH_2OH + H_2O$		1.81E+11	0.4	3.0	Li, 2004
165	$C_2H_5OH + OH \leftrightarrow CH_3CHOH + H_2O$		3.09E+10	0.5	-1.6	Li, 2004
166	$C_2H_5OH + OH \leftrightarrow CH_3CH_2O + H_2O$		1.05E+10	0.8	3.0	Li, 2004
167	$C_2H_5OH + H \leftrightarrow CH_2CH_2OH + H_2$		1.90E+07	1.8	21.3	Li, 2004
168	$C_2H_5OH + H \leftrightarrow CH_3CHOH + H_2$		2.58E+07	1.6	11.8	Li, 2004
169	$C_2H_5OH + H \leftrightarrow CH_3CH_2O + H_2$		1.50E+07	1.6	12.7	Li, 2004
170	$C_2H_5OH + O \leftrightarrow CH_2CH_2OH + OH$		9.41E+07	1.7	22.8	Li, 2004
171	$C_2H_5OH + O \leftrightarrow CH_3CHOH + OH$		1.88E+07	1.9	7.6	Li, 2004
172	$C_2H_5OH + O \leftrightarrow CH_3CH_2O + OH$		1.58E+07	2	18.6	Li, 2004
173	$C_2H_5OH + CH_3 \leftrightarrow CH_2CH_2OH + CH_4$		219	3.2	40.3	Li, 2004
174	$C_2H_5OH + CH_3 \leftrightarrow CH_3CHOH + CH_4$		728	3	33.3	Li, 2004
175	$C_2H_5OH + CH_3 \leftrightarrow CH_3CH_2O + CH_4$		145	3	32.0	Li, 2004
176	$C_2H_5OH + HO_2 \leftrightarrow CH_3CHOH + H_2O_2$		8200	2.5	45.2	Li, 2004
177	$C_2H_5OH + HO_2 \leftrightarrow CH_2CH_2OH + H_2O_2$		2.43E+04	2.5	66.1	Li, 2004

178	$C_2H_5OH + HO_2 \leftrightarrow CH_3CH_2O + H_2O_2$		3.80E+12	0	100.4	Li, 2004
179	$C_2H_4 + OH \leftrightarrow CH_2CH_2OH$		2.41E+11	0	-10.0	Li, 2004
180	$C_2H_5 + HO_2 \leftrightarrow CH_3CH_2O + OH$		4.00E+13	0	0.0	Li, 2004
181[a]	$CH_3CH_2O + M9 \leftrightarrow CH_3CHO + H + M9$		5.60E+34	-5.9	105.9	Li, 2004
182[a]	$CH_3CH_2O + M9 \leftrightarrow CH_3 + CH_2O + M9$		5.35E+37	-7	99.6	Li, 2004
183	$CH_3CH_2O + O_2 \leftrightarrow CH_3CHO + HO_2$		4.00E+10	0	4.6	Li, 2004
184	$CH_3CH_2O + CO \leftrightarrow C_2H_5 + CO_2$		468	3.2	22.5	Li, 2004
185	$CH_3CH_2O + H \leftrightarrow CH_3 + CH_2OH$		3.00E+13	0	0.0	Li, 2004
186	$CH_3CH_2O + H \leftrightarrow C_2H_4 + H_2O$		3.00E+13	0	0.0	Li, 2004
187	$CH_3CH_2O + OH \leftrightarrow CH_3CHO + H_2O$		1.00E+13	0	0.0	Li, 2004
188	$CH_3CHOH + O_2 \leftrightarrow CH_3CHO + HO_2$		4.82E+13	0	21.0	Li, 2004
189	$CH_3CHOH + O \leftrightarrow CH_3CHO + OH$		1.00E+14	0	0.0	Li, 2004
190	$CH_3CHOH + H \leftrightarrow C_2H_4 + H_2O$		3.00E+13	0	0.0	Li, 2004
191	$CH_3CHOH + H \leftrightarrow CH_3 + CH_2OH$		3.00E+13	0	0.0	Li, 2004
192	$CH_3CHOH + HO_2 \leftrightarrow CH_3CHO + OH + OH$		4.00E+13	0	0.0	Li, 2004
193	$CH_3CHOH + OH \leftrightarrow CH_3CHO + H_2O$		5.00E+12	0	0.0	Li, 2004
194[a]	$CH_3CHOH + M9 \leftrightarrow CH_3CHO + H + M9$		1.00E+14	0	104.6	Li, 2004
195	$C_3H_4 + O \leftrightarrow C_2H_4 + CO$		2.00E+07	1.8	4.2	Davis et al., 1999
196	$CH_3 + C_2H_2 \leftrightarrow C_3H_4 + H$		2.56E+09	1.1	57.1	Davis et al., 1999
197	$C_3H_4 + O \leftrightarrow HCCO + CH_3$		7.30E+12	0	9.4	Davis et al., 1999
198[b]	$C_3H_3 + H + M \leftrightarrow C_3H_4 + M$	k_0	9.00E+15	1	0.0	Petrova et al., 2006
		k_∞	3.00E+13	0	0.0	
199	$C_3H_3 + HO_2 \leftrightarrow C_3H_4 + O_2$		2.50E+12	0	0.0	Petrova et al., 2006
200	$C_3H_4 + OH \leftrightarrow C_3H_3 + H_2O$		5.30E+06	2	8.4	Wang et al., 1997
201	$C_3H_3 + O_2 \leftrightarrow CH_2CO + HCO$		3.00E+10	0	12.0	Slagle et al., 1986
202[b]	$C_3H_4 + H + M \leftrightarrow C_3H_5 + M$	k_0	3.00E+24	-2	0.0	Petrova et al., 2006
		k_∞	4.00E+13	0	0.0	
203	$C_3H_5 + H \leftrightarrow C_3H_4 + H_2$		1.80E+13	0	0.0	Tsang et al., 1991
204	$C_3H_5 + O_2 \leftrightarrow C_3H_4 + HO_2$		4.99E+15	-1.4	93.9	Bozelli et al., 1993
205	$C_3H_5 + CH_3 \leftrightarrow C_3H_4 + CH_4$		3.00E+12	-0.32	-0.5	Petrova et al., 2006
206[b]	$C_2H_2 + CH_3 + M \leftrightarrow C_3H_5 + M$	k_0	2.00E+09	1	0.0	Petrova et al., 2006
		k_∞	6.00E+08	0	0.0	
207	$C_3H_5 + OH \leftrightarrow C_3H_4 + H_2O$		6.00E+12	0	0.0	Petrova et al., 2006
208	$C_3H_3 + HCO \leftrightarrow C_3H_4 + CO$		2.50E+13	0	0.0	Wang et al., 1997
209	$C_3H_3 + HO_2 \leftrightarrow OH + CO + C_2H_3$		8.00E+11	0	0.0	Davis et al., 1999
210	$C_3H_4 + O_2 \leftrightarrow CH_3 + HCO + CO$		4.00E+14	0	175.0	Wang et al., 2001
211	$C_3H_6 + O \leftrightarrow C_2H_5 + HCO$		3.50E+07	1.65	-4.1	Tsang et al., 1991
212	$C_3H_6 + OH \leftrightarrow C_3H_5 + H_2O$		3.10E+06	2	-1.2	Tsang et al., 1991

213	$C_3H_6 + O \leftrightarrow CH_2CO + CH_3 + H$		1.20E+08	1.65	1.4	Tsang et al., 1991
214	$C_3H_6 + H \leftrightarrow C_3H_5 + H_2$		1.70E+05	2.5	10.4	Tsang et al., 1991
215[b]	$C_3H_5 + H + M8 \leftrightarrow C_3H_6 + M8$	k_0	1.33E+60	-12	25.0	Davis et al., 1999
		k_∞	2.00E+14	0	0.0	
216	$C_3H_5 + HO_2 \leftrightarrow C_3H_6 + O_2$		2.66E+12	0	0.0	Baulch et al.,1992
217	$C_3H_5 + HO_2 \leftrightarrow OH + C_2H_3 + CH_2O$		3.00E+12	0	0.0	Baulch et al.,1992
218[b]	$C_2H_3 + CH_3 + M8 \leftrightarrow C_3H_6 + M8$	k_0	4.27E+58	-11.94	40.9	Davis et al., 1999
		k_∞	2.50E+13	0	0.0	
219	$C_3H_6 + H \leftrightarrow C_2H_4 + CH_3$		1.60E+22	-2.39	46.8	Davis et al., 1999
220	$CH_3 + C_2H_3 \leftrightarrow C_3H_5 + H$		1.50E+24	-2.83	77.9	Davis et al., 1999
221[b]	$C_3H_8 + M \leftrightarrow CH_3 + C_2H_5 + M$	k_0	7.83E+18	0	272.0	Baulch et al., 1994
		k_∞	1.10E+17	0	353.2	
222	$C_3H_8 + O_2 \leftrightarrow IC_3H_7 + HO_2$		4.00E+13	0	198.8	Williams et al., 2000
223	$C_3H_8 + O_2 \leftrightarrow NC_3H_7 + HO_2$		4.00E+13	0	213.1	Williams et al., 2000
224	$C_3H_8 + H \leftrightarrow IC_3H_7 + H_2$		1.30E+06	2.4	18.7	Williams et al., 2000
225	$C_3H_8 + H \leftrightarrow NC_3H_7 + H_2$		1.33E+06	2.54	28.3	Tsang et al., 1988
226	$C_3H_8 + O \leftrightarrow IC_3H_7 + OH$		4.76E+04	2.71	8.8	Tsang et al., 1988
227	$C_3H_8 + O \leftrightarrow NC_3H_7 + OH$		1.90E+05	2.68	15.6	Tsang et al., 1988
228	$C_3H_8 + OH \leftrightarrow NC_3H_7 + H_2O$		1400	2.66	2.2	Davis et al., 1999
229	$C_3H_8 + OH \leftrightarrow IC_3H_7 + H_2O$		2.70E+04	2.39	1.6	Davis et al., 1999
230	$C_3H_8 + HO_2 \leftrightarrow IC_3H_7 + H_2O_2$		9640	2.6	58.2	Tsang et al., 1988
231	$C_3H_8 + HO_2 \leftrightarrow NC_3H_7 + H_2O_2$		4.76E+04	2.55	69.0	Tsang et al., 1988
232	$IC_3H_7 + C_3H_8 \leftrightarrow NC_3H_7 + C_3H_8$		8.40E-03	4.2	36.3	Tsang et al., 1988
233[b]	$C_3H_6 + H + M8 \leftrightarrow IC_3H_7 + M8$	k_0	8.70E+42	-7.5	19.8	Davis et al., 1999
		k_∞	1.33E+13	0	6.5	
234	$IC_3H_7 + O_2 \leftrightarrow C_3H_6 + HO_2$		1.30E+11	0	0.0	Tsang et al., 1988
235[b]	$NC_3H_7 + M \leftrightarrow CH_3 + C_2H_4 + M$	k_0	5.49E+49	-10	150.0	Tsang et al., 1988
		k_∞	1.23E+13	-0.1	126.4	
236[b]	$H + C_3H_6 + M8 \leftrightarrow NC_3H_7 + M8$	k_0	6.26E+38	-6.66	29.3	Tsang et al., 1988
		k_∞	1.33E+13	0	13.6	
237	$NC_3H_7 + O_2 \leftrightarrow C_3H_6 + HO_2$		9.00E+10	0	0.0	Tsang et al., 1988
238	$C_2H_2 + C_2H \leftrightarrow C_4H_2 + H$		3.00E+13	0	0.0	Warnatz et al.,1996
239	$C_4H_2 + OH \leftrightarrow C_2H_2 + HCCO$		1.50E+13	0	0.0	Warnatz et al.,1996
240	$C_2H_2 + C_2H \leftrightarrow NC_4H_3$		1.20E+12	0	0.0	Mauss et al., 1996
241	$2C_2H_2 \leftrightarrow NC_4H_3 + H$		2.00E+13	0	226.1	Bollig et al.,1998
242	$NC_4H_3 + M11 \rightarrow C_4H_2 + H + M11$		1.00E+16	0	249.8	Frenklach et al.,1994
243	$IC_4H_3 + M11 \leftrightarrow C_4H_2 + H + M11$		1.00E+16	0	194.7	Frenklach et al.,1994
244	$NC_4H_3 + H \leftrightarrow C_4H_2 + H_2$		2.00E+13	0	0.0	Frenklach et al.,1994

245	$IC_4H_3 + H \leftrightarrow C_4H_2 + H_2$	2.00E+13	0	0.0	Frenklach et al.,1994
246	$NC_4H_3 + O_2 \rightarrow C_2H + 2HCO$	1.00E+12	0	8.4	Frenklach et al.,1994
247	$IC_4H_3 + O_2 \rightarrow C_2H + CH_2O + CO$	1.00E+12	0	8.4	Mauss et al., 1996
248	$C_2H_2 + C_2H_3 \leftrightarrow C_4H_4 + H$	1.60E+13	0	105.1	Frenklach et al.,1994
249	$NC_4H_3 + H + M11 \leftrightarrow C_4H_4 + M11$	1.00E+15	0	0.0	Frenklach et al.,1994
250	$IC_4H_3 + H + M11 \leftrightarrow C_4H_4 + M11$	1.00E+15	0	0.0	Frenklach et al.,1994
251	$C_4H_4 + H \leftrightarrow NC_4H_3 + H_2$	1.50E+14	0	42.7	Frenklach et al.,1994
252	$C_4H_4 + H \leftrightarrow IC_4H_3 + H_2$	1.50E+14	0	42.7	Frenklach et al.,1994
253	$C_4H_4 + OH \leftrightarrow NC_4H_3 + H_2O$	7.00E+13	0	12.6	Frenklach et al.,1994
254	$C_4H_4 + OH \leftrightarrow IC_4H_3 + H_2O$	7.00E+13	0	12.6	Frenklach et al.,1994
255	$C_4H_4 + C_2H \leftrightarrow NC_4H_3 + C_2H_2$	4.00E+13	0	0.0	Frenklach et al.,1994
256	$C_4H_4 + C_2H \leftrightarrow IC_4H_3 + C_2H_2$	4.00E+13	0	0.0	Frenklach et al.,1994
257	$C_4H_4 + C_2H \leftrightarrow C_4H_2 + C_2H_3$	1.00E+13	0	0.0	Frenklach et al.,1994
258	$C_4H_4 + OH \rightarrow C_3H_3 + CH_2O$	1.00E+13	0	0.0	Frenklach et al.,1994
259	$C_2H_2 + C_2H_3 \leftrightarrow NC_4H_5$	1.20E+12	0	0.0	Mauss et al., 1996
260	$C_4H_4 + H \leftrightarrow IC_4H_5$	5.50E+12	0	10.0	Mauss et al., 1996
261	$C_4H_4 + H \leftrightarrow NC_4H_5$	5.50E+12	0	10.0	Frenklach et al.,1994
262	$IC_4H_5 + H \leftrightarrow C_4H_4 + H_2$	2.00E+13	0	0.0	Mauss et al., 1996
263	$NC_4H_5 + H \leftrightarrow C_4H_4 + H_2$	2.00E+13	0	0.0	Mauss et al., 1996
264	$NC_4H_5 + H \leftrightarrow IC_4H_5 + H$	1.00E+14	0	0.0	Mauss et al., 1996
265	$NC_4H_5 + O_2 \rightarrow C_2H_3 + 2HCO$	4.00E+11	0	8.4	Mauss et al., 1996
266	$IC_4H_5 + O_2 \rightarrow C_2H_3 + CO + CH_2O$	4.00E+11	0	8.4	Mauss et al., 1996
267	$C_4H_6 \rightarrow 2C_2H_3$	4.03+E19	-1	410.7	Pitz et al., 2000
268	$2C_2H_3 \rightarrow C_4H_6$	1.26E+13	0	0.0	Pitz et al., 2000
269	$C_4H_6 + H \leftrightarrow NC_4H_5 + H_2$	3.00E+07	2	0.0	Bikas et al., 2000
270	$C_4H_6 + H \leftrightarrow IC_4H_5 + H_2$	3.00E+07	2	0.0	Bikas et al., 2000
271	$C_4H_6 + OH \leftrightarrow NC_4H_5 + H_2O$	2.00E+07	2	0.0	Bikas et al., 2000
272	$C_4H_6 + OH \leftrightarrow IC_4H_5 + H_2O$	2.00E+07	2	54.4	Bikas et al., 2000
273	$C_4H_6 + OH \rightarrow CH_2O + C_3H_5$	1.00E+12	0	25.1	Pitz et al., 2000
274	$C_4H_6 + O \rightarrow C_2H_4 + CH_2CO$	1.00E+12	0	20.9	Pitz et al., 2000
275	$C_4H_6 + O \rightarrow CH_2O + C_3H_4$	1.00E+12	0	8.4	Pitz et al., 2000
276	$CYC_5H_5 \rightarrow C_2H_2 + C_3H_3$	2.00E+12	0	284.6	Moskaleva and Lin 2000
277	$CYC_5H_5 + CH_3 \rightarrow C_4H_6 + C_2H_2$	1.5E+12	0	12.6	E. Ranzi, 2001
278	$CYC_5H_6 + C_4H_6 \rightarrow C_6H_6 + CH_3 + C_2H_3$	3.00E+11	0	125.5	E. Ranzi, 2001
279	$CYC_5H_6 + CYC_5H_5 \rightarrow C_6H_6 + NC_4H_5$	3.00E+12	0	79.5	E. Ranzi, 2001
280	$CYC_5H_6 \leftrightarrow CYC_5H_5 + H$	5.00E+15	0	341.1	Marinov et al.,1996
281	$CYC_5H_6 + H \rightarrow H_2 + CYC_5H_5$	2.41E+07	2	16.5	Zhong and Bozzelli 1998
282	$CYC_5H_6 + O \rightarrow OH + CYC_5H_5$	1.35E+07	2	10.8	Zhong and Bozzelli 1998

283	$CYC_5H_6 + OH \rightarrow H_2O + CYC_5H_5$		3.99E+06	2	-9.5	Zhong and Bozzelli 1998
284	$CYC_5H_6 + O_2 \rightarrow HO_2 + CYC_5H_5$		1.70E+07	2	170.4	Zhong and Bozzelli 1998
285	$CYC_5H_6 + CH_3 \rightarrow CH_4 + CYC_5H_5$		3.90E+05	2	20.4	Zhong and Bozzelli 1998
286	$C_5H_8 \leftrightarrow CYC_5H_6 + H_2$		4.00E+12	0	251.1	Li et al., 2001
287	$C_5H_8 \rightarrow C_3H_6 + C_2H_2$		1.00E+16	0	305.2	Li et al., 2001
288	$C_5H_8 \rightarrow C_3H_4 + C_2H_4$		3.16E+12	0	238.8	Li et al., 2001
289	$C_5H_8 \rightarrow C_3H_5 + C_2H_3$		3.16E+12	0	238.8	Li et al., 2001
290	$C_5H_8 + O_2 \rightarrow C_2H_2 + C_3H_5 + HO_2$		3.00E+12	0	0.0	Li et al., 2001
291	$C_5H_8 + O_2 \rightarrow C_2H_3 + C_3H_4 + HO_2$		3.00E+12	0	0.0	Li et al., 2001
292	$C_5H_8 + HO_2 \rightarrow C_2H_2 + C_3H_5 + H_2O_2$		1.00E+14	0	0.0	Li et al., 2001
293	$C_5H_8 + HO_2 \rightarrow C_2H_3 + C_3H_4 + H_2O_2$		1.00E+14	0	0.0	Li et al., 2001
294	$C_{10}H_{16} \rightarrow H + C_3H_3 + C_2H_4 + C_5H_8$		6.00E+16	0	410.3	Li et al., 2001
295	$C_{10}H_{16} \rightarrow H + C_3H_5 + C_2H_2 + C_5H_8$		6.00E+16	0	410.7	Li et al., 2001
296	$C_{10}H_{16} \rightarrow C_2H_2 + 2C_2H_4 + C_4H_6$		5.00E+16	0	357.6	Li et al., 2001
297	$C_{10}H_{16} + H \rightarrow H_2 + C_3H_3 + C_2H_4 + C_5H_8$		1.32E+06	2.54	28.3	Li et al., 2001
298	$C_{10}H_{16} + O \rightarrow OH + C_3H_3 + C_2H_4 + C_5H_8$		2.88E+06	2.4	23.0	Li et al., 2001
299	$C_{10}H_{16} + OH \rightarrow H_2O + C_3H_3 + C_2H_4 + C_5H_8$		1.74E+07	1.8	4.1	Li et al., 2001
300	$C_{10}H_{16} + O_2 \rightarrow HO_2 + C_3H_3 + C_2H_4 + C_5H_8$		3.98E+13	0	213.1	Li et al., 2001
301	$C_{10}H_{16} + HO_2 \rightarrow H_2O_2 + C_3H_3 + C_2H_4 + C_5H_8$		4.76E+04	2.55	69.1	Li et al., 2001
302	$C_{10}H_{16} + H \rightarrow H_2 + C_3H_5 + C_2H_2 + C_5H_8$		2.60E+06	2.4	18.7	Li et al., 2001
303	$C_{10}H_{16} + O \rightarrow OH + C_3H_5 + C_2H_2 + C_5H_8$		2.76E+05	2.6	8.0	Li et al., 2001
304	$C_{10}H_{16} + OH \rightarrow H_2O + C_3H_5 + C_2H_2 + C_5H_8$		3.80E+06	2	-2.5	Li et al., 2001
305	$C_{10}H_{16} + O_2 \rightarrow HO_2 + C_3H_5 + C_2H_2 + C_5H_8$		7.92E+13	0	199.2	Li et al., 2001
306	$C_{10}H_{16} + HO_2 \rightarrow H_2O_2 + C_3H_5 + C_2H_2 + C_5H_8$		1.93E+04	2.6	58.2	Li et al., 2001
307	$C_6H_5 \rightarrow C_2H_2 + NC_4H_3$		4.50E+13	0	303.4	Westmoreland et al., 1989
308	$C_3H_3 + C_3H_3 + M11 \leftrightarrow C_6H_6 + M11$	k_0	5.00E+17	0	0.0	E. Ranzi, 2001
		k_∞	3.00E+12	0	0.0	
309	$C_3H_3 + C_3H_4 \rightarrow C_6H_6 + H$		1.00E+13	0	75.3	Musick et al., 1997
310	$NC_4H_5 + C_2H_2 \leftrightarrow C_6H_6 + H$		5.00E+11	0	20.9	Westmoreland et al., 1989
311	$C_6H_6 \leftrightarrow C_6H_5 + H$		5.75E+16	0	485.4	Baulch et al., 1992
312	$C_6H_6 + H \rightarrow C_6H_5 + H_2$		2.89E+07	2	42.5	Mauss et al., 1996
313	$C_6H_6 + O \rightarrow C_6H_5 + OH$		1.62E+07	2	36.8	Mauss et al., 1996
314	$C_6H_6 + OH \rightarrow C_6H_5 + H_2O$		1.70E+13	0	16.4	Baulch et al., 1992
315	$C_6H_6 + CH_3 \rightarrow C_6H_5 + CH_4$		4.68E+05	2	44.6	Tokmakov et al.,1999

Rate constant are written as $AT^n exp\left(^{-E}/_{RT}\right)$

Units are mol, cm^3, kJ, K.

The backward rates for all reversible reactions can be calculated from thermodynamic data.

[a] Third-body efficiencies are:

[M1] = 0.5[AR] + 0.5[HE] + 2.5[H2] + 12.0[H2O] + 1.9[CO] + 3.8[CO2]

[M2] = 0.38[AR] + 0.38[HE] + 2.5[H2] + 12.0[H2O] + 1.9[CO] + 3.8[CO2]

[M3] = 0.2[AR] + 0.2[HE] + 2.5[H2] + 12.0[H2O] + 1.9[CO] + 3.8[CO2]

[M4] = 0.75[AR] + 0.75[HE] + 2.5[H2] + 12.0[H2O] + 1.9[CO] + 3.8[CO2]

[M5] = 0.7[AR] + 0.7[HE] + 2.5[H2] + 16.0[H2O] + 1.2[CO] + 2.4[CO2] + 1.5[C2H6]

[M6] = 0.4[AR] + 0.4[HE] + 2.0[H2] + 6.0[H2O] + 1.5[CO] + 2.0[CO2] + 2.0[CH4] + 3.0[C2H6]

[M7] = 1.9[H2] + 12.0[H2O] + 2.5[CO] + 2.5[CO2]

[M8] = 0.7[AR] + 2.0[H2] + 6.0[H2O] + 1.5[CO] + 2.0[CO2] + 2.0[CH4] + 3.0[C2H6]

[M9] = 0.7[AR] + 2.0[H2] + 6.0[H2O] + 1.5[CO] + 2.0[CO2] + 2.0[CH4]

[M10] = 2.4[H2] + 15.4[H2O] + 1.8[CO] + 3.6[CO2]

[M11] = 0.4[AR] + 0.4[O2] + 1.0[H2] + 6.5[H2O] + 0.75[CO] + 1.5[CO2] + 3.0[CH4] + 3.0[C10H16]

[b] Pressure dependent reactions are described by the Troe-formulation [133].

$$k = k_\infty \left(\frac{\frac{k_0[M]}{k_\infty}}{1 + \frac{k_0[M]}{k_\infty}} \right) F$$

$$\log F = \left[1 + \left[\frac{\log\left(\frac{k_0[M]}{k_\infty}\right) + c}{n - 0.14\left(\log\frac{k_0[M]}{k_\infty} + c\right)} \right]^2 \right]^{-1} \log F_c$$

$$c = -0.4 - 0.67 \log F_c$$

$$n = 0.75 - 1.27 \log F_c$$

The troe centering parameters are given by:

Fc11 = 0.5

Fc17 = 0.265 exp(-T/94 K) + 0.735 exp(-T/1756 K) + exp(-5182 K/T)

Fc33 = 0.2176 exp(-T/271 K) + 0.7824 exp(-T/2755 K) + exp(-6570 K/T)

Fc54 = 0.217 exp (-T/74 K) + 0.783 exp(-T/2941 K) + exp(-6964 K/T)

Fc55 = 0.38 exp(-T/73 K) + 0.62 exp(-T/1180 K).

Fc83 = 0.16 exp(-T/125 K) + 0.84 exp(-T/2219 K) + exp(-6882 K/T)

Fc89 = 0.832 exp(-T/1203 K)

Fc101 = 0.7

Fc138 = 0.586 exp(-T/279 K) + 0.414 exp(-T/5459 K)

Fc150 = 1.0

Fc162 = 0.5

Fc163 = 0.5

Fc199 = 0.5

Fc202 = 0.2

Fc206 = 0.5

Fc215 = 0.98 exp(-T/1097 K) + 0.02 exp(-T/1097 K) + exp(-6860 K/T)

Fc218 = 0.825 exp(-T/1341 K) + 0.175 exp(-T/60000 K) + exp(-10140 K/T)

Fc221 = 0.24 exp(-T/1946 K) + 0.76 exp(-T/38 K)

Fc233 = exp(-T/645.4 K) + exp(-6844 K/T)

Fc235 = 2.17 exp(-T/251 K) + exp(-1185 K/T)

Fc236 = exp(-T/1310 K) + exp(-48100 K/T)

APPENDIX I

REACTION MECHANISMS OF JP-10 FOR 49 SPECIES

No.	Reactions		*A*	*n*	*E*	Ref.
1	$H + O_2 \leftrightarrow OH + O$		3.52E+16	-0.7	71.4	Rightley et al.,1997
2	$H + O_2$+AR $\leftrightarrow HO_2$+AR		7.00E+17	-0.8	0.0	GRI-Mech 3.0
3	$H_2 + O \leftrightarrow OH + H$		5.06E+04	2.67	26.3	Rightley et al.,1997
4	$H_2 + OH \leftrightarrow H_2O + H$		1.17E+09	1.3	15.2	Rightley et al.,1997
5	$H_2O + O \leftrightarrow 2OH$		7.60E+00	3.84	53.5	Rightley et al.,1997
6[a]	$H + H + M1 \leftrightarrow H_2 + M1$		1.30E+18	-1	0.0	Saxena et al.,2006
7[a]	$H + OH + M2 \leftrightarrow H_2O + M2$		4.00E+22	-2	0.0	Saxena et al.,2006
8[a]	$O + O + M3 \leftrightarrow O_2 + M3$		6.17E+15	-0.5	0.0	Saxena et al.,2006
9[a]	$H + O + M4 \leftrightarrow OH + M4$		4.71E+18	-1	0.0	Saxena et al.,2006
10[a]	$O + OH + M4 \leftrightarrow HO_2 + M4$		8.00E+15	0	0.0	Saxena et al.,2006
11[b]	$H + O_2 + M5 \leftrightarrow HO_2 + M5$	k_0	5.75E+19	-1.4	0.0	Troe,2000
		k_∞	4.65E+12	0.44	0.0	
12	$HO_2 + H \leftrightarrow 2OH$		7.08E+13	0	1.2	Mueller et al,1999
13	$HO_2 + H \leftrightarrow H_2 + O_2$		1.66E+13	0	3.4	Mueller et al,1999
14	$HO_2 + H \leftrightarrow H_2O + O$		3.10E+13	0	7.2	Rightley et al.,1997
15	$HO_2 + O \leftrightarrow OH + O_2$		2.00E+13	0	0.0	Warnatz,1984
16	$HO_2 + OH \leftrightarrow H_2O + O_2$		2.89E+13	0	-2.1	Rightley et al.,1997
17[b]	$2OH + M6 \leftrightarrow H_2O_2 + M6$	k_0	2.30E+18	-0.9	-7.12	Rightley et al.,1997
		k_∞	7.40E+13	-0.37	0.0	
18	$2HO_2 \leftrightarrow H_2O_2 + O_2$		3.02E+12	0	5.8	Rightley et al.,1997
19	$H_2O_2 + H \leftrightarrow HO_2 + H_2$		4.79E+13	0	33.3	Yetter et al.,1991
20	$H_2O_2 + OH \leftrightarrow H_2O + HO_2$		7.08E+12	0	6.0	Rightley et al.,1997
21	$CO + OH \leftrightarrow CO_2 + H$		4.40E+06	1.5	-3.1	Rightley et al.,1997
22	$CO + HO_2 \leftrightarrow CO_2 + OH$		6.00E+13	0	96.0	Rightley et al.,1997
23[a]	$HCO + M7 \leftrightarrow CO + H + M7$		1.86E+17	-1	71.1	Lindstedt et al.,1997
24	$HCO + OH \leftrightarrow CO + H_2O$		3.00E+13	0	0.0	Teang et al.,1986
25	$HCO + O_2 \leftrightarrow CO + HO_2$		7.58E+12	0	1.7	Timonen et al.,1988
26	$HCO + CH_3 \leftrightarrow CO + CH_4$		5.00E+13	0	0.0	Saxena et al.,2005
27[b]	$H + HCO + M8 \leftrightarrow CH_2O + M8$	k_0	1.35E+24	-2.57	1.78	GRI-Mech 3.0
		k_∞	1.09E+12	0.48	-1.1	
28	$CH_2O + H \leftrightarrow HCO + H_2$		5.74E+07	1.9	11.5	Li, 2004
29	$CH_2O + O \leftrightarrow HCO + OH$		3.50E+13	0	14.7	Rightley et al.,1997
30	$CH_2O + OH \leftrightarrow HCO + H_2O$		3.90E+10	0.89	1.7	Rightley et al.,1997
31	$CH_2O + HO_2 \leftrightarrow HCO + H_2O_2$		4.11E+04	2.5	42.7	Eiteneer et al.,1998
32	$CH_4 + H \leftrightarrow H_2 + CH_3$		1.30E+04	3	33.6	Hewson et al.,1999
33	$CH_4 + OH \leftrightarrow H_2O + CH_3$		1.60E+07	1.83	11.6	Hewson et al.,1999
34	$CH_4 + O \leftrightarrow CH_3 + OH$		1.90E+09	1.44	36.3	Frenklash et al.,1992

35	$CH_4 + O_2 \leftrightarrow CH_3 + HO_2$		3.98E+13	0	238.1	Lindstedt et al.,1997
36	$CH_3 + H \leftrightarrow TCH_2 + H_2$		1.80E+14	0	63.2	Frenklach et al.,1992
37	$CH_3 + H \leftrightarrow SCH_2 + H_2$		1.55E+14	0	56.4	Frenklach et al.,1992
38	$CH_3 + OH \leftrightarrow SCH_2 + H_2O$		4.00E+13	0	10.5	Grotheer et al., 1992
39	$CH_3 + O \leftrightarrow CH_2O + H$		8.43E+13	0	0.0	Frenklach et al.,1992
40	$CH_3 + TCH_2 \leftrightarrow C_2H_4 + H$		4.22E+13	0	0.0	Baulch et al.,1992
41	$CH_3 + HO_2 \leftrightarrow CH_3O + OH$		5.00E+12	0	0.0	Baulch et al.,1992
42	$CH_3 + O_2 \leftrightarrow CH_2O + OH$		3.30E+11	0	37.4	Zeller et al., 1988
43	$CH_3 + O_2 \leftrightarrow CH_3O + O$		1.10E+13	0	116.4	Zeller et al., 1988
44	$CH_3 + CH_3 \leftrightarrow C_2H_4 + H_2$		1.00E+14	0	133.9	Hidaka et al., 1990
45	$CH_3 + CH_3 \leftrightarrow C_2H_5 + H$		3.16E+13	0	61.5	Lim et al., 1994
46[b]	$H + CH_3 + M9 \leftrightarrow CH_4 + M9$	k_0	2.47E+33	-4.76	10.2	GRI-Mech 3.0
		k_∞	1.27E+16	-0.63	1.6	
47[b]	$2CH_3 + M8 \leftrightarrow C_2H_6 + M8$	k_0	1.27E+41	-7	11.6	Hewson et al.,1999
		k_∞	1.81E+13	0	0.0	
48	$SCH_2+AR \leftrightarrow TCH_2+AR$		9.00E+12	0	2.5	GRI-Mech 3.0
49	$SCH_2 + O_2 \leftrightarrow CO + OH + H$		3.13E+13	0	0.0	Frenklach et al.,1992
50	$SCH_2 + CO_2 \leftrightarrow CO + CH_2O$		3.00E+12	0	0.0	Leung et al., 1995
51[a]	$SCH_2 + M10 \leftrightarrow TCH_2 + M10$		6.00E+12	0	0.0	Frenklach et al.,1992
52	$TCH_2 + H \leftrightarrow CH + H_2$		6.02E+12	0	-7.5	Baulch et al.,1992
53	$TCH_2 + OH \leftrightarrow CH_2O + H$		2.50E+13	0	0.0	Frenklach et al.,1992
54	$TCH_2 + OH \leftrightarrow CH + H_2O$		1.13E+07	2	12.6	Frenklach et al.,1992
55	$TCH_2 + O \leftrightarrow CO+2H$		8.00E+13	0	0.0	Frank et al., 1986
56	$TCH_2 + O \leftrightarrow CO + H_2$		4.00E+13	0	0.0	Frank et al., 1986
57	$TCH_2 + O_2 \leftrightarrow CO_2 + H_2$		2.63E+12	0	6.2	Leung et al., 1995
58	$TCH_2 + O_2 \leftrightarrow CO + OH + H$		6.58E+12	0	6.2	Leung et al., 1995
59	$TCH_2 + TCH_2 \leftrightarrow C_2H_2+2H$		1.00E+14	0	0.0	Frenklach et al.,1992
60	$CH + O_2 \leftrightarrow HCO + O$		1.77E+11	0.76	-2.0	Markus et al., 1996
61	$CH + H_2O \leftrightarrow CH_2O + H$		1.17E+15	-0.75	0.0	Leung et al., 1995
62	$CH + CO_2 \leftrightarrow HCO + CO$		48	3.22	-13.5	Markus et al., 1996
63	$CH_3O + H \leftrightarrow SCH_2 + H_2O$		1.60E+13	0	0.0	Li et al., 1998
64	$CH_3O + O_2 \leftrightarrow CH_2O + HO_2$		4.28E-13	7.6	-14.8	Li et al., 1998
65[a]	$CH_3O + M9 \leftrightarrow CH_2O + H + M9$		7.78E+13	0	56.5	Saxena et al.,2005
66	$C_2H_6 + H \leftrightarrow C_2H_5 + H_2$		540	3.5	21.8	Frenklach et al.,1992
67	$C_2H_6 + O \leftrightarrow C_2H_5 + OH$		1.40E+00	4.3	11.6	Frenklach et al.,1992
68	$C_2H_6 + OH \leftrightarrow C_2H_5 + H_2O$		2.20E+07	1.9	4.7	Frenklach et al.,1992
69[b]	$C_2H_6 + M8 \leftrightarrow C_2H_5 + H + M8$	k_0	4.90E+42	-6.43	448	Hewson et al.,1999
		k_∞	8.85E+20	-1.23	427.8	

70	$C_2H_6 + HO_2 \leftrightarrow C_2H_5 + H_2O_2$		1.32E+13	0	85.7	Baulch et al.,1992
71	$C_2H_5 + H \leftrightarrow C_2H_4 + H_2$		3.00E+13	0	0.0	Frenklach et al.,1992
72	$C_2H_5 + O \leftrightarrow CH_3 + CH_2O$		4.24E+13	0	0.0	Frenklach et al.,1992
73	$C_2H_5 + O_2 \leftrightarrow C_2H_4 + HO_2$		2.00E+12	0	20.9	Frenklach et al.,1992
74[b]	$C_2H_5 + M9 \leftrightarrow C_2H_4 + H + M9$	k_0	3.99E+33	-4.99	167	Feng et al., 1993
		k_∞	1.11E+10	1.037	153.9	
75	$C_2H_4 + H \leftrightarrow C_2H_3 + H_2$		4.49E+07	2.12	55.9	Bhargava et al., 1998
76	$C_2H_4 + OH \leftrightarrow C_2H_3 + H_2O$		5.53E+05	2.31	12.4	Bhargava et al., 1998
77	$C_2H_4 + O \leftrightarrow CH_3 + HCO$		2.25E+06	2.08	0.0	Baulch et al.,1992
78	$C_2H_4 + O \leftrightarrow CH_2CHO + H$		1.21E+06	2.08	0.0	Baulch et al.,1992
79	$C_2H_4 + O_2 \leftrightarrow C_2H_3 + HO_2$		4.22E+13	0	241.1	Baulch et al., 1994
80	$C_2H_4 + HO_2 \leftrightarrow C_2H_4O + OH$		2.23E+12	0	71.9	Baulch et al.,1992
81	$C_2H_4O + HO_2 \leftrightarrow CH_3 + CO + H_2O_2$		4.00E+12	0	71.2	Baulch et al.,1992
82[a]	$C_2H_4 + M9 \leftrightarrow C_2H_3 + H + M9$		2.60E+17	0	404.1	Baulch et al., 1994
83[a]	$C_2H_4 + M9 \leftrightarrow C_2H_2 + H_2 + M9$		3.50E+16	0	299.3	Baulch et al., 1994
84	$C_2H_3 + H \leftrightarrow C_2H_2 + H_2$		4.00E+13	0	0.0	Saxena et al.,2005
85[b]	$C_2H_3 + M9 \leftrightarrow C_2H_2 + H + M9$	k_0	1.51E+14	0.1	137	Williams et al.,2001
		k_∞	6.38E+09	1	157.5	
86	$C_2H_3 + O_2 \leftrightarrow CH_2O + HCO$		1.70E+29	-5.312	27.2	Marinov et al., 1998
87	$C_2H_3 + O_2 \leftrightarrow CH_2CHO + O$		7.00E+14	-0.611	22.0	Williams et al.,2001
88	$C_2H_3 + O_2 \leftrightarrow C_2H_2 + HO_2$		5.19E+15	-1.26	13.9	Williams et al.,2001
89	$C_2H_2 + O \leftrightarrow HCCO + H$		4.00E+14	0	44.6	Frank et al., 1986
90	$C_2H_2 + O \leftrightarrow TCH_2 + CO$		1.60E+14	0	41.4	Frank et al., 1986
91	$C_2H_2 + O_2 \leftrightarrow CH_2O + CO$		4.60E+15	-0.54	188.0	Waly et al., 2001
92	$C_2H_2 + OH \leftrightarrow CH_2CO + H$		1.90E+07	1.7	4.2	Lindstedt et al.,1997
93	$C_2H_2 + OH \leftrightarrow C_2H + H_2O$		3.37E+07	2	58.6	Lindstedt et al.,1997
94	$CH_2CO + H \leftrightarrow CH_3 + CO$		1.50E+09	1.43	11.3	Petrova et al., 2006
95	$CH_2CO + O \leftrightarrow TCH_2 + CO_2$		2.00E+13	0	9.6	Lindstedt et al.,1997
96	$CH_2CO + O \leftrightarrow HCCO + OH$		1.00E+13	0	8.4	Lindstedt et al.,1997
97	$CH_2CO + CH_3 \leftrightarrow C_2H_5 + CO$		9.00E+10	0	0.0	Lindstedt et al.,1997
98	$HCCO + H \leftrightarrow SCH_2 + CO$		1.50E+14	0	0.0	Frank et al., 1986
99	$HCCO + O \leftrightarrow 2CO + H$		9.64E+13	0	0.0	Frank et al., 1986
100	$HCCO + O_2 \leftrightarrow 2CO + OH$		2.88E+07	1.7	4.2	Williams et al.,2001
101	$HCCO + O_2 \leftrightarrow CO_2 + CO + H$		1.40E+07	1.7	4.2	Williams et al.,2001
102	$C_2H + OH \leftrightarrow HCCO + H$		2.00E+13	0	0.0	Frenklach et al.,1992
103	$C_2H + O \leftrightarrow CO + CH$		1.02E+13	0	0.0	Frenklach et al.,1992
104	$C_2H + O_2 \leftrightarrow CH + CO_2$		4.50E+15	0	105.0	Frenklach et al.,1992
105	$C_2H + O_2 \leftrightarrow HCO + CO$		2.41E+12	0	0.0	Frenklach et al.,1992

106	$CH_2OH + H \leftrightarrow CH_2O + H_2$		3.00E+13	0	0.0	Li et al., 1998
107	$CH_2OH + H \leftrightarrow CH_3 + OH$		2.50E+17	-0.93	21.5	Saxena et al.,2005
108	$CH_2OH + OH \leftrightarrow CH_2O + H_2O$		2.40E+13	0	0.0	Li et al., 1998
109	$CH_2OH + O_2 \leftrightarrow CH_2O + HO_2$		5.00E+12	0	0.0	Li et al., 1998
110[a]	$CH_2OH + M9 \leftrightarrow CH_2O + H + M9$		5.00E+13	0	105.1	Li et al., 1998
111[a]	$CH_3O + M9 \leftrightarrow CH_2OH + M9$		1.00E+14	0	80.0	Li et al., 1998
112	$CH_2CO + OH \leftrightarrow CH_2OH + CO$		1.02E+13	0	0.0	Li et al., 1998
113	$CH_3OH + OH \leftrightarrow CH_2OH + H_2O$		1.44E+06	2	-3.5	Li et al., 1998
114	$CH_3OH + OH \leftrightarrow CH_3O + H_2O$		4.40E+06	2	6.3	Saxena et al.,2005
115	$CH_3OH + H \leftrightarrow CH_2OH + H_2$		1353.8	3.2	14.6	Jodkowski et al.,1999
116	$CH_3OH + H \leftrightarrow CH_3O + H_2$		68.3	3.4	30.3	Jodkowski et al.,1999
117	$CH_3OH + O \leftrightarrow CH_2OH + OH$		1.00E+13	0	19.6	Li et al., 1998
118	$CH_3OH + HO_2 \leftrightarrow CH_2OH + H_2O_2$		6.20E+12	0	81.1	Li et al., 1998
119[b]	$CH_3OH + M9 \leftrightarrow CH_3 + OH + M9$	k_0	2.95E+44	-7.35	399	Held et al., 1998
		k_∞	1.90E+16	0	383.9	
120	$CH_2CHO \leftrightarrow CH_2CO + H$		1.05E+37	-7.189	185.6	Marinov et al., 1995
121	$CH_2CHO + H \leftrightarrow CH_2CO + H_2$		2.00E+13	0	0.0	Li, 2004
122	$CH_2CHO + O \leftrightarrow CH_2O + HCO$		1.00E+14	0	0.0	Li, 2004
123	$CH_2CHO + O_2 \leftrightarrow CH_2O + CO + OH$		3.00E+10	0	0.0	Li, 2004
124	$CH_2CHO + CH_3 \leftrightarrow C_2H_5 + CO + H$		4.90E+14	-0.5	0.0	Li, 2004
125	$CH_2CHO + HO_2 \leftrightarrow CH_2O + HCO + OH$		7.00E+12	0	0.0	Li, 2004
126	$CH_2CHO + HO_2 \leftrightarrow CH_3CHO + O_2$		3.00E+12	0	0.0	Li, 2004
127	$CH_2CHO \leftrightarrow CH_3 + CO$		1.17E+43	-9.8	183.3	Li, 2004
128	$CH_3CHO \leftrightarrow CH_3 + HCO$		7.00E+15	0	341.9	Li, 2004
129[b]	$CH_3CO + M9 \leftrightarrow CH_3 + CO + M9$	k_0	1.20E+15	0	52.3	Li, 2004
		k_∞	3.00E+12	0	69.9	
130	$CH_3CHO + OH \leftrightarrow CH_3CO + H_2O$		3.37E+12	0	-2.6	Li, 2004
131	$CH_3CHO + O \leftrightarrow CH_2CHO + OH$		3.72E+13	-0.2	14.9	Li, 2004
132	$CH_3CHO + H \leftrightarrow CH_3CO + H_2$		4.66E+13	-0.3	12.5	Li, 2004
133	$CH_3CHO + H \leftrightarrow CH_2CHO + H_2$		1.85E+12	0.4	22.4	Li, 2004
134	$CH_3CHO + CH_3 \leftrightarrow CH_3CO + CH_4$		3.90E-07	5.8	9.2	Li, 2004
135	$CH_3CHO + CH_3 \leftrightarrow CH_2CHO + CH_4$		2.45E+01	3.1	24.0	Li, 2004
136	$CH_3CHO + HO_2 \leftrightarrow CH_3CO + H_2O_2$		3.60E+19	-2.2	58.6	Li, 2004
137	$CH_3CHO + O_2 \leftrightarrow CH_3CO + HO_2$		1.00E+14	0	176.6	Li, 2004
138[b]	$C_2H_5OH + M9 \leftrightarrow CH_3 + CH_2OH + M9$	k_0	3.00E+16	0	243	Saxena et al.,2005
		k_∞	5.00E+15	0	343.1	
139[b]	$C_2H_5OH + M9 \leftrightarrow C_2H_4 + H_2O + M9$	k_0	1.00E+17	0	226	Saxena et al.,2005
		k_∞	8.00E+13	0	272.0	

140	$C_2H_5OH + OH \leftrightarrow CH_2CH_2OH + H_2O$		1.81E+11	0.4	3.0	Li, 2004
141	$C_2H_5OH + OH \leftrightarrow CH_3CHOH + H_2O$		3.09E+10	0.5	-1.6	Li, 2004
142	$C_2H_5OH + OH \leftrightarrow CH_3CH_2O + H_2O$		1.05E+10	0.8	3.0	Li, 2004
143	$C_2H_5OH + H \leftrightarrow CH_3CHOH + H_2$		2.58E+07	1.6	11.8	Li, 2004
144	$C_2H_5OH + O \leftrightarrow CH_2CH_2OH + OH$		9.41E+07	1.7	22.8	Li, 2004
145	$C_2H_5OH + O \leftrightarrow CH_3CHOH + OH$		1.88E+07	1.9	7.6	Li, 2004
146	$C_2H_5OH + O \leftrightarrow CH_3CH_2O + OH$		1.58E+07	2	18.6	Li, 2004
147	$C_2H_5OH + CH_3 \leftrightarrow CH_3CHOH + CH_4$		728	3	33.3	Li, 2004
148	$C_2H_5 + HO_2 \leftrightarrow CH_3CH_2O + OH$		4.00E+13	0	0.0	Li, 2004
149[a]	$CH_3CH_2O + M9 \leftrightarrow CH_3CHO + H + M9$		5.60E+34	-5.9	105.9	Li, 2004
150[a]	$CH_3CH_2O + M9 \leftrightarrow CH_3 + CH_2O + M9$		5.35E+37	-7	99.6	Li, 2004
151	$CH_3CH_2O + CO \leftrightarrow C_2H_5 + CO_2$		468	3.2	22.5	Li, 2004
152	$CH_3CH_2O + H \leftrightarrow C_2H_4 + H_2O$		3.00E+13	0	0.0	Li, 2004
153	$CH_3CHOH + O_2 \leftrightarrow CH_3CHO + HO_2$		4.82E+13	0	21.0	Li, 2004
154	$CH_3CHOH + O \leftrightarrow CH_3CHO + OH$		1.00E+14	0	0.0	Li, 2004
155	$CH_3CHOH + H \leftrightarrow C_2H_4 + H_2O$		3.00E+13	0	0.0	Li, 2004
156	$CH_3CHOH + H \leftrightarrow CH_3 + CH_2OH$		3.00E+13	0	0.0	Li, 2004
157[a]	$CH_3CHOH+M9 \leftrightarrow CH_3CHO + H + M9$		1.00E+14	0	104.6	Li, 2004
158	$C_3H_4 + O \leftrightarrow C_2H_4 + CO$		2.00E+07	1.8	4.2	Davis et al., 1999
159	$CH_3 + C_2H_2 \leftrightarrow C_3H_4 + H$		2.56E+09	1.1	57.1	Davis et al., 1999
160	$C_3H_4 + O \leftrightarrow HCCO + CH_3$		7.30E+12	0	9.4	Davis et al., 1999
161[b]	$C_3H_3 + H + M \leftrightarrow C_3H_4 + M$	k_0	9.00E+15	1	0.0	Petrova et al., 2006
		k_∞	3.00E+13	0	0.0	
162	$C_3H_3 + HO_2 \leftrightarrow C_3H_4 + O_2$		2.50E+12	0	0.0	Petrova et al., 2006
163	$C_3H_4 + OH \leftrightarrow C_3H_3 + H_2O$		5.30E+06	2	8.4	Wang et al., 1997
164	$C_3H_3 + O_2 \leftrightarrow CH_2CO + HCO$		3.00E+10	0	12.0	Slagle et al., 1986
165[b]	$C_3H_4 + H + M \leftrightarrow C_3H_5 + M$	k_0	3.00E+24	-2	0.0	Petrova et al., 2006
		k_∞	4.00E+13	0	0.0	
166	$C_3H_5 + H \leftrightarrow C_3H_4 + H_2$		1.80E+13	0	0.0	Tsang et al., 1991
167	$C_3H_5 + CH_3 \leftrightarrow C_3H_4 + CH_4$		3.00E+12	-0.32	-0.5	Petrova et al., 2006
168[b]	$C_2H_2 + CH_3 + M \leftrightarrow C_3H_5 + M$	k_0	2.00E+09	1	0.0	Petrova et al., 2006
		k_∞	6.00E+08	0	0.0	
169	$C_3H_5 + OH \leftrightarrow C_3H_4 + H_2O$		6.00E+12	0	0.0	Petrova et al., 2006
170	$C_3H_3 + HO_2 \leftrightarrow OH + CO + C_2H_3$		8.00E+11	0	0.0	Davis et al., 1999
171	$C_3H_4 + O_2 \leftrightarrow CH_3 + HCO + CO$		4.00E+14	0	175.0	Wang et al., 2001
172	$C_3H_6 + O \leftrightarrow C_2H_5 + HCO$		3.50E+07	1.65	-4.1	Tsang et al., 1991
173	$C_3H_6 + OH \leftrightarrow C_3H_5 + H_2O$		3.10E+06	2	-1.2	Tsang et al., 1991
174	$C_3H_6 + O \leftrightarrow CH_2CO + CH_3 + H$		1.20E+08	1.65	1.4	Tsang et al., 1991

175	$C_3H_6 + H \leftrightarrow C_3H_5 + H_2$		1.70E+05	2.5	10.4	Tsang et al., 1991
176[b]	$C_3H_5 + H + M8 \leftrightarrow C_3H_6 + M8$	k_0	1.33E+60	-12	25.0	Davis et al., 1999
		k_∞	2.00E+14	0	0.0	
177	$C_3H_5 + HO_2 \leftrightarrow C_3H_6 + O_2$		2.66E+12	0	0.0	Baulch et al.,1992
178	$C_3H_5 + HO_2 \leftrightarrow OH + C_2H_3 + CH_2O$		3.00E+12	0	0.0	Baulch et al.,1992
179[b]	$C_2H_3+CH_3+M8 \leftrightarrow C_3H_6 + M8$	k_0	4.27E+58	-11.94	40.9	Davis et al., 1999
		k_∞	2.50E+13	0	0.0	
180	$C_3H_6 + H \leftrightarrow C_2H_4 + CH_3$		1.60E+22	-2.39	46.8	Davis et al., 1999
181	$CH_3 + C_2H_3 \leftrightarrow C_3H_5 + H$		1.50E+24	-2.83	77.9	Davis et al., 1999
182[b]	$C_3H_8 + M \leftrightarrow CH_3 + C_2H_5 + M$	k_0	7.83E+18	0	272	Baulch et al., 1994
		k_∞	1.10E+17	0	353.2	
183	$C_3H_8 + O_2 \leftrightarrow IC_3H_7 + HO_2$		4.00E+13	0	198.8	Williams et al., 2000
184	$C_3H_8 + H \leftrightarrow IC_3H_7 + H_2$		1.30E+06	2.4	18.7	Williams et al., 2000
185	$C_3H_8 + H \leftrightarrow NC_3H_7 + H_2$		1.33E+06	2.54	28.3	Tsang et al., 1988
186	$C_3H_8 + O \leftrightarrow IC_3H_7 + OH$		4.76E+04	2.71	8.8	Tsang et al., 1988
187	$C_3H_8 + O \leftrightarrow NC_3H_7 + OH$		1.90E+05	2.68	15.6	Tsang et al., 1988
188	$C_3H_8 + HO_2 \leftrightarrow NC_3H_7 + H_2O_2$		4.76E+04	2.55	69.0	Tsang et al., 1988
189[b]	$C_3H_6 + H + M8 \leftrightarrow IC_3H_7 + M8$	k_0	8.70E+42	-7.5	19.8	Davis et al., 1999
		k_∞	1.33E+13	0	6.5	
190[b]	$NC_3H_7 + M \leftrightarrow CH_3 + C_2H_4 + M$	k_0	5.49E+49	-10	150.0	Tsang et al., 1988
		k_∞	1.23E+13	-0.1	126.4	
191[b]	$H + C_3H_6 + M8 \leftrightarrow NC_3H_7 + M8$	k_0	6.26E+38	-6.66	29.3	Tsang et al., 1988
		k_∞	1.33E+13	0	13.6	
192	$C_4H_6 \rightarrow C_2H_2 + C_2H_3 + H$		1.58E+16	0	460.3	Li et al., 2001
193	$C_4H_6 \rightarrow 2C_2H_3$		1.80E+13	0	356.2	Li et al., 2001
194	$2C_2H_3 \rightarrow C_4H_6$		1.26E+13	0	0.0	Li et al., 2001
195	$C_4H_6 + H \rightarrow C_2H_3 + C_2H_4$		5.00E+11	0	0.0	Li et al., 2001
196	$C_4H_6 + H \rightarrow H_2 + C_2H_2 + C_2H_3$		6.30E+10	0.7	25.1	Li et al., 2001
197	$C_4H_6 + OH \rightarrow CHO + H + C_3H_5$		5.00E+12	0	0.0	Li et al., 2001
198	$C_4H_6 + CH_3 \rightarrow CH_4 + C_2H_2 + C_2H_3$		7.00E+13	0	77.1	Li et al., 2001
199	$C_3H_3 + CH_3 \rightarrow C_4H_6$		5.00E+12	0	0.0	Li et al., 2001
200	$C_5H_8 \rightarrow C_3H_6 + C_2H_2$		1.00E+16	0	305.2	Li et al., 2001
201	$C_5H_8 \rightarrow C_3H_4 + C_2H_4$		3.16E+12	0	238.8	Li et al., 2001
202	$C_5H_8 \rightarrow C_3H_5 + C_2H_3$		3.16E+12	0	238.8	Li et al., 2001
203	$C_5H_8 + O_2 \rightarrow C_2H_2 + C_3H_5 + HO_2$		3.00E+12	0	0.0	Li et al., 2001
204	$C_5H_8 + O_2 \rightarrow C_2H_3 + C_3H_4 + HO_2$		3.00E+12	0	0.0	Li et al., 2001
205	$C_5H_8 + HO_2 \rightarrow C_2H_2 + C_3H_5 + H_2O_2$		1.00E+14	0	0.0	Li et al., 2001
206	$C_5H_8 + HO_2 \rightarrow C_2H_3 + C_3H_4 + H_2O_2$		1.00E+14	0	0.0	Li et al., 2001

207	$C_{10}H_{16} \rightarrow H + C_3H_3 + C_2H_4 + C_5H_8$	6.00E+16	0	410.3	Li et al., 2001
208	$C_{10}H_{16} \rightarrow H + C_3H_5 + C_2H_2 + C_5H_8$	6.00E+16	0	410.7	Li et al., 2001
209	$C_{10}H_{16} \rightarrow C_2H_2 + 2C_2H_4 + C_4H_6$	5.00E+16	0	357.6	Li et al., 2001
210	$C_{10}H_{16} + H \rightarrow H_2 + C_3H_3 + C_2H_4 + C_5H_8$	1.32E+06	2.54	28.3	Li et al., 2001
211	$C_{10}H_{16} + O \rightarrow OH + C_3H_3 + C_2H_4 + C_5H_8$	2.88E+06	2.4	23.0	Li et al., 2001
212	$C_{10}H_{16} + OH \rightarrow H_2O + C_3H_3 + C_2H_4 + C_5H_8$	1.74E+07	1.8	4.1	Li et al., 2001
213	$C_{10}H_{16} + O_2 \rightarrow HO_2 + C_3H_3 + C_2H_4 + C_5H_8$	3.98E+13	0	213.1	Li et al., 2001
214	$C_{10}H_{16} + HO_2 \rightarrow H_2O_2 + C_3H_3 + C_2H_4 + C_5H_8$	4.76E+04	2.55	69.1	Li et al., 2001
215	$C_{10}H_{16} + H \rightarrow H_2 + C_3H_5 + C_2H_2 + C_5H_8$	2.60E+06	2.4	18.7	Li et al., 2001
216	$C_{10}H_{16} + O \rightarrow OH + C_3H_5 + C_2H_2 + C_5H_8$	2.76E+05	2.6	8.0	Li et al., 2001
217	$C_{10}H_{16} + OH \rightarrow H_2O + C_3H_5 + C_2H_2 + C_5H_8$	3.80E+06	2	-2.5	Li et al., 2001
218	$C_{10}H_{16} + O_2 \rightarrow HO_2 + C_3H_5 + C_2H_2 + C_5H_8$	7.92E+13	0	199.2	Li et al., 2001
219	$C_{10}H_{16} + HO_2 \rightarrow H_2O_2 + C_3H_5 + C_2H_2 + C_5H_8$	1.93E+04	2.6	58.2	Li et al., 2001

Rate constant are written as $AT^n exp\left(^{-E}/_{RT}\right)$

Units are mol, cm^3, kJ, K.